UNIVERSITY OF SOUTHAMPTON
FACULTY OF ENGINEERING, SCIENCE & MATHERMATICS
School of Engineering Sciences

CHARACTERISATION AND COMPUTATIONAL MODELLING OF ACRYLIC BONE CEMENT POLYMERISATION

Adam Briscoe

A thesis submitted in partial fulfilment of the requirements for the degree of

Doctor of Philosophy

School of Engineering Sciences

Bioengineering Sciences Research Group

September 2006

Abstract
Bioengineering Sciences Research Group
School of Engineering Sciences
University of Southampton
Doctor of Philosophy

by Adam Briscoe

Total joint replacement is one of the most successful surgical procedures and is a proven treatment for arthritis. Despite low failure rates, the wide application of the treatment means that large numbers of prostheses fail and must be revised. Improved pre-clinical testing methods for these orthopaedic devices may assist in developing new prostheses with improved clinical results. Computational modelling of biological systems is becoming increasingly accurate and is a much quicker and cheaper alternative to physical testing, but continued development is necessary to ensure computational models produce accurate and reliable predictions of implant behaviour.

Acrylic bone cements have been used as a method of fixation for over 50 years but despite improvements in cement handling techniques and numerous attempts to improve the mechanical properties of the cement in other ways, the cement is often highlighted as the weak link in the joint replacement system. Aseptic loosening is cited as the cause for the majority of revision operations and cement degradation has been shown to be a contributor to the loosening process. *In-vivo*, cement is subject to cyclic loads and these are the primary cause of cement damage. Residual stresses generated during the polymerisation of the cement are now thought to play a significant role in cement failure.

This thesis examines the development of residual stresses as a result of thermal and chemical changes during polymerisation of the cement. Experimental techniques for characterising the evolution of materials properties during the polymerisation reaction are discussed. Differential scanning calorimetry was used to measure the reaction variables such as the activation energy of polymerisation. The development of an ultrasonic rheometry technique for monitoring the mechanical property evolution within a bone cement specimen is discussed. Computational models were generated to predict the reaction behaviour of the cement in terms of the heat produced and the evolution of the physical properties of the curing mass. Some advantages and disadvantages of candidate mathematical models have been evaluated and are discussed, along with applications in several implant fixation scenarios.. The model compared well with experimental data and was used to predict thermal necrosis in the bone surrounding both a hip resurfacing implant and a knee replacement. Using the output reaction path produced by the thermal model a mechanical model was also produced simulating the shrinkage and mechanical property evolution exhibited by the polymerising cement. Two material models were compared with and without the effects of plasticity. Residual stress magnitudes were assessed in comparison with published values and showed better agreement when plasticity was included. Peak stresses were observed to occur during polymerisation. The location of the peak stresses were compared with experimental data on pre-load crack locations in the literature and showed good agreement.

TABLE OF CONTENTS

TABLE OF FIGURES

TABLE OF TABLES

ACKNOWLEDGEMENTS

As with most degrees at this level, this doctorate has been undertaken with commitment, dedication and determination on my own part. For this, I want to thank my parents who imparted and occasionally imposed these qualities upon me through my upbringing. Not only have they always sought to provide the best for me but have always been able to see the best way to advise me on all matters in life. Also, I must thank, Simon, for his counsel and for being a big brother to me.

I thank all of my colleagues; from everyone in the office to the technicians in the workshop and of course the academic staff here at the University of Southampton. Thank you to Dr. Nader Saffari of University College London without whom the ultrasonic testing would have been a non-starter. A large thank you also has to go to my supervisor and good friend Dr. Andrew New. Thank you for your guidance and support. Thank you also to my advisors, Dr. Martin Browne and Prof. Mark Taylor.

The biggest thanks of all has to go to whom I return home each day and who usually has a smile on her face to bring me back from the brink of despair, that we all approach once in a while. Anna, you have been my inspiration, during this project, which kept me going throughout. For your continued, unconditional love and unquestioned support I cannot thank you enough.

1 Introduction

At this time the cause of osteoarthritis is unknown. However, in middle-aged to elderly people the early features of the disease include roughening of the joint surfaces, loss of articular cartilage and the appearance of osteophytes (bony spurs). The joint responds by producing excessive synovial fluid resulting in swelling and restricted movement. In severe cases the cartilage may be completely rubbed away resulting in bone-on-bone contact, pain and alteration to joint loading. The resulting condition is often debilitating due to limited movement at the joint or pain during motion of the joint.

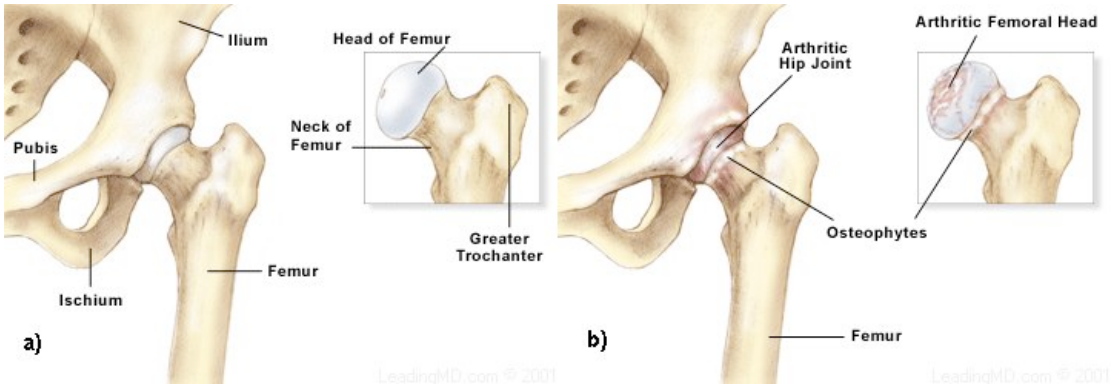

Figure 1-1 - Main features of a (a) normal hip and (b) osteoarthritic hip [105]

Throughout medical history many treatments for osteoarthritis have been used with varying degrees of success. Drugs have been used to suppress pain and to reduce swelling, restoring some function to the joint. Joint replacement surgery is usually a last resort for the treatment of osteoarthritis and has in the past been reserved for the elderly, who will have reduced requirements of the joint due to the lower levels of activity associated with old-age. More recently the age of candidates for joint replacement surgery has been slowly declining as a result of the success of the treatment, in turn creating greater need for robust and long lasting joint replacements.

Joint replacement surgery is one of the most successful procedures available today. Total joint replacement components have gone through several iterations before

arriving at the range available to surgeons in modern orthopaedics. The first joint replacements were interpositional spacers aiming to separate the joint surfaces and provide a better bearing surface. This procedure has been used for 150 years with variable success due to the variety and standard of manufacture of materials used. Materials have been a limiting factor throughout the history of joint replacement therapy. The early Judet prostheses were polymethylmethacrylate mouldings, positioned between the acetabulum and femoral head with a cobalt chrome rod inserted into the neck of the femur (Figure 1-2). Unfortunately the head of the prosthesis tended to be sheared off at the stem. Longer stemmed prostheses were developed to transfer load to the shaft of the bone rather than the neck.

Judet's attempts to produce a smooth polymer replacement, while unsuccessful, inspired Haboush in New York to develop self curing polymethylmethacrylate (PMMA) as a material for the fixation of dental prostheses into the bone [115]. At this time joint replacements addressed the loss of the bearing surface on the femoral head by replacing the head but did not modify the acetabulum.

Figure 1-2 - Radiographs and photographs of Charnley (left) and Judet (right) prostheses.

A surgeon named John Charnley (later Sir John Charnley) produced a novel concept in total hip arthroplasty. He proposed a long stemmed, low frictional-torque arthroplasty with a reduced head size articulating against a polymer insert in the

acetabulum. Early attempts used PTFE in the acetabulum but extreme wear of the acetabular component and severe tissue reactions due to wear debris were noted and caused Charnley to introduce ultra high molecular weight polyethylene (UHMWPE). For the first time, orthopaedic components were cemented in place using new PMMA based cement. With this combination, remarkable durability and previously unseen success rates and reliability were observed. A gold standard of total hip replacement was established against which modern designs are still routinely compared.

Since Charnley's success the design has been refined and cementing techniques have been developed to improve the mechanical properties of the cement and the interface between cement and bone. Broadly, there are three generations of cementation technique which have achieved increasing success with each generation. Initially the cement was mixed manually in a bowl and then finger packed into the prepared bone. Second generation techniques involved the insertion of a plug for the femoral cavity and insertion of cement using a cementation gun or syringe which assisted with pressurisation of the cement and in so doing increased interdigitation with trabecular bone. The current third generation cementing procedure requires the cement to be mixed under vacuum (for porosity reduction). The stem surface is also often treated (roughened to improve mechanical interlock with cement, or polished to reduce friction after debonding with cement) and a centraliser used to ensure the implant has a uniform cement mantle.

While over the past 25 years data has shown that joint replacement (in the hip at least) has been improving steadily (Figure 1-3, results from the Swedish Hip Register), in England and Wales in 2005 there were still over 4000 hip and 1500 knee revision procedures carried out. This represents a significant percentage of the operations being carried out annually. Currently the most common cause for revision operations in both hips and knees is aseptic loosening (Table 1-1 & Table 1-2) [113].

While the exact mechanism remains unclear, aseptic loosening has been attributed to damage in the cement mantle of cemented total joint arthroplasty. Damage of the cement mantle in total hip replacement is a product of the cyclic loading which is generated during patient activity. This cyclic loading causes fatigue failure of the cement. Cracks can initiate within the cement mantle in a number of different areas;

geometry generated areas of high stress, pores and/or inclusions and agglomerates of material within the matrix. If sufficient cracking of the cement mantle occurs, there may eventually be loss of support for the prosthesis. Also debris may be generated due to the damage process and should this debris reach bone tissue there is an opportunity for it to cause an osteolytic reaction and in turn resorption of bone.

Indications for Revision	Number of patients	Percentage of patients
Aseptic loosening	3367	78.8
Lysis	1053	24.6
Pain	687	16.1
Dislocation/subluxation	537	12.6
Periprosthetic fracture	298	7
Infection	293	6.9
Malalignment	256	6.0
Fractured acetabulum	93	2.2
Fractured stem	79	1.8
Fractured femoral head	18	0.4
Incorrect sizing/head socket mismatch	17	0.4
Other	802	18.8
Total	4274	100

Table 1-1 - Cause of hip revision operations in England and Wales during 2004 [113].

Indications for Revision	Number of patients	Percentage of patients
Aseptic loosening	1012	58.5
Pain	311	18.0
Lysis	301	17.4
Wear of polyethylene component	292	16.9
Instability	279	16.1
Infection	255	14.7
Malalignment	139	8.0
Dislocation/subluxation	93	5.4
Periprosthetic fracture	46	2.7
Implant fracture	41	2.4
Other	254	14.7
Total	1729	100

Table 1-2 - Cause of knee revision operations in England and Wales during 2004 [113].

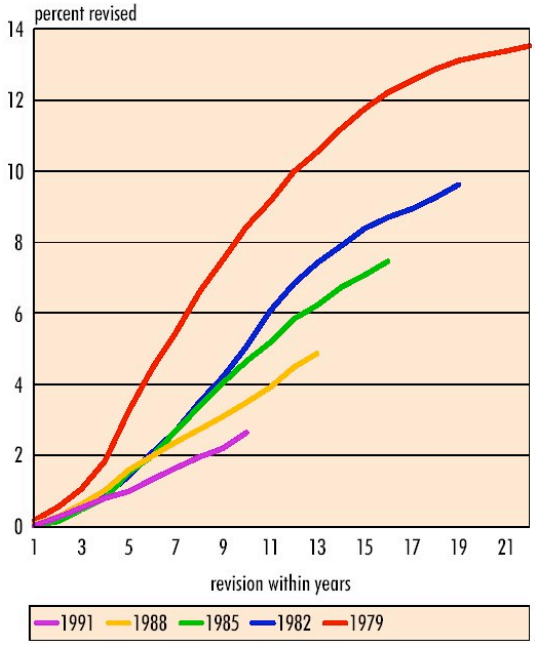

Figure 1-3 - Percent of cemented total hip arthroplasties revised due to aseptic loosening. Different coloured lines represent implants inserted in a different 5 year period between 1979 and 1991 [72].

A large number of studies have considered the mechanical performance of the cement mantle surrounding implants and how it relates to loosening [11, 34, 56]. To date very few studies have looked at the effects of the cement curing process on the mechanical performance. One aspect of the behaviour of cement which is of clinical relevance is heat release during curing. The polymerisation of polymethylmethacrylate (PMMA) bone cement is known to be an exothermic reaction. Bone is known to begin to die when held at temperatures above 40-50˚C for more than 1 minute. For this reason it is desirable to predict the temperature history of the cement during cure.

PMMA cement also undergoes a volume change during polymerisation. This volume change is generally negative (a shrinkage) [83]. If the cement is constrained during cure, as for example by the implant and bone in a joint replacement, the volume change may result in a residual stress field being generated in the cement. Alternatively, the shrinkage may be deleterious to the properties of the interfaces between bone and cement and cement and prosthesis. It is therefore necessary to investigate cement cure in terms of volume changes and mechanical property evolution alongside the temperature changes.

2 Statement of Problem and Objectives of Research

PMMA bone cement remains one of the most popular materials for prosthetic joint fixation. In the cementation process pre-polymerised powder is mixed with liquid monomer to form a paste, the paste is inserted into prepared bone stock and the prosthesis is then forced into contact with the mixture. The cement has no adhesive properties but pressurisation of the cement as a separate step or as the prosthesis is positioned generates a mechanical interlock between cement and prosthesis and cement and bone which secures the prosthesis to the bone once polymerisation is complete.

The fatigue life of the bone cement used is critical to the service life of the implant. If the bone cement fails then a revision operation may be required. Aseptic loosening was the cause for the large majority of revision operations carried out in Sweden between 1979 and 1998 [72]. Bone cement damage has been cited as a potential cause of loosening of the implant.

Revision operations involving retrieval of the prosthesis and cement mantle as well as x-ray imaging of cement mantles *in-vivo* have shown cement damage accumulation as a result of service loads. Several theories have been proposed as to the cause of this damage accumulation. Porosity, localised material defects and debonding of the stem-cement interface have all been cited as major contributing factors in the damage accumulation problem [48, 117, 118]. Jeffers *et al*. have shown that although these are indeed contributing factors, they may have less significance in increasing damage accumulation rates than residual stresses generated within the cement mantle during cure [53]. Several other studies have also shown that residual stress may have a major effect on the fatigue life of bone cement [18, 58, 63], but many authors have considered residual stresses to reduce to insignificant levels over time due to visco-elastic processes. Jeffers *et al*. have shown that this is unlikely to be the case since loading begins soon after insertion surgery and the residual stresses generated in the cement during surgery have insufficient time to relax post-operatively prior to

loading. While the residual stresses drop as a result of stress relaxation, they stabilise at a significant value even when visco-elastic effects are accounted for.

Attempts have been made to model the residual stress present in bone cement. Nuno *et al*. modelled the residual stress using a finite element contact model containing a cylindrical stem forced into a concentric cement mantle with interference between stem and cement [88]. This is an entirely empirical method based on generating a finite element model to fit previously established experimental data. Because this method is not based on a simulation of the curing process itself no allowance for the relative timing of different processes within the curing mass is made. The relative timings of the change in mechanical properties, the point at which peak temperature occurs and the change in volume may have considerable effects on the resulting residual stress field in the cured cement.

Lennon *et al*. developed a finite element model based on the results of experiments involving a cast block of PMMA [58]. By monitoring the temperature change and strain in the cement during polymerisation, a comparison between the peak temperature and a degree of polymerisation was possible, a noted improvement over many other models. The empirical function used to calculate the degree of polymerisation and in turn the temperature was previously published by Baliga *et al*. and Starke *et al*.

Empirical methods of residual stress prediction and cement polymerisation modelling such as these that depend on large numbers of parameters may cause problems when model parameters are fitted to match *in-vivo* results. Alternative cement compositions will require extensive testing before any modelling can be performed. By developing a model from first principles it may be possible to include all aspects of polymerisation such as temperature, mechanical property and volume changes. This will give a better idea of the residual stresses that develop in the cement mantle.

Research objectives were therefore to build a finite element model of bone cement polymerisation based on a more fundamental understanding of the polymerisation process. Simple methods for the determination of model variables have been investigated so as to enable future modelling of new innovations in cement

technology. Chemical, thermal and physical changes in cement have been modelled as a function of time. The resulting models may be used to generate a specification for the bone-cement-prosthesis system in order to minimise residual stresses induced during cure and extend the fatigue life of the cement mantles produced *in vivo*.

Modelling should begin with models predicting the thermal behaviour as well as the degree of polymerisation throughout the cement mantle during the polymerisation process. A parametric analysis should be undertaken and the model, validated experimentally.

Results from the parametric analysis should yield data indicating particular sensitivity to specific input variables and these should be determined experimentally.

A mechanical model of the shrinkage of polymerisation should be produced using mechanical property inputs defined using experimental analysis including the shrinkage strain and the mechanical properties at all stages of cure. This mechanical model should yield useful results of the residual stress due to cure and should be validated against published data.

3 Literature Review

3.1 Joint Replacement

3.1.1 Anatomy of Synovial Joint

Most of the large joints of the body, including the hip and the knee, are synovial joints. Characteristic features are that they:

- Provide a large range of motion.
- Form the junction of two bones, whose articular surfaces are covered with hyaline cartilage.
- Contain a joint space enclosed by a fibrous capsule. Thickened and organized areas of this capsule comprise the named ligaments.
- Have a synovial membrane lining the joint space. This membrane secretes synovial fluid, which fills the joint space and provides lubrication and nourishment to the articular cartilage.
- Have position(s) in the joint's range of motion where the joint space's volume is at a minimum, and the joint is close packed.

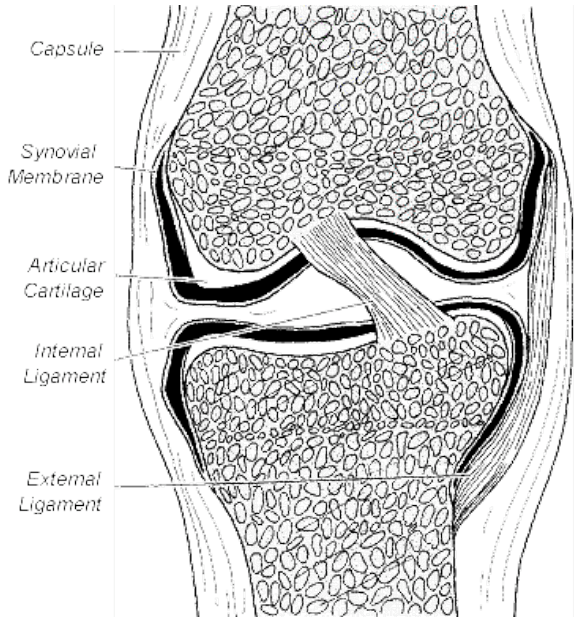

Figure 3-1 - Structure of a typical synovial joint [76].

Hyaline cartilage covers the articular surfaces of both bones in a synovial joint. This cartilage serves to lubricate the joint as well as to prevent abrasion and impact of bone against bone, which would damage the surfaces causing pain and restricting movement. The cartilage is lubricated by synovial fluid, secreted by the synovial membrane that lines the joint cavity. Ligaments connecting bone to bone control and restrict the motion of the joint. Muscles spanning the joint apply tension via tendons which connect muscle to bone to pull the bones in specific directions and articulate the joint.

The structure of bone is extremely complex on both a micro and macroscopic scale. Macroscopically, the bone occurs in two forms: a dense outer layer of cortical bone and a spongy layer of cancellous bone as shown in Figure 3-2.

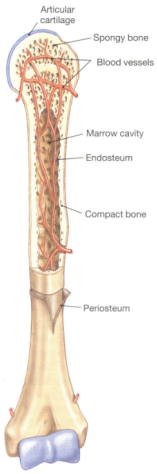

Figure 3-2 - Structure of a typical long bone [76].

Bone is continually remodelled in adult skeletons. Allowing the skeleton to adapt to changes in stress state, remodelling involves the continual removal and re-deposition of bone material mediated by local mechanical conditions. Osteocytes (bone cells) continually remove and replace the surrounding calcium salts. Osteoclasts dissolve bone by secreting acids and releasing stored minerals. Osteoblasts lay down new bone. When an osteoblast becomes completely surrounded by calcified matrix it becomes an osteocyte.

3.1.2 Joint Degradation

There are certain degenerative medical conditions associated with synovial joints that can cause sufficient stiffness or pain to warrant consideration of the replacement of the joint surfaces with artificial components. Arthritis is amongst the most common forms of joint complaint and affects all synovial joints but causes can vary. There are several types of arthritis that affect different components of the joint. For example, osteoarthritis, also known as degenerative arthritis or degenerative joint disease, usually results from cumulative wear and tear of joint surfaces or from genetic factors that affect the formation of cartilage. Osteoarthritis is by far the most common reason for joint replacement, accounting for 75.8% of all hip replacements in Sweden between 1979 and 1998 [72].

Rheumatoid arthritis is believed to be caused by the immune system mistakenly attacking the joint tissues and affects nearly 2.5% of the adult population in the USA. Because rheumatoid arthritis is not directly associated with wear and tear of the joint cartilage, it is not primarily found in the elderly, unlike osteoarthritis, which is relatively rare in patients under the age of 60 [76]. Allergies, bacteria, viruses and genetic factors, alone or in combination, may be causes of rheumatoid arthritis. Drugs and physical therapy can slow the progression or mitigate the effects of these diseases but in more extreme cases the joint may need replacement.

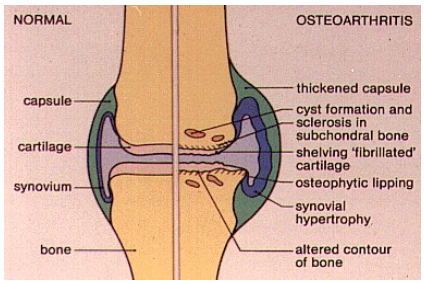

Figure 3-3 – Normal joint (left) compared to an osteoarthritic (right) joint [76].

Figure 3-3 illustrates the effects of osteoarthritis and depicts the features of joint swelling and cartilage erosion as well as those labelled in the figure. These features may cause pain, stiffness and grating in the joint. Another effect of osteoarthritis may be deformity of the joint leading to deformity of the limb and irregular motion at the joint. This may be particularly obvious at the knee as shown in Figure 3-4.

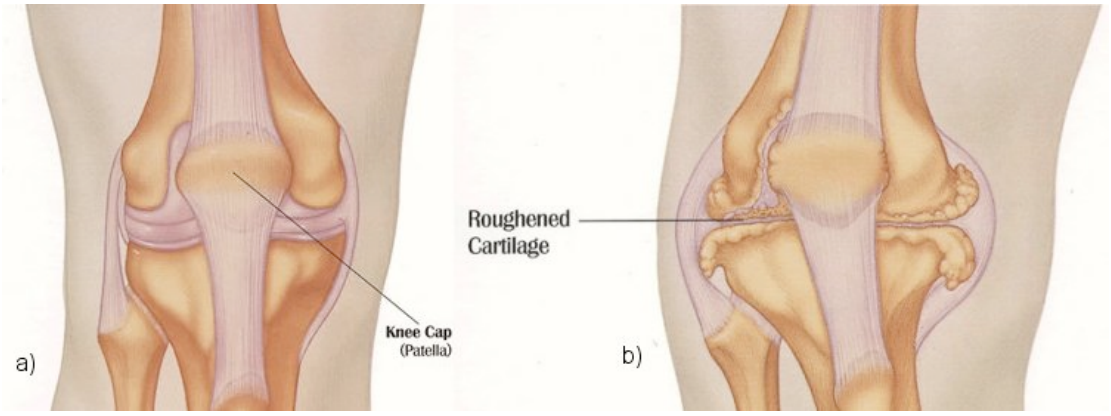

Figure 3-4 - Diagram of; a) a normal knee joint and b) a knee joint suffering from osteoarthritis [76]

Arthritis can be controlled to some extent by adopting a healthy diet and exercise programme. Diet can help to minimise body weight, thereby reducing the loads on the joint. Exercise helps to maintain joint strength and range of motion although high impact aerobic exercise such as jogging can be counter-productive by causing excessive stresses in the joint.

A drug called Cortisone has been used in the past as a short-term treatment for the symptoms of osteoarthritis. This treatment was found to actually accelerate the condition in a number of patients and so its use was discontinued. If the condition is beyond the use of drugs (now aspirin related courses are used) then minor surgery can be used to remove bone irregularities. A joint replacement is a last course of action and is the treatment we are concerned with.

3.1.3 Different Types of Joint Replacement

Joint replacement consists of the exchange of the diseased and/or damaged bone and articular cartilage in the vicinity of the joint with artificial materials to form replacement bearing surfaces. This reduces pain and inflammation at the joint.

Most joint replacements can be performed as either a cemented or cementless operation. For initial fixation to the skeleton, cementless components commonly rely on under-reaming the bone cavity in order to produce a press-fit between implant and bone, which allows load transfer without excessive movement. The inserted prosthesis

may have a porous coating to promote bony ingrowth and integration with the surrounding tissue in the long term. Due to the material properties and natural adaptation mechanisms of bone, the press fit will reduce over time to be replaced by so called “secondary fixation” due to bone ingrowth. This technique is popular in the United States. In Europe however, it is less common, being more often reserved for younger patients in order to preserve bone and to reduce complication in future revision surgery. The cementless technique requires a high degree of accuracy while reaming the cavity to produce an even transfer of load to the bone.

Cemented joint replacements involve creating an oversized cavity in the bone into which cement is injected; the new component is then inserted into this mass. The cement is then allowed to harden around the implant, the resulting cement mantle fusing the implant to the bone and facilitating load transfer across the joint.

Each procedure has its own benefits and the choice of cemented or cementless joint replacement is made based on the individual patient anatomy and complaint. For example, by using the cemented technique a rapid fixation is achieved and there is no time required for bone ingrowth. The addition of an extra component (a cement layer) may contribute to a shorter implant life however, due to degradation of the cement mantle. Also this extra layer of material can complicate revision surgery by fragmenting during retrieval.

Figure 3-5 - X-ray of a Charnley hip replacement in-situ.

Bone cement was first developed and used for hip replacement by Professor Sir John Charnley (1911-1982) acting on advice from a dental materials scientist, Dennis Smith, who introduced Charnley to self curing polymethylmethacrylate (PMMA). Since then, cement has been tried in all joint replacement procedures with varying degrees of success.

Figure 3-6 - Three designs of conventional cemented femoral hip stem (left-right: Charnley, C-stem from DePuy™ and Exeter from Stryker™ Howmedica)

Charnley produced large improvements in hip replacement by using a long stem, providing better fixation with the bone and smaller head sizes to reduce frictional torque and consequently stresses at the fixation of the acetabular component (Figure 3-5). This type of stem has been the reference against which all developments since have been compared. There is a marketing requirement for orthopaedic manufacturing companies to continually develop new designs of devices although experience has shown they are not always an improvement on what has gone before (Figure 3-6) [35].

Figure 3-7 - A metal on metal hip resurfacing joint in its acetabular cup [22]

In order to preserve as much bone stock as possible, shorter stems have become more common, and recently a procedure in which only the joint surface is replaced has become widely available. These so called resurfacing methods for the hip involve removing a thin layer of bone from the femoral head and re-covering it with a metal implant which articulates within a metal acetabular component (Figure 3-7). This has been enabled by improved manufacturing processes which allow the larger head size to be made with sufficient accuracy that reproducible tribological performance can be ensured [106]. The resurfacing procedure has shown good success rates. Amstutz states a survival of 94.4% of resurfacing components after four years [2]. Treacy *et al.* showed a 98% survival of resurfaced hips in their study in the sixth year and that 130 hips of 144 were being used to play sport [114].

The general form of the cemented total joint arthroplasty remains the same throughout the body, whether it is at the hip, knee, shoulder or ankle. A typical configuration for a total joint replacement is to have a metal component which is cemented into one bone and which bears on a polyethylene bearing surface, which may be metal backed, cemented into the other bone (Figure 3-8). This has been the most popular design for many years now although new manufacturing technologies and materials developments have allowed alternatives to be considered for modern surgery. The use of metal-on-metal, ceramic-on-ceramic and ceramic-on-polyethylene bearings has become increasingly popular with many orthopaedic device manufacturers now offering them as part of their range.

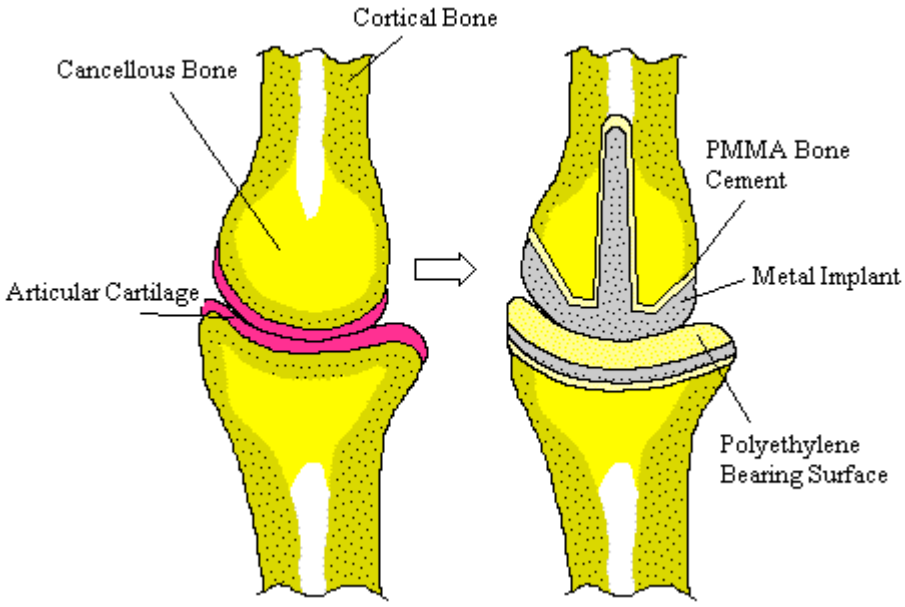

Figure 3-8 - Generic joint showing the natural joint (left) and the make up of a cemented total joint replacement (right).

At the tibio-femoral joint of the normal knee, the load bearing surface is divided in two, but the two are traditionally replaced simultaneously with a single artificial joint (shown as a conventional knee in Figure 3-9). Again, there are many different joint designs that are available for the knee but a more recent trend for minimally invasive surgery has encouraged the use of components which replace just one of the two condyles allowing for the other side to remain natural (unicondylar implant, Figure 3-9). At present the lowest coefficients of friction that can be reproduced within the body using artificial bearings are still significantly higher than the natural joint

surfaces [67]. This is another reason why preservation of one of the condyles is desirable.

There are different options which can be used for different joints throughout the skeleton. However, the type of cement used is similar for every joint.

Figure 3-9 - Conventional knee implant (left) compared to uni-condylar knee implant (right) [22]

3.1.4 Cemented Joint Replacement Procedure

As explained in section 3.1.3 all cemented joints have the same basic structure. They also share the same basic procedure of insertion: The patient is first anaesthetised; both local and general anaesthetics may be used. When the anaesthesia has taken effect, the initial surgical cut is performed and is of a suitable size and position to allow access to the joint for prosthesis insertion. Muscles are generally cut and/or retracted (held out of the way), so that the joint capsule can be visualised. The capsule is then opened revealing the joint.

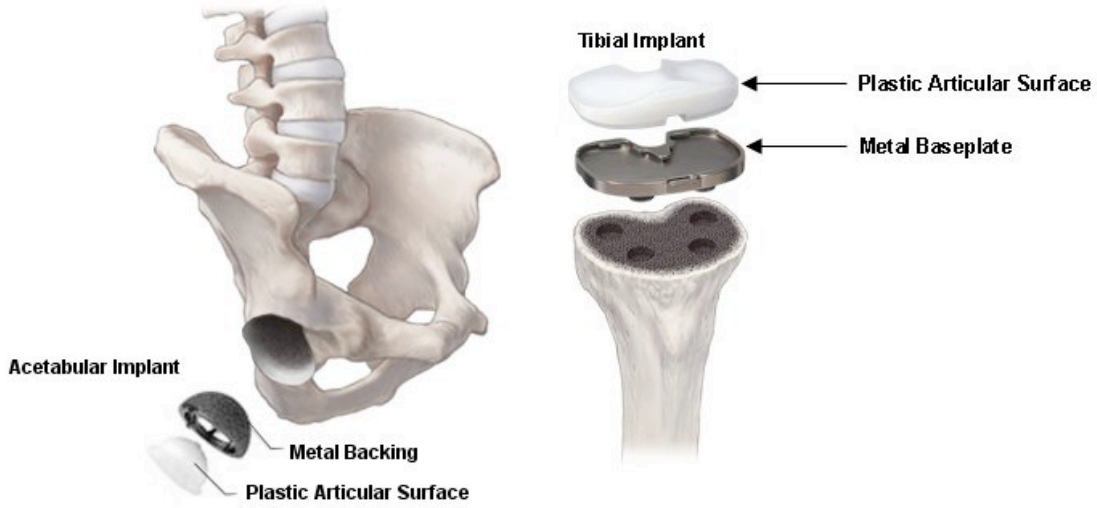

Figure 3-10 - Prepared acetabulum and tibia with their respective joint replacement components (cement not shown) [129]

The joint can then be dislocated by manipulating the limb. The concave side of the joint (acetabulum in the hip, tibial plateau in the knee, glenoid in the shoulder etc.) is then reamed to remove damaged cartilage and bone and to shape it so that it will match that of the implant (Figure 3-10). Pre-mixed bone cement is pushed onto the prepared bone surface and a metal backing component* is then inserted and pushed firmly into the cement. Modern cementing techniques may include pressurisation of the cement before component insertion to ensure cement enters the pores of the cancellous bone, leading to greater "interdigitation" of cement and bone at the interface between the two and a mechanically stronger interface. Once the metal backing is secured in place, the plastic insert can be fitted into the metal backing.

The other portion of the joint is prepared and a component inserted in a very similar way (Figure 3-11).

When all implants are in place the joint is relocated, the soft tissues repaired and finally the wound closed (Figure 3-12).

* Used in many popular joint replacements in the UK currently. Some components are all-polyethylene.

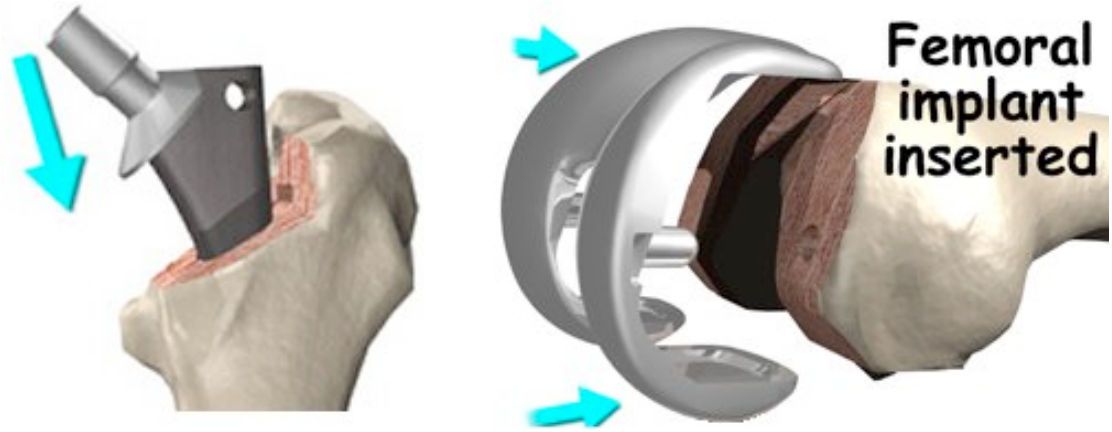

Figure 3-11 - Insertion of femoral hip (left) and femoral knee (right) components into the prepared femur (cement not shown) [22]

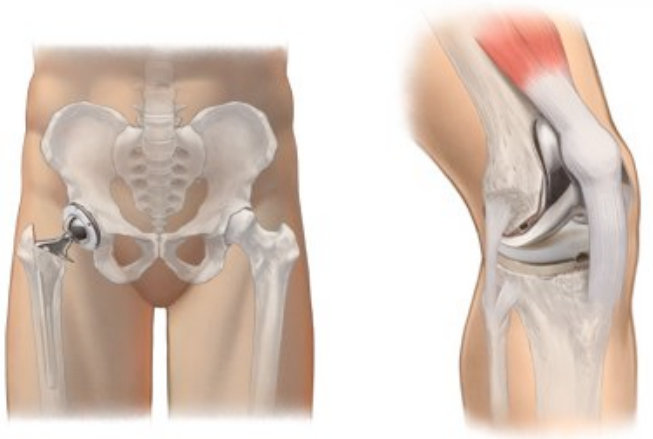

Figure 3-12 - Diagrams of completed and closed hip and knee total arthroplasty [129]

3.2 Bone Cement

Bone cement is the generic term used to describe all grouting agents used in joint surgery. It is most commonly a polymethylmethacrylate (PMMA) based polymer. When used in the operating theatre, two components are mixed (liquid monomer and polymer powder blend). Immediately after mixing the monomer begins to polymerise which eventually causes the whole mass to harden into a solid. Three stages typically occur during the production of bone cement; mixing of the two phases, gel formation and polymerisation of the monomer [89].

3.2.1 Cement Ingredients

Modern bone cement has several different ingredients, many of which are involved in or control the rate of the polymerisation reaction. There are also several different additives, which are introduced for various reasons but play little part in the reaction kinetics.

The bone cement is mixed from two components; a powder blend of different compounds and a liquid mixture of different compounds. Certain ingredients are common to most if not all brands of bone cement:

The powder typically contains:

- Polymethylmethacrylate beads, which make up the majority of the powder blend and are pre-polymerised under controlled conditions by the manufacturer. Other co-polymer based cements with compositions involving styrenes, methylacrylates and butyl-methacrylates among others.
- Barium sulphate, used as a radiopacifier. This reduces the translucency of the cement to x-rays so as to make it visible in x-ray images taken post-operatively. Zirconium dioxide is an alternative to barium sulphate.
- A reaction initiator such as benzoyl peroxide.

The liquid generally contains:

- Methylmethacrylate monomer, which polymerises to form the solid bone cement.
- A reaction accelerator such as N, N-dimethyl-p-toluidine (N, N-DMPT).
- An inhibitor such as hydroquinone to prevent premature polymerisation during storage.

Manufacturers often supplement this recipe with additional ingredients in order to produce the desired mechanical properties, reaction time or other properties making the cement more appropriate for particular operations or applications. For example Simplex P™ has a low viscosity in the period immediately after mixing, making it flow a lot more easily but making it more difficult to handle. Palacos R™ has chlorophyll added to colour the cement green making it more easily distinguishable in the surgical wound.

Some of the most common additives for cement are antibiotics such as gentamicin. These are aimed at resisting infection, which may be induced as a result of surgery. Hydroxyapatite (HA) has also been experimented with as an ingredient for encouraging the growth of bone onto the cement surface. The addition of many of these ingredients, while useful in certain circumstances, is often to the detriment of mechanical properties of the cement [6].

3.2.2 Mixing Techniques

Since the use of PMMA bone cements was first established, various different techniques have been used for the mixing of the two components. Methods have been refined over this time to produce the techniques that are used in modern surgery.

When first used, cement was mixed in a bowl before being manually packed into the bony cavity as a paste. Problems were quickly identified with this procedure as it proved difficult to obtain a perfect mantle free of large pores. Pores are known to act as sites of stress concentration within the cement mantle from which cracks can initiate and grow.

Syringes were introduced as an insertion method in order to reduce the entrapment of air within the cavity. This method works very well in certain situations such as inserting cement in long cavities, like the femoral component of total hip replacement. However, many joint replacements require the cement to be moulded around or on top of much wider and flatter or even convex geometry. For these procedures, manual insertion is still preferred.

Following the recognition of pores as sites of crack initiation in the cement mantle, a number of methods for mixing the cement were developed to minimise the production of pores. When mixing in air, the agitation required to mix the cement entraps air into the cement. By removing the air it is possible to drastically reduce the amount of porosity. Vacuum mixing methods have been developed by many different cement manufacturers. Many have been shown to improve the quality of the bone cement by reducing the number of pores [60].

Other methods have also been developed in attempts to further reduce the porosity in the cement. By spinning the cement in a centrifuge after mixing it is possible to further reduce the porosity in the cement, although the effect of additionally centrifuging the cement following vacuum mixing on porosity has been shown by Macaulay *et al.* to be insignificant [70].

The most popular techniques used in modern surgery generally involve mixing the cement within the barrel of a cement syringe. A vacuum is applied to the barrel and the two components are inserted through a funnel. The barrel is then sealed creating a vacuum in the syringe. The cement is then mixed under vacuum using an agitator which runs inside the sealed syringe barrel. Once mixed thoroughly the vacuum is removed and the syringe barrel is inserted into a cement insertion gun. The cement can then be used by injection (Figure 3-14). The CEMVAC© system, manufactured by DePuy CMW™, operates on this principle and is shown in Figure 3-13.

Figure 3-13 - Photograph of Cem-Vac™ cement mixing system. Syringe with funnel, sealing plunger, nozzle cutter, cement delivery gun, sachet of cement powder and vial of liquid monomer are shown.

Many other manufacturers use slightly different techniques but the methods are generally similar. However, the quality of the cement that results can vary from one manufacturer to another. Dunne *et al.* showed the variation between the porosity and subsequent fatigue performance of 6 different vacuum mixing kits to be of statistical significance (porosity ranging from 1.44% using Mitab Optivac™ and 10.3% using Zimmer Osteobond™ when Palacos R™ cement was mixed in each, according to the manufacturers instructions [26].)

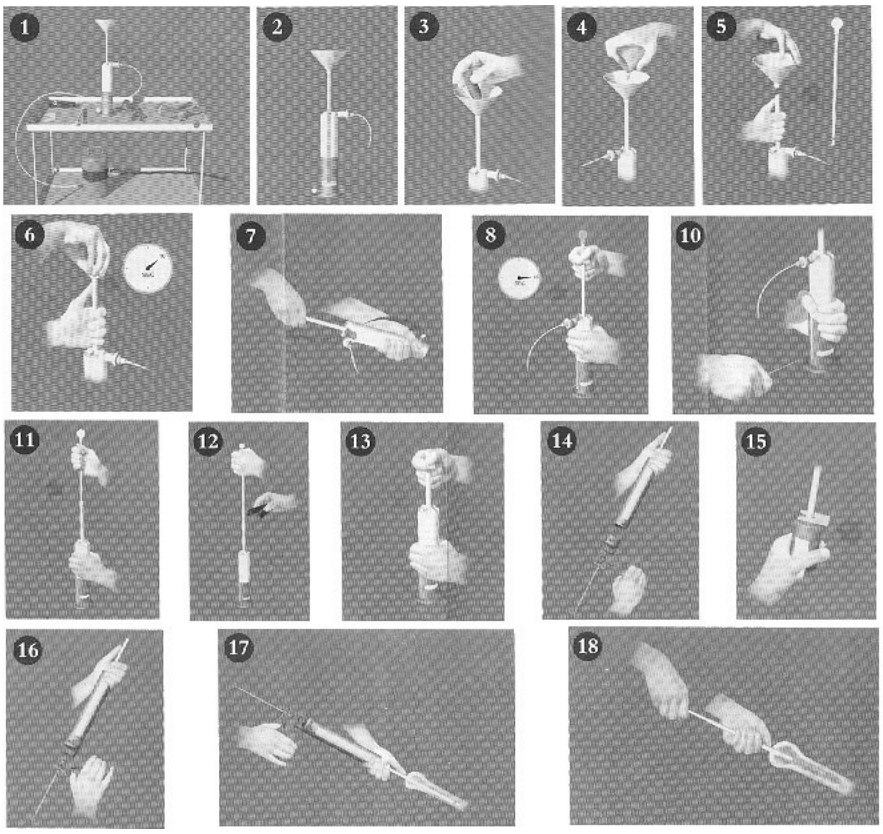

Figure 3-14 – Typical procedure for vacuum mixing cement [21].

There are still ongoing studies into techniques for mixing of bone cement, in an attempt to improve not only the resulting mechanical performance of the cement but also the heat produced during cure (discussed in 3.3.2 Aseptic Loosening). Wang *et al.* investigated changes to the thermal behaviour of cement as a result of vacuum mixing. Little change in polymerisation temperature was observed due to changes in pressure at which the cement was mixed [123]. McCullough *et al.* looked into the effects of initial temperature of the cement and also the effects of using an automated cement mixing machine on the homogeneity and the porosity of the final product [77]. It was seen that colder cement could be mixed for longer as the reaction ran more slowly (discussed in 3.2.3) and that this created more homogeneous cement as did automated mixing when compared to hand mixed cement. Conversely Lewis investigated the fatigue performance of cements that had been stored at different temperatures and found no significant difference between cement stored at room temperature (21°C) and cement stored at 4°C [60]. The effect of sterilisation method has been investigated by Graham *et al.* [34]. Et-O sterilisation produced little effect on the fatigue performance of the cement. Radiation sterilisation at increasing

intensities caused a degradation of the cements' fatigue performance. This deleterious effect upon the mechanical performance seen in radiation sterilised, vacuum mixed bone cement is attributed to a decrease in molecular weight caused by scission of the polymer chain during the sterilisation process. An additional parameter, investigated by Bettencourt *et al.* is the liberation of methylmethacrylate monomer from the cement and the effect that vacuum mixing has on it [10]. It was seen that after low pressure (0.15bar) vacuum mixing, the liberation of potentially harmful methylmethacrylate to the atmosphere was reduced significantly. This is due to mixing the cement in a closed system with filtration on the vacuum line.

3.2.3 Cement Polymerisation Kinetics

As discussed earlier, bone cement is mixed in the operating theatre and is then injected as a fluid into a bone cavity before hardening around an orthopaedic joint implant. Bone cement hardens due to the formation of polymer from the monomer present in the liquid component.

When the liquid and powder components are mixed, the accelerator in the liquid component causes decomposition of (commonly) benzoyl peroxide in the powder component, generating free radicals. These radicals initiate an addition polymerisation of the MMA monomer and PMMA polymer as shown schematically below.

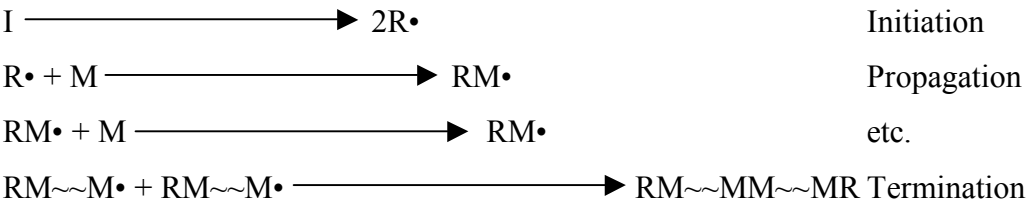

The polymerisation reaction is complex and involves the generation and subsequent continued reaction of many chemical species. The rates of these reactions are dependent upon "activation energy", the degree of polymerisation and the local temperature. Various authors have attempted to mathematically model the kinetics of the reaction, the fundamental equation being that which describes the relationship between heat generation rate and degree of polymerisation. An example is the equation proposed by Baliga *et al.*-

$$S = f(T)(1-\alpha)^n \alpha^m \quad \textbf{1-1}$$

where S is the volumetric rate of heat generation, α is the degree of polymerisation, m & n are exponents controlling the effect of the degree of polymerisation and $f(T)$ is a function defining an instantaneous rate constant as a function of temperature (T). The form of the function $f(T)$ is generally the aspect upon which some authors disagree.

Baliga *et al.* ran a series of differential scanning calorimetry (DSC) tests at constant temperature and used a least squares method to fit a polynomial to the data to determine $f(T)$;

$$f(T) = 4.4 \times 10^6 \left[a_0 + a_1 \left(\frac{T}{100} \right) + a_2 \left(\frac{T}{100} \right)^2 + a_3 \left(\frac{T}{100} \right)^3 + a_4 \left(\frac{T}{100} \right)^4 + a_5 \left(\frac{T}{100} \right)^5 \right] \quad \textbf{1-2}$$

where a_i (i=0-5) are coefficients determined experimentally and T is the temperature in ºC [7].

Borzacchiello *et al.* used the Arrhenius equation to describe the temperature dependence of the rate constant;

$$f(T) = K_0 e^{\frac{-Ea}{RT}} \quad \textbf{1-3}$$

where K_0 is a constant, E_a is the activation energy, R is the universal gas constant and T is the local instantaneous temperature in Kelvin [12]. The advantage of the Arrhenius approach is that the reaction parameters can be determined simply and with relatively few experiments using the DSC techniques described by Starink [109].

It is known that following cure under clinical conditions, cement contains residual monomer content of up to 2-3% of the original amount. The degree of polymerisation does not, therefore, ever appear to reach 1. The effect of the residual monomer is not

completely known though it is possible that the effect of pockets of residual monomer would be to reduce the fatigue strength of the bulk material. The degree of residual monomer present at the end of polymerisation can be found using DSC experiments as demonstrated by Borzacchiello *et al.* [12]. Un-reacted MMA monomer is believed to leak from the cement mantle into the surrounding tissues, impairing bone remodelling and its presence in the hardened polymer influences the mechanical properties of the polymer because it acts as a plasticizer [117].

Lee *et al.* found that it is possible to reduce the amount of MMA monomer that is eluted into water after polymerisation by 80% by increasing the reaction temperature to 50°C [57]. Borzacchiello *et al.* also noted that for a higher temperature the cement would cure faster and give a higher degree of conversion measured by a fraction of the total amount of heat produced in a non-isothermal experiment [12]. By assuming that the same polymer is produced in every case and that there is no change in the amount of monomer lost due to evaporation they state that this indicates that more polymerisation has taken place and so there must be less residual monomer within the sample.

3.2.4 Mechanical Properties of Curing Cement

During cure, bone cement experiences a complete change in mechanical properties. The properties at the two extreme stages (initially a two phase fluid with solid and liquid phases and finally a solid) can each be modelled mathematically but require very different techniques. During the early stages of cure the properties are best described using viscosity parameters alone. Viscosity describes the ratio of the shear stress to the shear rate in a flowing fluid [75]. Immediately after mixing the cement is best described as a power-law (pseudoplastic) fluid. The power law relationship describes the dependence of the apparent viscosity on the shear rate [25]. A greater shear rate reduces the apparent viscosity. In certain circumstances the mechanical properties of cement may be simplified to those of a Newtonian fluid, meaning that the viscosity is independent of shear rate. This idealisation requires determination of a viscosity at a particular shear rate appropriate for the problem at hand and simplification to a Newtonian model is only a realistic approximation if the problem involves a limited range of shear rates.

As the cement cures the properties evolve such that the cement is better described as a viscoelastic solid [27]. During the latter stages of polymerisation the properties require characterisation using two parameters, the storage modulus and the loss modulus. These parameters are often expressed as a complex number, with the real part representing the storage modulus and the imaginary part representing the loss modulus, which can be represented in an Argand diagram (Figure 3-15 where $t_1<t_2<t_3$).

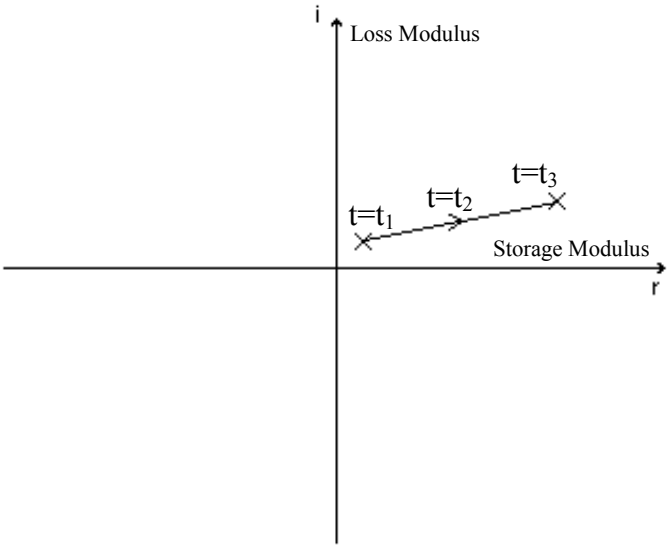

Figure 3-15 - Argand diagram of rheological properties of cure over time showing that both the storage and loss modulus increase during polymerisation.

Viscosity parameters can be determined using rheometers [54]. Rheometers are usually of rotational or capillary design. A rotational rheometer calculates viscous parameters from the resisting torque produced between a rotating cone and a flat plate separated by the material of interest. Capillary rheometers calculate these variables from the rate at which material is extruded through a capillary tube with a pressure difference between the ends. The different rheometers are used depending on the shear rate required in the material under test (for high shear rates the capillary rheometer is used).

Oscillatory rheometers can be used to determine the viscoelastic behaviour of the cement (storage and loss modulus). The moduli determined using these methods can

be thought of in terms of spring and dashpot models. Springs of a particular stiffness represent the elastic contribution and dashpots of a particular damping coefficient the viscous contribution to the material behaviour. By combining a single spring and dashpot in series or parallel, Voigt and Maxwell elements can be generated respectively (Figure 3-16). These elements can be used very effectively to show creep (when in parallel) and stress relaxation (when in series) behaviour of a material. By combining several elements in an array a generalised Maxwell model is generated, which can be used to describe the mechanical properties of a material to high degree of accuracy [103]. However, relatively few studies in which measurements of the mechanical properties of the cement during the curing period have been published.

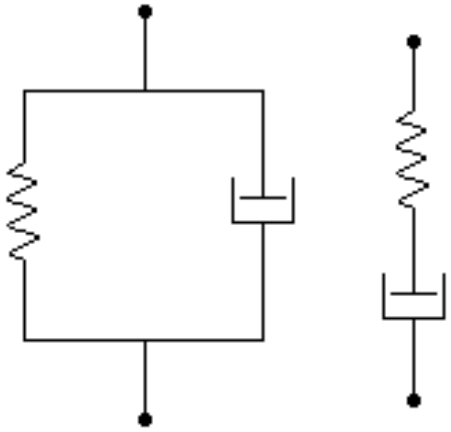

Figure 3-16 – Maxwell (left) and Voigt (right) elements.

Carlson *et al.* used ultrasound as a means of measuring the mechanical properties of cement during cure and used their value of the elastic modulus to determine the degree of polymerisation [16]. The method adopted in the study by Carlson *et al.* (and by Nilsson *et al.* [85]) was to assume a perfectly elastic material and therefore calculate a simple value for the elastic modulus which was then assumed to be proportional to the degree of polymerisation. This assumption becomes more accurate towards the end of polymerisation when the cement sample behaves elastically, however at the beginning of polymerisation the sample was a fluid and the elastic modulus in this case is not a complete picture of the mechanical properties. As stated above, the modulus of the cement throughout cure is complex and must be calculated from complex values for the shear and compressional moduli.

Cement additives have a bearing on the mechanical properties. In general, additives (discussed in section 3.2.1) are included for non-mechanical reasons, for example antibiotics may be included in order to reduce the risk of infection, or barium sulphate may be added to enable the cement mantle to be seen under x-ray. Often the addition of these useful ingredients is to the detriment of mechanical properties and possibly the service life of the cement. Baleani *et al.* showed that radiopacifying agents did indeed reduce the fatigue strength of bone cements (Figure 3-17) [6].

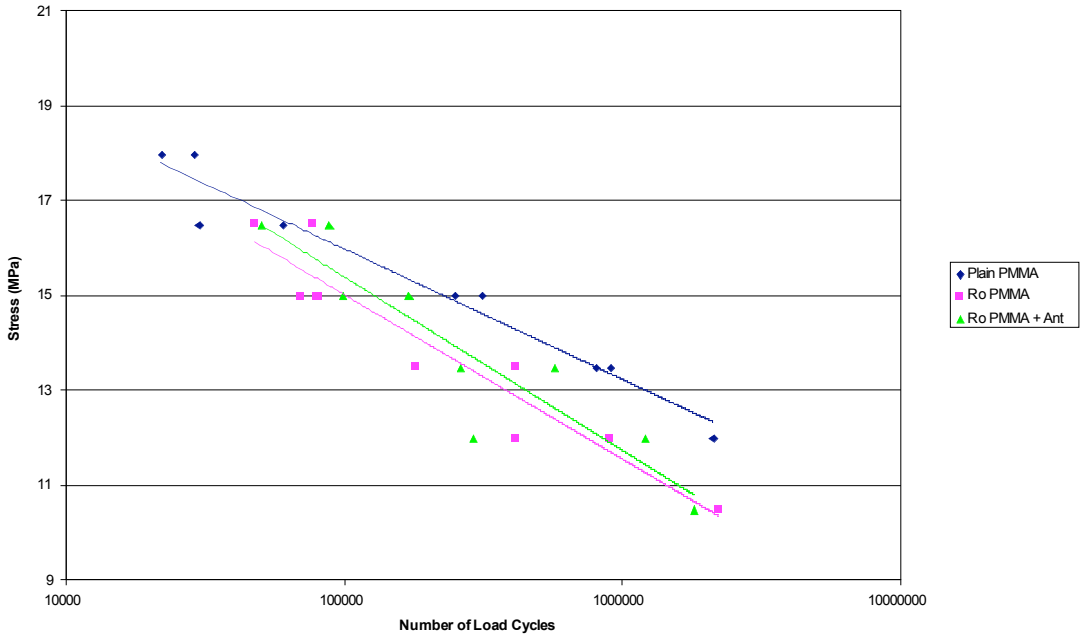

Figure 3-17 - S-N curves for plain PMMA compared to PMMA with radiopacifier (Ro PMMA) and PMMA with both radiopacifier and antibiotics (Ro PMMA + Ant) (reproduced from [6]).

3.2.5 Volumetric Changes in Curing Cement

PMMA bone cement undergoes a density change during polymerisation as the liquid monomer is converted to a polymer of higher density [30]. Assuming mass conservation, this density increase must result in a decrease in cement volume (shrinkage). This shrinkage may account for some of the pores found in retrieved bone cement mantles. Void elimination by vacuum mixing increases cement shrinkage, possibly compromising the mantle interfaces [83]. Another cause for concern due to the shrinkage of cement is residual tensile stresses produced when the

cement is prevented from contracting by the presence of the stem. These stresses can seriously compromise the life of the cement mantle resulting in high damage accumulation rates and the necessity for revision operations [91].

Although the net effect of cement cure appears always to be a shrinkage, the study by Müller *et al.* showed the change in volume as a function of time for a sample of curing bone cement suspended within a water bath to be non-linear [83]. Volume changes observed in hand mixed cement and vacuum mixed cement are shown in Figure 3-18. It can be seen that in the case of the hand mixed cement a volume increase is often recorded in the early stages of cure. This may be due to thermal expansion of air trapped in the cement, since an initial expansion was not seen in vacuum mixed cement. The chemical shrinkage may be 'masked' by this effect until the latter stages of cure. This effect also reduces the overall shrinkage of hand mixed compared to vacuum mixed cement.

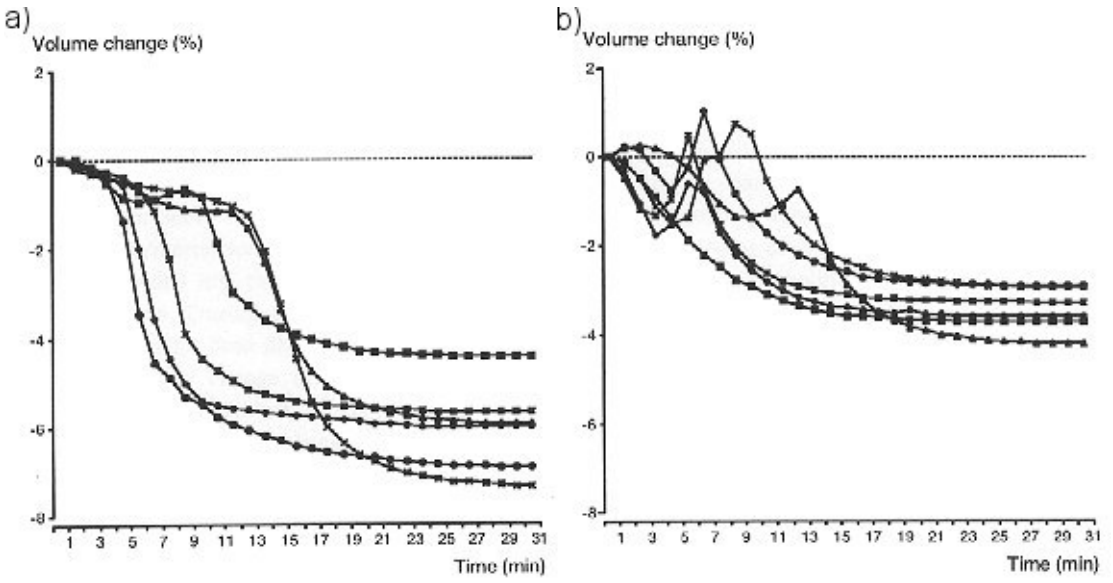

Figure 3-18 - Volume change as a function of time exhibited in (a) vacuum mixed and (b) hand mixed bone cement [83].

3.3 Reasons for Joint Revision

There are many problems associated with the use of bone cement in total joint replacement, many being thought to be a direct cause of failure of the artificial joint. Despite these problems however data published in the Swedish Total Hip Replacement Register shows that cemented implants outperform uncemented joints. Cemented implants have a revision rate of 5.2% after 10 years while uncemented implants have a revision rate of 12.3% after 10 years [71].

3.3.1 Surgical Trauma

A total joint replacement may require revision in the short term due to infection or technical error during the operation. These are uncommon causes of joint revision compared to aseptic loosening (loosening of the implant in the medium to long term in the absence of infection) [72]. Only 8% of joint revision operations are accounted for by infection and only 3.5% by technical error.

There are several different sources of infection. It may come from the operation itself (any major operation carries with it a certain risk of infection) or may be the result of the prosthesis creating an environment where infections from other sources can establish themselves.

3.3.2 Aseptic Loosening

The 2002 report of the National Swedish Hip Register [72] states that aseptic loosening accounted for 75.7% of joint revision operations in cemented implants between 1979 and 1998. Aseptic loosening involves the loosening of one, or sometimes both, components of a THR due to non-infection related causes. Although many joint revisions are attributed to aseptic loosening, the mechanism of loosening remains unclear. There are several different processes that may play a part in the aseptic loosening process. Figure 3-19 shows radiographic evidence of aseptic loosening in a femoral component of a total hip replacement; there is a proximal radiolucency due to prosthesis subsidence (A) and distal radiolucencies due to

osteolysis ("bone breakdown") (B) and distal cement damage (C) [111]. Radiolucencies indicate regions where soft non-structural tissues or gaps are present between bodies.

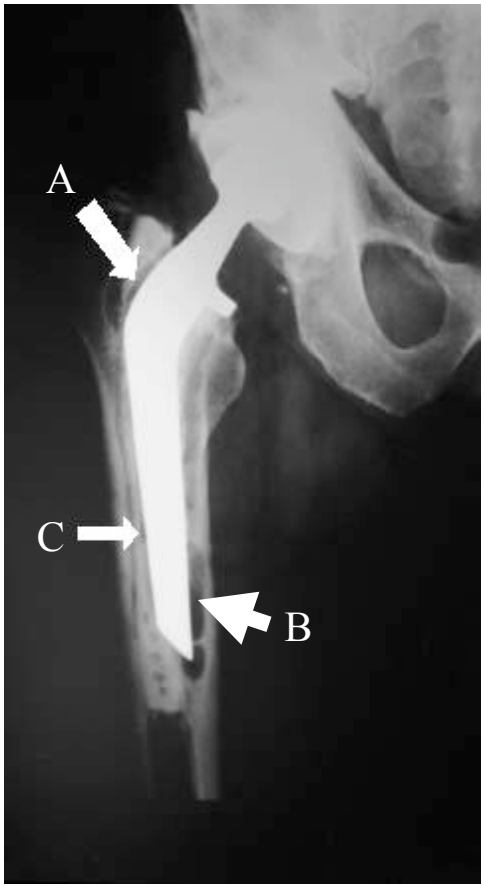

Figure 3-19 - Radiograph indicating distal and proximal loosening of the femoral hip component [20].

Destructive Wear

The polyethylene insert in the acetabular cup of a total hip replacement is significantly softer than the metal or ceramic head of the femoral component and so articulation of the joint causes wear, primarily of the softer component, which is dependent on the contact pressure and range of motion [78]. The problem is exaggerated in the knee where contact pressures are often higher and kinematics more destructive. The wear particles generated from metal-on-polyethylene or ceramic-on-polyethylene are generally of a larger size than those generated by metal-on-metal or ceramic-on-ceramic bearings and many of the particles are of biologically active size of between 0.1 and 1μm [46]. These wear particles can be transported through tissues

where they can cause biological reactions and osteolysis (the breakdown of bone). Particles can even be transported down a debonded cement-implant interface [104]. It is believed that these particles may then be transported through cracks in the cement mantle to the cement-bone interface. Athanasou *et al.* [3] showed that these particles could cause osteolysis. The threshold for determining whether osteolysis will cause clinical problems is loss of about 0.1mm of polyethylene thickness through wear per year [73]. This is also the case for many other materials, for example titanium implants as shown by Lombardi *et al.* [66].

As well as causing osteolysis, wear in the knee can cause destruction of the bearing surface and cause a change in the motion, often causing grating and sometimes pain and changes in the walking pattern. This wear can also cause an increase in joint laxity and instability during normal motion. This is less of a cause for concern in the hip due to the geometry of the joint creating an inherent stability. Wear in the hip will affect the offset but the joint motion will be little affected.

Verdonschot *et al.* [120] also showed that, where a femoral stem becomes debonded at its interface with cement, wear of the cement mantle might also take place due to motion. This effect is increased with increased stem surface roughness. It is believed that all stems will debond from the cement over time (although this process might be slower for rough stems than polished stems) and so to minimise damage to the cement mantle, smooth polished stems should be used. The particles produced by this wear mechanism can also promote bone resorption through osteolysis.

Stress Shielding Leading to Bone Remodelling

Insertion of implants of greater stiffness than bone will greatly alter the stress distribution experienced by the bone during activity. Bone is an adaptive material. Where high stresses are experienced in the bone more material will be laid down and the opposite is true for areas of low stress, in which case bone is resorbed. This process is known as bone remodelling and is summarised as Wolff's law [101, 127]. It has been proposed that the areas of bone resorption due to 'stress shielding' as a result of reduced bone stresses due to the presence of a stiff implant will lead to loosening of the implant and cement mantle within the bone. Loss of bone stock as a result of bone

remodelling is also of major concern should a revision operation be necessary. It may be possible to reduce the size of reduced stress regions by using a hollow stem, which will be more flexible and generate a more even distribution of stress to the cancellous bone. It is, however, impossible to completely eliminate the effect of stress shielding since even if using material with identical properties to the removed bone, there is often a high percentage of the volume occupied by the prosthesis, which is non-structural in the natural bone (for example; the medullary canal replaced by a femoral hip replacement component).

Bone Necrosis

Bone may die as a direct result of surgical trauma. There are two main areas of concern during the surgical procedure. Firstly, the reaming of the medullary canal causes a sharp elevation in temperature, which may cause local necrosis (death) of bone [41]. Secondly, heat evolved during cement cure causes an increase in bone temperature. Bone is believed to die as a direct result of exposure to high temperature for long periods of time. The higher the temperature, the less exposure time is required before necrosis begins. Specifically, Baliga *et al*. states that a temperature of 50˚C for more than one minute will cause necrosis of cancellous bone [7]. Reaming should be performed slowly to reduce mechanically induced temperature increases. The temperature increase of bone cement is difficult to control as it polymerises via an exothermic reaction. Meyer *et al.* have measured and reported temperatures of 70ºC *in-vivo* [80]. Bone-cement interface temperatures of similar values have been reported from *in-vitro* experimentation, which is potentially damaging to the surrounding bone and in turn the implant life [7, 23, 62]. Starke *et al*. published finite element models produced using Abaqus™ comparing different cement thicknesses and their effect on bone necrosis (Figure 3-20) [110]. The high temperature areas observed in the study by Starke *et al.* were not uniformly distributed. The variations between proximal and mid-section areas may be explained by a non-uniform cement mantle – high temperatures were associated with areas containing more cement than others. The distal areas of high temperature were most likely caused by boundary conditions at this end (body temperature was assumed at the distal section, room temperature at the proximal section). The more bulky proximal part of the stem may be considered to act a as a more effective heat sink than the distal part.

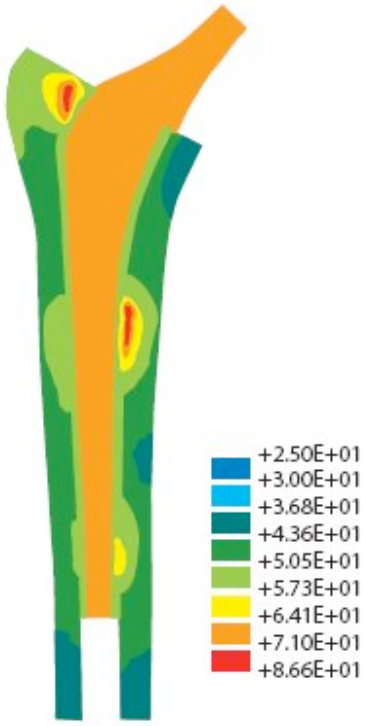

Figure 3-20 - Temperatures of cement and bone during polymerisation, reproduced from Starke *et al.* [110].

In general, the temperature that the cement will reach will depend on many different variables: -

- Cement chemistry – cements with higher activation energy for polymerisation will have lower reaction rates and therefore reach lower temperatures.
- Physical properties of stem, cement and bone - specific heat capacities and thermal conductivities of the stem, cement and bone will affect the temperature reached.
- Initial conditions – higher stem or cement temperatures will affect the temperature - at a higher initial temperature, the polymerisation reaction will proceed at a higher rate [12].
- Cement mantle geometry - a thicker cement mantle will cause a greater build up of heat internally which must then dissipate through the bone.

The necrosis of bone which may be induced by high bone cement temperatures is perceived as a problem by some surgeons and may contribute to short-term loosening,

although there is little clinical evidence directly supporting the claim of necrosis leading to aseptic loosening in the long term. However, Willert and Puls found, during a post-mortem study, a zone of necrotic tissue (both bone and marrow) of 3mm thickness in places around a cemented prosthesis a few weeks after implantation [125].

Necrosis can also be caused by the residual monomer content of the bone cement (discussed in section 3.2.3). This chemical effect has, however, been shown to be insignificant when compared to mechanical and thermal trauma during surgery [28, 64].

Cement Mantle Damage

According to James *et al*. "mechanical failure of the cement mantle is the most common cause of aseptic loosening in cemented types of femoral prostheses" [48]. Stauffer *et al*. states that the most common mode of loosening in total hip replacement is cement cracking due to circumferential (hoop) stresses [111]. Cement damage accumulation reduces the ability to transmit load locally due to cracks and degradation causing a reduction in local materials properties. This may cause an increase in stress seen in other areas of the cement mantle and damage there may be accelerated.

Due to advances in stem designs, stem fracture is now a rare mode of failure, accounting for only 1.6% of revision operations reported in the Swedish hip register between 1979 and 1998 [72]. Early stems were prone to fracture and it was a heavily studied area until the 80's when the results of improvements in stem design began to be observed in clinical data. Gruen *et al*. showed in 1978 that although stem fracture was of concern, the cause of stem fracture in all of the cases studied was loss of cement support due to mantle degradation [37].

Damage accumulation is the most common means of mechanical failure of the cement. Debonding of the cement-stem interface, residual tensile stresses within the cement mantle and porosity and local flaws within the mantle are all thought to be important factors in cement damage accumulation [53].

Damage accumulation occurs in the cement mantle as a direct result of fatigue of the polymer. As the polymer is under cyclic load due to walking and other activities that involve the hip joint, the fatigue process begins as soon as the patient regains mobility.

The rate of damage accumulation can be greatly affected by the polymerisation process due to the formation of residual stresses within the cement mantle. These residual stresses can be sufficient to cause cracking through the cement mantle even before load has been applied [24].

Debonding

Debonding can occur at both the cement-bone and cement-prosthesis interfaces but most often will be found at the cement-prosthesis interface [48]. The cement-bone interface relies on interdigitation as a means of fixation. The quality of the bone into which the cement is implanted therefore plays a large part in determining the life span of this interface. The interface at the bone has been the subject of radiographic study. It is possible that debonding at the cement bone interface is a result rather than a cause of aseptic loosening, whereas at the implant-cement interface, it is believed to be a cause. Cement-stem debonding can cause the generation of debris which may be transported to the bone interface where if of an appropriate size and shape, this debris may cause osteolysis and in turn debonding at the bone interface. Cement-bone debonding found using radiographic techniques has been used clinically as a sign of aseptic loosening [37]. The amount of cement-bone debonding observed in clinical studies has been steadily reducing [111]. This may be due to more modern cementing techniques, where careful preparation of the bone bed and pressurisation of the cement allow deeper penetration of cement into the cancellous bone, improving interlock at the interface. This also helps to prevent fibrous tissue formation at the bone cement interface [49].

The majority of debonding is found at the stem-cement interface. All radiographic studies found in the literature have shown signs of radiolucency in more than 50% of stems observed [20, 37, 81, 93, 111]. In a study by Paterson *et al*. there was some

radiolucency observed in 100% of the samples considered [93]. It may be concluded from these studies that debonding occurs more readily at the cement-stem interface than at the bone-cement interface. Further evidence was provided by the article by Jasty *et al*. who found debonding around the entire circumference of the implant at the stem-cement interface of some post-mortem total hip replacements where the bone-cement interface remained intact [49]. This debonding occurred mainly in the superolateral region of the stem but often extended to include some proximal debonding. In all but the worst cases the stem-cement interface remained bonded in the middle region of the stem.

The material and surface finish of the stem can greatly affect the timing and degree of debonding at the stem-cement interface. Prostheses with a smooth polished surface will debond more readily than those with a matt 'roughened' surface. Surface roughness and its effect on damage accumulation through debonding has therefore been the topic of several studies. Verdonschot *et al.* modelled surface roughness using a finite element method in Marc™ and showed that an increase in surface roughness reduced the stress on the cement mantle and reduced prosthetic subsidence [121]. However, roughened stems have a major disadvantage in that they will cause abrasion of the cement mantle if debonding does occur. This was found to be the case in some experimental work by Verdonschot *et al.* and damage accumulation in the cement increased as a result [121].

Some authors believe that it is preferable to have a completely debonded stem from the outset as this allows the stem to initially subside a short distance (causing a wedge effect holding it more securely in place) and reduces the wear on the mantle after the stem has debonded (which may be inevitable). This was shown by Heuer *et al.* where a reduced coefficient of friction reduced the fatigue fracture rate in the cement mantle [42].

In several studies it has been assumed that complete debonding of the stem and cement occurs once a load of sufficient magnitude has been experienced by the stem-cement interface. Verdonschot showed that the debonding process is gradual at the stem-cement interface [118]. Mann *et al.* states that a large amount of energy is absorbed before complete debonding occurs at the cement bone interface due to

interdigitation of cement and cancellous bone [74]. It was shown that the cement bone interface actually shows non-linear debonding behaviour and should be modelled as such in all cases. The stem-cement interface generally debonds at a higher rate than that of the bone-cement interface and hence in computational studies has often been modelled as completely debonded as an initial condition. Finite element models have shown that debonded cement-stem interfaces can lead to localised stress concentrations in the cement, leading to local crack initiation [119]. Figure 3-21 shows the effect of stem-cement interface conditions on the damage accumulation rate in the cement mantle in a finite element model of a total hip replacement. For a completely bonded stem-cement interface the condition of the bone had minimal effect, but a much greater effect in the case of an unbonded interface.

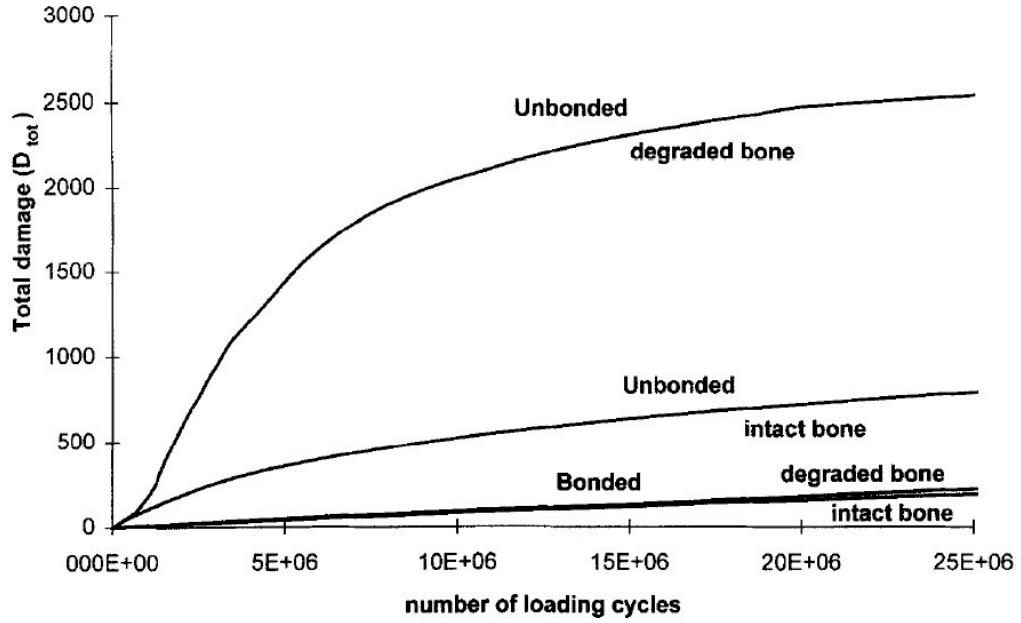

Figure 3-21 - Damage accumulation of bonded and unbonded stem cement mantles [119].

Porosity

Damage accumulation is greatly affected by the initial condition of the cement mantle as well as the loading that the mantle is subjected to during its life. High levels of porosity and other flaws, which may be exacerbated by poor mixing or handling techniques, would be expected to raise the rate of damage accumulation. It has been observed in many publications that cracks tend to originate at pores in the cement [30, 48].

Modern cementing techniques involve mixing cement under vacuum in an effort to reduce porosity generated by air inclusion. These techniques have been shown in several studies to significantly reduce overall porosity [70]. Other factors affecting porosity include storage and mixing temperature, thermal environmental conditions, pressurisation of cement and stem surface roughness.

Mixing temperature influences porosity in a minor way when compared to the mixing method used (hand mixed or vacuum mixed). A reduction in macro-porosity is observed for a reduction in storage temperature. This is believed to be because the cement polymerisation rate is reduced and so any shrinkage affects the entire bolus of cement rather than nucleating local pores [60].

By reducing the polymerisation rate it is possible to reduce the nucleation of pores within the cement mantle. Reducing the stem temperature allows a small reduction in the number and size of pores generated during cure [84].

By pressurising the cement during cure it is possible to reduce pore nucleation and growth within the cement mantle. This is achieved by reducing the local internal shrinkage by ensuring that the entire mantle shrinks uniformly [9].

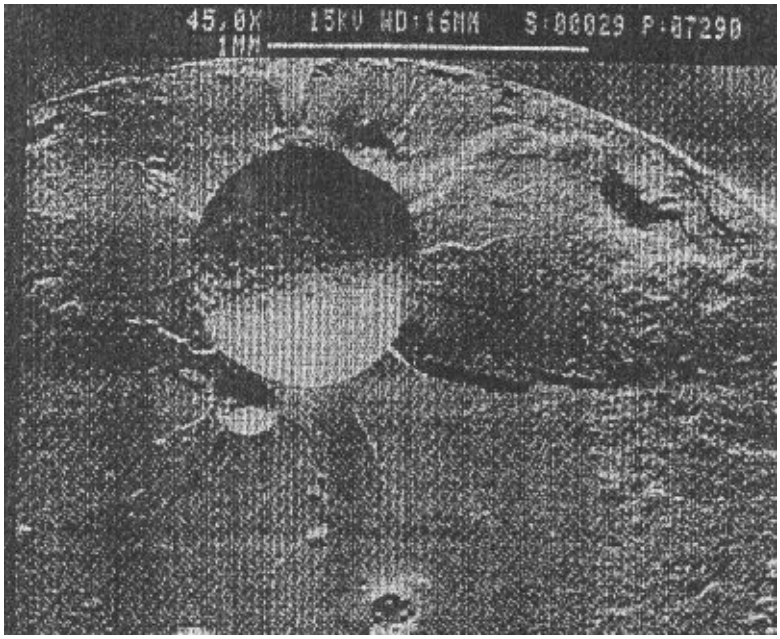

Figure 3-22 - Fracture surface showing large pore and smaller adjacent pores where cracks have initiated [48].

Increased stem surface roughness is believed to increase porosity at the stem cement interface by increasing entrainment of air during stem insertion.

Jafri *et al*. showed that porosity is related to the temperature of the stem, with a heated stem causing a dramatic reduction in the surface porosity at the stem-cement interface. This may help to improve the life of the cement mantle *in-vivo* [47].

Residual Stress

Residual tensile stresses are produced in bone cement mantles for two reasons. Firstly there is a thermal contraction that takes place after stress locking has occurred (stress locking is considered to be point at which the cement has hardened sufficiently for any further volume change to generate residual stresses in the constrained cement). There is also a volumetric change related to the polymerisation of the cement.

The necessity of including residual stress in bone cement fatigue models has been a matter of contention for some time. While residual stresses of 2.5MPa [88] to 12.6MPa [91] have been measured, the ultimate tensile strength of typical bone

cement is 40-50MPa [39] and for this reason the residual stress has been considered by many to be insignificant when modelling the life of the cement. The viscoelastic properties of the cement (stress relaxation) have also been used to justify neglecting residual stresses.

Stress relaxation is defined as "the change in stress in a sample held at constant strain" [56]. Stress relaxation is a known phenomenon in acrylic bone cements and will tend to reduce the residual stress in the mantle. This reduction in the residual stress has been assumed to occur before the first loading cycle in fatigue and damage accumulation models published to date. For all these reasons the residual stress has been discounted in many previous studies as the effect on the damage accumulation rate was deemed insignificant.

Recently it has been shown that these assumptions may not be accurate. Residual stresses in typical cement mantles are significantly lower than the ultimate tensile strength of the cement. However, residual stresses are of the same order as the stresses induced by load application, and hence in the worst case, when the first load cycle is applied, the stress experienced by the cement mantle may approximately double. This change in the stress may significantly shorten the fatigue life of the cement. Stress relaxation will reduce the residual stress but the residual stress will nevertheless stabilise at a level that is still a significant fraction of the total stress in the material when under external load.

There is some evidence that residual stresses generated during polymerisation are sufficiently high to initiate cracks in the cement prior to load application [91]. This pre-load cracking may be extremely important in determining the life of the total joint replacement. In a brittle polymer such as PMMA the fatigue life is usually dominated by crack initiation [49]. If cracks are already present (initiation has already taken place) prior to the application of load then it is reasonable to assume that the life of the component will be dramatically reduced. Lennon *et al.* showed that an area of high residual stress lead to pre-load damage in several *in-vitro* 2-dimensional models of femoral components of hip replacement (Figure 3-23) [58].

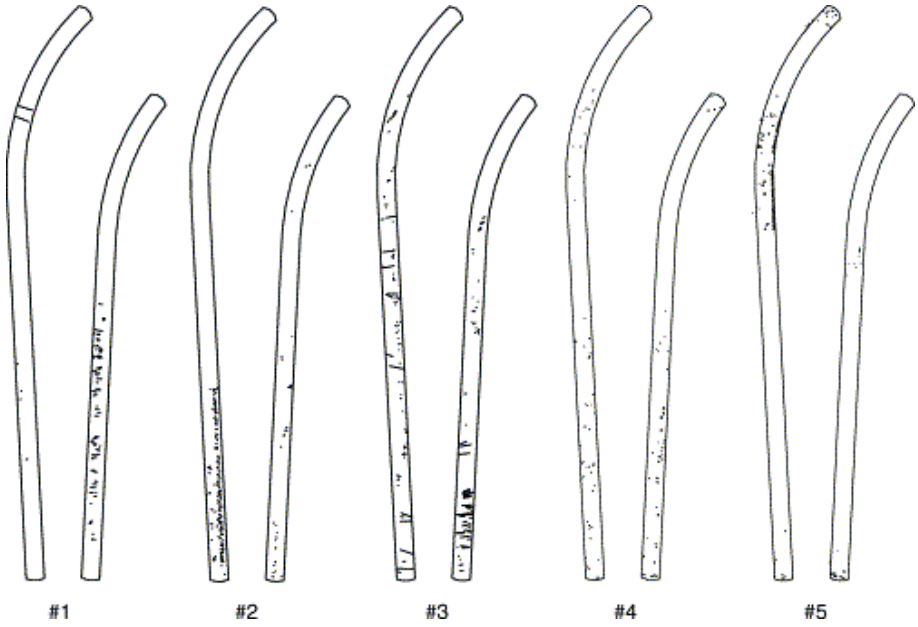

Figure 3-23 - Pre-load cracking (shown as specks) in 5 *in-vitro* 2-dimensional models of femoral hip component replacement [58]

Orr *et al.* has also seen these pre-load shrinkage cracks at the cement-implant interface using microscopy of a cylindrical representation of a hip stem (Figure 3-24) [91]. The bone was represented by a tube of Tufnol™. A gap at the cement bone interface was also noticed (Figure 3-25). This can be explained by shrinkage of the cement in the hoop direction causing a contraction away from the bone and onto the implant, causing both a gap at the cement-bone interface and high stresses in the hoop direction which might cause radial cracks at the cement-implant interface.

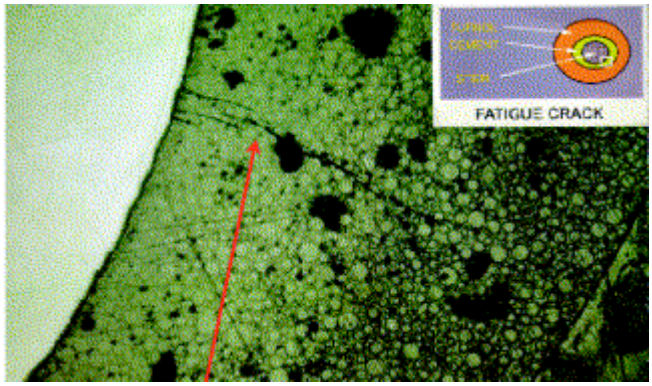

Figure 3-24 - Radial crack observed after polymerisation [91]

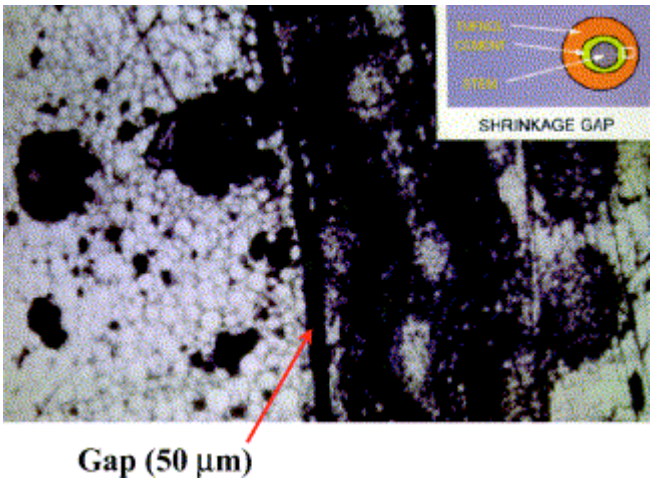

Figure 3-25 - Gap at the cement-bone interface observed after polymerisation [91]

Orr *et al.* also noted that these cracks were not seen after hand mixing the cement [91]. Hand mixing bone cement is known to produce specimens with greatly increased porosity. This is currently thought to be the cause of a reduction in the degree of shrinkage observed (typically 1-2% volumetrically with hand mixed cement, 7-8% with Vacuum mixed cement) - pores generated by hand mixing expand during cure and compensate for contraction due to density change. As a result Orr *et al.* noticed significantly less pre-load cracking surrounding the implant when using a hand mixed cement.

It is stated in several recent studies that the residual stress is an important parameter to consider when modelling the life of a joint prosthesis [87, 100]. Pre-load cracks add an extra difficulty when trying to produce an accurate model of the residual stress field, as they cause relaxation of stress in the vicinity of the crack.

3.4 Finite Element Modelling of Bone Cement

Bone cement failure has been observed as the most prominent cause of revision for several different total joint replacements (section 3.3.2). In an attempt to reduce the propensity for cement failure it is firstly important to understand the mechanisms of failure and how they interact with each other. This is most easily achieved through numerical modelling of the entire system which can be undertaken using Finite Element Modelling (FEM).

Finite element methods have proved to be the most popular computational methods for predicting the behaviour of implant-bone systems. Finite element packages now allow optimisation studies on implant designs long before manufacture. This is because a mesh of finite elements can be generated to suit most complex geometries and can be sufficiently refined to accurately predict results in specific areas. Prendergast *et al.* reviewed the use of FEM for skeletal analysis, orthopaedic device analysis and in modelling of bone remodelling and tissue growth [96].

Since the early 1980's 3D modelling has been the standard for computational analysis of biomechanical implants albeit using fairly crude geometry approximations in the earlier studies due to limitations in computing power and consequent restrictions on the number of elements that could be used to represent the structures of interest. The first large 3D model of a femoral component hip replacement was presented by Rohlmann *et al*. in 1983 and showed stresses in the bone cement and prosthesis due to muscle and joint reaction forces [98]. Since this first model several different aspects of implants have been investigated for their effects on the stresses within the bone-cement-prosthesis system, for example, the effect of different shaped collars and the size of the prosthesis. [44]. Gross *et al.* showed how finite element analysis could be used to determine the effect of a hollow hip stem on stress shielding in the femur [36].

Inclusion of the effects of creep and other time-dependent processes have been further refinement to the models, as most early models assumed linear-elastic behaviour. Lu *et al*. demonstrated how such a model can be produced and used to predict the effects of visco-elastic behaviour of materials (in this case the cement) [68].

3.4.1 Finite Element Modelling of Damage

Since FEM became a viable option for the analysis of this type of problem, attempts have been made to model the fatigue of bone cement and ultimately the life of total joint replacements. Two fundamentally different approaches have emerged:-

The first, mechanistic approach is that of fracture mechanics [11, 15, 74]. In this method, individual cracks through the material are modelled and crack growth paths and rates predicted directly. This method requires very detailed information about the behaviour of the crack through the material such as the effect of crack closure, pores and material defects and similar.

The second method is to use a continuum damage mechanics approach [29, 40, 53]. In this method, individual cracks are not considered, only the effects of the presence of the cracks on the materials properties of the cement. It is a more empirical approach, usually relying on S-N data from experimental tests. Due to the simplicity of this method it is easy to evaluate global effects of different boundary conditions and cement conditions.

Jeffers *et al.* have developed a damage accumulation model and have investigated the effects of porosity, residual stresses and stress relaxation on cement mantle fatigue failure. Using stochastic methods to determine pore distribution it was possible to investigate the effect of porosity on the failure rates of total hip replacements due to cement damage. The results show that porosity (especially in cases of high pore concentrations) has a deleterious effect on the cement mantle fatigue life, typically reducing predicted fatigue life by a factor of 10 (Figure 3-26, the four curves which include porosity have different, random initial porosity distributions)[51].

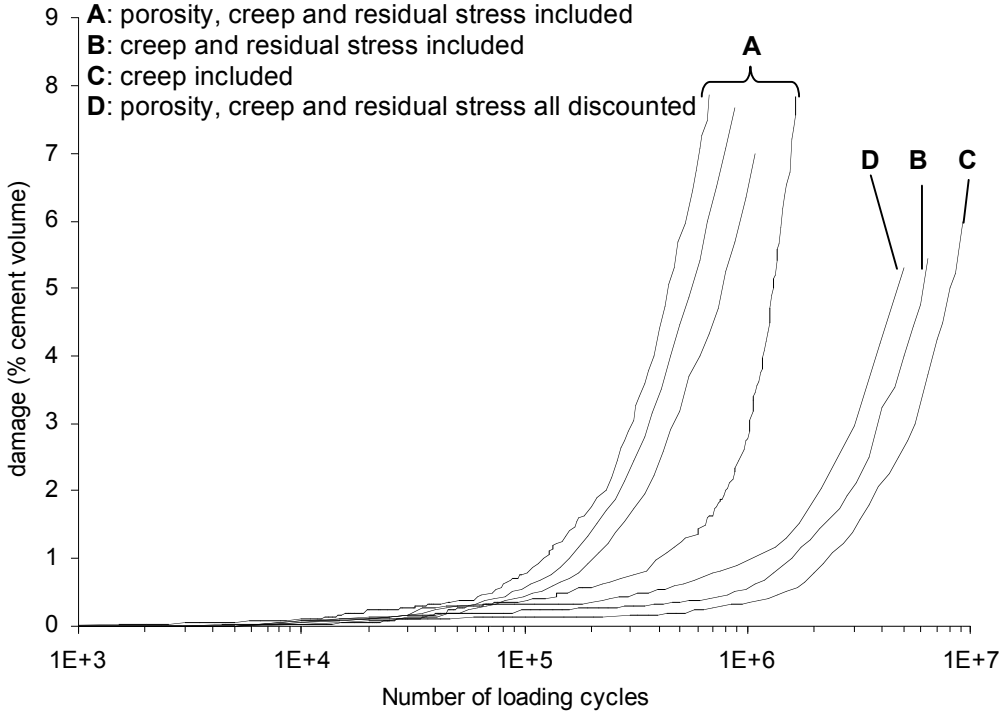

Figure 3-26 - Comparison of damage accumulation predicted including porosity, creep and residual stress [51].

Cement residual stress effects were also modelled using a quasi-thermal technique. The model was cooled prior to loading and by choosing an appropriate thermal expansion coefficient for the cement the maximum stress experienced within the cement could be tuned to a desired level. Using an average residual stress of 9.6MPa, an increase in the damage accumulation rate of approximately 10 times was established. The effect of stress relaxation was to reduce the damage accumulation rate by gradually reducing the residual stress in the cement. The effects modelled agreed well with experimental *in-vitro* testing.

3.4.2 Cement Polymerisation Modelling

When modelling the cure of the cement several factors must be accounted for. The polymerisation rate is not only time dependent but also dependent upon temperature and degree of polymerisation. Polymerisation produces heat as well as volume changes. Any mathematical model employed must account for (or make reasonable

assumptions accounting for) all of these factors. Several models have been proposed [7, 12, 110]. Each of these models is capable of predicting instantaneous temperatures and degrees of cure. They do not however, include any method of calculating residual stress.

The model published by Baliga *et al*. uses an experimentally determined function to describe the dependence of the polymerisation rate upon temperature and degree of polymerisation in order to predict polymerisation as a function of time. This method was also used by Starke [7, 110]. Both studies used a similar approach to generate temperature histories within curing cement mantles, although both used simplified geometries to represent the prosthesis-cement-bone systems under consideration. Figure 3-27 shows the 2-dimensional geometries used by Starke *et al*. (modelling the frontal plane) and Baliga *et al*. (modelling the transverse plane). Such geometrical simplifications may induce error when applied to *in-vivo* conditions.

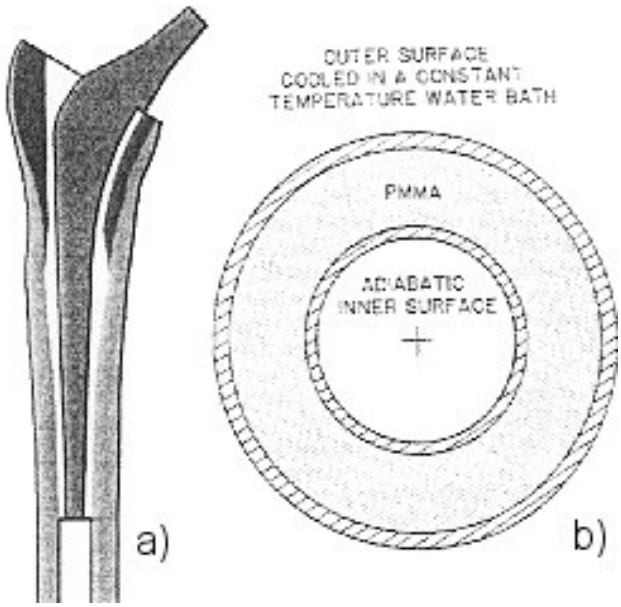

Figure 3-27 - Geometry used in finite element models of cement polymerisation adopted by (a) Starke *et al*. [110] and (b) Baliga *et al*. [7].

Borzacchiello *et al*. and Li *et al*. have published models which used an Arrhenius expression, which has a basis in chemical kinetics, to describe the dependence of polymerisation rate on temperature [12, 62]. Simplified geometries were also used (Figure 3-28).

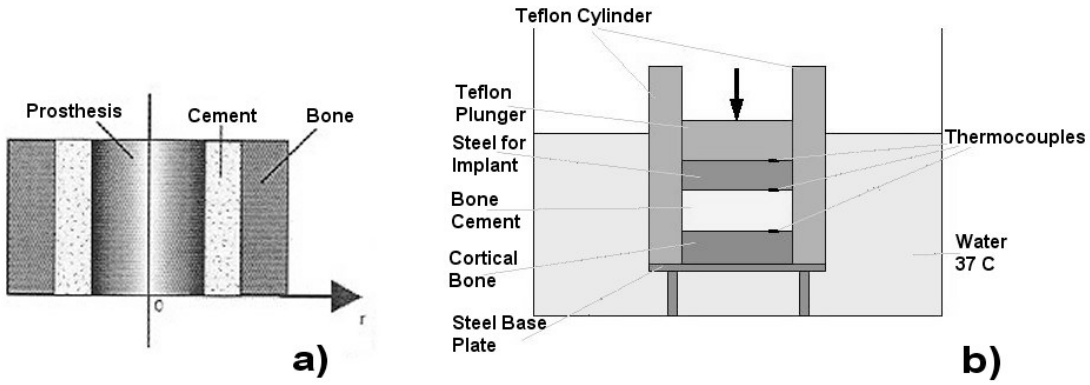

Figure 3-28 - Geometry used in finite element models of cement polymerisation adopted by (a) Li *et al.* [62] and (b) Borzacchiello *et al.* reproduced from [12].

Stańczyk *et al.* have also used the Arrhenius relationship to model cement polymerisation [107]. The model was used in conjunction with complex cancellous bone geometry to show the temperature that would be expected within individual trabeculae and to investigate the potential for thermal bone necrosis within such complex geometries at the cement-bone interface.

Thermal Material Properties During Polymerisation

Since cure rate is not only dependent upon time but also temperature and degree of polymerisation, knowledge of the thermal properties of the materials in the model is critical to any attempt at modelling. Some material properties are simple to find in the literature and have consistent values, such as those for the implant materials. Even varying the implant material from cobalt-chrome to titanium only varies the thermal conductivity from ~16.5 [5] to ~22$Wm^{-1}K^{-1}$ [126].

For biological tissue (bone, in the present case) representative values are more difficult to establish, owing to great variation from patient to patient and with anatomical site. A thermal model requires values for the density, conductivity and specific heat capacity and these can be found from varying sources in the literature.

Clattenburg *et al.* examined the thermal properties of bovine cancellous bone and reported values of 2.1-2.3x10^3kgm^{-3} for density, 1.15-1.73x10^3Jkg^{-1}K^{-1} for specific heat capacity and 0.39Wm^{-1}K^{-1} for thermal conductivity [19].

Values for density vary greatly since some articles do not distinguish between relative density and specific density. The specific density of cancellous bone is generally taken to be the same or very close to that of cortical bone. The relative density takes into account the porosity of cancellous bone and so is much lower. In general terms any bone with a relative density of less than 0.7x10^3kgm^{-3} is considered to be cancellous bone [31]. Relative densities as low as 0.05x10^3kgm^{-3} are found for human bone.

Values for the conductivity of cancellous bone varied from 0.29-0.60Wm^{-1}K^{-1} [13, 33, 112].

The reported values of the thermal properties of cortical bone are much more consistent than those for cancellous bone, presumably because of smaller variation in the density of cortical bone. Density has been reported to vary between 1.86-2.9x10^3kgm^{-3} [41, 55, 69, 102]. Both Henschel and Lundskog reported the same value for the specific heat capacity of cortical bone; 1.26x10^3Jkg^{-1}K^{-1}. Thermal conductivity of cortical bone has been reported by several authors [17, 69, 116]. Vachon *et al.* used bovine bone and Lundskog various other mammals. Only Chato has reported a value for human bone, 0.38Wm^{-1}K^{-1}.

Since bone cement is a commercially available material it is a lot simpler to define its thermal properties though these properties may be different before and during polymerisation. Baliga *et al.* quoted figures of the specific heat capacity, density and thermal conductivity of 1.25x10^3 + 6.5T J/kg ºC (where T is specified in ºC), 1.1x10^3 kg/m^3 and 0.2W/m ºC respectively [7].

3.4.3 Residual stress prediction

Although the evidence presented in section 3.3.2 suggests that residual stress potentially has a large, deleterious effect on the life of a THA [100], few authors have

achieved a satisfactory computational method for predicting the stress field within the cement mantle due to polymerisation of bone cement.

Nuno *et al.* used FEM to model a bone-cement-prosthesis system [88]. The stem was inserted into the cement mantle with a "press fit" (i.e. the stem was slightly larger than the cavity into which it was inserted). This method produced a residual stress field but does not take into account variations in polymerisation conditions within the cement mantle.

In order to predict the residual stress field it is necessary to relate the volumetric change to the degree of polymerisation. This is a complex process as the cement is thought to shrink at the same time as it heats up due to the exothermic polymerisation reaction. This heat causes an expansion due to thermal expansion coefficients. The volumetric change due to polymerisation must be coupled with mechanical property development and the thermal volumetric change, as the relative timing of the three separate events will have a great bearing on the residual stress field generated. If the polymerisation shrinkage happens when the properties of the cement are close to the initial fluid state then there will be little residual stress generation. If the polymerisation shrinkage happens when the cement is heating up, it may be masked by the thermal expansion of the cement.

Some attempts to measure and model the relative timing of these processes have been made. Lennon *et al.* produced a model using Ansys™ based on functions published by Baliga *et al.* and Starke *et al.*, which generated a temperature profile during cure in a simplified hip replacement geometry [7, 59, 110]. The model used an assumption of stress locking at differing moments during polymerisation and then the residual stress generated due to thermal contraction after this point was calculated. This, however, does not explicitly account for the shrinkage due to polymerisation. The model was validated using a geometrically identical physical model. After full polymerisation this physical model exhibited pre-load cracks formed in the cement mantle due to shrinkage during polymerisation (Figure 3-23). The model used in this study is highly sensitive to the timing of stress locking, which was hypothesised as a single instant and assumed to occur at the same instant in all elements.

Li *et al.* used finite element modelling techniques to predict residual stresses in cement mantles [63]. A model based on an Arrhenius equation was used to predict the polymerisation as a function of time. Again complete stress locking was assumed to occur at one moment, at the point of maximum temperature. From this point the entire cement mantle began to cool to ambient temperature. During the period of cooling a thermal contraction led to net shrinkage of the cement. Two different stem temperatures were examined; one at ambient initial temperature and one at 45ºC initial temperature. The residual stresses in the cement were compared in the hoop, radial and longitudinal directions. The stresses seen were consistently ranked with the radial stress being the lowest and the hoop stress being the highest with the longitudinal stresses somewhere in the middle. Changing the initial stem temperature to 45ºC caused the peak stress to move away from the cement-implant interface.

Stress locking is a simplification employed by many models. This method assumes that there is one instant during the polymerisation at which a complete transition from a Newtonian fluid to an elastic solid is experienced within the material. This will therefore mean that there is no ability for the material to transfer load prior to transition and that immediately after transition any mechanical change will result in stresses being developed.

Stress locking assumes an instantaneous change in the mechanical properties of bone cement from a fluid to a solid. In reality this will take a finite amount of time however and so to state that there is one instant when the material changes from fluid to solid is something of a simplification. The peak temperature will occur before polymerisation is complete and so there must be some time during which the material is not in its fully solid final state where some thermal shrinkage is taking place. Also, there must be some time before the peak temperature when the material is stiff enough to transfer some load as the volume changes. These effects should be investigated and accounted for in any future modelling of residual stress generation during polymerisation of acrylic bone cement.

No papers could be found in the literature that reported the temperature as well as the viscosity parameters during polymerisation. This may be because rheometers

generally run isothermally to eliminate any effect on the viscosity due to a change in temperature.

3.5 Literature Review Summary

- More than 75% of total hip arthroplasty revision operations are as a result of aseptic loosening.
- Mechanical failure of the cement is one of the most common causes of aseptic loosening, observed in many *ex vivo* total hip cement mantles.
- Damage accumulation is a result of fatigue loading of the cement mantle and the rate of damage accumulation is increased by residual stress.
- Residual stresses within the implanted cement mantle are a result of the dynamic nature of the curing process including mechanical property evolution and volume changes as well as evolved heat.
- Residual stress prediction has not yet been adequately addressed in the published literature.
- No authors have shown a method of residual stress prediction that accounts for all dynamic aspects of polymerisation in order to generate a model of the residual stress fields in the fully cured cement mantle.

4 Thermal Modelling of Bone Cement Cure

4.1 Introduction

Polymerisation of bone cement results in the generation of heat. In this chapter, the development and validation of finite element models to enable prediction of heat generation and the progress of the polymerisation reaction are described.

The polymerisation of bone cement was modelled for four separate situations. A concentric cylinders model was initially examined in order to enable comparison with models published by Baliga *et al*. and Borzacchiello *et al*. [7, 12]. A more realistic idealised hip stem model was then created to further develop the finite element modelling technique and to perform a sensitivity analysis, in which the model parameters important in determining the fidelity of the model predictions was determined. A set of validation experiments was also performed based on this idealised hip stem geometry. Using the same polymerisation model, temperatures generated when different thicknesses of cement were used to implant a resurfacing hip prosthesis were investigated. The model was also used to estimate bone necrosis following implantation of the tibial component of a total knee replacement. The four model geometries are shown in Figure 4-1.

By modelling polymerisation for every element in the finite element models it was possible to observe the cure process noting any gradient in the cure and also peaks in the bone-cement interface temperature.

Bone has been reported to begin to die if held above a temperature of 50°C for more than approximately 1 minute [7]. Other authors have developed methods by which the likelihood of thermal necrosis can be predicted using the concept of a necrosis index. The necrosis index includes the effects of both time and temperature and can be calculated from the temperature history in each element. It indicates the level of

damage that an element has incurred due to heat evolved by the polymerisation reaction [82].

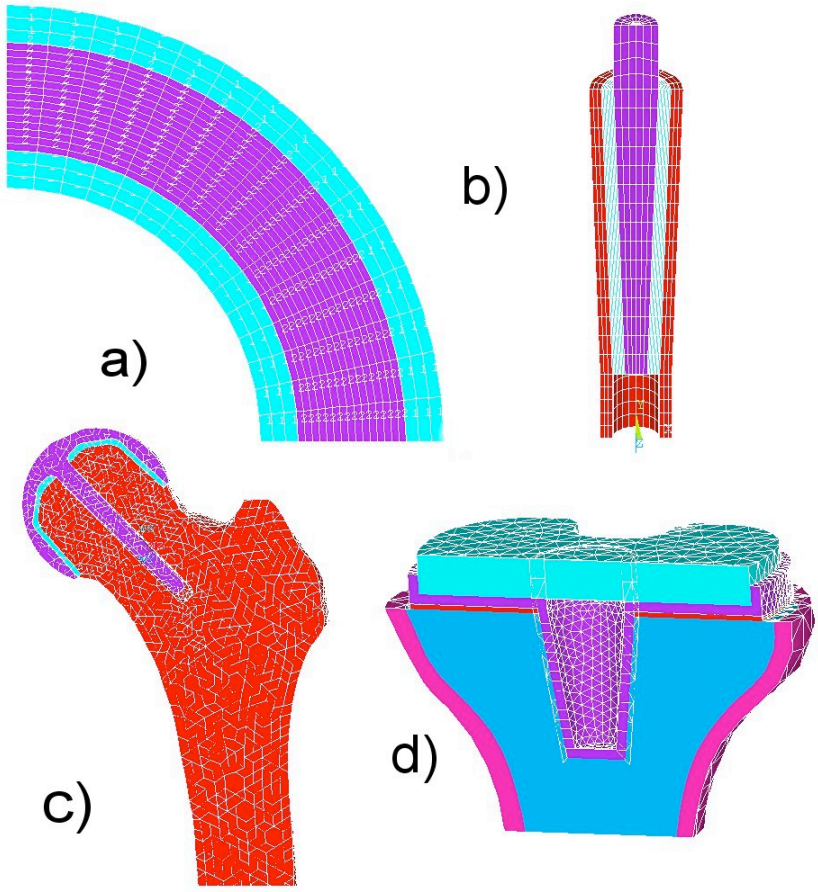

Figure 4-1 - Model geometries used in different chapters of the present work: a) Concentric cylinders, b) Idealised stem, c) Femoral head resurfacing, d)Tibial component of TKR

4.2 Polymerisation Model

The polymerisation model is common to all the finite element models, but each has a different set of boundary conditions, initial conditions, geometry and/or mathematical model describing the reaction rate as a function of temperature.

The polymerisation model makes it possible to calculate, using one of two separate methods (detailed later in this chapter), the polymerisation rate at any instant based on the current and local temperature and degree of polymerisation. From this rate of polymerisation a rate of heat release can be established and used to calculate the new temperature at some later time.

For a uniform element of polymerising cement with current temperature T_0 and current degree of polymerisation (α_0), the instantaneous heat generation rate S is given by the equation

$$S = f(T_0) \times (1 - \alpha_0)^n \alpha_0{}^m \qquad \textbf{4-1}$$

where n and m are independent rate constants. α_0 must be greater than 0 for polymerisation to begin and so is set to 1×10^{-6} at the beginning of polymerisation. The heat generation rate can then be assumed constant over a small time interval (t) and can be substituted into the standard equations of heat transfer [92] to calculate the temperature T_1 after time interval t. A new degree of polymerisation can then be calculated using equation 4-2;

$$\alpha_1 = \frac{Q_1}{Q_{tot}} \qquad \textbf{4-2}$$

where Q_1 is the amount of heat liberated per unit volume during interval t. The total amount of heat per unit volume liberated during the entire reaction is designated Q_{tot}, which is measured using Differential Scanning Calorimetry.

The new, calculated values of α and T are then used to generate heat generation and polymerisation rates for the next time step and the model runs in a continuous loop, summarised in Figure 4-2.

The time interval (t) between each step in the model is allowed to vary and is calculated based on a maximum allowable change in the degree of polymerisation (0.025) between steps. By varying the time step it is possible to capture rapid changes in polymerisation rate but also to use large time intervals when polymerisation is proceeding slowly or has nearly completed, giving better computational efficiency. The time interval t was calculated as inversely proportional to the heat generation rate, subject to a maximum value of 25s. Each model was allowed to run for 2000s after which polymerisation was considered complete. In reality, residual monomer may remain in the cement after this time – the residual monomer was assumed to be a small fraction of the amount present at the start of reaction and to not contribute to heat generation. This assumption is reasonable as the amount of heat liberated and the material property change caused by any subsequent polymerisation of residual monomer will be insignificant.

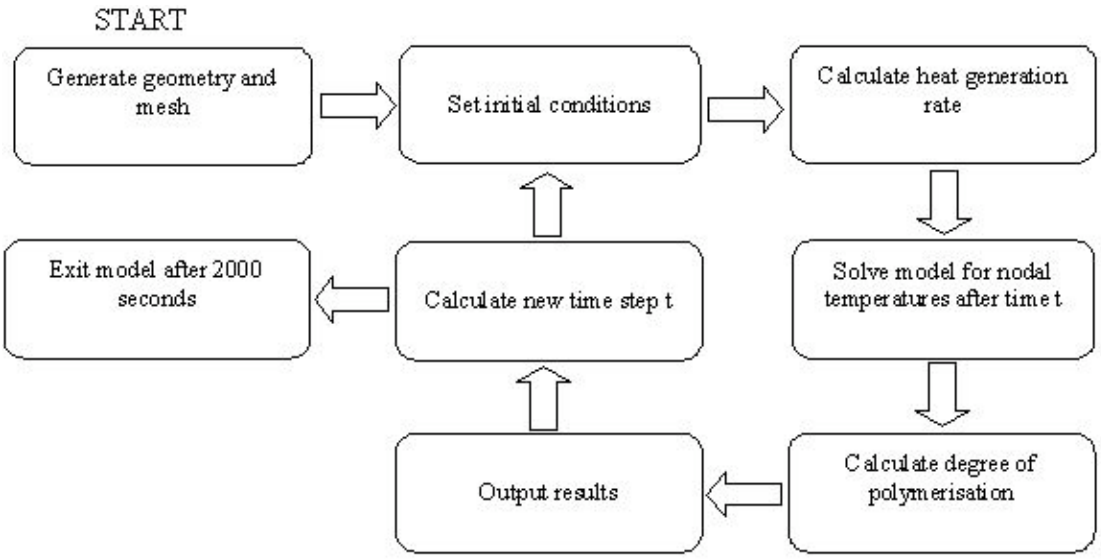

Figure 4-2 - Flow chart describing method of thermal computational modelling.

4.3 Concentric Cylinders Model

4.3.1 Method

In order to assess the feasibility of implementation of the polymerisation model within the Ansys™ environment a finite element model was created based on experiments carried out by Baliga *et al.* [7]. The model consisted of two concentric copper cylinders containing a layer of bone cement. The inner surface of the inner cylinder was assumed to be adiabatic (no heat could flow across the surface). The external surface of the cylinders was considered to be at a constant temperature of 37˚C.

The thermal materials properties of copper were not given in Baliga *et al.*'s paper and so were found in alternative literature [4]. All other model conditions remained identical to those used by Baliga *et al.* The model was experimentally validated by Baliga and so it was possible to make a direct comparison between the models. One quarter of the cylinders was modelled and edges along the x & y-axis were considered adiabatic to model symmetry. The geometry of this model is given in Appendix I – Model Drawings and Dimensions.

The geometry was planar and so quadrilateral elements were used with a fine mesh in the cement and a relatively coarse mesh on the copper cylinders as the cement temperature was of main concern (Figure 4-3).

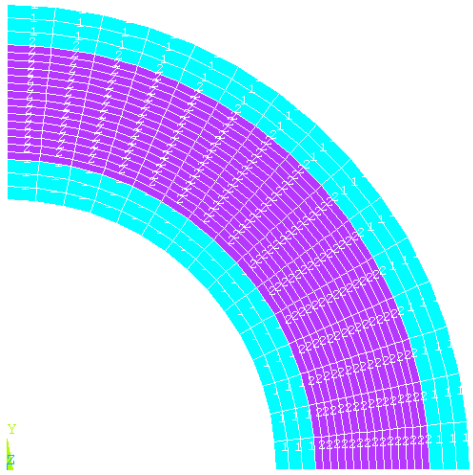

Figure 4-3 - Quadrilateral mesh of concentric cylinders model

The heat generation rate at each time step was calculated using equation 4-3;

$$f(T_0) = 4.4\times10^6\left(a_0 + a_1\frac{T_0}{100} + a_2\left(\frac{T_0}{100}\right)^2 + a_3\left(\frac{T_0}{100}\right)^3 + a_4\left(\frac{T_0}{100}\right)^4 + a_5\left(\frac{T_0}{100}\right)^5\right) \quad \textbf{4-3}$$

where a_n are polynomial coefficients determined experimentally using differential scanning calorimetry. In this study the parameter values published by Baliga were used and are shown in Table 4-1.

a_0=-23.89	a_1=296.74	a_2=-1352.97
a_3=2894.76	a_4=-2806.62	a_5=1009.84

Table 4-1 - Model parameters from Baliga *et al.* [7].

4.3.2 Results and Discussion

The model was run in three different conditions. The first model was run with thermal properties identical to those set out by Baliga *et al*. [7]. This model produced peak temperatures greater than those reported by Baliga (Figure 4-4), although the

polymerisation process ran at a similar rate, producing complete polymerisation across the entire cement mantle after approximately 600s (Figure 4-5).

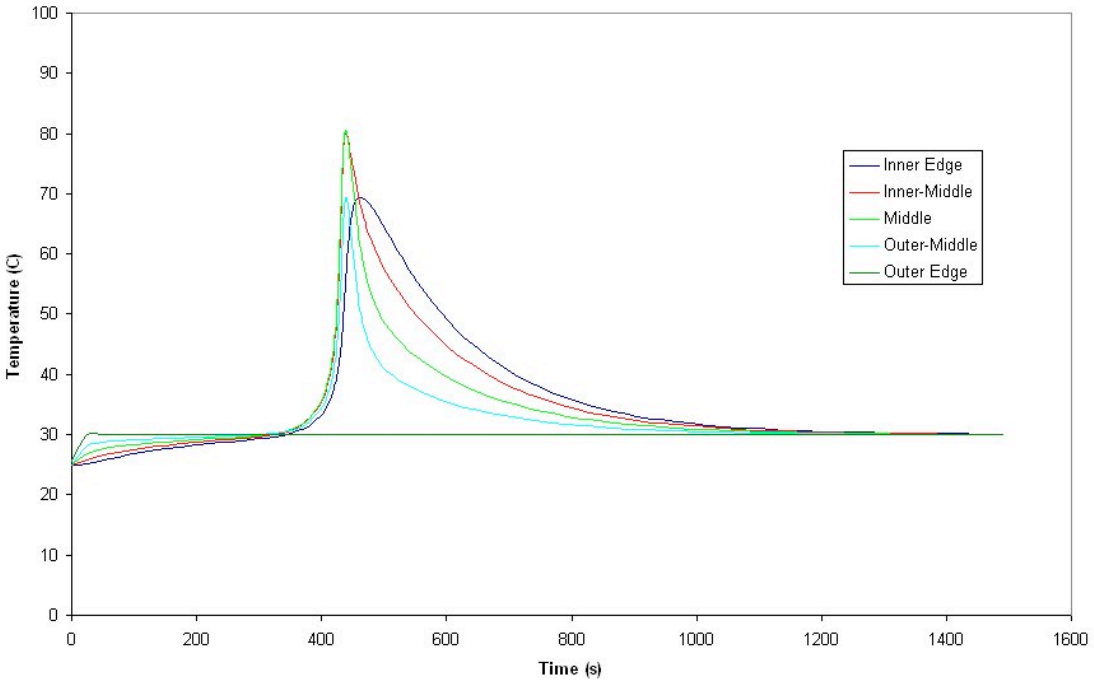

Figure 4-4 - Temperature history across cement mantle in the radial direction.

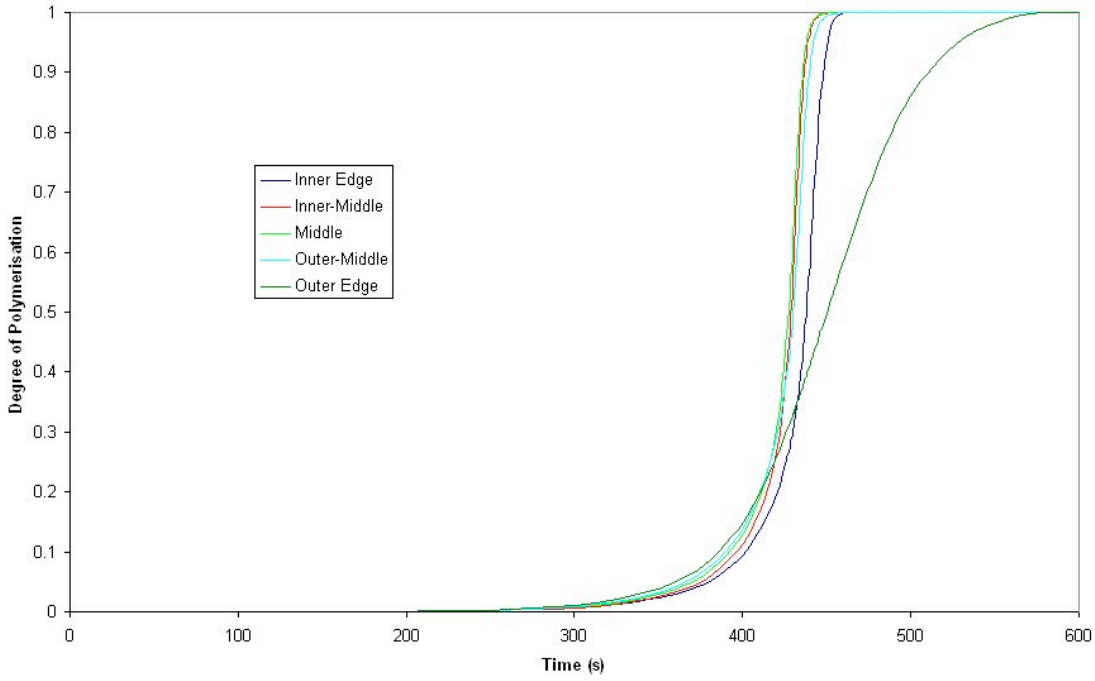

Figure 4-5 - Polymerisation history across cement mantle in the radial direction.

Given the discrepancy between the published and calculated results a sensitivity study was performed in which some of the model parameters were altered to establish which parameters the value of the peak temperatures was most sensitive.

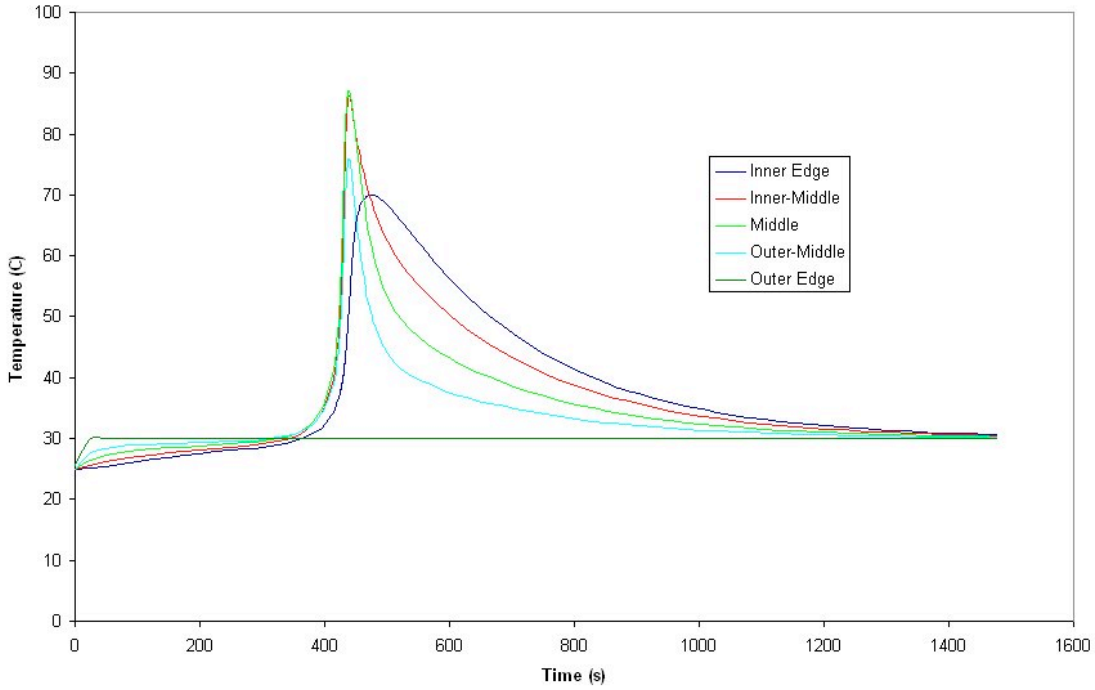

Figure 4-6 - Temperature history of Baliga model with low conductivity (0.14W/m-˚C).

A range of values for both the cement conductivity and the total amount of heat liberated were given by Baliga *et al.* In the present study, the cement conductivity, k, was varied between 0.14W/m-˚C and 0.2W/m-˚C. By reducing the conductivity of the cement, it was found that the peak temperature increased by a small amount (Figure 4-6). By reducing the total heat liberated, Q_{tot}, from $1.55 \times 10^8 J/m^3$ to $1.4 \times 10^8 J/m^3$ the peak temperature was reduced by approx 11ºC (Figure 4-7).

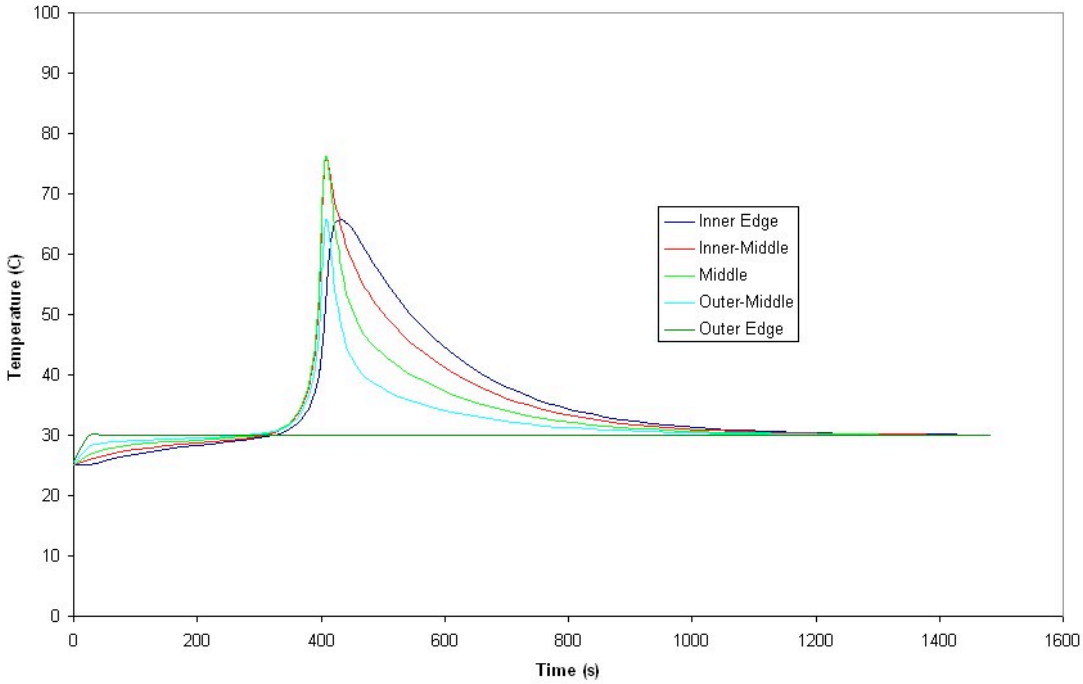

Figure 4-7 -Temperature history of Baliga model with low total heat liberated (1.4x108J/m3).

Baliga found a peak temperature of no more than 65˚C. The lowest peak temperature that the current model produced was approximately 80˚C. This is an unacceptable difference and the reason for it could not be identified. The model was investigated and compared with alternative mathematical models of cure found in the literature. Eventually, the Baliga model was abandoned in favour of one presented by Borzacchiello *et al*. [12]. This model also has the advantage of not needing the definition of so many experimentally determined parameters. It was also decided that the geometry of the current model was too abstract and not sufficiently clinically relevant. An idealised prosthesis-cement-bone model for the hip was therefore developed and is discussed in the following section.

4.3.3 Conclusions

The simple geometry and well characterised boundary conditions of the concentric cylinders model allows rapid analysis of variations to the model conditions and provides a good platform for model development.

There are unexplained discrepancies between the results calculated in this study and those published by Baliga.

The fitting of a polynomial to DSC data to generate the function describing heat generation rate as a function of temperature may not be the most accurate or straightforward method. The polynomial contains coefficients with no physical or chemical interpretation.

4.4 Idealised Stem Model

4.4.1 Introduction

It is useful to observe the cure process in a 3-dimensional geometry as this allows us to investigate the effect of more geometry effects such as adding a taper and misalignment of the stem. However, in order to enable a simple method of validation and to keep computational costs low, it is necessary to keep geometric and material property models simple. A concentric cylinders model with a tapered section was generated and investigated in order to better approximate a femoral hip replacement component within a femur. Using this model the sensitivity of the results to various model parameters and inaccuracies that might be encountered in surgery was examined.

4.4.2 Method

The geometric model consisted of a simplified bone-cement-prosthesis system. The stem consisted of a 30mm cylindrical section of diameter 18mm proximally, with a 110mm tapered distal section. The distal section was tapered to a tip diameter of 9mm. The cement formed a 2mm thick layer around this distal section. A layer of cortical bone 5 mm thick surrounded the cement with a section of cortical bone protruding 30mm distal to the tip of the stem. Drawings are shown in Appendix I – Model Drawings and Dimensions. These dimensions correspond to those of an existing fatigue model, which it is intended will accept as an input the residual tensile stress in the cement mantle output by the present model. Due to symmetry only 180˚ of the model was created.

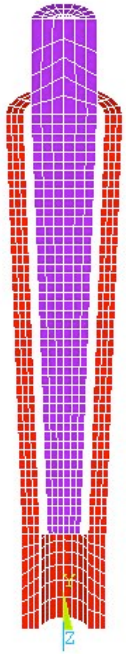

Figure 4-8 - Hexahedral mesh of idealised hip stem model.

The geometric model was meshed using hexahedral finite elements. The mesh across the cement was increased in density compared with the bone and prosthesis. There were 10 elements across the cement mantle and 3 across the bone and stem in the radial direction (Figure 4-8). There were 15 elements in the distal-proximal direction between the stem shoulder and the distal tip, five in the distal bone projection and four elements in the stem neck.

The algorithm simulating the effects of polymerisation ran as previously described (Chapter 4.2), with the exception that the function describing the dependence of the heat generation rate on temperature was modified to be;

$$f(T) = K_0 e^{\frac{-Ea}{RT}} \qquad \textbf{4-4}$$

Materials properties and other constants required to specify the model were as shown in Table 4-2.

Variable	Value
Thermal Conductivity of Bone [17]	0.38 W/m-K
Specific Heat Capacity of Bone [17]	1260 J/kg-K
Density of Bone [41]	2100 kg/m^3
Thermal Conductivity of Stem [4]	14.6 W/m-K
Specific Heat Capacity of Stem [4]	450 J/kg-K
Density of Stem [4]	8870 kg/m^3
Thermal Conductivity of Cement [7]	0.2 W/m-K
Specific Heat Capacity of Cement [7]	6.5*(Temp in Centigrade)+1250 J/kg-K
Density of Cement [7]	1100 kg/m^3
Polymerisation Activation Energy, E_a [12]	31285.582 kJ/kg
Reaction Rate Coefficient, K_0 [12]	9.1574
Reaction Rate Power, m [12]	0.98
Reaction Rate Power, n [12]	1.064
Total Heat Liberated, Q_{tot} [7]	1.55x10^8 J/m^3
Initial Stem Temperature	296 K
Initial Cement Temperature	296 K
Body Temperature	310 K

Table 4-2 - Input variables for idealised hip stem model

Certain variables, which it may be possible to control either clinically or during manufacture of the cement, were altered about these central values in order to observe the effect each one has on the peak temperature and the cure rate profile. These variables were the activation energy of the polymerisation reaction, the reaction rate constants (K_0, m and n), the total amount of heat liberated by the cement and the initial temperature of the stem. The Ansys™ log file used to generate the standard model is provided in Appendix II – Finite Element Modelling and Results Processing Codes.

Effects due to cooling produced by fluid flow through the bone were ignored in order to allow experimental validation. This effect may be significant *in-vivo* .

4.4.3 Results and Discussion

Results were recorded and plotted for 12 nodes in the cement mantle. Graphs of the cement-bone interface temperature were drawn up and compared. Also the nodal degree of polymerisation was plotted for each time step as a contour map.

Standard Test

With the standard set of parameters as shown in Table 4-2, the results showed a higher peak temperature than would be expected *in-vitro* (typically around 40-50˚C) [7]. The peak temperature in the distal region reached 66˚C (339K) which was the highest temperature seen throughout the cement mantle (Figure 4-10). This may be due to the thinner stem section at the distal tip and so less stem volume to act as a heat sink. The reaction was complete in all areas after 500s (8min20sec), which is comparable to that seen *in-vitro* (Figure 4-9). The cement experienced a greater rate of polymerisation distally and cure proceeded from distal to proximal (Figure 4-11). This cure gradient may cause local increases in residual stress or residual stress gradients in the fully polymerised mantle.

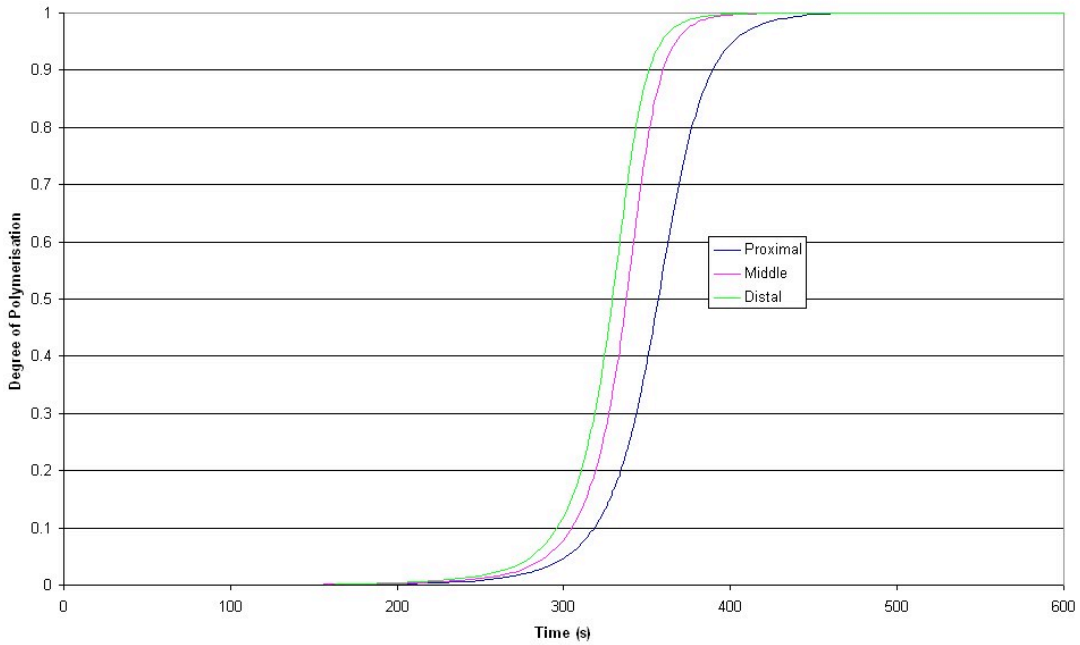

Figure 4-9 - Polymerisation curves for standard model.

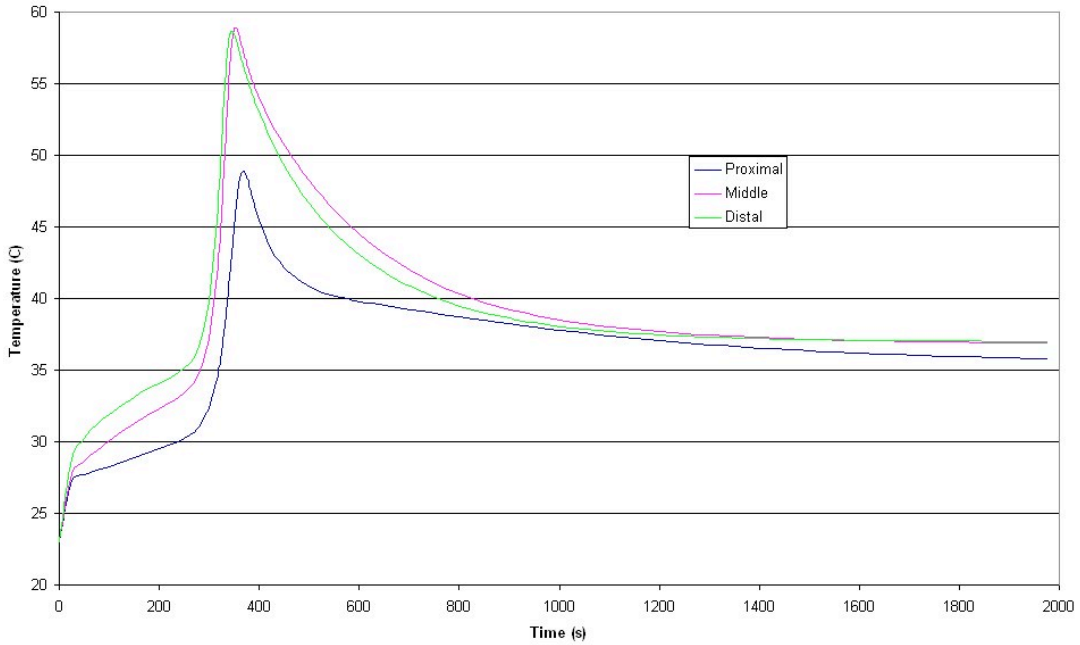

Figure 4-10 - Temperature profiles for standard model.

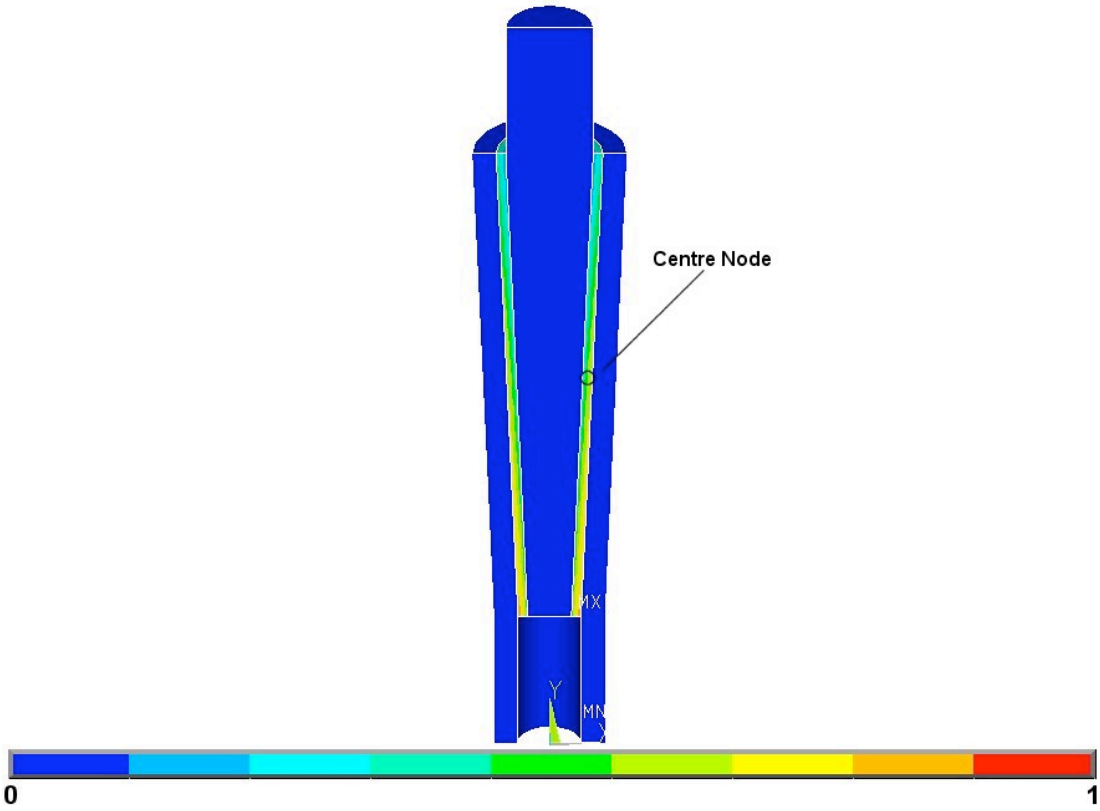

Figure 4-11 - Degree of polymerisation during cure of standard model at the time when the node at the radial and longitudinal centre of the mantle reaches a degree of polymerisation of 0.5.

Contact Analysis

Huiskes *et al.* stated that at a boundary between two materials (in this case the cement-bone or cement-stem interfaces), the surfaces of the two materials will not necessarily be at the same temperature [43]. There is a heat flow resistance related to the temperature drop over the interface and an interface conductivity value specific to the materials involved.

In order to more accurately represent the behaviour of the interfaces in the present model, contact conditions between cement and stem were introduced. The model mesh was refined in the longitudinal direction to better allow for local temperature and polymerisation gradients. The interface at the stem-cement interface was debonded and re-linked using thermal contact with an interface conductivity of 5500W/m^{2}K [43]. This gave a spread of cement temperatures as shown in Figure 4-13 and polymerisation curve spread shown in Figure 4-12. In a second series of analyses,

the cement-bone interface was also considered debonded. The interface conductivity in this case was 375W/m^{2}K [43]. The addition of this heat resistance had a large effect at the cooler end of the stem reducing peak temperatures by approximately a further 5°C as can be seen in Figure 4-15. Polymerisation curves are shown in Figure 4-14.

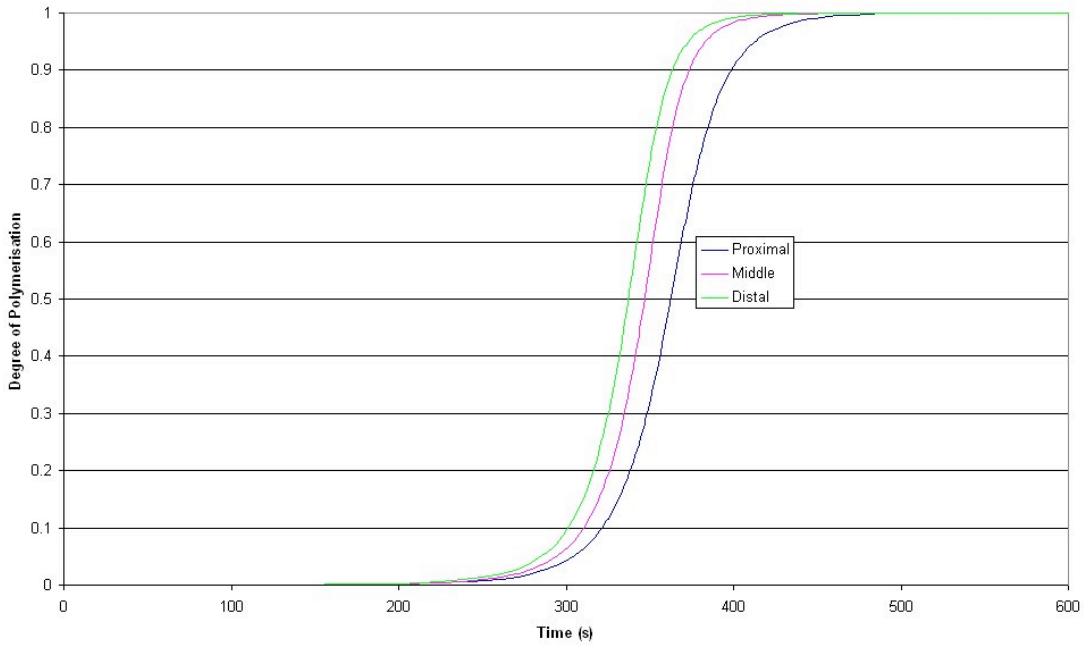

Figure 4-12 - Polymerisation curves from a model with just the stem-cement interface modelled as debonded.

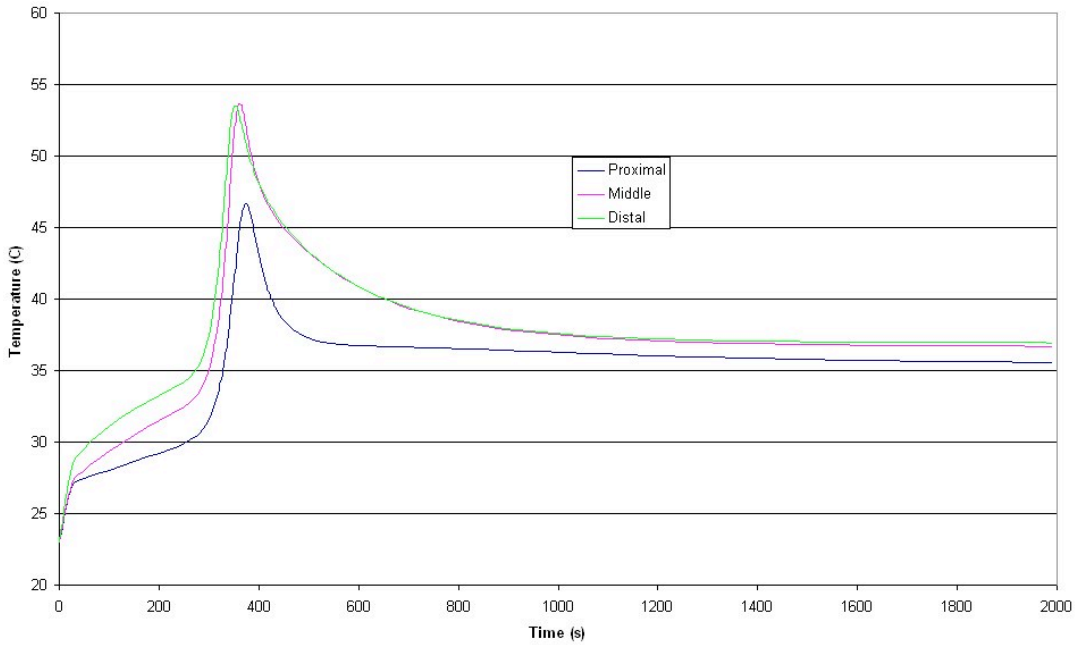

Figure 4-13 - Temperature curves from a model with just the stem cement interface modelled as debonded.

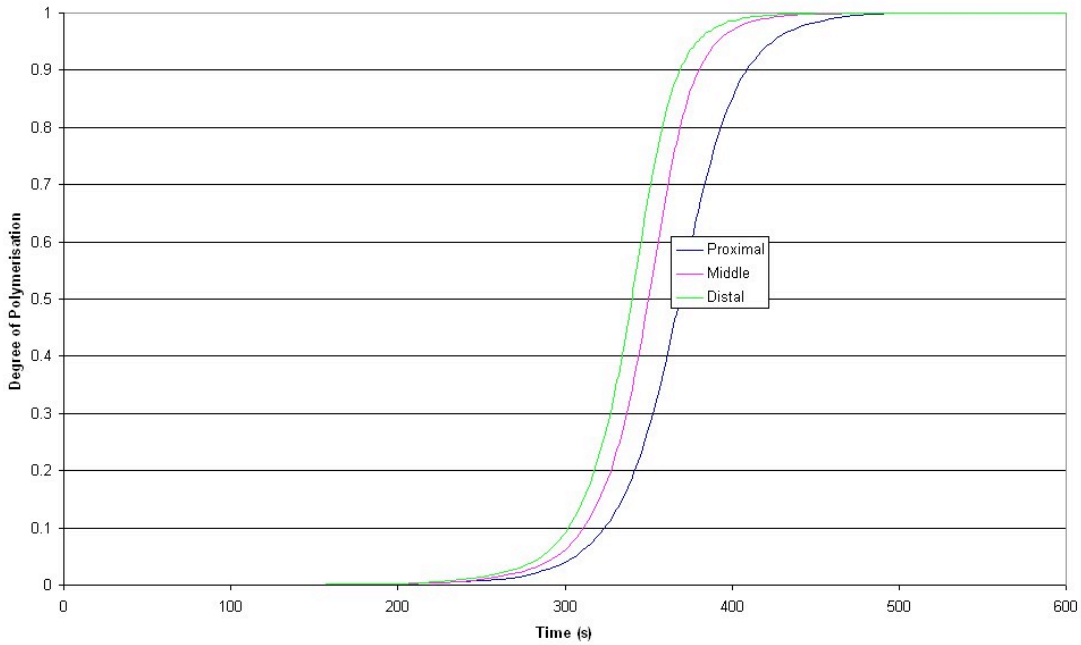

Figure 4-14 - Polymerisation curves for model with both stem-cement and cement-bone interfaces modelled as debonded.

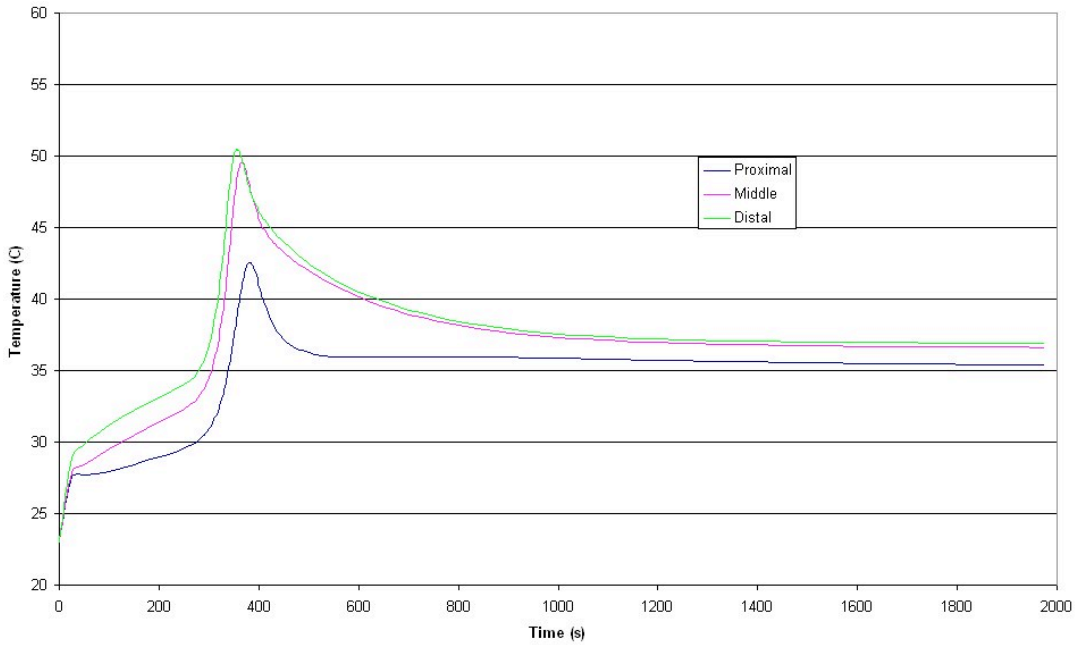

Figure 4-15 - Temperature curves for model with both stem-cement and cement-bone interfaces modelled as debonded.

The effects of the addition of contact resistances to the implanted stem model are summarised in Figure 4-16 and Figure 4-17. Figure 4-16 shows that modelling contact causes a small decrease in the rate of polymerisation, but Figure 4-17 shows a significant drop in the average temperature.

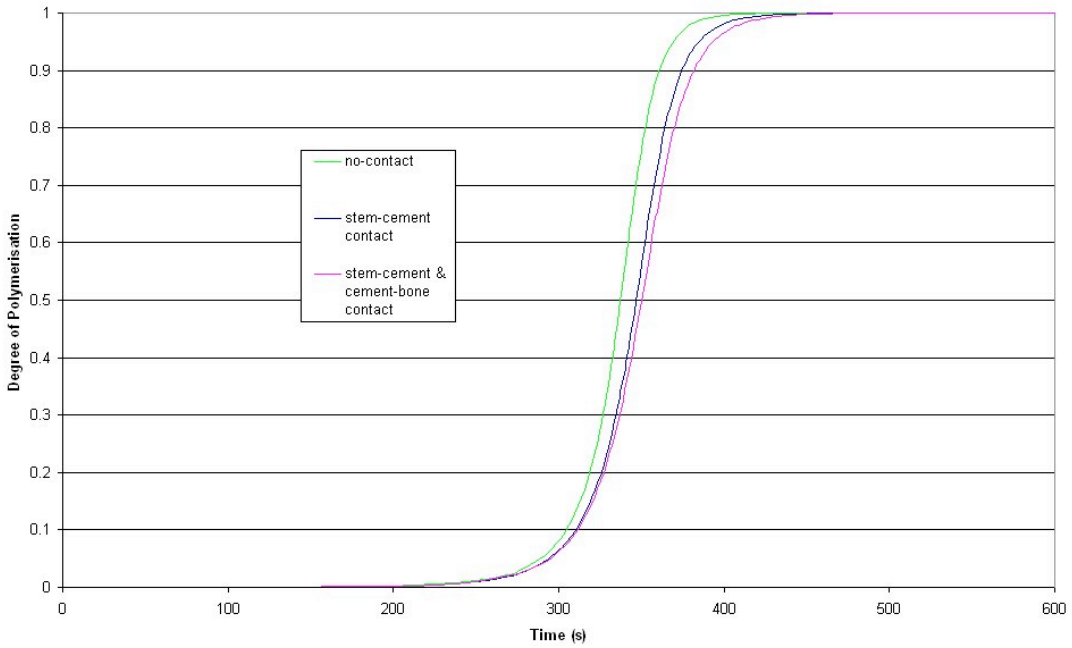

Figure 4-16 - Comparison of average degree of polymerisation curves from models with perfectly conductive (bonded) interfaces, stem-cement interface contact resistance and stem-cement & cement-bone interface contact resistances.

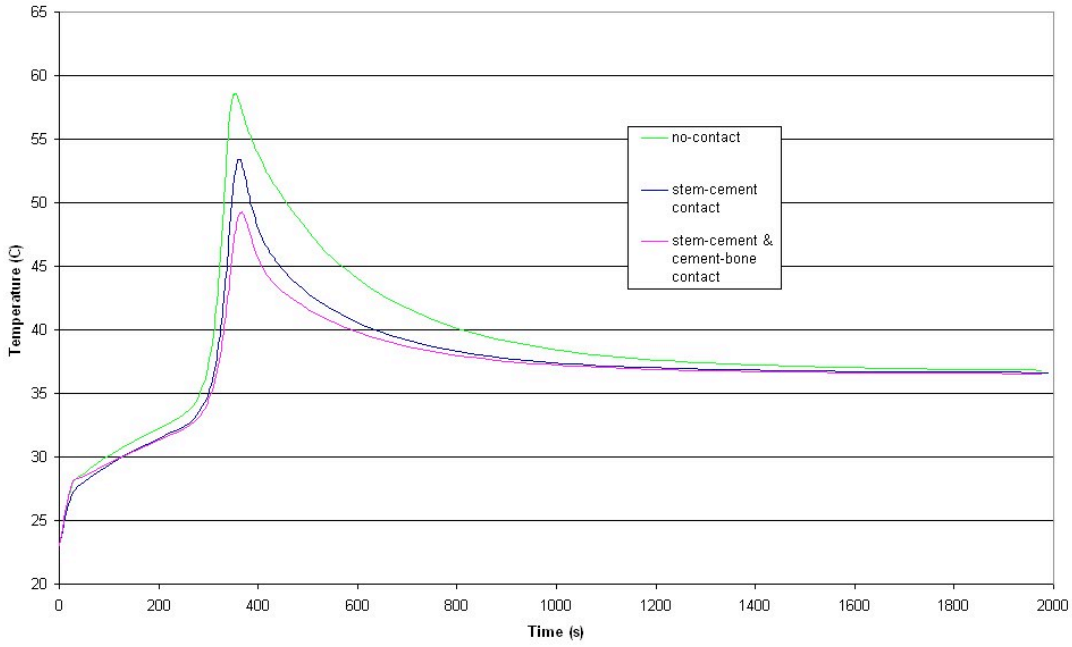

Figure 4-17 - Comparison of average temperatures from models with contact, stem-cement interface contact and stem-cement & cement-bone contact modelled.

Mesh Convergence of Thermal model

To investigate the effects of mesh density five models with increasing numbers of elements through the cement mantle thickness were compared. Beginning with a single element through the thickness, the mesh density was successively increased to two, three, five and seven elements. Temperature was recorded at four locations in the cement mantle - locations 1 and 2 were at the centre of the cement in the radial direction and at, respectively 1/3 and 2/3 of the extent of the cement in the proximal to distal direction. Where there was no node on the centre line an average was taken using the two adjacent nodes. The third and fourth locations were half way along the length of the cement in the proximal to distal direction, on the cement-bone (3) and stem-cement (4) interfaces.

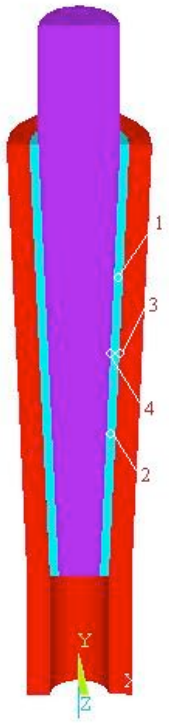

Figure 4-18 - Location of nodes taken for mesh convergence results analysis.

Results at all four locations were plotted for each model for each mesh density (Figure 4-19 - Figure 4-23).

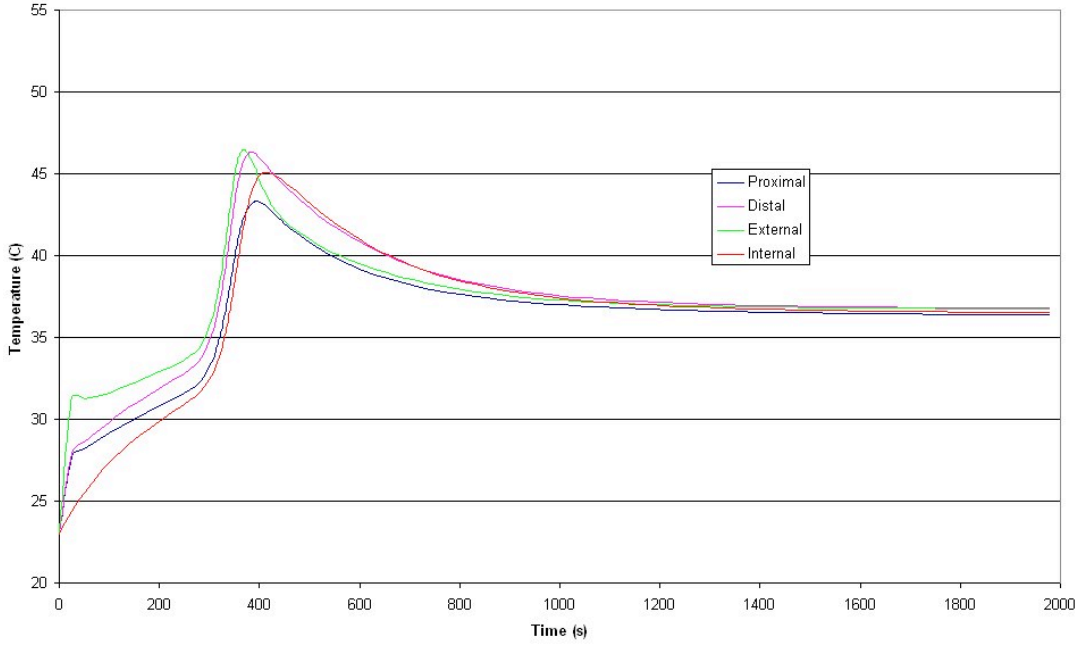

Figure 4-19 – Results with one element through cement thickness.

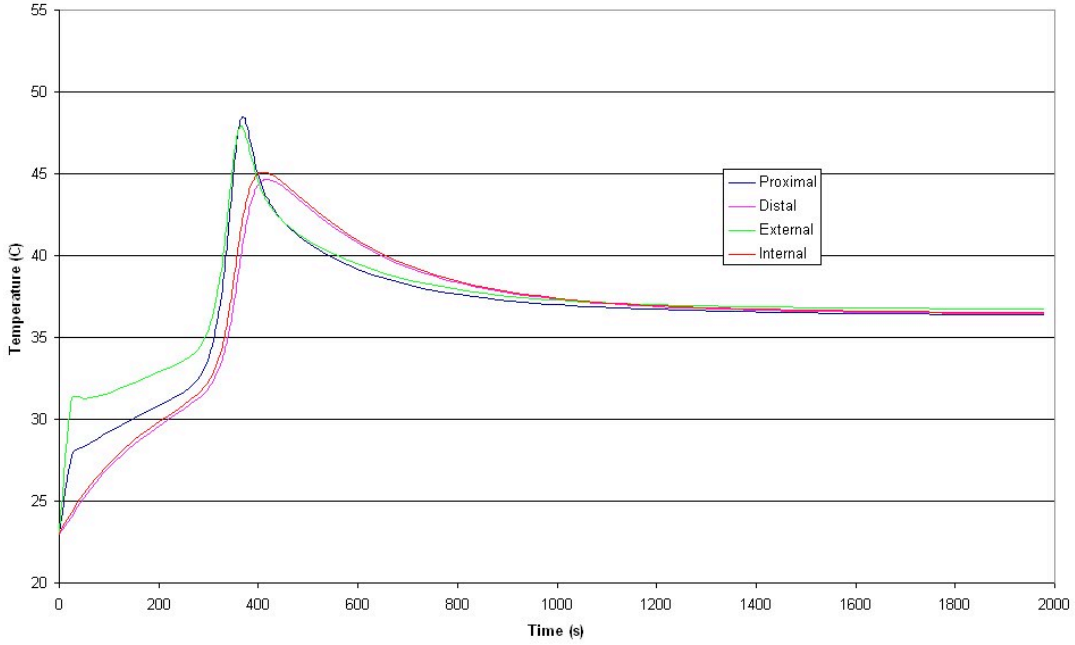

Figure 4-20 - Results with two elements through cement thickness.

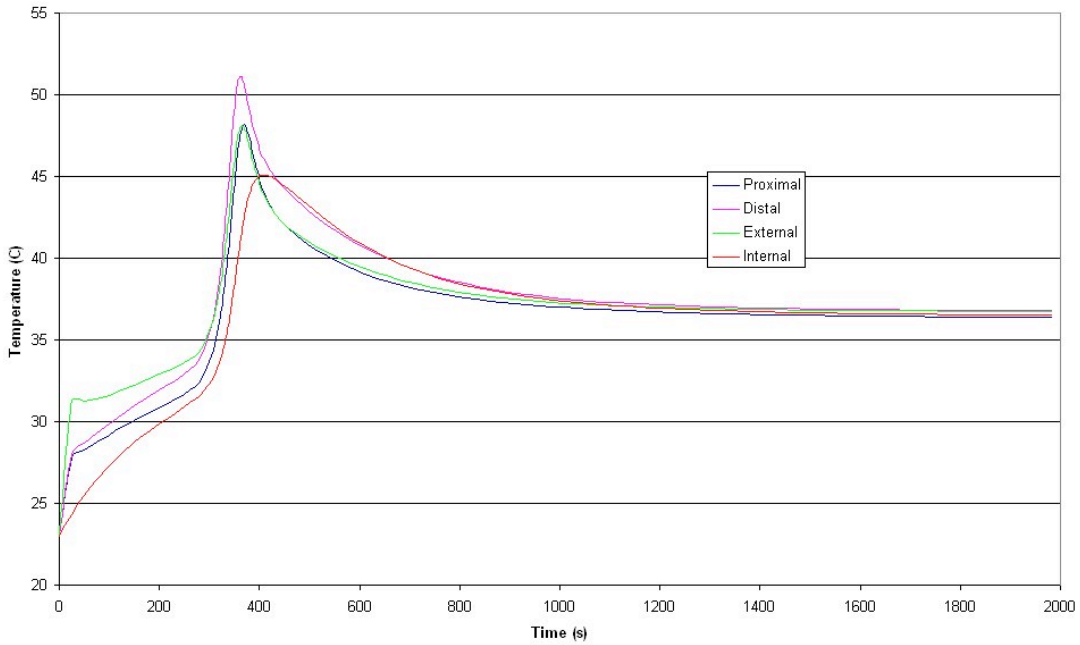

Figure 4-21 - Results with three elements through cement thickness.

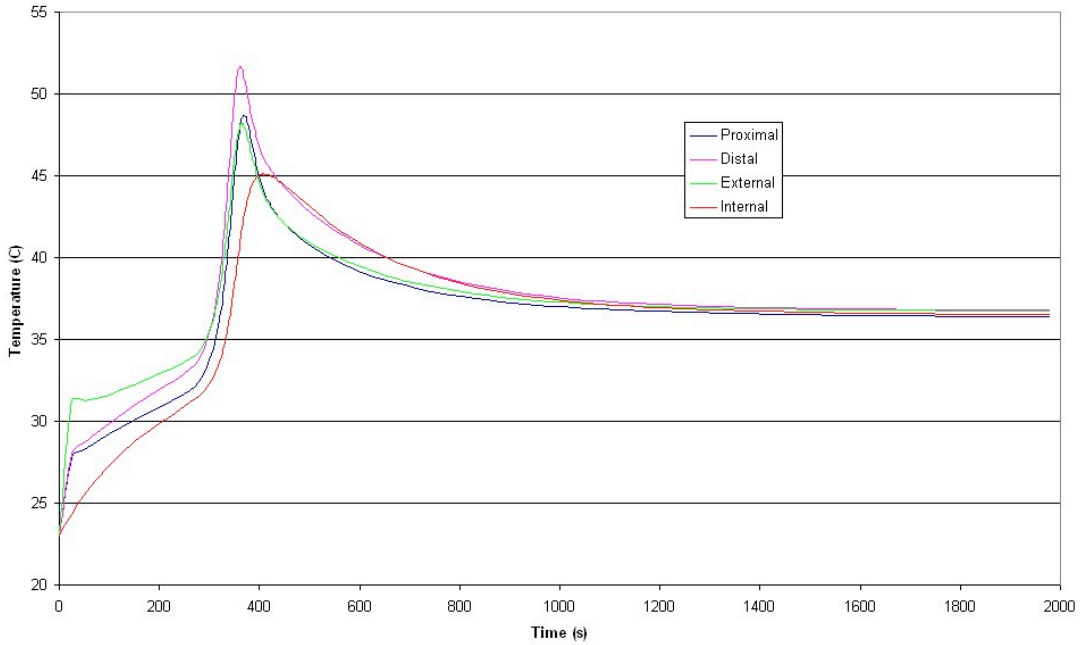

Figure 4-22 - Results with five elements through cement thickness.

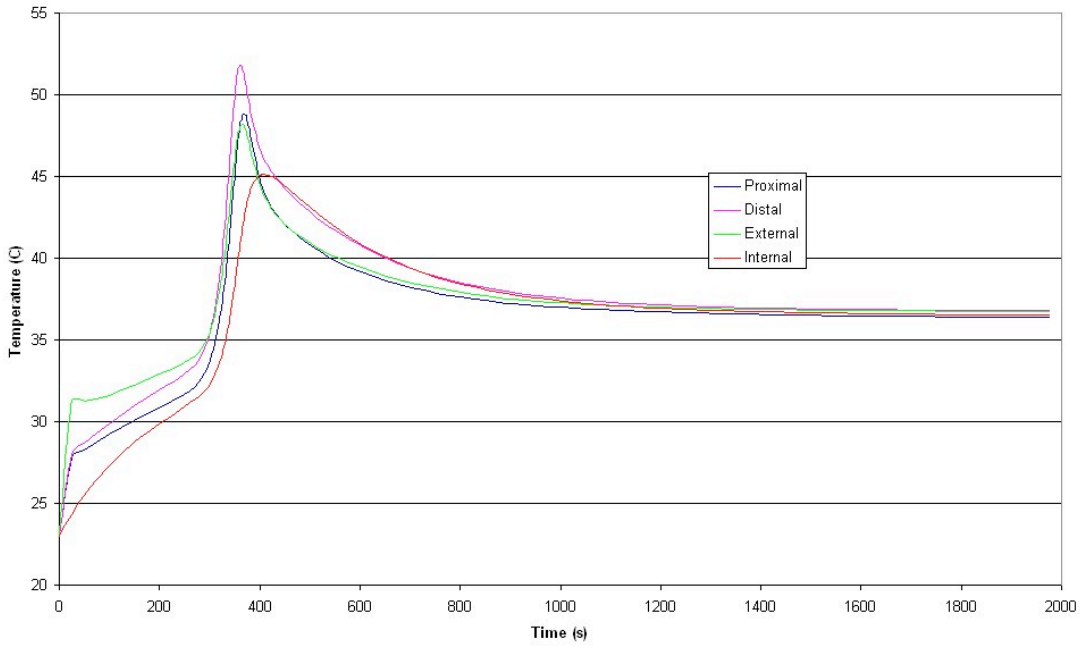

Figure 4-23 - Results with seven elements through cement thickness.

Temperature at the distal point was most sensitive to mesh density, and relatively greater mesh density was required at this point before convergence was achieved. Temperature at the distal point for the various mesh densities is shown in Figure 4-24.

From Figure 4-24 it can be seen that three elements across the cement mantle thickness are sufficient to eliminate uncertainty in cement temperatures due to mesh density. Increasing mesh density further does not produce a significantly greater accuracy. With two elements across the cement mantle, temperatures differed from those produced using higher mesh densities by more than they did in the case of a single element. This may be because there were no nodes exactly on the centre line in any other model, where results for the centre line were determined by averaging between adjacent nodes. For an even number of elements the results were taken directly from the centre line node.

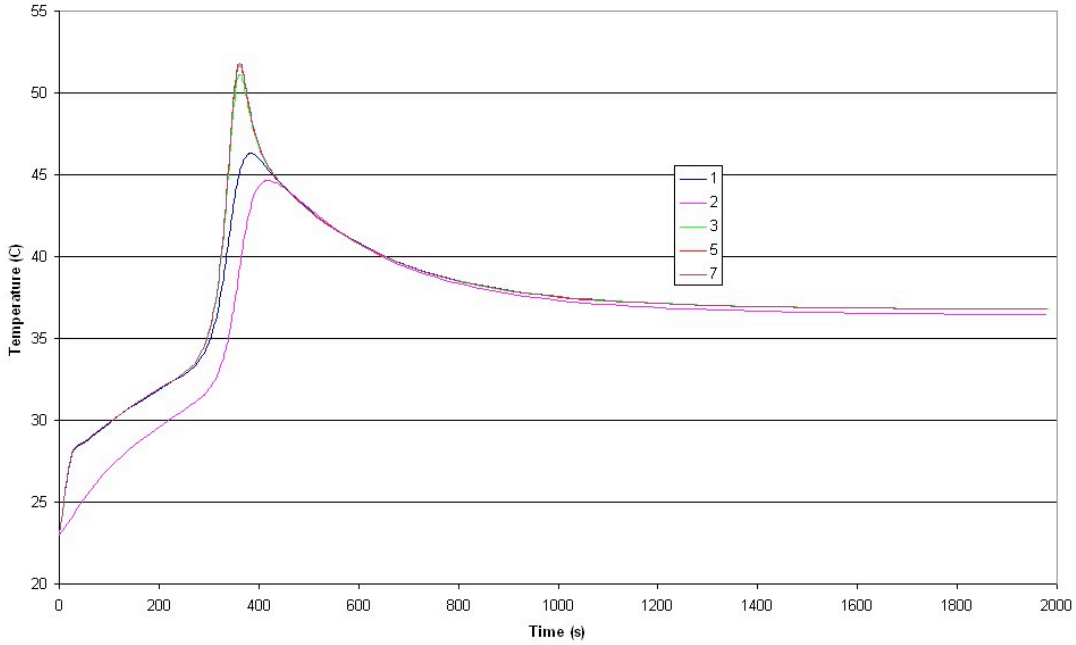

Figure 4-24 - Distal node temperature with different density of elements through thickness, summarising Figure 4-19 - Figure 4-23 for just the distal node enabling quick mesh convergence review.

Chemical Parameter Sensitivity Analysis

A sensitivity analysis was performed to determine the importance of measurement accuracy in each cure model variable. The model was run 20 times with 1 variable altered independently in each model. High and low values for each variable were calculated as 10% from the nominal value found in the literature and extreme high and low values were taken as 25% from the nominal (Table 4-3).

Parameter	Very Low	Low	Nominal	High	Very High
E_a	23464	28157	31285	34414	39106
K_0	7113	8535	9484	10432	11855
m	0.735	0.882	0.98	1.078	1.225
n	0.798	0.9576	1.064	1.1704	1.33
Q_{tot}	1.1625×10^8	1.395×10^8	1.55×10^8	1.705×10^8	1.9375×10^8

Table 4-3 - Sensitivity analysis parameter variation

The results for each model were calculated at the same six nodes (picked in pairs of nodes at 1/4, 1/2, and 3/4 in the longitudinal direction with each pair having one node at 1/3 and another at 2/3 of the thickness in the radial direction) and averaged to allow for any local effects.

Effect of Activation Energy

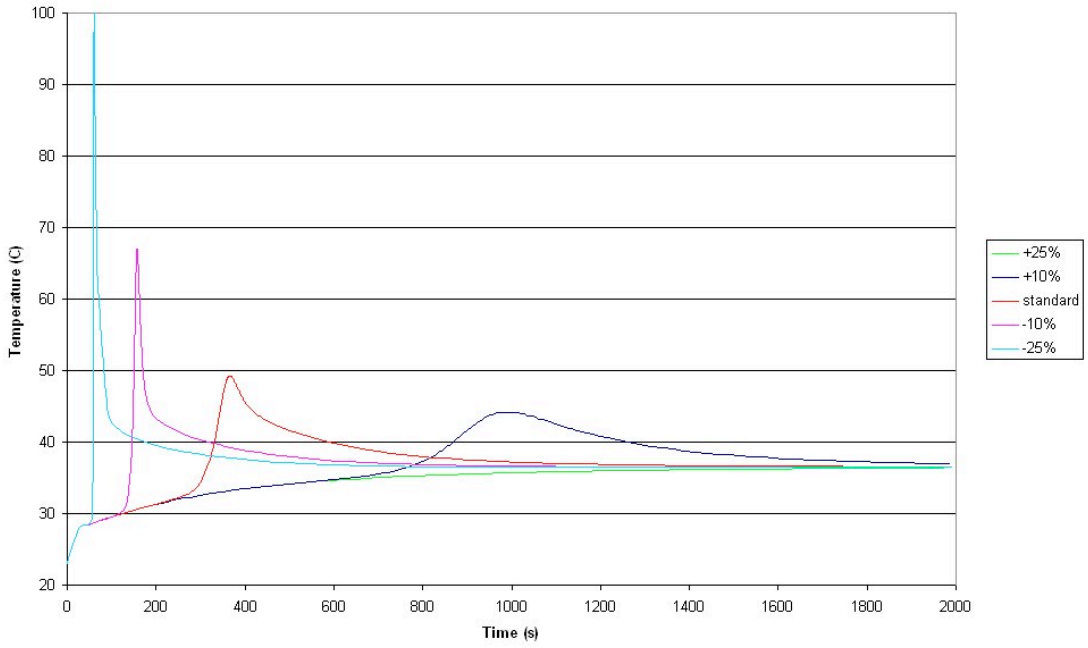

Figure 4-25 - Change in temperature profiles during cure as a result of variation in activation energy.

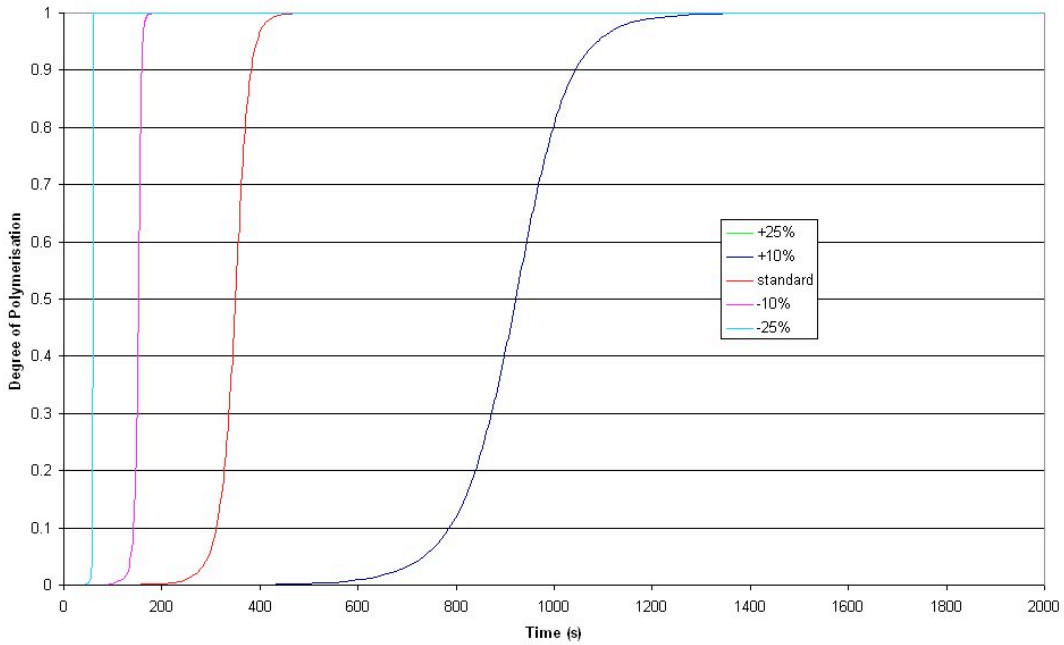

Figure 4-26 - Change in degree of polymerisation during cure as a result of variation in activation energy.

Activation energy had a strong effect on both the degree of polymerisation curve and on the peak temperature (Figure 4-25 and Figure 4-26). By reducing the activation energy, the point of maximum rate of polymerisation occurred earlier and also the rate of polymerisation was increased. This had the effect of increasing the peak temperature significantly. Reducing the activation energy by 25% increased peak temperature by approximately 51°. Increasing the activation energy by 25% meant the reaction was so slow that no polymerisation noticeable on this scale had occurred after 2000s - after 2000s. The maximum degree of polymerisation throughout the cement mantle was approximately 0.002. This also meant that there was no increase in the temperature other than baseline warming from room to body temperature. For a 10% increase in the activation energy, a 6º reduction in peak temperature occurred. The time at which maximum polymerisation rate occurred increased from 340s to 910s.

Effect of Rate Constant

By reducing the constant K_0 by 25% the point at which the polymerisation rate was at its maximum was delayed from 320s to 420s (Figure 4-28). This effect is small compared to that caused by altering the activation energy. The peak temperature produced by a 25% reduction in K_0 was just 2° lower than in the standard model (Figure 4-27). A 10% reduction produced a 1° reduction in peak temperature. This shows that the effect of reducing K_0 on the peak temperature is non-linear. Increasing K_0 by 25% increased the peak temperature by 2° and caused the point at which the polymerisation rate was at its maximum to occur approximately 50s earlier than in the standard model.

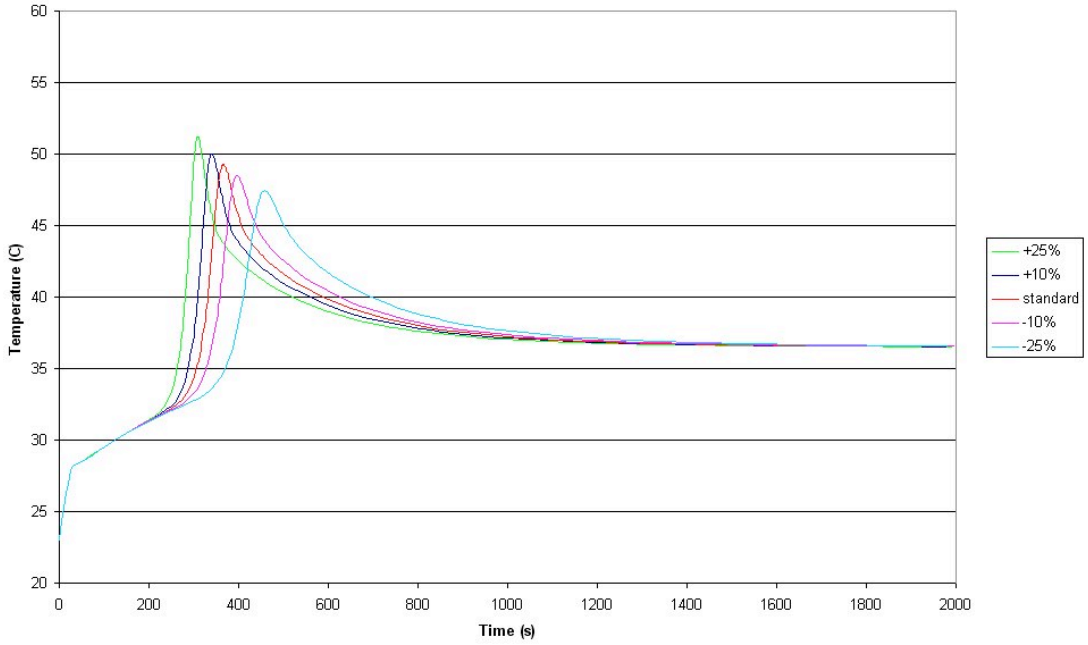

Figure 4-27 - Change in temperature profiles during cure as a result of varying K_0.

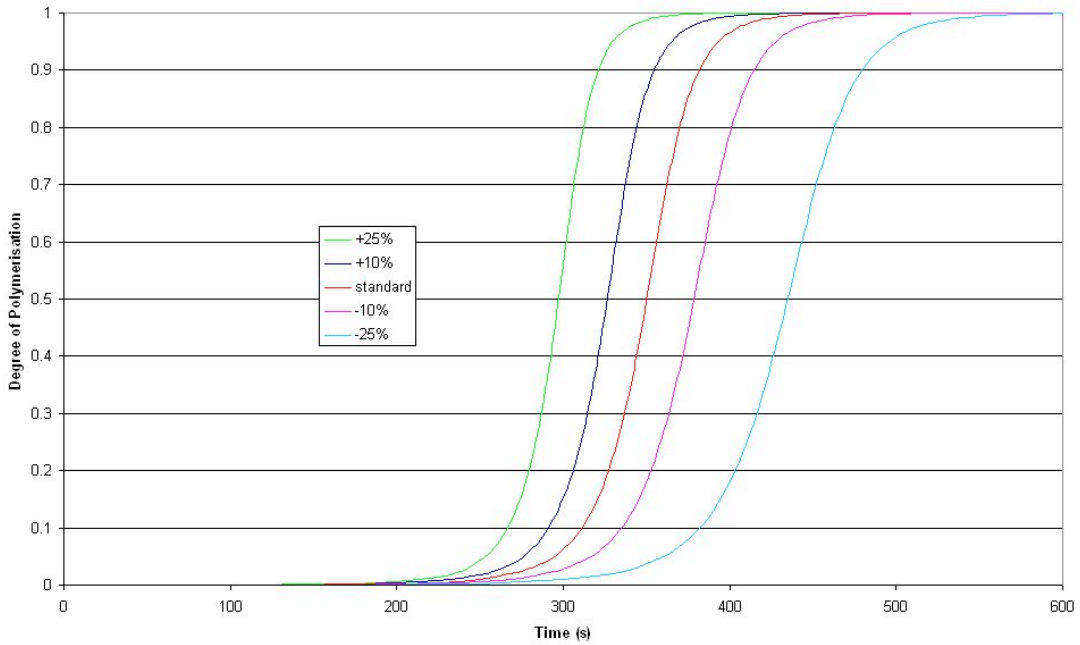

Figure 4-28 - Change in degree of polymerisation during cure as a result of varying K_0.

A 50% increase or decrease in K_0 produced a 4° increase or decrease respectively in the peak temperature. This is again small compared to the changes observed as a result of changing the activation energy.

Effect of Rate Parameters

A reduction in the rate parameter *m* caused polymerisation to occur earlier, and an increase caused polymerisation to occur later (Figure 4-30). The magnitude of the polymerisation rate decreased as *m* increased. The point of maximum polymerisation rate occurred at 130s when *m* was reduced by 25%. A change in *m* of 50% caused the point at which the polymerisation rate is a maximum to shift by 1300s. The peak temperature changed very little throughout the 50% range of *m* tested (Figure 4-29).

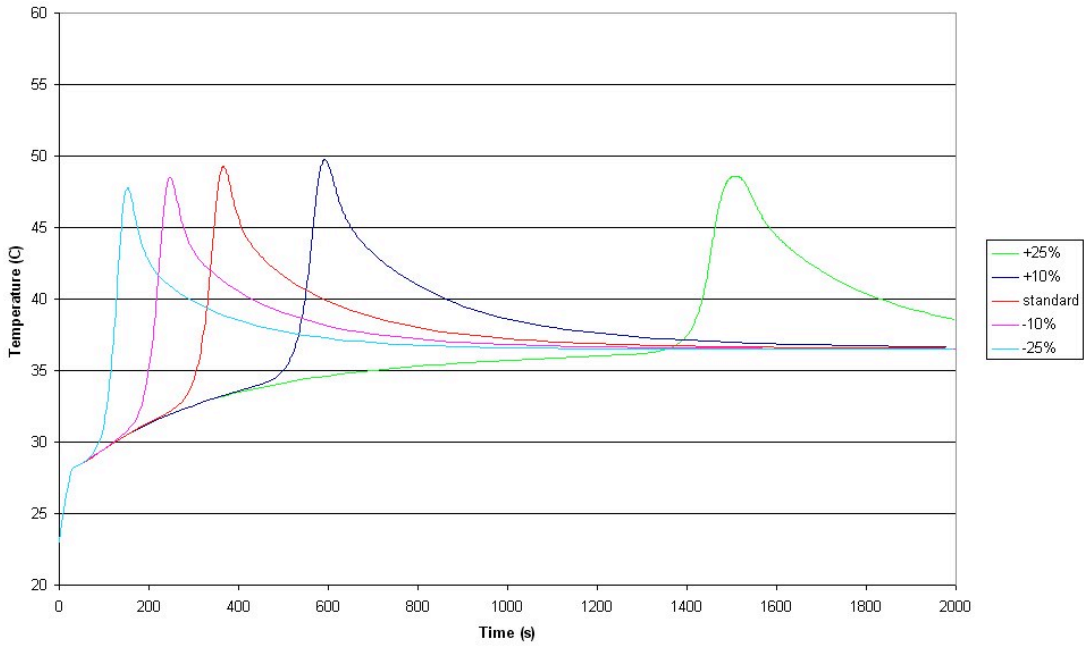

Figure 4-29 - Change in temperature profiles during cure as a result of different m input.

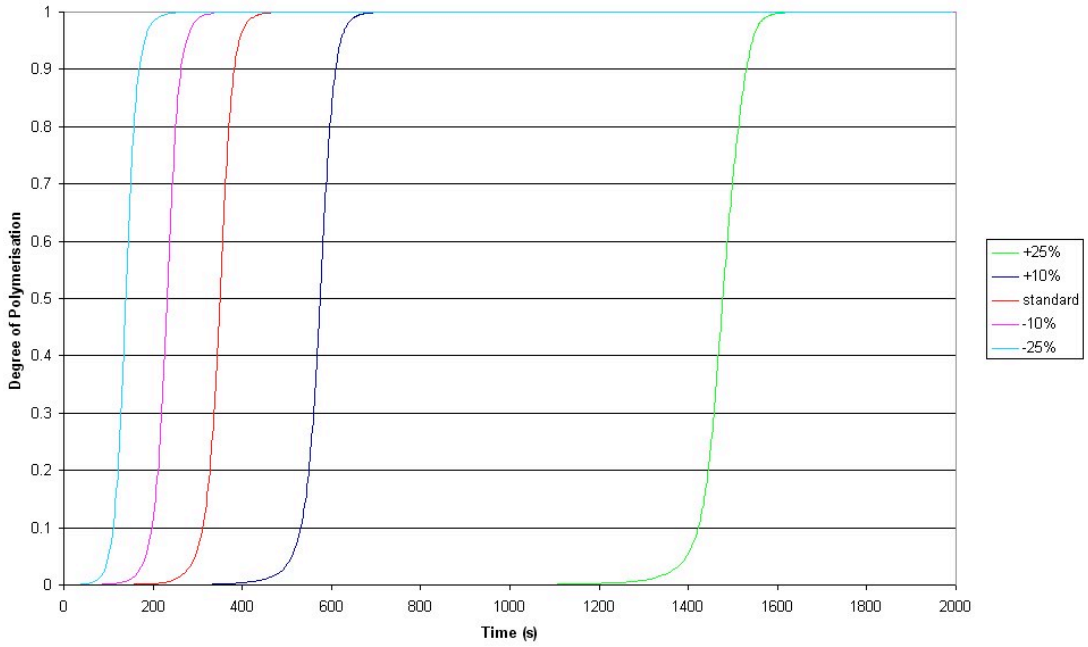

Figure 4-30 - Change in degree of polymerisation during cure as a result of different m input.

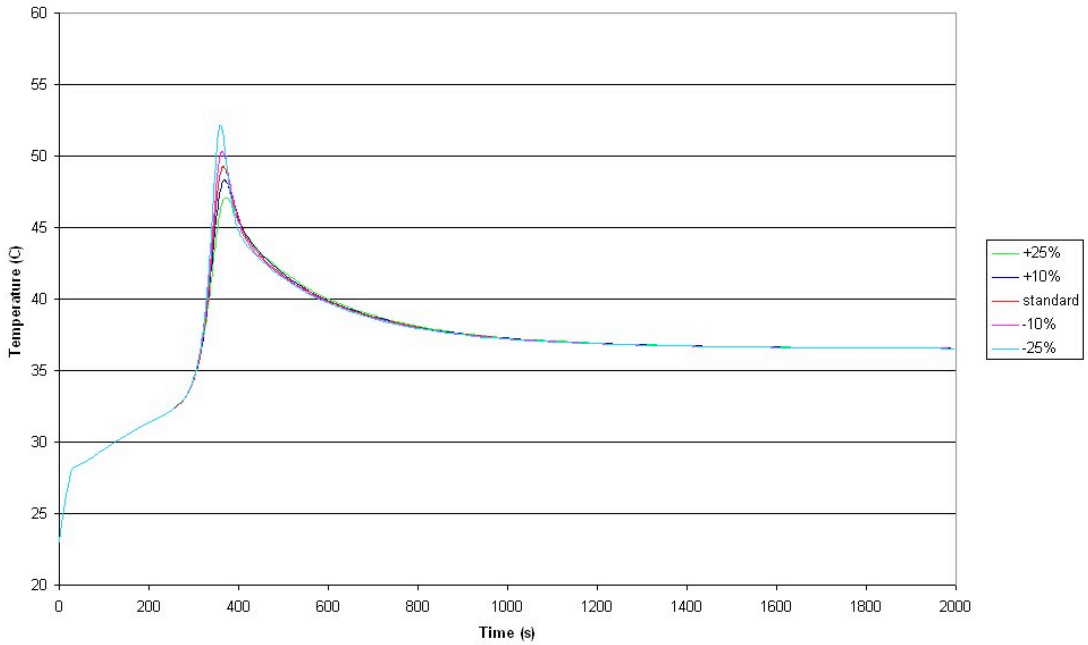

Figure 4-31 - Change in temperature profiles during cure as a result of different n input.

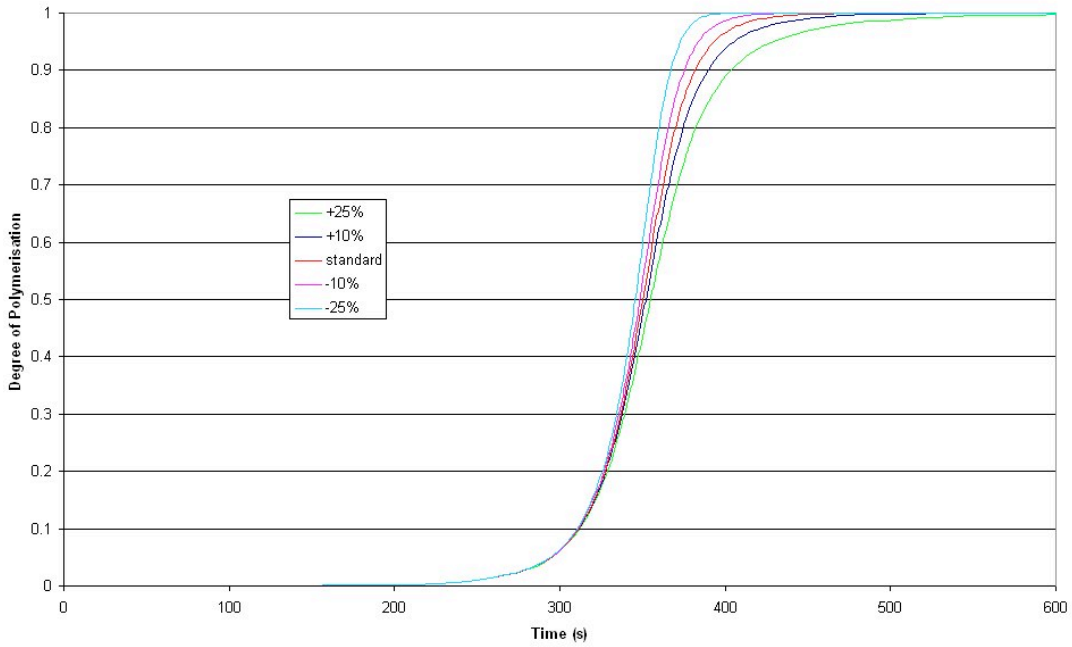

Figure 4-32 - Change in degree of polymerisation during cure as a result of different n input.

The value of *n* had a small effect on the polymerisation rate. While the gradient of the polymerisation curve changed slightly, the time at which the rate of polymerisation was at a maximum was almost independent of *n* (Figure 4-32).

The effect of *n* upon the peak temperature was minimal (Figure 4-31). There was a small reduction in peak temperature with a large value of *n* as the polymerisation rate was reduced.

Effect of Total Heat of Reaction

Q_{tot} denotes the total amount of heat that is liberated throughout the polymerisation process. An increase in Q_{tot} produced an increase in the peak temperature (Figure 4-33). A 25% increase in Q_{tot} produced a 6° increase in peak temperature. For a 25% decrease in Q_{tot} there was a 5° reduction in the peak temperature. The relationship between peak temperature and Q_{tot} was approximately linear. Although there was no effect on the timing of the polymerisation period due to changes in Q_{tot} (Figure 4-34), a higher cure rate resulted from an increase in Q_{tot}.

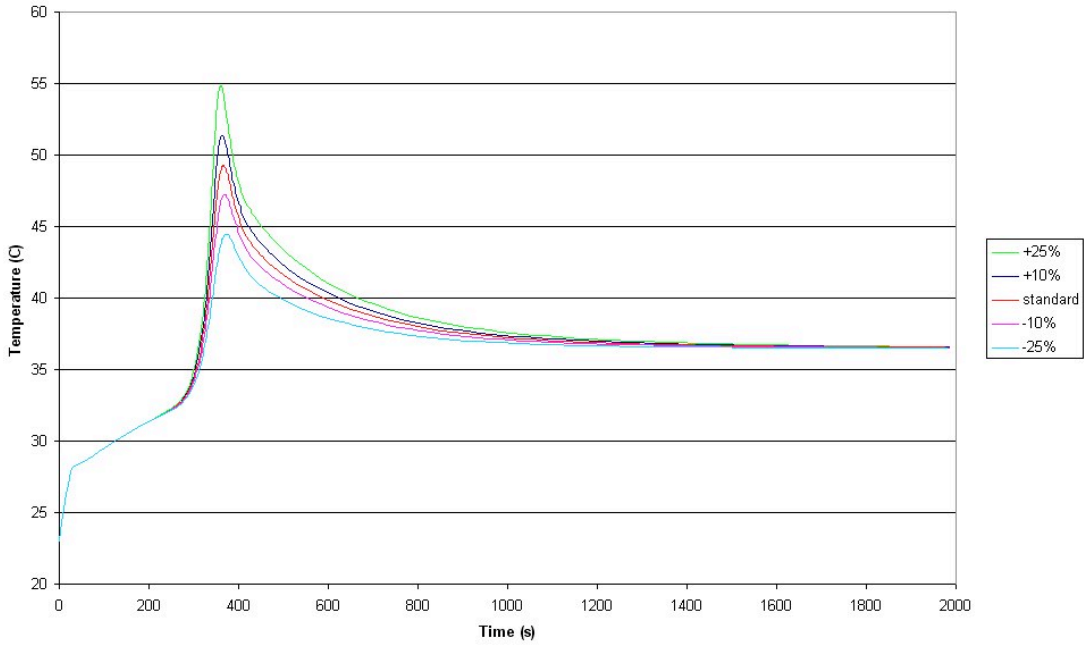

Figure 4-33 - Change in temperature profiles during cure as a result of different Q_{tot} input.

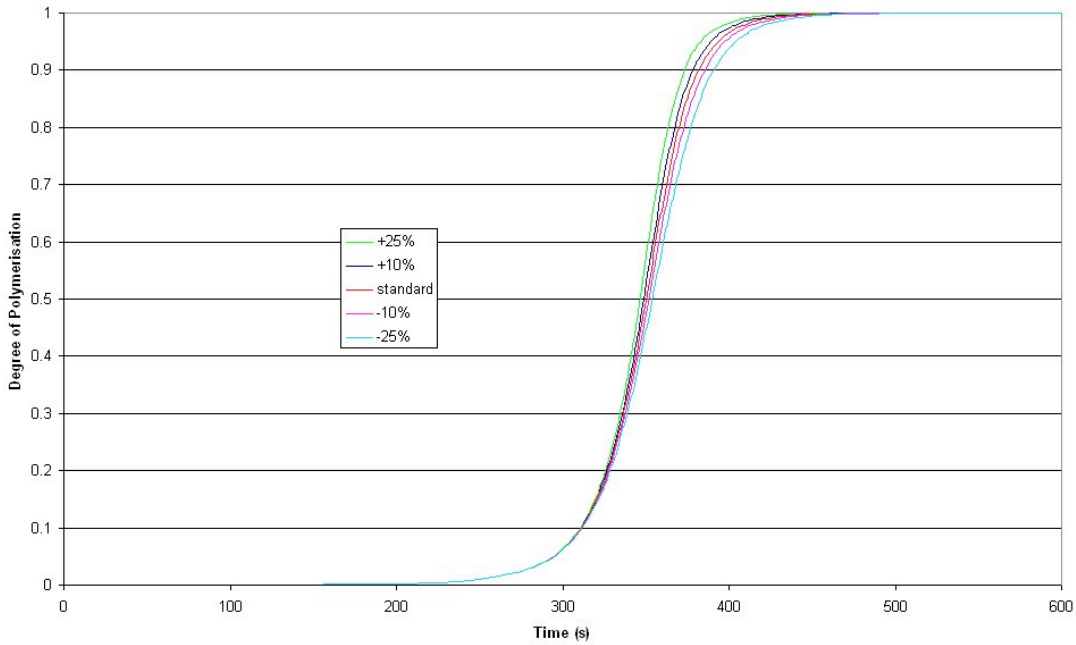

Figure 4-34 - Change in degree of polymerisation during cure as a result of different Q_{tot} input.

Summary of Sensitivity Analysis

- Activation energy has a large effect on both polymerisation rate and peak temperature.
- Activation energy has an inverse relationship with the peak temperature and the rate of polymerisation.
- A reduction in K_0 produced a small reduction in the peak temperature and polymerisation rate.
- Reaction rate parameter *m* had a large effect on the polymerisation timing but little effect on the temperature.
- The polymerisation rate decreased a large amount with a decrease in *m* but did not increase an equal amount with an increase in *m*.
- The reaction rate parameter *n* had little effect on the peak temperature or the polymerisation rate.
- Variation in Q_{tot} yielded changes in peak temperature without much change in polymerisation rate.

- The model was most sensitive to the activation energy and so this parameter must be accurately determined experimentally.
- No parameter altered the cure gradient from distal to proximal.
- Activation energy (E_a) is the most critical parameter.

Effect of Initial Stem Temperature

As one of the only variables that the surgeon may have any control over in an operating theatre, the initial temperature of the stem was varied between realistic limits in this series of analyses. An upper bound of 50˚C was set, as the surgeon would find it difficult to handle a stem hotter than this temperature. A lower bound of 5˚C was set, as below this temperature the stem would tend to collect condensation from the atmosphere prior to insertion. These were compared to the room temperature model.

Temperature plots during polymerisation for the three initial stem temperatures are shown in Figure 4-35. The temperature curves shown are averaged over 6 nodes in the cement mantle, located in three pairs (one proximal, one middle and one distal) with one node at 1/3 and the other at 2/3 through the thickness for each pair. Contour plots of the degree of polymerisation when a node located at the centre of the cement mantle in the radial and longitudinal directions reached 0.5 are shown in Figure 4-36.

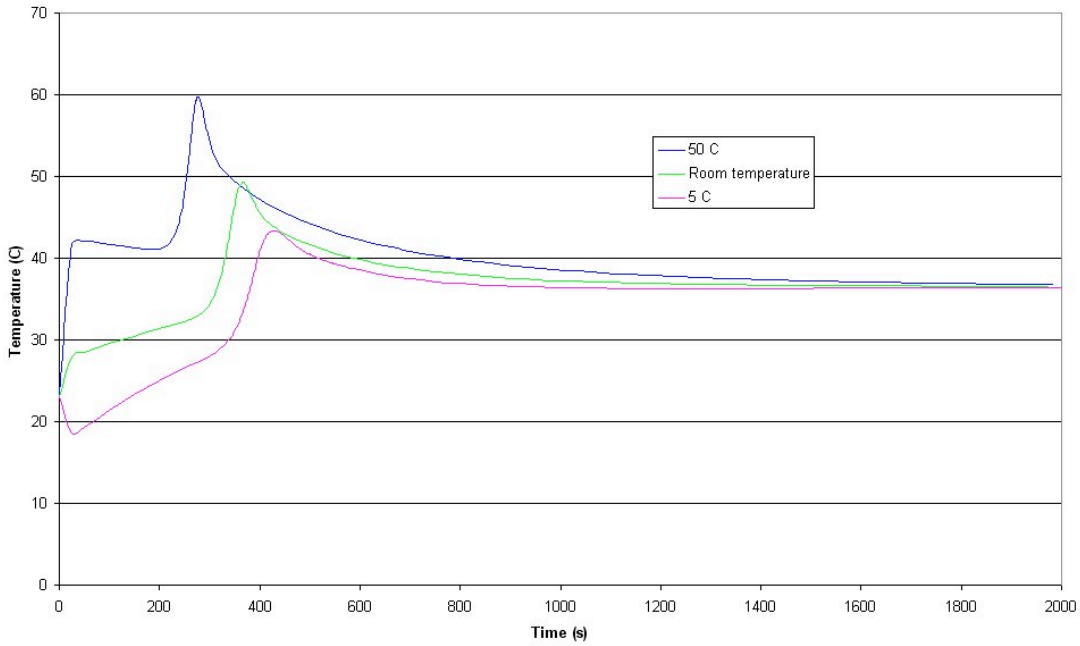

Figure 4-35 - Temperatures during cure using different initial stem temperatures.

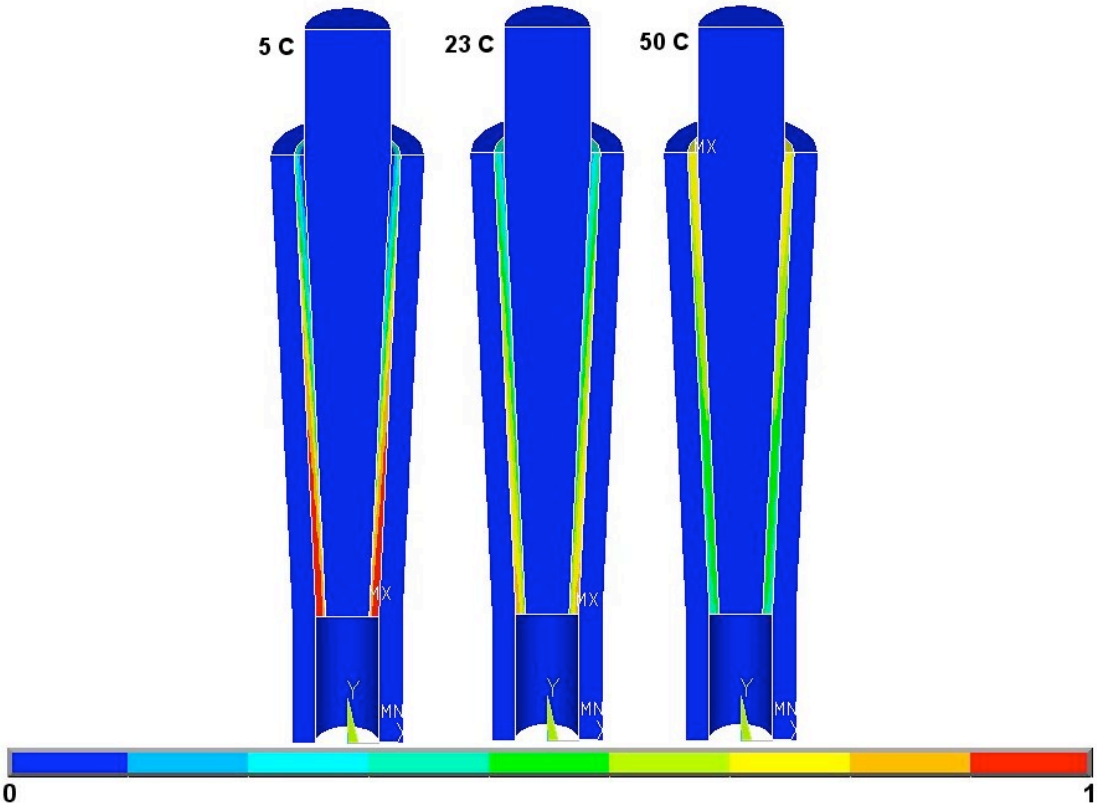

Figure 4-36 – Degree of polymerisation profiles for low, room and high temperature stem models taken at time when a node in the centre of the cement mantle is at 0.5 degree of polymerisation.

As would be expected the polymerisation rate increased with an increase in initial stem temperature and so too the peak temperature. However, the cure direction from distal to proximal observed in previous analyses had almost completely reversed. In all other models the distal section was first and the proximal last to polymerise (this effect being most exaggerated at low stem temperatures). This may be because the stem is acting as a heat sink and because of the taper there is more material for heat dissipation into the stem in the proximal region, which in turn slows the reaction there. When the stem is heated the opposite effect becomes apparent with the proximal region of the stem transferring more heat to the surrounding cement and so with a hot stem the proximal cement mantle polymerises first (Figure 4-36).

The model was used to optimise polymerisation in terms of the initial stem temperature in order to minimise the cure gradient. For a body temperature stem, very little cure gradient was observed in the distal-proximal direction (Figure 4-37).

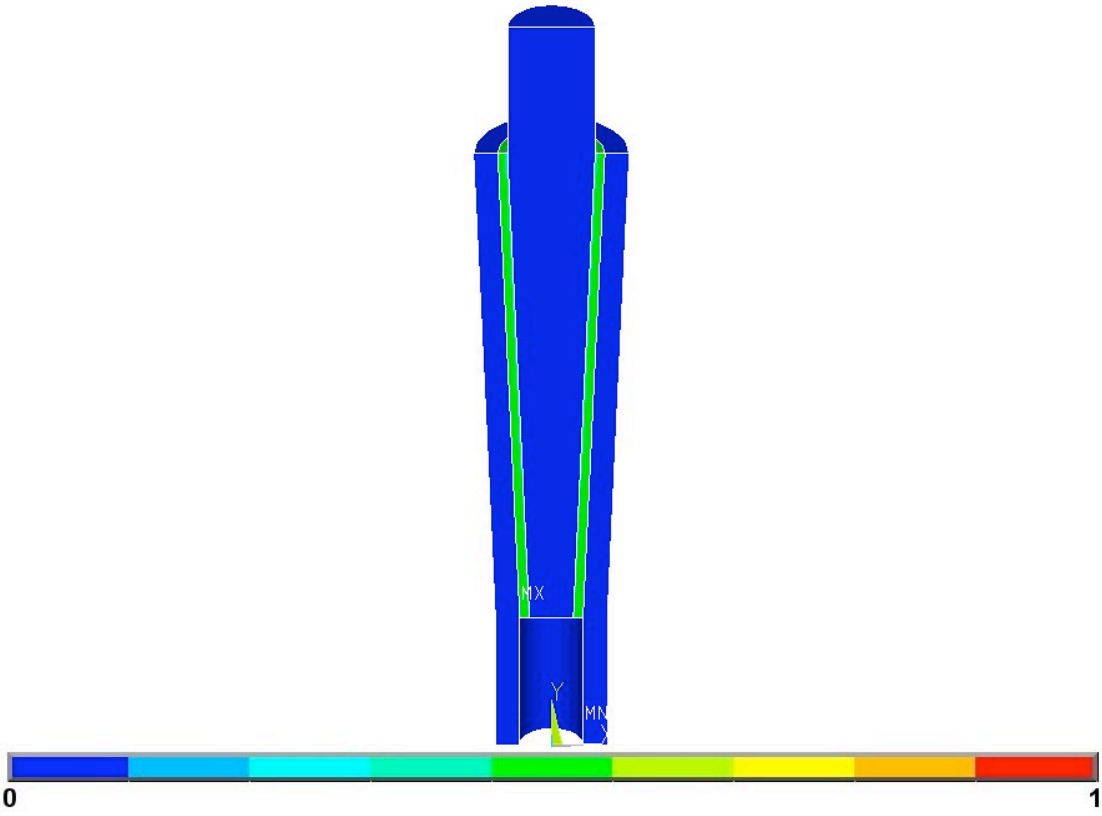

Figure 4-37 - Polymerisation profile for body temperature (37ºC) stem taken at a time when a node in the centre of the cement in the longitudinal and radial direction has reached a degree of polymerisation of 0.5.

Effect of Cement Thickness

In the previous analyses, cement mantle thickness has been assumed to be 2mm. Thinner cement mantles have been reported to perform poorly *in vivo* [8]. Thicker cement mantles have been reported to evolve large amounts of heat which may cause bone necrosis [12]. In this section, the results of an investigation of the effect of cement mantle thickness on temperatures and polymerisation kinetics are presented.

The standard idealised stem model was modified to incorporate a 5mm cement mantle to represent the thickest cement mantle likely to be generated in primary hip surgery (Figure 4-38). This increase in the cement mantle thickness is accommodated by increasing the bone dimensions such that 5mm of bone still surrounds the cement.

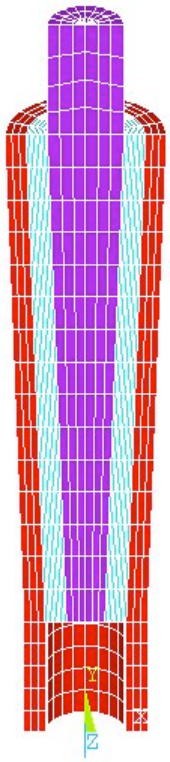

Figure 4-38 - Geometry for model with 5mm cement mantle.

Materials properties, boundary and initial conditions were set as described in Chapter 4.2.

Figure 4-39 shows a comparison of the polymerisation curves in a model with a 5mm cement mantle with those produced by a 2mm cement mantle model. The cure gradients and rates of polymerisation are similar to those seen in the 2mm cement mantle model.

For all models, cure began at the distal tip and progressed proximally (Figure 4-40). The 5mm cement mantle caused a cure gradient in the radial direction more severe than that in the proximal-distal direction. The radial cure gradient was such that the cement at the cement-bone interface completely cured before the cement at the stem interface had begun to polymerise. This gradient was caused by the difference in the initial temperatures of the bone and stem. The additional heat at the warm cement-bone interface provides sufficient energy for the polymerisation process to take place rapidly. This effect is not seen in the 2mm model as heat can travel through the cement to the stem more easily.

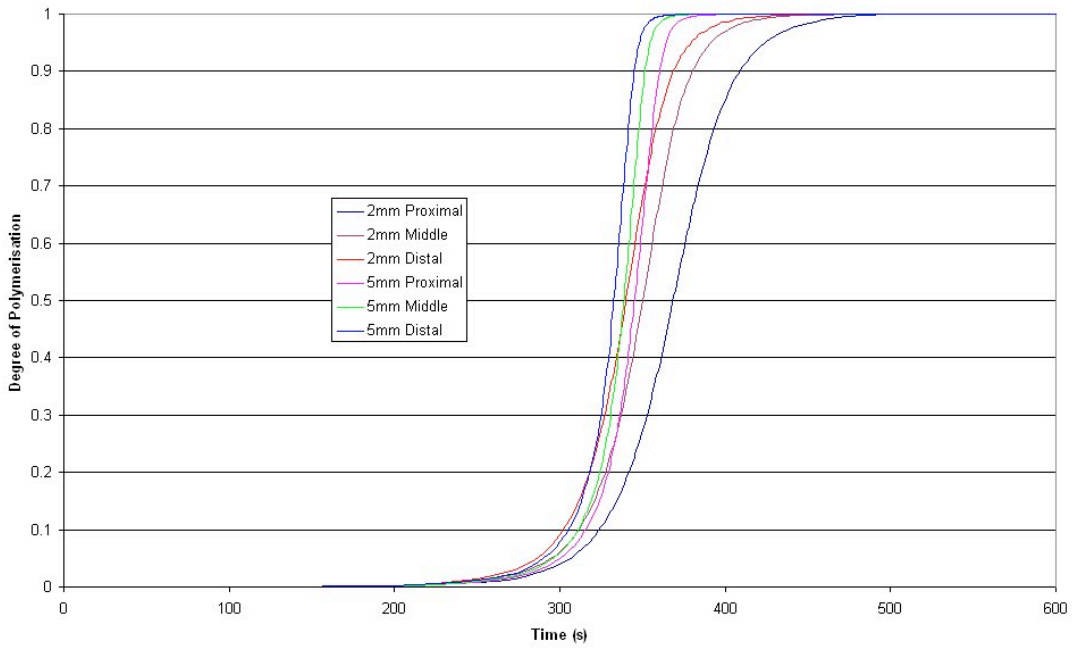

Figure 4-39 - Polymerisation curves for model with 5mm cement mantle and 2mm cement mantle.

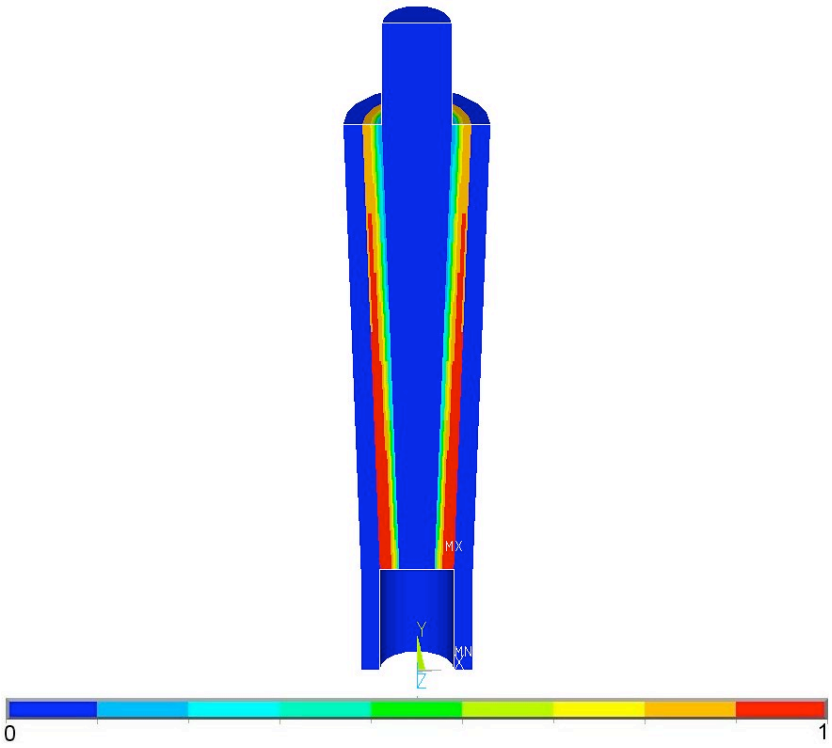

Figure 4-40 - Degree of polymerisation for model with 5mm cement mantle taken at the time when a node in the centre of the cement in the longitudinal and radial direction has reached a degree of polymerisation of 0.5.

The rapid cure at the bone-cement interface caused a higher peak temperature to be seen on this side of the cement mantle than at the stem interface (Figure 4-41). Also the greater bulk of cement increased the amount of heat liberated during the polymerisation process for the entire mantle. This additional heat caused an increase in peak temperature of approximately 9° when compared to a 2mm cement mantle.

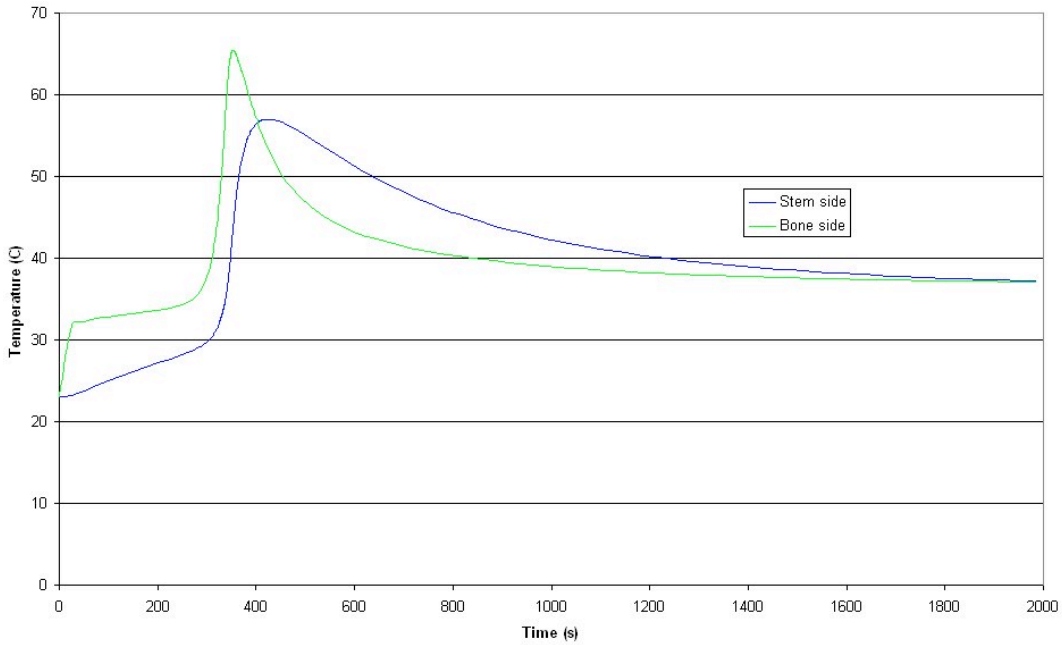

Figure 4-41 - Differences in temperatures at the interfaces during cure of a 5mm cement mantle.

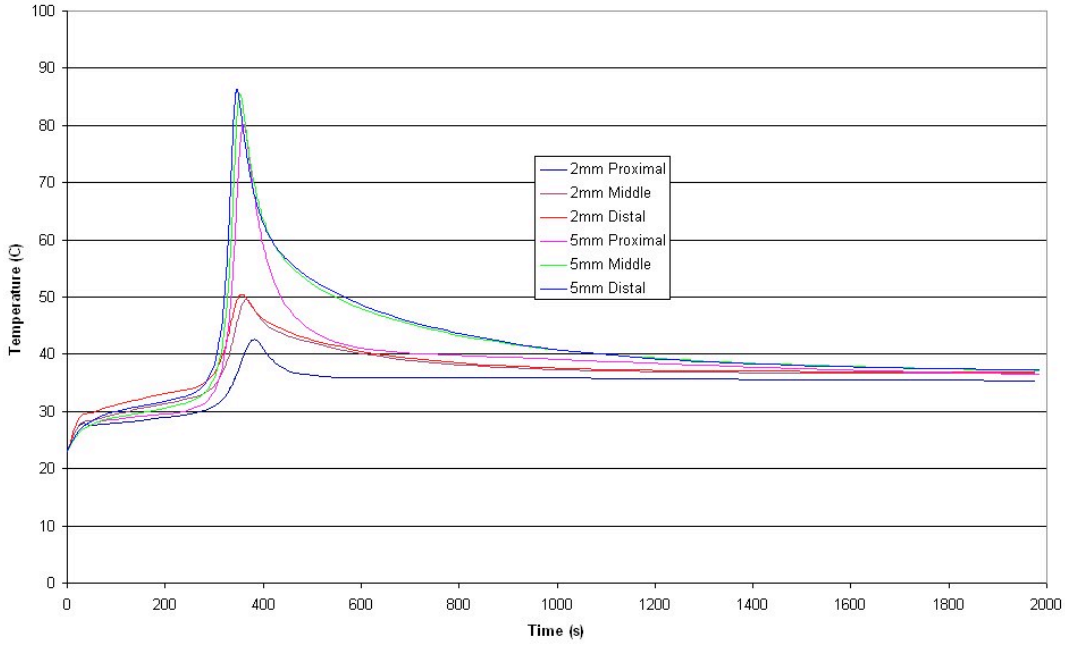

Figure 4-42 - Temperature profiles for model with 5mm cement mantle and 2mm cement mantle.

Effect of Stem Misalignment

Many clinical cases of stem misalignment (either in varus or valgus) have been reported [86]. A model was generated to investigate the effect that this may have on the cure gradient and the temperatures produced during cure.

The model described in Chapter 4.4- Idealised Stem Model was used with the stem rotated 1° anti-clockwise (Figure 4-43). Although this is smaller than some extreme misalignments that have been reported clinically, it was the largest possible in the present model if a 2 mm cement mantle and acceptable mesh quality were to be maintained. The stem was rotated about the mid-point along the length of the tapered section.

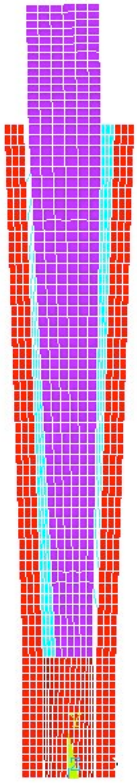

Figure 4-43 - Idealised stem model with 1 degree of misalignment.

Material properties, boundary and initial conditions were set as described in Chapter 4.4 - Idealised Stem Model, the initial stem temperature was set at 23°C.

Figure 4-44 shows a contour plot of the degree of polymerisation at a point when a node situated centrally in both the longitudinal and radial direction within the cement is at 0.5 degree of polymerisation and Figure 4-45 and Figure 4-46 temperatures along the left and right hand cement-bone interfaces respectively for an idealised stem with 1 degree of misalignment.

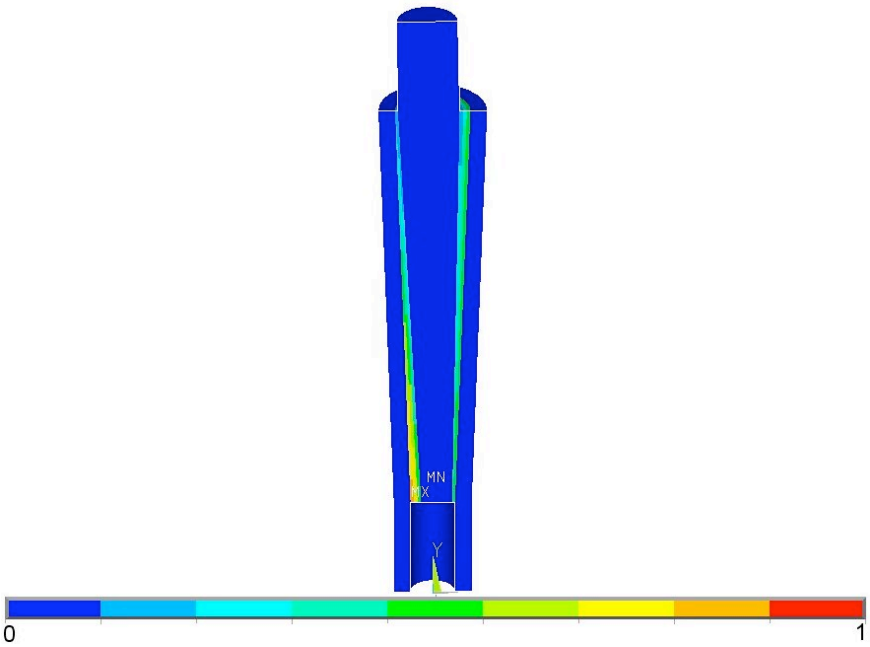

Figure 4-44 - Contour plot of the degree of polymerisation during cure of an idealised stem with 1 degree of misalignment taken at the time when a node in the centre of the cement in the longitudinal and radial direction has reached a degree of polymerisation of 0.5.

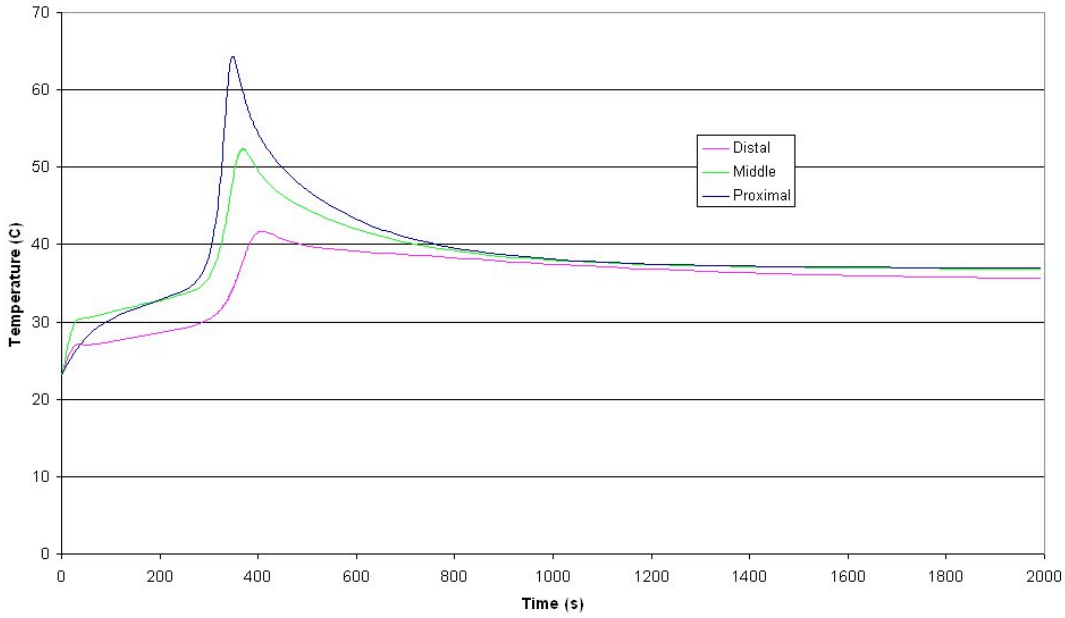

Figure 4-45 - Temperature along bone-cement interface on left side of misalignment model.

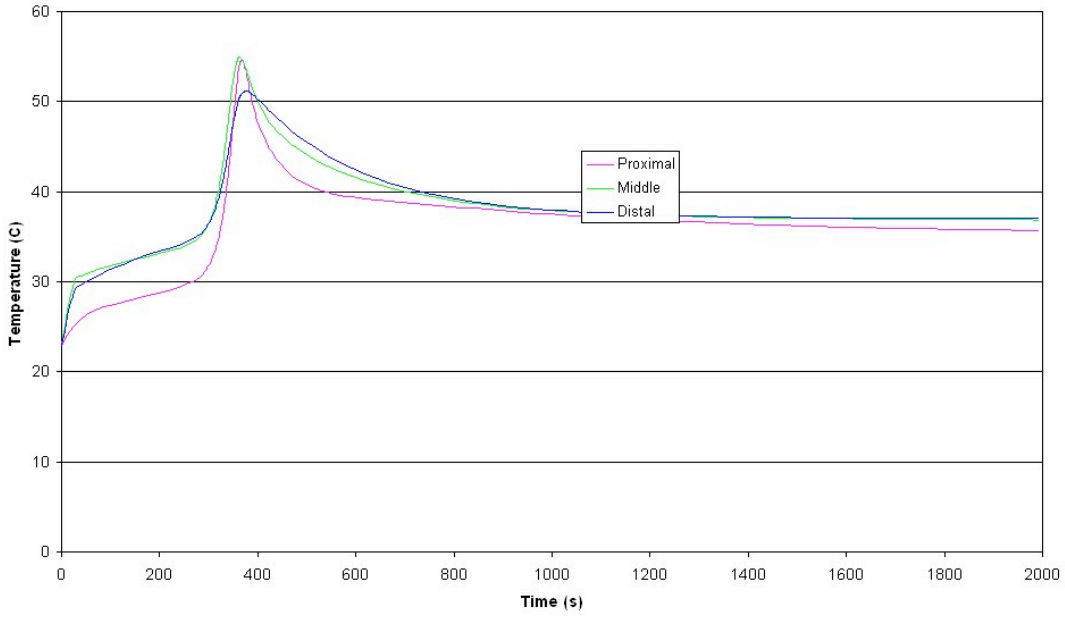

Figure 4-46 - Temperature along bone-cement interface on right side of misalignment model.

On the left side of the model cure was most rapid in the distal section where cement was thickest. Polymerisation was complete at this location approximately 20s before the proximal section. The cure gradient, seen on the left side of the model shown in

Figure 4-44, was in the same direction as the standard model. The difference in timing of distal and proximal section polymerisation was increased with a thicker cement mantle distally.

On the right hand side of the model the cement mantle became thin at the distal tip and thicker proximally. This change in geometry caused a complete reversal in the cure gradient. Where the cement was thicker a greater amount of heat evolved and so the polymerisation rate increased. The increase in proximal polymerisation rate was sufficient to overcome all effects of the taper geometry seen in the standard model.

A plot of the temperature at different locations in the longitudinal direction shows that the distal section became hotter than the thinner, proximal section on the left side (Figure 4-45). This is to be expected, as heat evolved is a linear function of the volume.

4.5 Comparison of Idealised Stem Model with Experimental Results

4.5.1 Introduction

All finite element models require validation before results can be relied upon. To ensure all parameters fit *in-vivo* conditions validation of the temperature predictions of the idealised stem model was undertaken using an experimental rig. *In vitro* boundary conditions replicated the computational model.

4.5.2 Methods

The experimental model geometry was altered slightly from the original finite element model geometry (Chapter 4.4) in order to reduce manufacturing difficulties associated with the long tapered section. The new geometry is shown in Appendix I – Model Drawings and Dimensions. In order to prevent any cement distal to the stem, a plug was inserted at the distal end of the model.

A new finite element model was generated to replicate this change in geometry. To replicate the boundary conditions applied to the finite element model, the femur was mounted in an environment chamber and sealed into a hole through the bottom using silicone sealant. During testing the environment chamber (Figure 4-47) was filled with water circulated from a constant temperature water bath held at 37°C. This water was pumped in through a pipe connected to the bottom of the tank and drained through an overflow, level with the top of the femur. The bath contained more than 50 litres of water, ensuring that there was sufficient volume of water at the correct temperature to keep a constant temperature condition at the external surface of the femur.

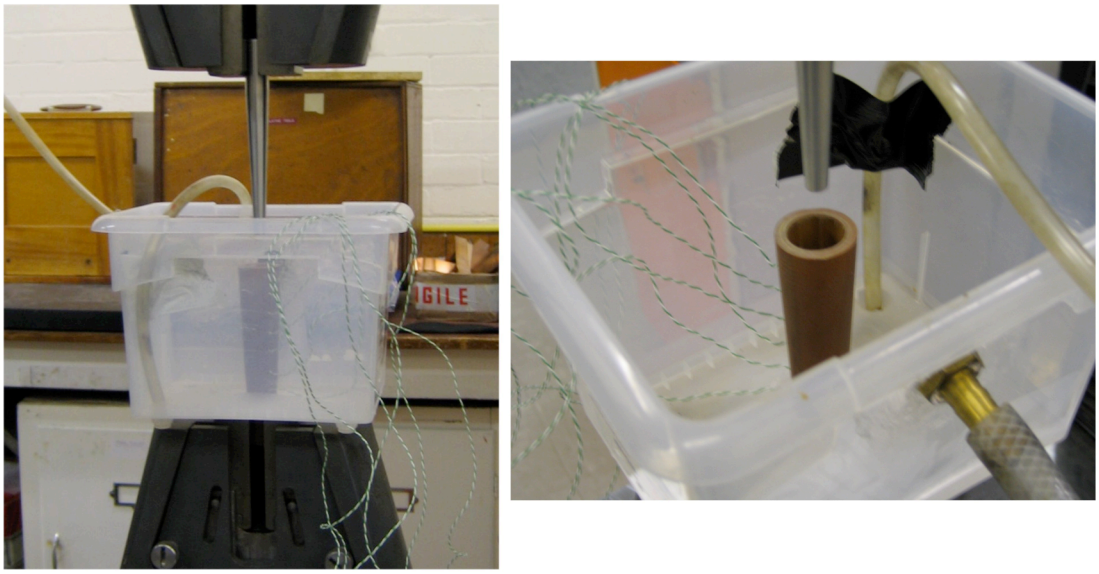

Figure 4-47 - Experimental apparatus used for validation experimentation.

The materials used in the manufacture of the experimental model were chosen such that their materials properties were consistent with the properties used in the finite element model. The stem was manufactured from stainless steel; the femur model was manufactured from Tufnol™ and the cement used was CMW1™. Tufnol™ has very similar thermal properties to cortical bone (Table 4-4).

	Material	
Property	Cortical Bone	Tufnol™
Thermal Conductivity	0.38 W/mK	0.37 W/mK
Specific Heat Capacity	1.26 kJ/kgK	1.5kJ/kgK
Density	2100 kg/m^3	1500 kg/m^3

Table 4-4 - Comparison table for properties of Tufnol(TM) and Cortical bone. Values taken from Henschel *et al.* and Bay Plastics website [41, 95].

The bone model had six 1mm radial holes drilled at regular intervals in the longitudinal direction. A thermocouple was inserted into each of these holes and then connected to a National Instruments™ SC-2345 signal conditioning connector block. Thermocouples were inserted deep enough for the tip to protrude into the cement 1mm. The signal conditioner was connected to a computer equipped with a National Instruments™ data acquisition card and Labview© data logging software.

CMW 1 bone cement (DePuy CMW Ltd) was vacuum mixed (Cemvac vacuum mixing system, DePuy CMW Ltd) in accordance with the manufacturers' instructions and injected into the femur at 1min 30sec after first mixing. The stem was inserted at 2min after first mixing at a constant rate of 200mm/min. Constant stem insertion velocity was ensured by performing the experiments in an Instron™ screw driven mechanical testing machine. By using the Instron™ mechanical testing rig centralisation was also improved as this proved to be very difficult to achieve over the length of stem by hand.

The data logger was started at the same time as cement mixing. Data was recorded for 45min.

4.5.3 Results and Discussion

Experimental results were plotted on temperature-time axes and compared to results produced by finite element modelling. Temperatures predicted by the finite element models were averaged through the width of the bone at each position, because it was not possible to resolve the temperature gradient through the thickness of the cement with the thermocouples used in the experimental tests.

Figure 4-48 shows the results of experiments using standard conditions. The temperature rises correlated very well with finite element predictions. The ordering of the results as well as the peak temperature at the distal measurement matches well with the results produced by finite element modelling (Figure 4-48). The discrepancies prior to polymerisation are due to the thermocouples already being at 37ºC due to being located in the body temperature Tufnol™ bone representation whereas the nodes in the model are initially at room temperature of 23ºC. Discrepancies after polymerisation may be due to differences in contact and boundary conditions assumed in the finite element model.

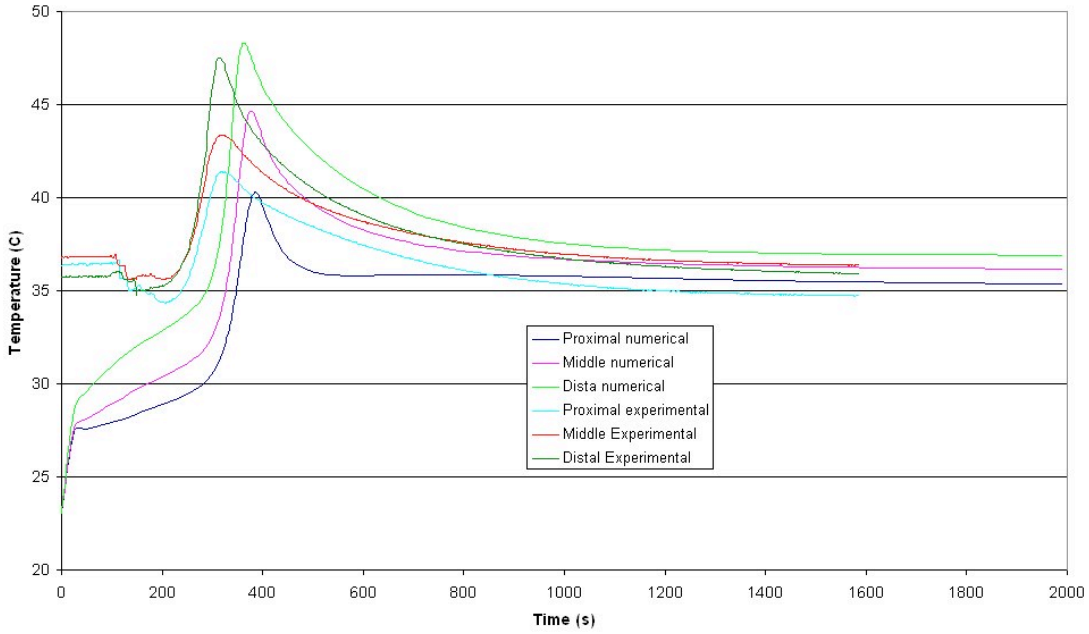

Figure 4-48 - Graph of temperatures produced from finite element simulation of experiment combined with temperatures measured during experimental validation.

4.6 Resurfacing Hip Arthroplasty Model

4.6.1 Introduction and Objectives

The femoral head resurfacing prosthesis is a component which may be cemented. Several authors have measured or predicted bone temperatures during cement polymerisation around conventional stems high enough to cause local bone cell death and structural damage to the bone matrix [7, 110]. It has also been proposed that these effects are responsible for or contribute to aseptic loosening of the prosthesis components [65].

In this study, finite element modelling techniques have been used to predict the thermal history of the prosthesis-cement-bone system during the cementation of a femoral head resurfacing prosthesis. The effects of the thickness of the cement layer on the thermal history were investigated and the likelihood of thermal necrosis of the bone was calculated.

4.6.2 Methods

The geometry of the femur used was generated using CT scan data and is made up of just one material, which was taken to be cortical bone, which has higher density and higher thermal conductivity than cancellous bone. The resurfacing component geometry, provided by DePuy International™ (ASR™ size 44) is shown together with the bone geometry in Figure 4-49. The internal surface of the component was offset radially to create the cement geometry. Cement thicknesses of 2 and 4mm were considered in this study. The resurfacing component was positioned on the femoral head to preserve the natural centre of rotation of the hip. The bone, cement and prosthesis were then meshed using first order tetrahedral elements and imported into the finite element software, Ansys™.

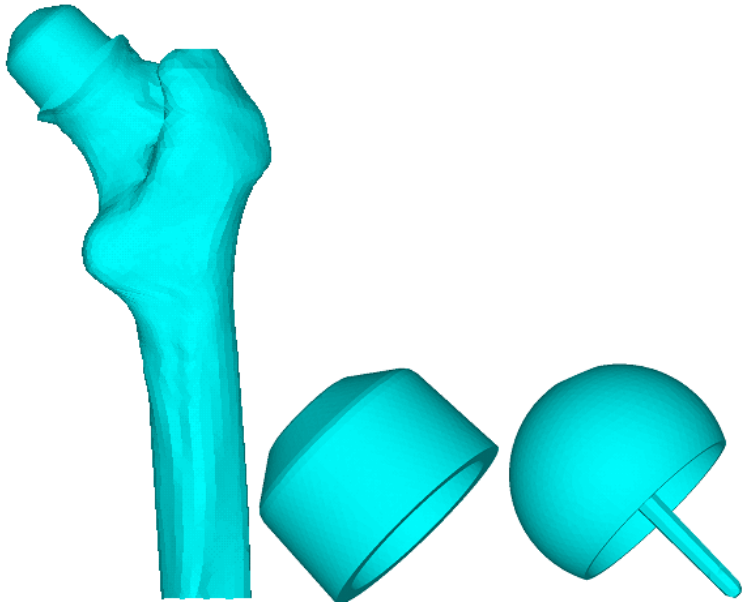

Figure 4-49 - Bone, cement and prosthesis geometry

Materials properties for the regions of the model corresponding to bone were assigned using data from the literature [43]. The prosthesis was assumed to be manufactured from cobalt chromium alloy, and all materials were assumed homogeneous and isotropic. Material properties required for the specification of the model are shown in Table 4-5.

Material	Density (kgm^{-3})	Specific Heat Capacity ($Jkg^{-1}K^{-1}$)	Thermal conductivity ($Wm^{-2}K^{-1}$)
Cortical Bone	$2.1x10^3$	$1.26x10^3$	0.38
Prosthesis	$8.87x10^3$	$0.45x10^3$	14.6
Bone Cement	$1.1x10^3$	$6.5T + 1.25x10^{3}$ *	0.2

Table 4-5 - Materials Properties (T=Temperature)

The temperature of the nodes on the whole of the external surface of the cortical bone was fixed at body temperature (37˚C, 310K) throughout the simulation. The initial temperature of the cement and prosthesis was room temperature (23°C, 296K) and the initial temperature of the bone component was body temperature.

Calculation of Necrosis Index

Necrosis of the bone is a function of time and temperature. In this study, a "necrosis index" was calculated at each of three nodes on a line running from the cement-bone interface into the bone as shown in Figure 4-50 using the method of Revie *et al.* [97]. For each node and each time step in the analysis, a necrosis index increment was calculated by dividing the time step size by the time to thermal damage at temperature T, where T is the average temperature in the element over the time step. The time to thermal damage at temperature T was calculated using an exponential function fitted to the data of Moritz and Henriques [82]. In order to avoid problems with extrapolating beyond the range of temperatures for which Moritz and Henriques provide data, temperatures above 65°C were assumed to cause a necrosis index increment of 1 for the time step, and temperatures below 44°C, a necrosis index increment of 0. Finally, the necrosis index increments were summed to calculate the necrosis index, with total values at the end of the analysis greater than 1 indicative of thermal necrosis of the bone.

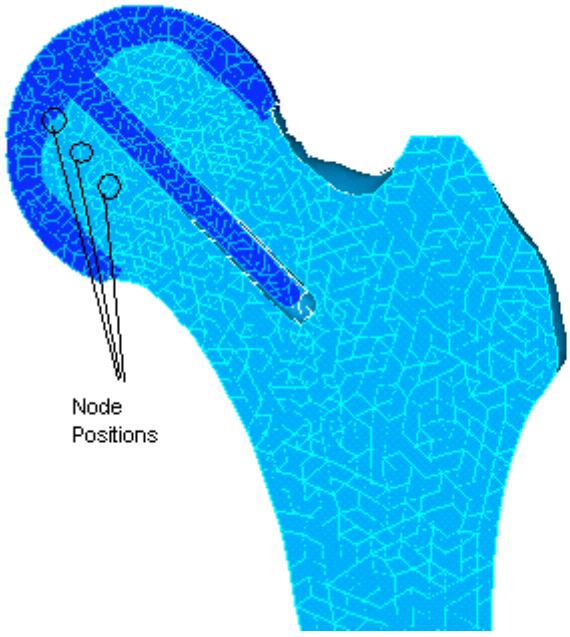

Figure 4-50 - Nodes from which results were calculated

4.6.3 Results and Discussion

Graphs of the temperature (Figure 4-51, Figure 4-52) and the degree of necrosis (Figure 4-53, Figure 4-54) at each of the three nodes are shown for both 2 and 4 mm cement mantle thicknesses

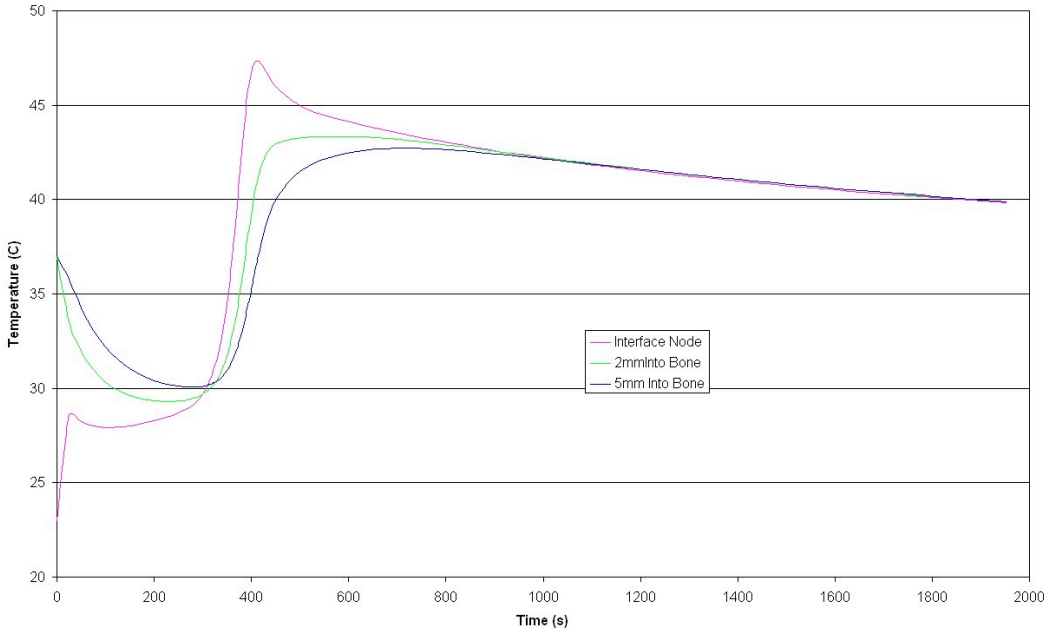

Figure 4-51 - Temperature history in resurfaced femoral head with 2mm cement mantle.

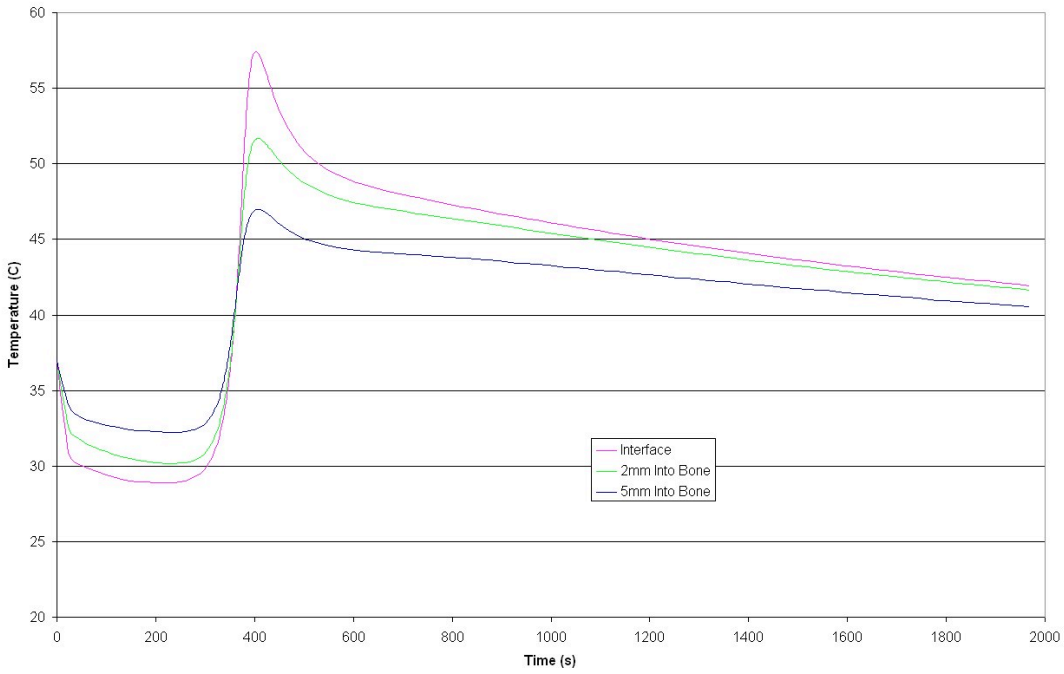

Figure 4-52 - Temperature history in resurfaced femoral head with 4mm cement mantle.

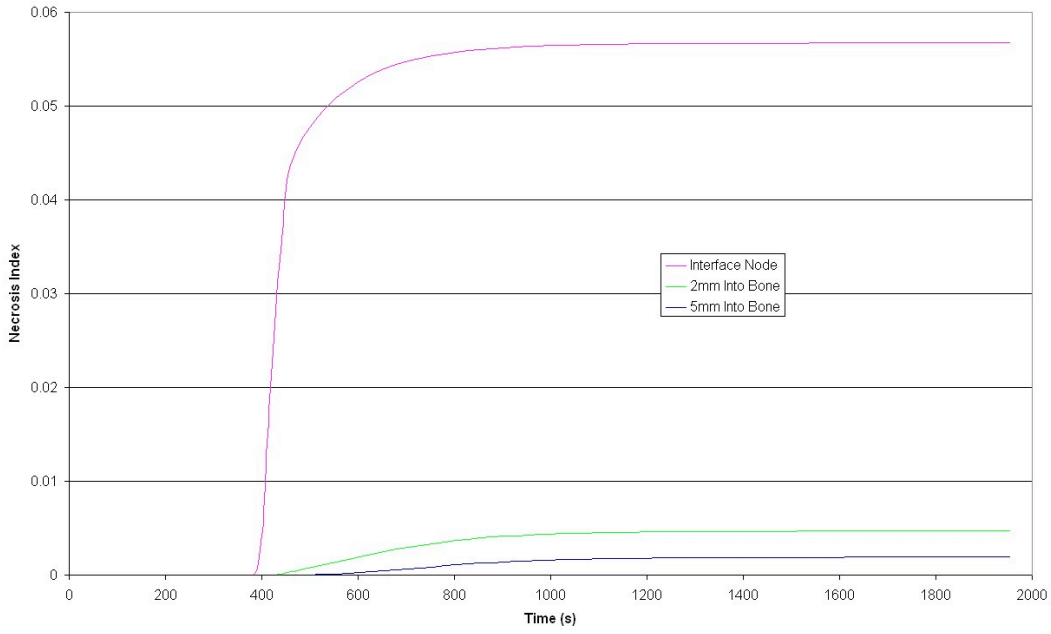

Figure 4-53 - Necrosis index in resurfaced femoral head with 2mm cement mantle.

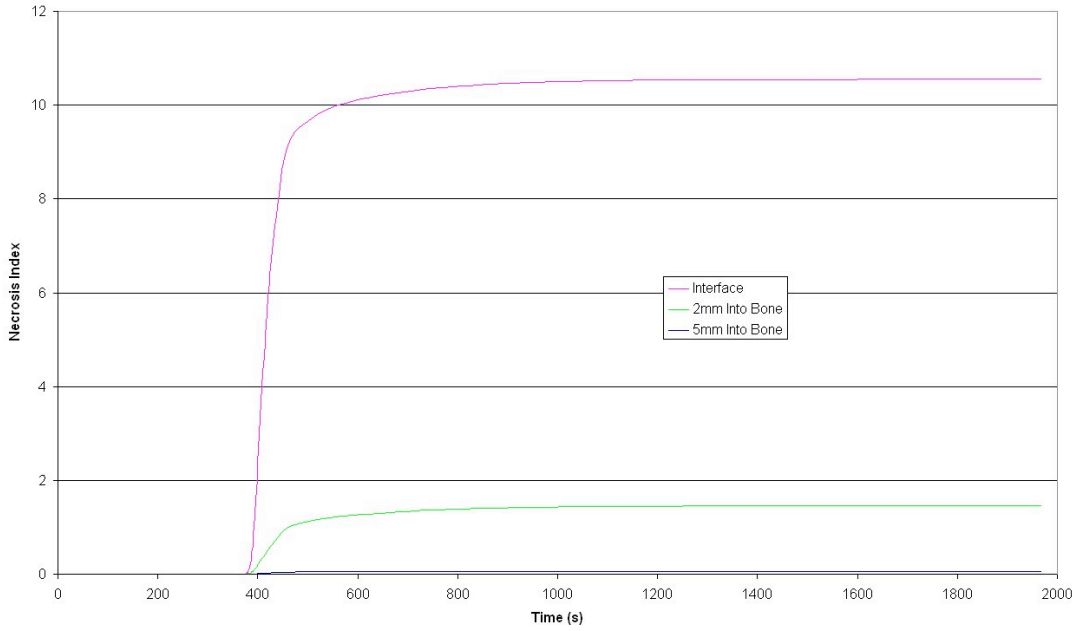

Figure 4-54 - Necrosis index in resurfaced femoral head with 4mm cement mantle.

The temperature plots show that cement mantle thickness had a significant effect on the amount of heat generated during cure. Increasing the cement thickness introduced a zone of necrosis in the bone surrounding the cement. The thin cement mantle (2mm) generated a maximum temperature of 320K (47˚C), the thick cement mantle (4mm) produced a maximum temperature of 330K (57˚C). This 10˚ difference in temperature reduced the amount of time that it takes for bone necrosis to take place. It also meant that the bone experienced these elevated temperatures for an extended period. These two factors produced a necrosis depth of >2mm when a thick cement mantle was used.

4.7 Total Knee Replacement Model

4.7.1 Introduction

The objectives of this study were to investigate the effects on temperatures and the likelihood of thermal necrosis in the surrounding bone of different aspects of cementation of the tibial component of a generic total knee replacement prosthesis. Whether or not the stem of the component was cemented, the thickness of the cement layer (thicknesses of 1 and 4mm) and the size of the tray were varied giving a total of 8 models.

4.7.2 Methods

The geometry of the bone was generated from CT scan data. The prosthesis and cement geometries were generated manually using dimensions typical for a total knee replacement tibial prosthesis. The geometries were meshed using 2^{nd} order tetrahedral elements. All computational modelling was undertaken using Ansys™ v7.1.

Each model is identified by a code. The number designates the cement thickness in mm; the first letter gives a yes (Y) or no (N) value, for whether or not there was cement along the length of the stem; the second letter shows whether the tibial tray was large (L) or small (S). For examples of this coding system refer to Figure 4-55.

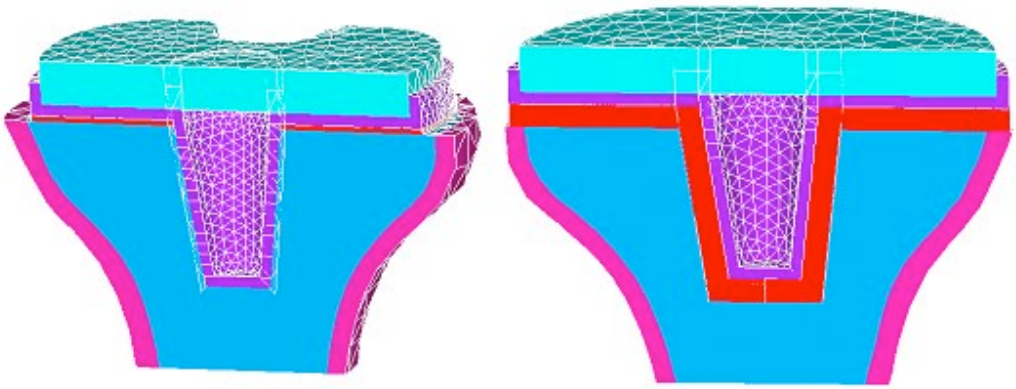

Figure 4-55 - Two geometries used in the simulations; the first is a view of the posterior half of a 1mm cement layer, no stem cement and small tray (1_N_S), the second shows the anterior half of a 4mm cement layer with stem cement and a large tray (4_Y_L).

Each model consisted of five different material components; the cortical bone, the cancellous bone, the cement, the tibial tray and the polyethylene insert (Figure 4-55 shows the individual material components in the models). Each of these materials was given properties as shown in Table 4-6. The temperature of the external surface of the bone was fixed at 37˚C (310K) throughout the simulation. The initial temperature of the cement, tray and insert was room temperature (296K) the initial temperature of the bone components was body temperature. The cement was given an initial degree of polymerisation of $6x10^{-6}$, as previously described this was necessary for the model to begin to polymerise at all.

After each time step, a necrosis index for each element was calculated as described in section Calculation of Necrosis Index0.

Material	Material Property	Value
Cement	Density	$1.1x10^{3}kgm^{-3}$
	Specific Heat Capacity	$6.5T + 1.25x10^{3}Jkg^{-1}K^{-1}$
	Thermal Conductivity	$0.2Wm^{-2}K^{-1}$
Tibial Tray	Density	$8.870x10^{3}$ kgm^{-3}
	Specific Heat Capacity	$0.450x10^{3}$ $Jkg^{-1}K^{-1}$
	Thermal Conductivity	14.6 $Wm^{-2}K^{-1}$
Insert	Density	$0.960x10^{3}$ kgm^{-3}
	Specific Heat Capacity	$2.220x10^{3}$ $Jkg^{-1}K^{-1}$

	Thermal Conductivity	0.29 $Wm^{-2}K^{-1}$
Cortical Bone	Density	$2.3x10^3$ kgm^{-3}
	Specific Heat Capacity	$1.3x10^3$ $Jkg^{-1}K^{-1}$
	Thermal Conductivity	0.4 $Wm^{-2}K^{-1}$
Cancellous Bone	Density	$2.1x10^3$ kgm^{-3}
	Specific Heat Capacity	$1.26x10^3$ $Jkg^{-1}K^{-1}$
	Thermal Conductivity	0.38 $Wm^{-2}K^{-1}$

Table 4-6 - Materials Properties (T=Temperature).

Each simulation was allowed to run for 2000s. This ensured that all polymerisation was complete. Contour plots of the degree of necrosis in the cancellous and cortical bone were produced at the end of each simulation.

4.7.3 Results and Discussion

Necrosis index contours are shown in Figure 4-56. In this plot the degree of bone necrosis is plotted over a section through the tibia. The predominant colour blue represents bone with no necrosis, the red shows the boundary between the non-necrotic and necrotic regions, which are shown in grey. The grey areas represent areas where the bone has reached or exceeded a necrosis index of 1.

From Figure 4-56 it can be seen that different cement geometries produced differing amounts of bone necrosis after polymerisation is complete. By increasing the cement thickness the amount of necrosis in the cancellous bone increased dramatically. When no cement was positioned along the length of the stem and a 1mm cement layer was used there was no bone necrosis predicted. By including cement in the bone cavity (along the length of the stem) bone necrosis increased significantly. When the large tibial tray was used there was little difference when compared to the small tray in the amount of necrosis in the cancellous bone.

By using a thinner cement layer it may be possible to dramatically reduce the amount of bone necrosis due to cure. Also by cementing only the tray section of the implant (not the stem) necrosis may be reduced. The size of the tray has little effect.

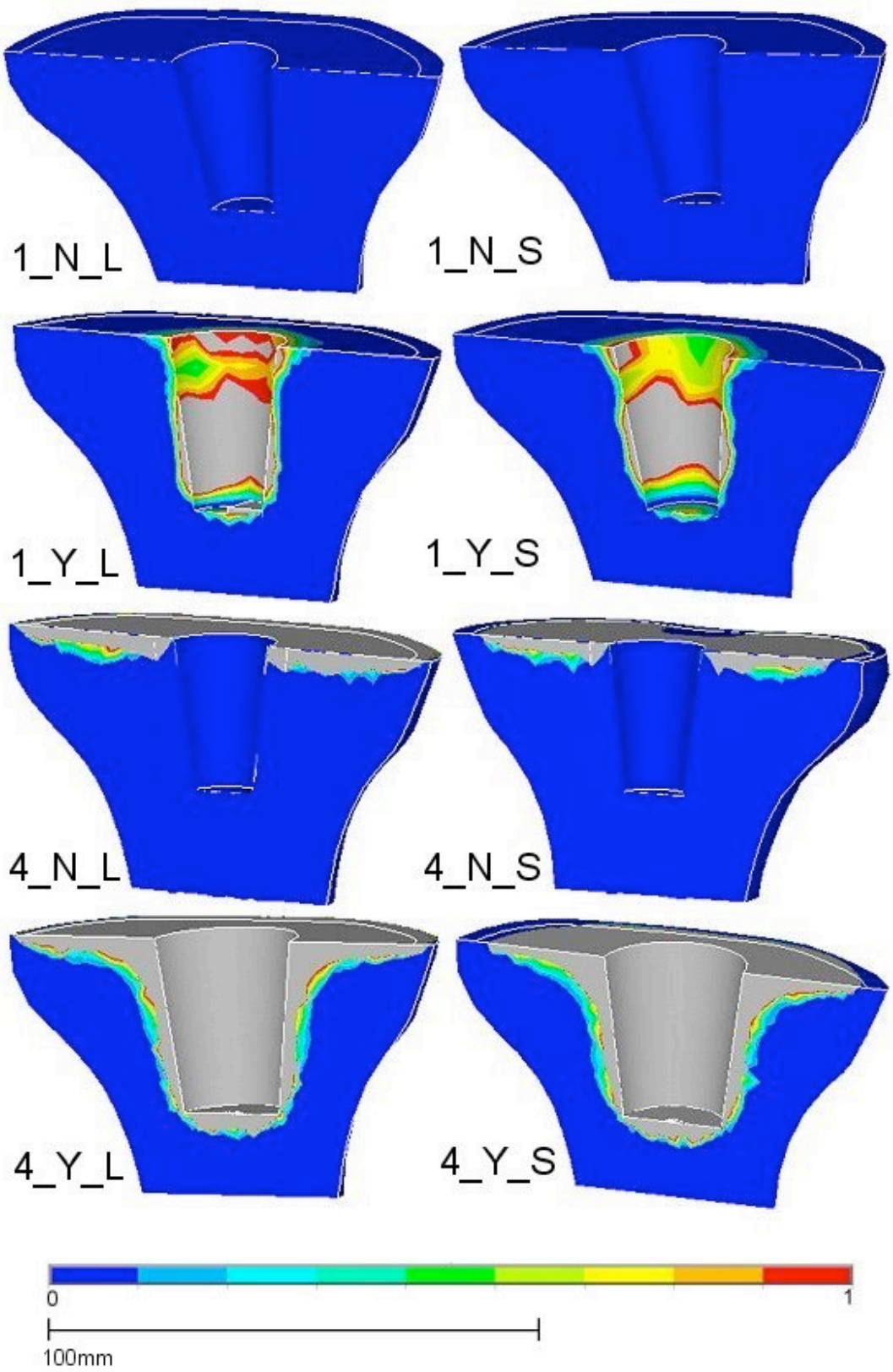

Figure 4-56 - Necrosis index contour plots (1 or 4 refers to cement thickness in mm, Y or N refers to whether or not cement is used on the stem and L or S refers to the use of a large or small tibial tray).

4.8 Thermal Modelling Summary

- A chemical reaction based polymerisation model was adapted due to the number and relevance of the model variables.
- Modelling of contact at interfaces is essential for model to agree with experimental tests.
- A minimum of 3 elements is required across the thickness of cement being modelled.
- Changes in cement thickness was shown to affect the peak temperature and the radial cure gradient.
- Stem temperature and stem alignment changes were able to reverse the polymerisation gradient.
- Thermal model was shown to be most sensitive to the activation energy.
- Thermal necrosis in different cement configurations of knee replacement operations were investigated and different thickness of cement in resurfacing arthroplasty.

5 Measurement of PMMA Curing Parameters Using Differential Scanning Calorimetry (DSC)

5.1 Introduction

During polymerisation of PMMA based bone cement several significant changes take place. Most notably, the material hardens from a fluid to form a viscoelastic solid. A large amount of heat is evolved during this process due to the exothermic nature of the polymerisation reaction. A volume change (shrinkage) has also been observed due to an increase in material density.

In vivo, the shrinkage generally occurs when the cement surrounds a joint replacement implant. The implant constrains the shrinkage of the cement leading to the generation of residual stress within the cured cement mantle. The residual stresses observed within cement mantles have been shown to have the potential to cause an increase in the rate of damage accumulation in the cement mantle upon subsequent loading and may cause pre-load damage to the cement.

In order to evaluate methods for reducing the residual stresses seen in the *in-vivo* cement mantle it is important to first understand the causes of the stresses. To this end a finite element model may be a useful tool to model the polymerisation process and the associated changes in materials properties.

The finite element model developed for predicting heat generation in curing cement (described in detail in Chapter 4 - Thermal Modelling of Bone Cement Cure) uses an Arrhenius function of the temperature (*f(T)*) to describe the temperature dependence of the reaction rate during the polymerisation process (Equation 4-4). It was shown in Chapter 4 that variables involved in the modelling of polymerisation, i.e. activation energy (*Ea*), total amount of heat liberated during polymerisation (Q_{tot}) and the rate

constant, *m,* have considerable effects on the polymerisation curve and/or the temperatures reached during polymerisation. It was therefore important to ensure that these values are established accurately in order to accurately model the polymerisation.

This chapter describes the measurement of the activation energy and the total amount of heat liberated during polymerisation using differential scanning calorimetry (DSC).

5.2 Materials and Methods

5.2.1 Theory

A method for determining the activation energy of reactions using Differential Scanning Calorimetry (DSC) has been described by Starink [109]. With this method it is possible to use relatively few experiments to completely characterise the reaction kinetics parameters compared to other methods presented in the literature [7, 110].

In Starink's article a novel technique for the determination of the activation energy of a reaction by application of the Kissinger-Akahira-Sunose (KAS) method (more commonly referred to as the generalised Kissinger method) is described.

The DSC instrument provides an extremely accurately electronically controlled temperature chamber. The temperature is controlled using liquid nitrogen and an electric heating element. By measuring the amount of heat input (by applying a current to the element) or extraction (by injecting an amount of liquid nitrogen), exotherms and endotherms can be quantified. The samples used are generally very small (of the order of mg's) which allows the sample to be more easily temperature controlled. In this way the DSC can be used to measure kinetics of many different reactions.

In this method, the reactants are mixed and a small sample placed into the DSC instrument. A constant rate temperature increase is then applied to the sample.

If it is assumed that the transformation rate of monomer to polymer is a product of two functions, one depending on the fraction transformed (α) and the other on the temperature (T), the rate of transformation ($d\alpha/dT$)can be written;

$$\frac{d\alpha}{dt} = f(\alpha)f(T) \qquad \textbf{5-1}$$

Substituting into the Arrhenius expression (equation 4-4) for *f(T)* (equation 5-1) and integrating gives

$$\int_0^{\alpha} \frac{d\alpha}{f(\alpha)} = \frac{k_0}{\beta} \int_0^{T_f} \exp\left(\frac{-E_a}{RT}\right) dT = \frac{k_0 E_a}{\beta R} \int_{y_f}^{\infty} \frac{e^{(-y)}}{y^2} dy \qquad \textbf{5-2}$$

where $y = \frac{E_a}{RT}$, $y_f = \frac{E}{RT_f}$, T_f is the temperature at a fixed state of transformation (eg. α =0.5) and β is the rate of temperature increase of the sample. The right hand side is generally called the temperature integral and can be written;

$$\int_{y_f}^{\infty} \frac{\exp(-y)}{y^2} dy = p(y_f) \qquad \textbf{5-3}$$

This can be integrated by parts and simplified, by assuming $y_f >> 1$ (reasonable since $15 < y_f < 60$ for most reactions of this type), to give;

$$p(y_f) \cong p_K(y_f) = \frac{\exp(-y_f)}{{y_f}^2} \qquad \textbf{5-4}$$

By taking the logarithm of equation 5-4 and inserting the approximation for the temperature integral we obtain;

$$\ln \int_0^{\alpha} \frac{d\alpha}{f(\alpha)} = \ln \frac{k_0 E_a}{R} + \ln \frac{1}{\beta {y_f}^2} - y_f \qquad \textbf{5-5}$$

At a constant degree of polymerisation (=0.5) this leads to:-

$$\ln\left(\frac{\beta}{T_f^{\,2}}\right) = \frac{-E_a}{RT_f} + C \qquad \textbf{5-6}$$

where C is a constant, independent of temperature and heating rate.

Plotting $\ln\left(\frac{\beta}{T_f^{\,2}}\right)$ against $\frac{-1}{RT_f}$ gives the activation energy as the gradient of the straight line. Once the activation energy has been determined, running isothermal tests and fitting equation 4-4 to the data produced gives K_0.

In a separate publication, Starink stated that this method may not be entirely reliable with reactions for which the start temperature, T_0, is within about 50-70K of the reaction temperature and those with particularly low activation energy [108]. This is considered to be the case for the polymerisation of PMMA bone cement. For this purpose it may be more accurate to use an alternative value in place of T_f. Alternative values to be considered may be the temperature at which the reaction is at its peak (T_p) or the temperature at which a fixed amount of heat is left to be evolved before the end of the reaction.

For example, should some of the reaction have already taken place before the reactants have been placed into the DSC, it may be necessary to ignore the early readings. By taking T_f as a point with a fixed amount of reaction left to take place, the early missing results from the reaction are ignored. This may be illustrated better using Figure 5-1, which shows a typical heat liberation curve for polymerising bone cement.

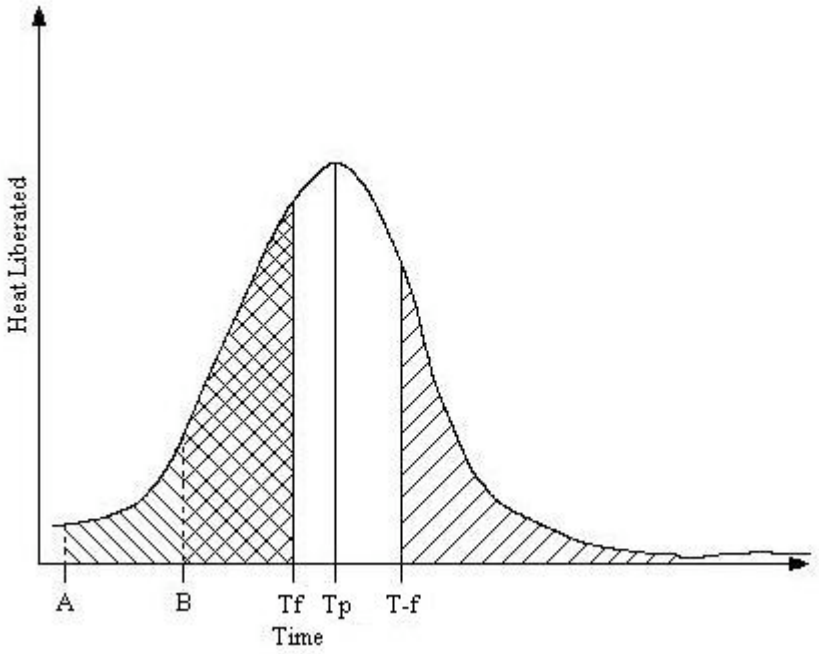

Figure 5-1 - Heat liberation curve showing possible errors produced by late start on the DSC.

If the cement is not inserted into the DSC instrument and the instrument started until point B then by taking T_f as a percentage of the reaction having taken place (T_f), poor accuracy will result as the area (cross-hatched in the diagram) will not be a true representation of the chosen fixed amount of heat liberated.

By taking T_f at a point where there is a fixed amount of heat left to be liberated we may be able to eliminate this problem of an early reaction. This may however suffer from any effects of the polymerisation reaction at the end. For example if there should be any secondary phase change or similar due to the higher temperatures at the end of our constant heat ramp experiments.

By looking at the temperature of the peak heat output it may be possible to eliminate the effects of both end reactions and of late entry. However if there is a late entry into the DSC then this will cause the peak temperature to occur at a slightly different temperature from that seen if begun soon after mixing.

Should none of these methods yield appropriate results then it may be possible to find the activation energy as well as Q_{tot} and m by forcing a numerical model to fit experimentally determined data. This method may require much more time and so should be used as a last resort.

5.2.2 Experimental Technique

Prior to using the DSC instrument it was necessary to obtain a "baseline" at the intended rate of temperature increase with an empty sample pan. This baseline was then subtracted from the heat results from the bone cement experiments to remove any effects of heating the sample pan itself.

Cement was stored in a freezer (-20ºC) for at least 24hrs prior to mixing to minimise the amount of reaction which occurred outside of the DSC instrument following cement mixing. CMW1™ cement was used and was hand mixed in a glass bowl. Vacuum mixing was not used as it was found that mixing and delivery of the cement to the DSC using a vacuum mixing system was too slow. Immediately after mixing the cement to a visually homogeneous paste, a small sample was placed into a DSC sample pan and weighed. The sample was then inserted into the DSC instrument and the constant rate of temperature increase started. The time taken between the moment of pouring the liquid monomer into the polymer powder and the beginning of the DSC test was noted as well as the mass of the cement sample placed in the DSC. Experiments were performed at heating rates of 2.5, 5, 7.5, 10, 12.5 and 15ºC/min.

After results had been obtained from each experiment, the baseline was subtracted and a curve was fitted to be coincident with the minima of the heat curve. This extra curve was subtracted to remove any effect of the specific heat capacity of the cement. This left just the heat produced due to the cement polymerisation reaction.

5.3 Results

The set of heat curves produced from the DSC are shown in Figure 5-2.

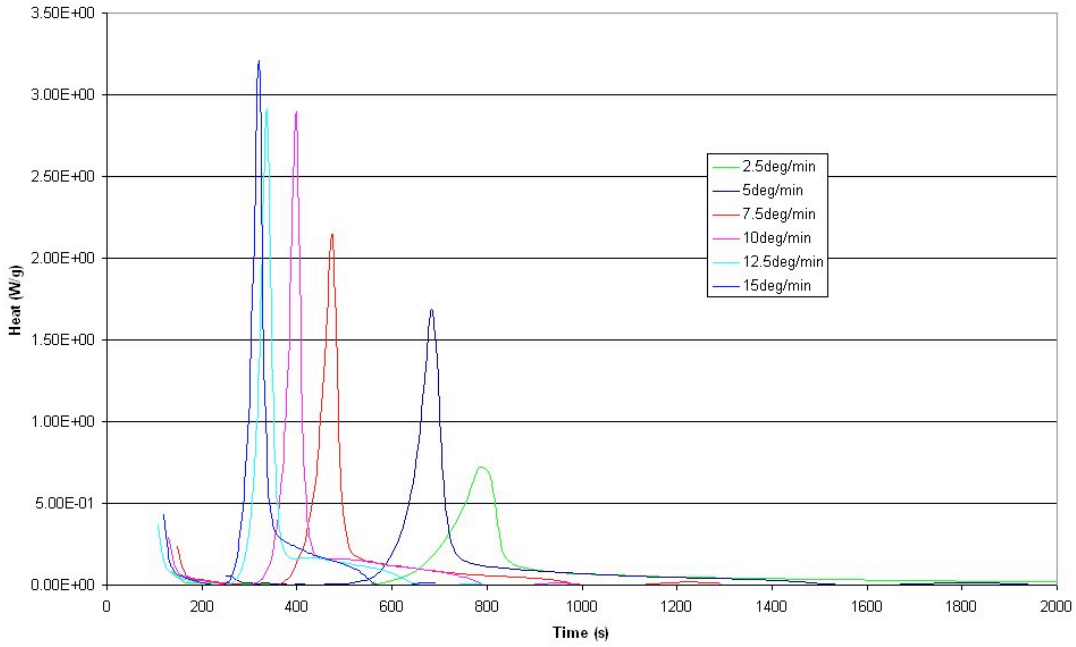

Figure 5-2 - Heat curves from DSC experiments after subtraction of sample pan and bone cement specific heat capacity baselines.

The trend is for the cement in the higher heating rate experiments to have polymerised (and therefore evolved heat) earlier and faster than with the slower heating rates. This is because there is more energy available early in the fast heating rate experiments.

T_f was taken to be the time at which 50% of the total heat evolved by the polymerisation, $Q_{tot,}$ had been liberated. Using this value a plot of $\ln\left(\frac{\beta}{T_f^{\,2}}\right)$ against $\frac{-1}{T_f}$ was obtained (Figure 5-3).

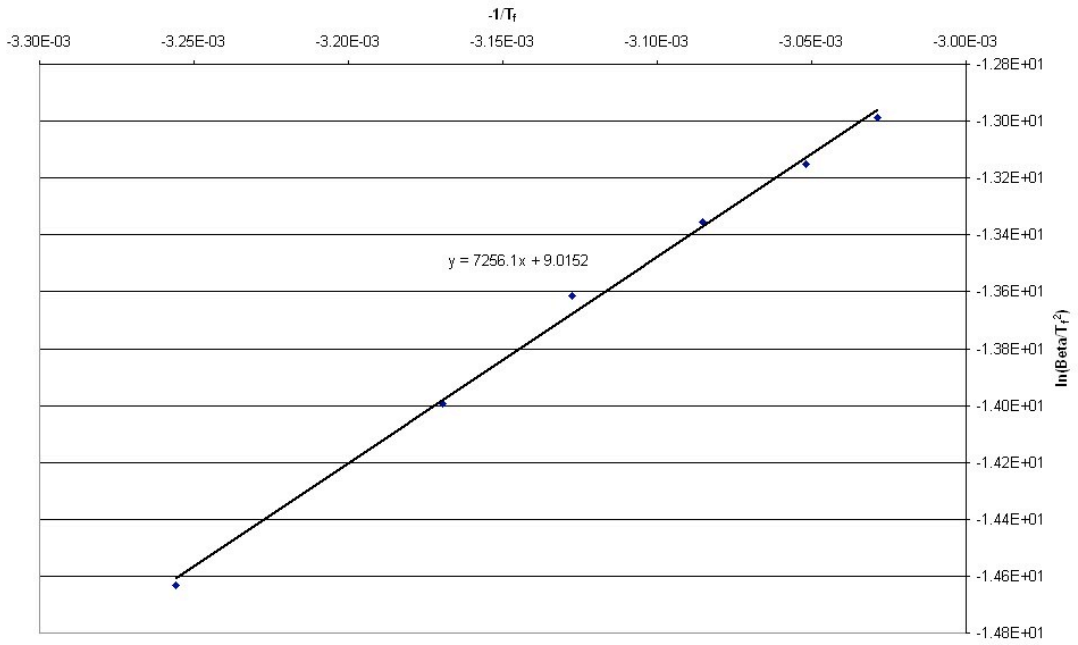

Figure 5-3 - Plot for the determination of the activation energy from T_f.

The plotted results conform well to a straight line. The gradient of this line is 7256.1. If the universal gas constant is 8.314kJ/kg mol K then the activation energy is 60327.2kJ/kg. Borzacchiello *et al.* have published a value of 31285.6kJ/kg. Since there is a large discrepancy between the two values it was necessary to repeat calculations looking at the peak temperature (T_p) instead of T_f. This gives the line plotted in Figure 5-4.

Again the result obtained for the activation energy (58224.6kJ/kg) has a large discrepancy with the published data. The result as seen using T_{-f} (the temperature at which a fixed fraction of the heat remains to be evolved) is used to further examine this problem. This plot is shown in Figure 5-5.

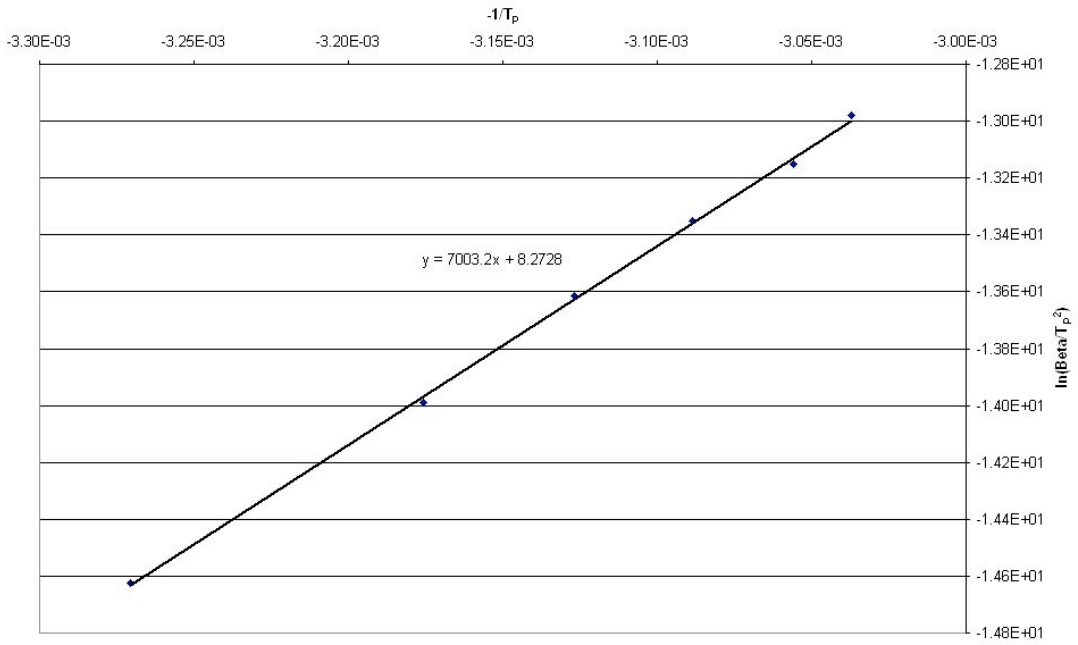

Figure 5-4 - Plot for the determination of the activation energy from T_p.

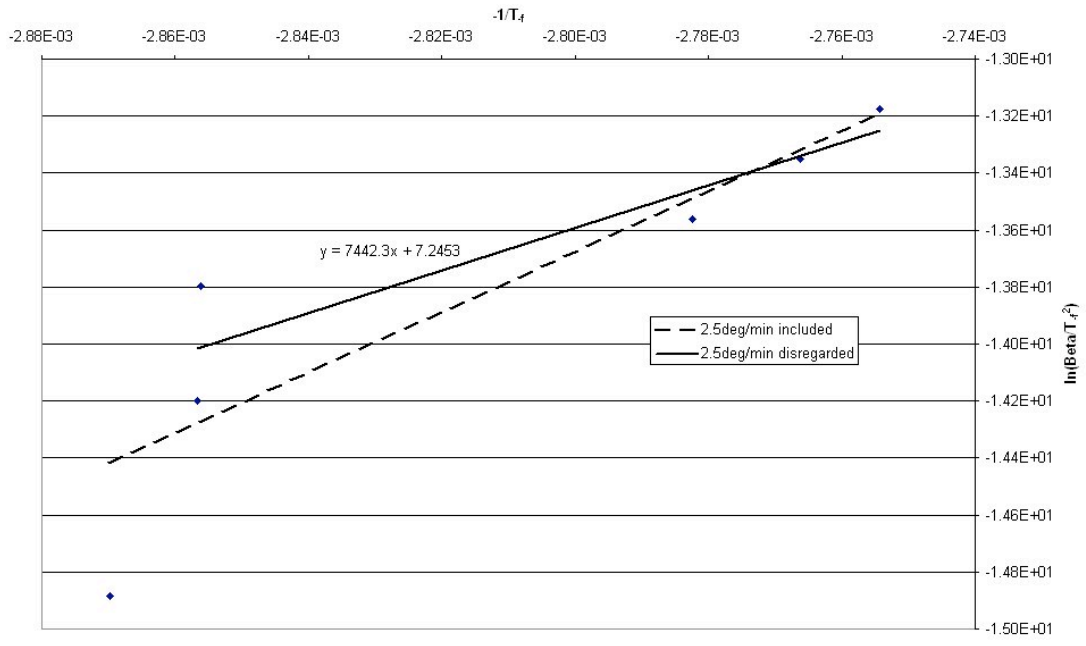

Figure 5-5 - Plot for the determination of the activation energy from T_{-f}.

The results using T_{-f} do not show a clear straight line and so some uncertainty in the line of best fit exists. If the point for the 2.5ºC/min is disregarded for this line then the gradient produced is 7442.3 giving a value for the activation energy of 61875.3kJ/kg.

Based on these values and the discrepancy with published data it was decided to force fit the polymerisation model to the DSC data.

5.3.1 Fitted Model

The constant temperature gradient maintained by the DSC means that the temperature within the apparatus and hence the temperature of the cement sample is known at all times during the test. This means that the input temperature at each time interval (required in equation 4-4) is known. The model described in Chapter 4 was used such that the heat output of a sample of cement, "cured" under the same polymerisation conditions as those produced by the DSC, was calculated at the known temperatures given by the rate of temperature increase (β). These curves were then plotted on the same axes as the experimentally determined heat output curves (some of the plots have two experimental results curves as they were repeated when initial results were unexpected). The curves do not coincide very well although at lower temperature gradients they seem to agree better than at higher ones.

Some adjustment was made to the input variables in an attempt to manually fit the model curves to the experimental data. Not all temperature gradient curves could be matched at the same time but some optimisation was possible to maximise the best fit. The new variables are shown in Table 5-1.

Variable	Q_{tot} (W)	E_a/R (/molK)	K_0	n	m
Published value	1.55×10^8	3763	9.1574	1.064	0.98
Fitted value	9.5×10^7	3690	9.2	1.06	0.98

Table 5-1 - Published and fitted input variables

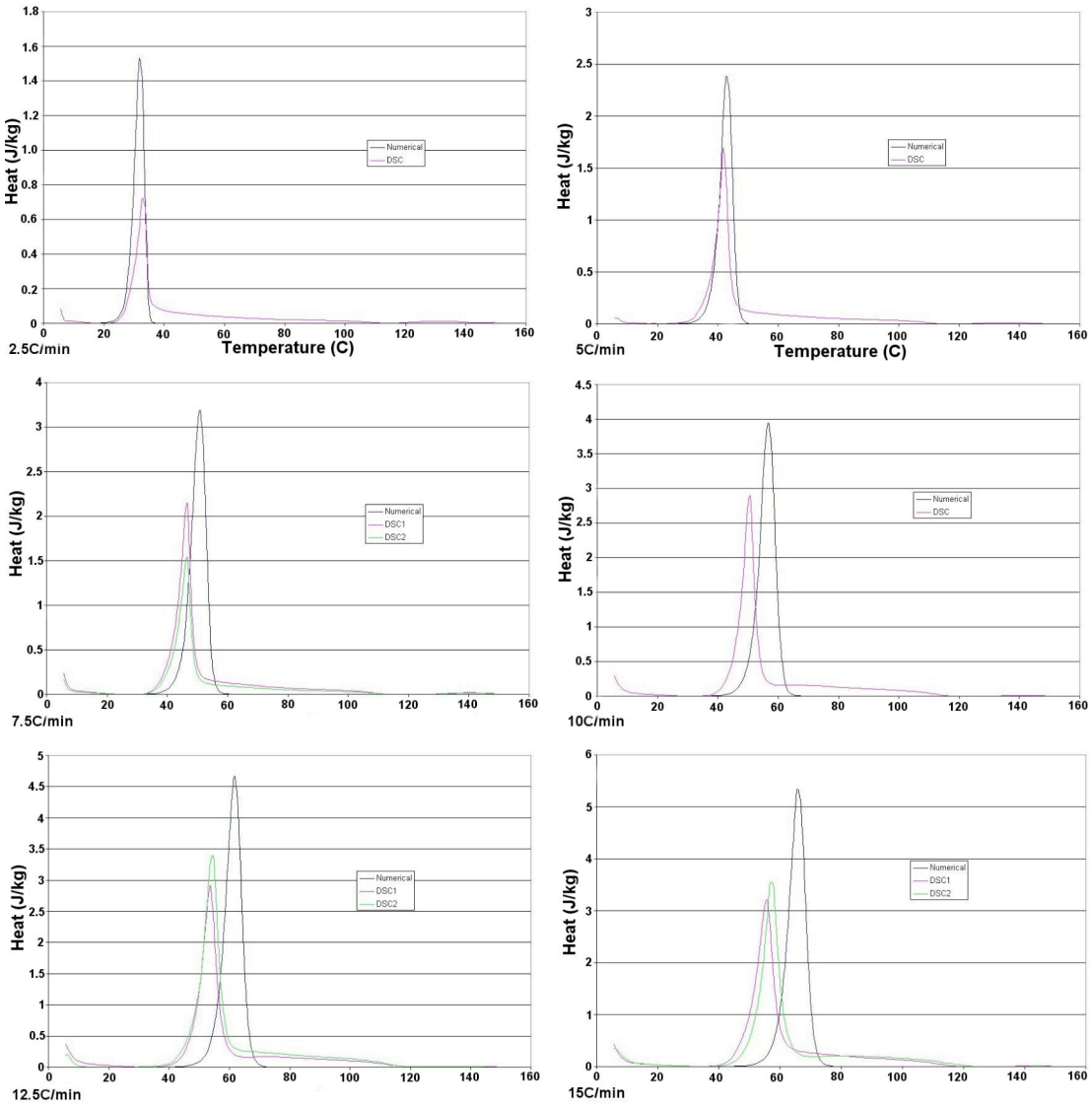

Figure 5-6 - Experimental and numerical curves using published variables for all different rates of temperature increase. Some experiments were run twice after the first set of results gave unexpected results others were only run this second time.

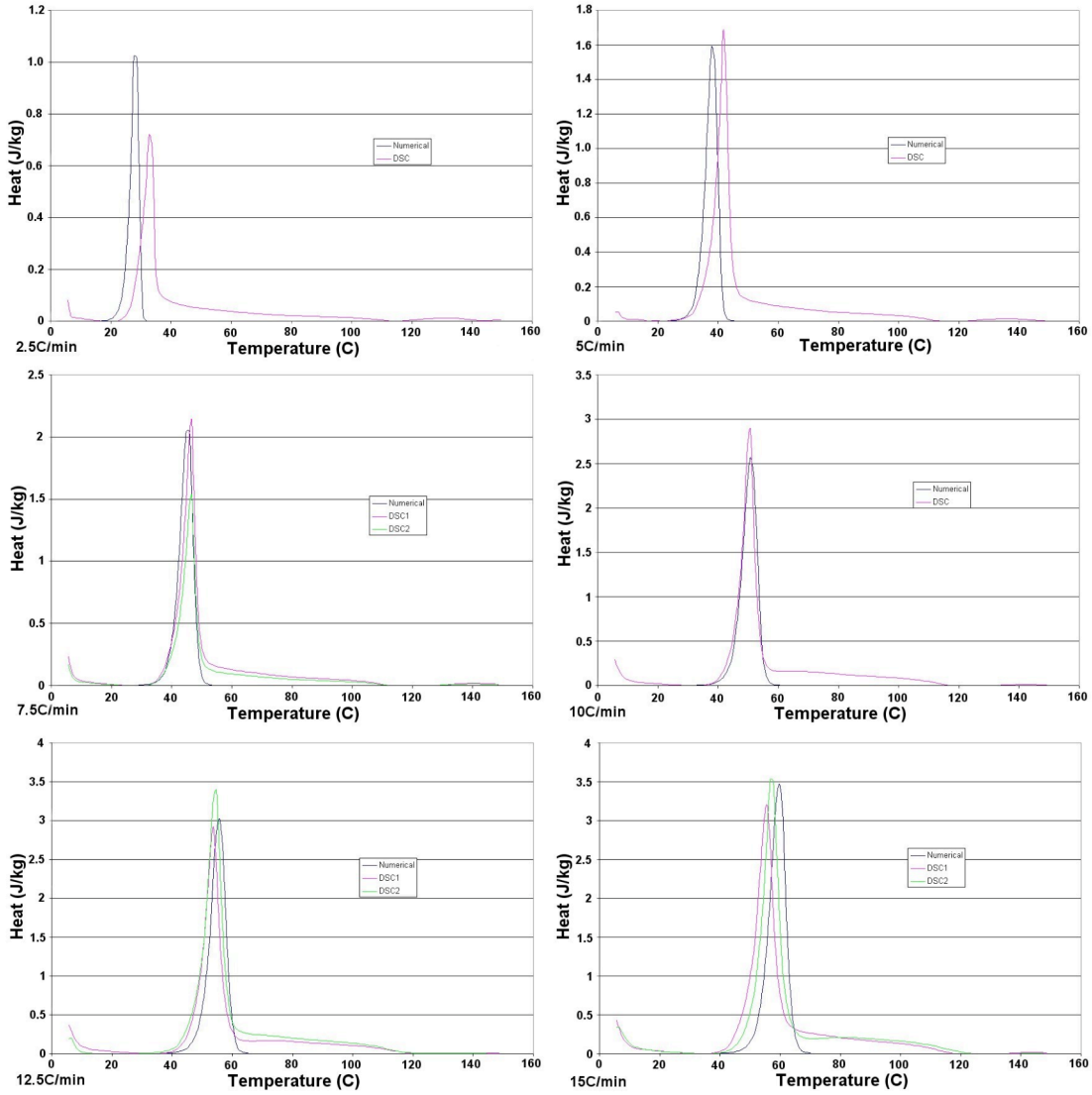

Figure 5-7 - Experimental and numerical curves using fitted variables for all different rates of temperature increase.

5.4 Discussion

To better fit the model curves to the experimentally determined data, Q_{tot} was altered significantly to bring the peak height down to a similar level in 5 of the 6 experiments. More minor changes were then made to the other input variables to better align the curves with the DSC data. At higher rates of temperature increase the models exhibited better conformity with the experimental data. It was not possible to fit the model to both the high and low rate of temperature increase experiments. This may mean that an element of model tuning may be required before using this model. For example if modelling a bulky cement mass (in a vertebroplasty application, perhaps), higher temperatures and higher rates of temperature increase would be expected. The opposite is true for a thin cement mantle in, say, a knee joint replacement application.

It has recently been shown by Starink that there are a group of reactions for which the activation energy determination techniques initially used here and previously published by Starink, cannot be applied [108]. The polymerisation of polymethylmethacrylate falls into this category since it has a relatively low activation energy and the starting temperature for the experiments was within 50-70K of the reaction stage to be investigated. This may explain the discrepancy between the calculated activation energy and the published value.

Previous DSC studies of the polymerisation reaction of polymethylmethacrylate have been carried out under isothermal conditions, which is less representative of the *in-vivo* conditions. By carrying out a DSC investigation at varied rates of temperature increase it may be possible to better characterise the reaction variables. Tuning of variables to the individual situation is important when using empirical variables.

5.5 DSC Cure Parameter Measurement Summary

- Constant temperature increase experiments were used and may be more clinically relevant than isothermal polymerisation tests.
- Values for the Activation energy were calculated using methods published by Starink [109].
- The reaction was shown to be inappropriate for this method of activation energy determination.
- Fitting techniques were used to show that the model may not hold true for all situations using the same variables.
- It may be necessary to 'tune' the reaction variables to an individual set of boundary conditions and geometry.

6 Ultrasonic Cure Monitoring

6.1 Introduction

During polymerisation the material properties of PMMA based bone cement go through significant changes. After mixing, bone cement is inserted into the bone cavity as a power-law pseudoplastic fluid [25]. The cement polymerises *in-situ* and hardens over a period of approximately 5-10 minutes to form a visco-elastic solid. Volume has also been reported to change during polymerisation and if mass conservation is assumed, this must be accompanied by a change in density [83]. Residual stress may be produced in the cement mantle due to the change in volume in the presence of a constraining implant – residual stress generation will be affected by the relative timing of the changes in density and mechanical properties. Residual stress has been proposed as a factor in the failure of cemented arthroplasty [53, 58].

In order to predict the residual stress generation in acrylic bone cement it is necessary to understand the mechanical property changes that accompany polymerisation. Farrar and Rose used a mechanical rheometry technique to determine the viscoelastic parameters of the cement in terms of the storage and loss moduli and the loss angle [27]. Hanson *et al.* have developed a self-sensing mechanical rheometer to monitor the dynamic viscosity of the cement in the operating theatre so that the operating surgeon can better determine when to insert the cement [38].

It is important to ensure a minimal energy input from the measurement technique if measurements of curing cement representative of surgical conditions are to be obtained. Kinetic energy from mechanical rheometers can disturb the normal polymerisation process, but by keeping the energy input to a minimum, conditions close to those in surgery can be maintained. An alternative method is to use an ultrasonic technique to measure the material properties. Viano *et al.* performed a series of experiments to characterise the cure of bone cement [122]. They used measurements of the sonic velocity and the broadband ultrasonic attenuation (BUA) during cure to establish the cure time. Carlson *et al.* and Nilsson *et al.* used ultrasonic techniques to monitor the density and adiabatic bulk modulus in calcium based bone

cements [16, 85]. An approximation of the bulk modulus was derived from the velocity and the density. Since no shear wave measurements were taken, the true bulk modulus and the Lamè constants could not be determined. The moduli could therefore not be calculated in their complex form as they must be to fully characterise a visco-elastic material.

In this work a method for using ultrasound to monitor the cure of a PMMA bone cement was developed to calculate the density and complex modulus during polymerisation. Also the frequency response of each of these parameters was investigated for both compressive and shear waves.

6.2 Materials and Methods

A jig was developed to house the sample and the ultrasound transducer and incorporate a method of measurement of the thickness of the sample. At the beginning of polymerisation bone cement is a fluid and must be contained and prevented from flowing freely. During polymerisation a volume change takes place and so the sample dimensions will change which must be accommodated by the jig. Due to dimension changes the cement thickness over which the ultrasonic signal is being sampled must be constantly measured.

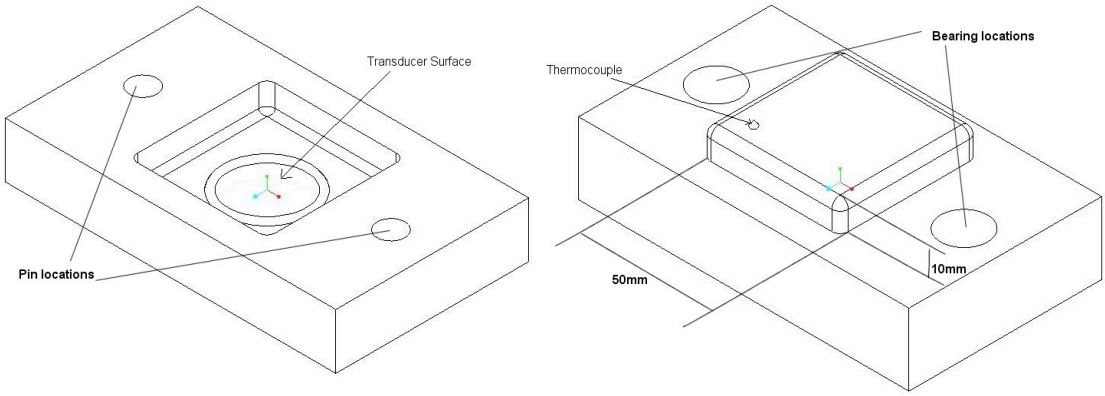

Figure 6-1 - Isometric views of the mould cavity and reflective top faces of the ultrasound experimental jig.

A jig was designed with a cavity to contain the mixed cement and a threaded hole to locate the transducer underneath the cavity (Figure 6-1). The upper part of the jig has a flat steel surface opposite the transducer and is free to move towards or away from the transducer as dimensional changes occur in the cement. The top surface acts as a reflective surface to return the ultrasonic signal from the far side of the cement sample. Guide pins mounted beside the cavity upon which the upper component was free to slide ensured the reflective top surface remained parallel to the face of the transducer throughout the experiment. A micrometer was used to measure the relative position of the upper and lower parts of the jig. The sample thickness at any time could then be found by reference to the sample thickness measured at the end of testing.

A frequency dependence of the impedance of the transducer surface was established during initial testing and to eliminate this artefact a 3mm polyethylene buffer was inserted on top of the transducer. The transducer was coupled to the buffer using honey.

A Panametrics V604, 2.25MHz, 1.0”dia. transducer was used for compressive wave measurements and a Panametrics V154, 2.25MHz, 0.5”dia. transducer for shear waves (unlike a conventional transducer the piezoelectric ceramic within the shear transducer is adapted to provide an oscillation in the same plane as the face of the transducer, this is then propagated through the test material in the normal direction). A Panametrics™ 5052 pulser/receiver was used to excite the transducer and a LeCroy™ 9310 oscilloscope was used to digitise the received signal, which could then be recorded on a PC.

6.2.1 Experimental Procedure

Experiments were performed at room temperature. Initially a recording of the signal received without any steel jig top or PMMA in place was taken. This was used to provide a reference value with air (a very well defined material) as a reflective surface. Ultrasonic energy is well reflected at the interface between two materials with dissimilar material properties and well transmitted through materials with similar material properties (e.g. a polyethylene-air interface is strongly reflective, a polyethylene-polytetrafluoroethylene (PTFE) interface is strongly transmissive).

CMW1 DePuy™ cement was used throughout the experiments and was mixed under vacuum using the Cem-Vac™ mixing system. Mixing was carried out in accordance with the manufacturer’s instructions. Cement was inserted into the jig cavity 2 minutes after initial mixing of the liquid monomer and polymer powder. The jig top was placed on the jig and the first measurement was recorded 2.5 minutes after initial mixing.

A measurement of the cement thickness and a recording of the received signal were taken every 30 seconds while little change was occurring. During periods of rapid change measurements were taken as often as possible and the timing noted.

In order to maximise the signal on the oscilloscope, the pulser/receiver attenuation was altered for each measurement and these values were stored for use in data processing. The difference in attenuation was removed in the results processing to ensure all measurements were on a common scale.

Measurements were taken until 720 seconds after the initial mixing for the compressive and 900 seconds for the shear test. At these times there was little further change in the signal and so polymerisation was assumed to be complete.

Results were processed using Matlab™ and an example of the code used is contained in Appendix II – Finite Element Modelling and Results Processing Codes.

6.2.2 Acoustic Theory and Data Processing

Consider a layer of cement sandwiched between a piece of steel and a piece of polyethylene with a transducer mounted behind the polyethylene. A pulser/receiver excites the transducer to produce a signal. The path of the signal is illustrated in Figure 6-2. This pressure wave passes into the polyethylene with amplitude $A_0\tau$, where A_0 is the initial amplitude of the pressure wave and τ is the transmission coefficient into the system. A portion of the pressure wave is reflected at the far surface of the polyethylene and a portion continues through the PMMA cement. The ratio of the amplitudes of the reflected and transmitted wave is the 'reflection coefficient' R_{12}. The reflected portion of amplitude A returns to the transducer where it is recorded. The transmitted portion of the signal continues to the opposite side of the PMMA where it is reflected at the PMMA/steel interface, again with loss of amplitude due to transmission into steel. The reflection coefficient at the PMMA/steel interface is denoted by R_{23}. The pressure wave then returns through the PMMA suffering further losses due to reflection as it passes back into the polyethylene (in this case characterised by the transmission coefficient T_{12}). The signal is then recorded at the transducer and has amplitude B. The signal taken with air backed polyethylene is denoted A'.

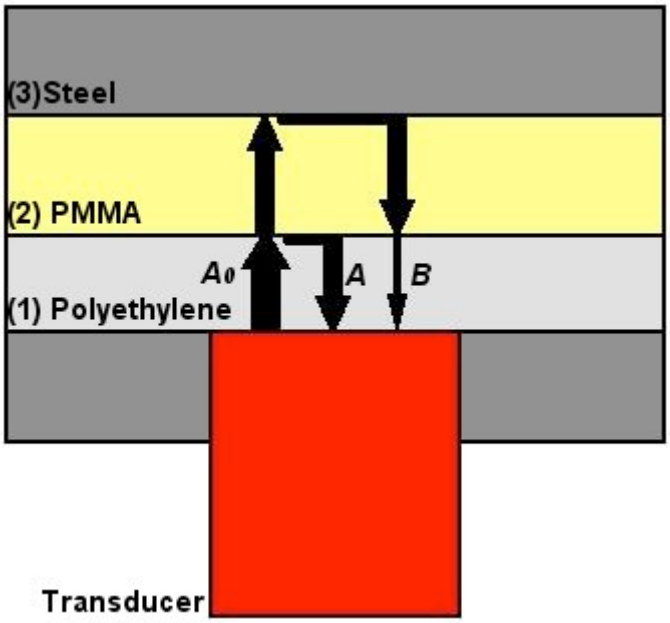

Figure 6-2 - Diagram showing path of recorded signals through polyethylene and PMMA.

As the pressure wave passes through the polyethylene and PMMA it is attenuated and the calculation of this attenuation is required to derive both the density and the complex modulus of PMMA.

The amplitude of the wave reflected at the polyethylene-PMMA interface can be calculated using equation 6-1;

$$A = A_0 \tau R_{12} e^{-2\alpha_1(f)t_1} \qquad \textbf{6-1}$$

where A_0 is the incident wave amplitude, τ is the transfer coefficient from the transducer into the polyethylene, R_{12} is the reflection coefficient at the polyethylene/PMMA interface, $\alpha_1(f)$ is the attenuation of polyethylene as a function of frequency and t_1 is the thickness of the polyethylene.

Similarly, the amplitude A' can be calculated using equation 6-2;

$$A' = A_0 \tau e^{-2\alpha_1(f)t_1} \quad \textbf{6-2}$$

Dividing A by A' allows the reflection coefficient at the polyethylene/PMMA interface R_{12} to be calculated;

$$\frac{A}{A'} = R_{12} \quad \textbf{6-3}$$

The impedance of PMMA can then be found;

$$R_{12} = \frac{z_2 - z_1}{z_2 + z_1} \quad \textbf{6-4}$$

where z_1 and z_2 are the impedance in polyethylene and PMMA respectively. The impedance of polyethylene can be obtained from the literature and so the impedance of PMMA can be derived and used together with the sonic velocity to give the density;

$$\rho_n = \frac{z_n}{v_n} \quad \textbf{6-5}$$

To calculate the complex moduli the attenuation of the cement is also required. This can be found by using the relationship between the first and second echo signals. The second echo has amplitude (B), which can be calculated using equation 6-6.

$$B = A_0 \tau T_{12} R_{23} T_{21} e^{-2\alpha_1(f)t_1} e^{-2\alpha_2(f)t_2} \quad \textbf{6-6}$$

where T_{12} and T_{21} are the transmission coefficients for passage of the ultrasonic wave from polyethylene to PMMA and from PMMA to polyethylene respectively, R_{23} is the reflection coefficient at the PMMA/steel interface and $\alpha_2(f)$ and t_2 are the attenuation and thickness of the PMMA respectively. By relating T_{12} and T_{21} to the reflection coefficient R_{12} (equations 6-7 and 6-8) the amplitude of B can be reduced to;

$$T_{12} = 1 - R_{12} \qquad \textbf{6-7}$$

$$T_{21} = 1 + R_{12} \qquad \textbf{6-8}$$

$$B = A_0 \tau (1 - {R_{12}}^2) R_{23} e^{-2\alpha_1(f)t_1} e^{-2\alpha_2(f)t_2} \qquad \textbf{6-9}$$

Dividing B by A gives;

$$\frac{B}{A} = \frac{(1 - {R_{12}}^2)}{R_{12}} R_{23} e^{-2\alpha_2(f)t_2} \qquad \textbf{6-10}$$

R_{23} can be found from;

$$R_{23} = \frac{z_3 - z_2}{z_3 + z_2} \qquad \textbf{6-11}$$

z_2 has been calculated using equation 6-4 and z_3 (the impedance of the steel) can be calculated using equation 6-5.

R is a term used to identify a function of the reflection coefficients and is given by equation 6-12.

$$R = \frac{(1 - R_{12}{}^2)}{R_{12}} R_{23} \qquad \textbf{6-12}$$

By substituting equation 6-12 into equation 6-10, attenuation can be found from;

$$\ln\left(\frac{B}{A}\right) = \ln R - 2\alpha_2(f)t_2 \qquad \textbf{6-13}$$

in the form;

$$\alpha_2 = \frac{\ln R - \ln\left(\frac{B}{A}\right)}{2t_2} \qquad \textbf{6-14}$$

6.2.3 Dispersion Adjustment

Initial experiments revealed a problem due to dispersion of the ultrasonic wave in the PMMA and polyethylene. This dispersion was most likely caused by the visco-elastic nature of the two materials and would be expected to be more prominent in the PMMA layer at the beginning of polymerisation. Dispersion of an ultrasonic wave results from the frequency dependence of the transmission properties of the transmitting medium. Since a broadband transducer (which emits ultrasonic waves of multiple frequencies) was used in this study different components of the signal of different frequency within the signal were attenuated differently and travelled at different velocities. These effects of dispersion result in difficulty in determining the velocity of the ultrasonic wave. An adjustment must be made to the velocity of the signal through the PMMA to allow for these effects.

In a non-dispersive material the velocity can be measured by inspecting the signal and in particular the time between peaks in successive echoes. By dividing the time between peaks from successive echoes by the distance the signal has travelled (twice the thickness of material it has passed through) the velocity can be calculated. In a dispersive material this technique will not find the velocity for all frequencies in the signal - the velocity found is that of the centre frequency of the transducer. To find the velocity at other frequencies in the range of the transducer signal the following equation may be applied

$$v_2(\omega) = v_2(\omega_0) + \frac{2v_2(\omega_0)}{\pi}\int_{\omega_0}^{\omega}\frac{\alpha(\omega)}{\omega^2}d\omega \qquad \textbf{6-15}$$

where ω is the rotational frequency in radians/s, $v_2(\omega)$ is the velocity as a function of ω and ω_0 is the centre rotational frequency of the transducer. This technique uses a Kramers-Kronig technique to relate the phase velocity and attenuation [124]. When this adjustment has been made $v_2(\omega)$ can be used in the calculations of the material properties as shown in 6.2.2 - Acoustic Theory and Data Processing.

The ultrasonic velocity through polyethylene is also affected by dispersion. For polyethylene, $v_1(\omega)$ was adapted from the literature. Wu measured both the longitudinal and shear ultrasonic velocities as a function of frequency through a similar (though not identical) density polyethylene and they are shown in fig. 5 of that publication [128]. In a study by Piché, longitudinal phase velocity was plotted against the density in polyethylene (fig. 2 in that publication) and showed a proportional relationship between the two variables [94]. Using the relationship published by Piché, the velocities published by Wu were scaled according to the density. In this way a complete spectrum for the velocity of sound as a function of frequency was determined for the buffer rod of polyethylene. Using equation 6-4 the impedance of polyethylene was then calculated (z_1). The calculated impedance of the polyethylene is plotted against the frequency over the useful frequency range in Figure 6-3.

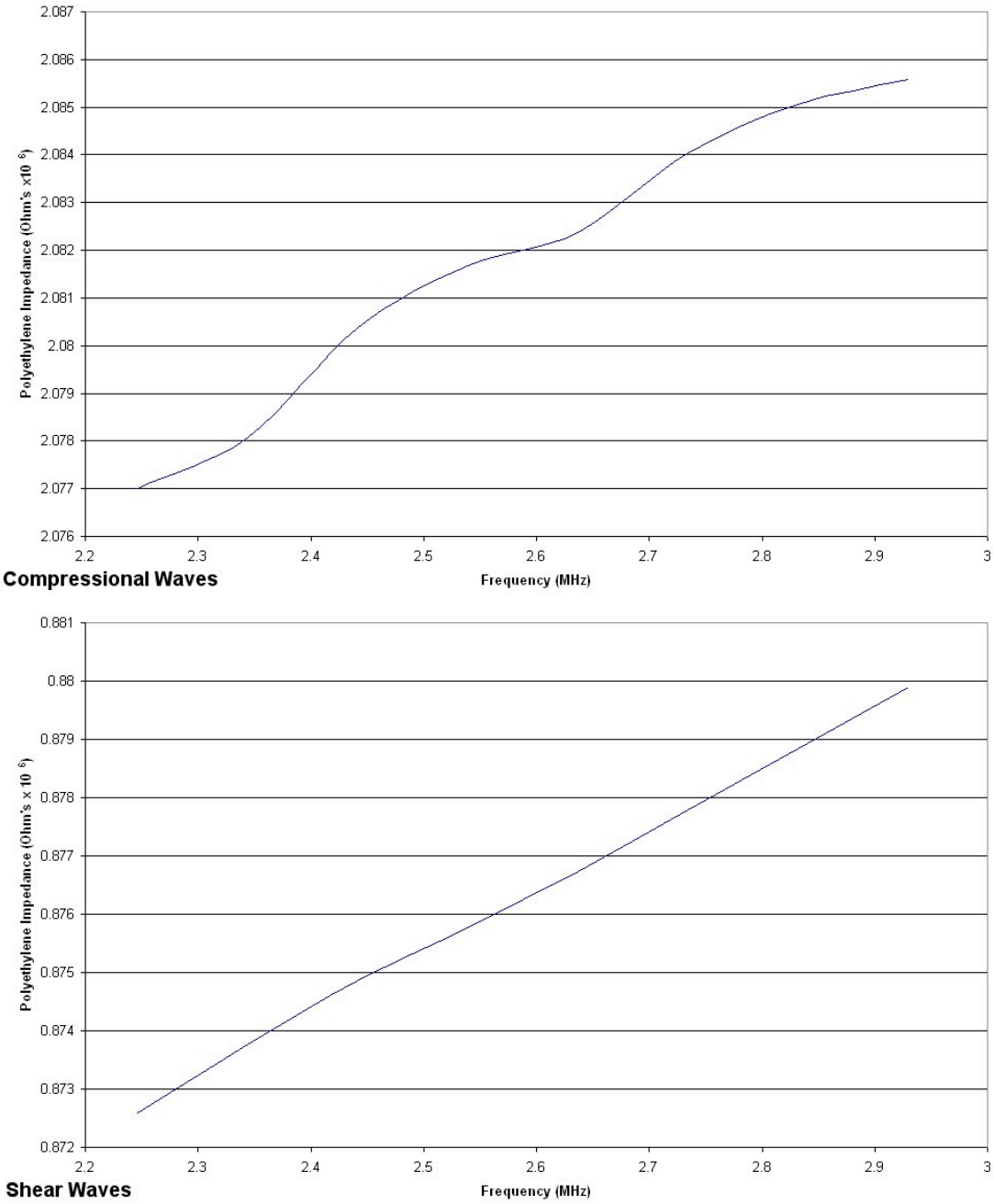

Figure 6-3 - Ultrasonic wave impedances for both compressive and shear waves through polyethylene converted using a relationship of density to velocity for polyethylene [94] from experimental data for the impedance with frequency for a similar polymer with different density [128].

6.2.4 Material Property Calculation

From the theory in sections 6.2.2 - Acoustic Theory and Data Processing and 6.2.3 - Dispersion Adjustment, the density, ultrasonic velocity and attenuation in PMMA

were calculated. Using these three variables it was possible to calculate the complex moduli.

According to McSkimin the real and imaginary parts of both the compressive and shear moduli of a visco-elastic material can be calculated from ultrasonic variables [79]. The real and imaginary parts correspond to storage and loss modulus respectively.

For compressive waves;

$$E_c^{\,*} = E_c' + jE_c'' = C_{11}^{\,*} \qquad \textbf{6-16}$$

For shear waves;

$$E_s^{\,*} = E_s' + jE_s'' = C_{44}^{\,*} \qquad \textbf{6-17}$$

E denotes the elastic modulus and C_{11}, C_{12} and C_{44} denote the individual stiffness constants that make up a materials stiffness matrix. A '*' is used in this instance to indicate when a value is complex. The real and imaginary parts of the compressive and shear moduli can be calculated from equations 6-18 to 6-23 using values obtained from the corresponding set of experiments (compressive variables to calculate the compressive moduli and shear variables to calculate the shear moduli);

$$E' = \frac{\rho_2 v_2^{\,2}\left(1 - \alpha_2^{\,2}\dfrac{v_2^{\,2}}{\omega^2}\right)}{\left(1 + \alpha_2^{\,2}\dfrac{v_2^{\,2}}{\omega^2}\right)^2} \qquad \textbf{6-18}$$

$$E'' = \frac{2\rho_2 v_2^{\,2}\alpha_2 \frac{v_2}{\omega}}{\left(1+\alpha_2^{\,2}\frac{v_2^{\,2}}{\omega^2}\right)^2} \qquad \textbf{6-19}$$

These complex values can be used to find the bulk and shear moduli. Bulk modulus (K) is given by;

$$K^* = \frac{1}{3}\left(C_{11}^{\,*} + 2C_{12}^{\,*}\right) \qquad \textbf{6-20}$$

where;

$$C_{12}^{\,*} = C_{11}^{\,*} - 2C_{44}^{\,*} \qquad \textbf{6-21}$$

and shear modulus (G) is given by;

$$G^* = C_{44}^{\,*} = \frac{1}{2}\left(C_{11}^{\,*} - C_{12}^{\,*}\right) \qquad \textbf{6-22}$$

From the bulk and shear moduli the Young's modulus can be extracted in its complex form;

$$Y^* = \frac{\left(C_{11}^{\,*} - C_{12}^{\,*}\right)\left(2C_{12}^{\,*} + C_{11}^{\,*}\right)}{C_{12}^{\,*} + C_{11}^{\,*}} \qquad \textbf{6-23}$$

6.3 Results

The thickness measurements were taken throughout polymerisation and are plotted in Figure 6-4.

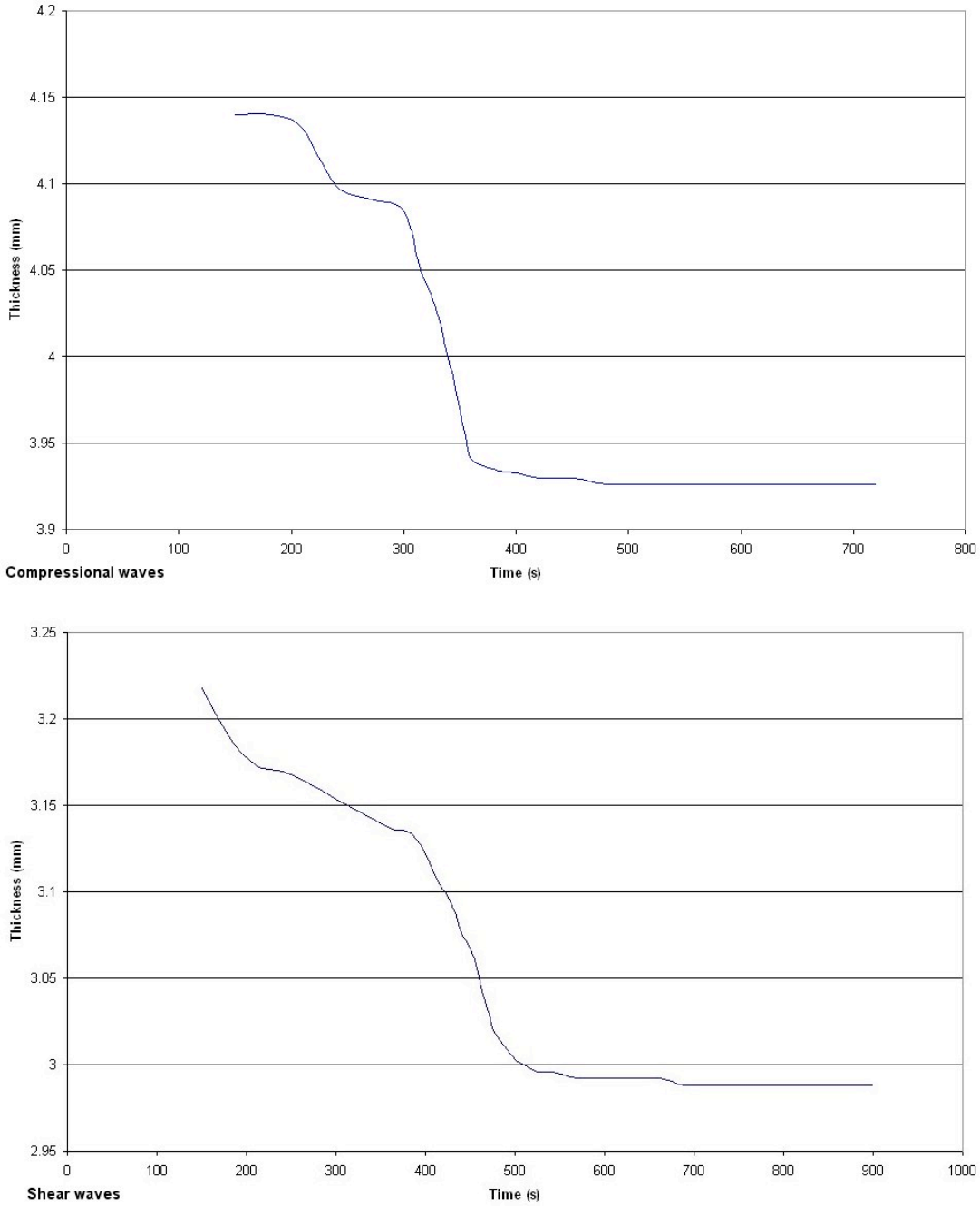

Figure 6-4 - Thickness over time for both compressive and shear wave tests measured using a micrometer during exsperiments.

Initially it was important to ensure that a change could be recorded during the polymerisation process and to ensure that all measurements could be taken and correlated.

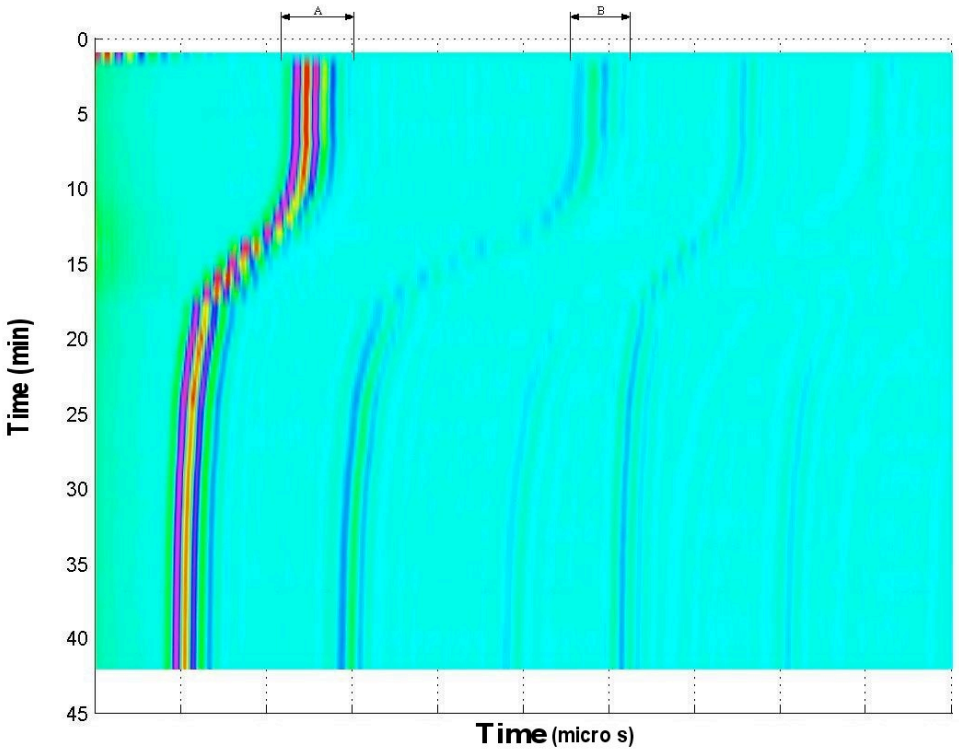

Figure 6-5 - Initial experimental data showing the recorded change in the ultrasonic signal during polymerisation. The vertical axis shows time from mixing of the cement, the horizontal axis shows propagation time for the signal, contour colours denote the amplitude of the signal with red denotinging a high peak and blue denoting a low trough.

Figure 6-5 shows a contour plot of the trace from an initial compressive test over time produced by collating all raw echo signals (such as Figure 6-6) taken throughout the experiment into one contour plot. The y-axis shows the time from mixing the cement and the x-axis shows the time taken for the signal to travel through the material and return back to the transducer. The bands of colour mark a peak or trough in the received signal. In this way the progress of an individual echo during the polymerisation process can be followed. Although velocity is the most obvious feature to monitor using this method it is also possible to qualitatively monitor the strength of an echo by looking at the colour of the contour. Two echoes (*A* and *B*) can be seen clearly throughout the experiment. The increase in separation of echoes *A* and

B indicates a change in the velocity of the ultrasonic wave and the change in colour of the echoes indicates a change in signal strength, both effects being due to changes in the attenuation properties of the material.

6.3.1 Compressive Wave Results

Figure 6-6 shows the last captured trace for the compressive wave experiment taken at 720s. The signal was scaled according to the attenuation settings of the pulser/receiver. This scaling ensured that all signals were on the same scale as the echo from an air backed piece of polyethylene (*A'*). The trace was separated into components *A* and *B*.

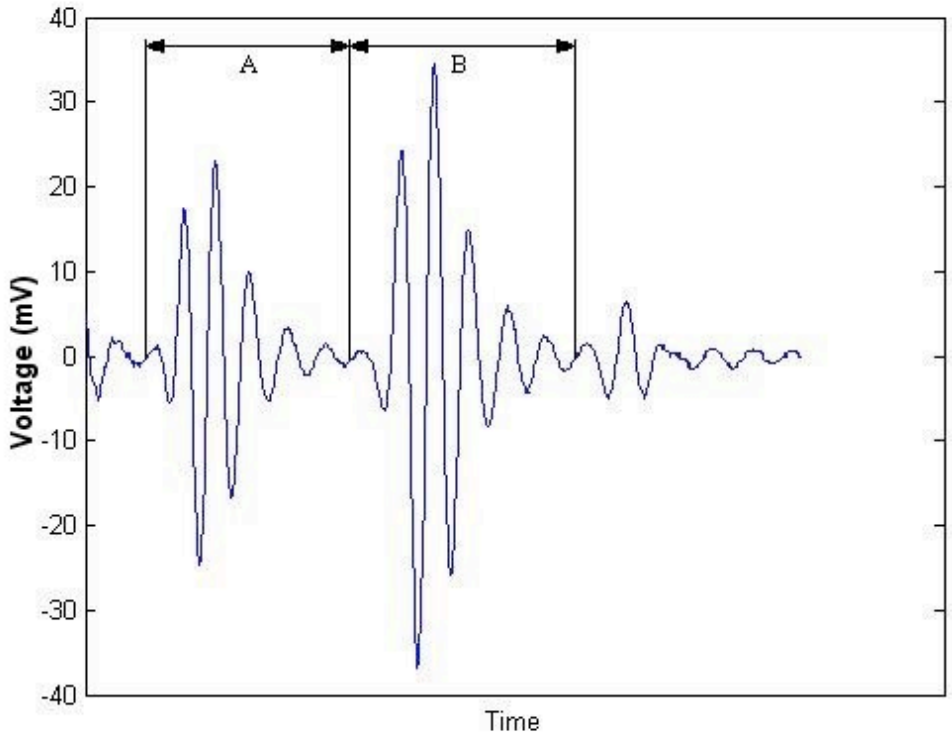

Figure 6-6 - Raw signal taken at 720s from compressive wave experiment.

The similarity of regions *A* and *B* of Figure 6-6 shows that the first and second echoes were in phase and little acoustic dispersion was present. Therefore velocity could be measured easily by measuring the time between corresponding peaks in the two

echoes. This gave the velocity at the centre frequency of the transducer to use as $v_2(\omega_0)$.

The Fourier transform of the two waves can be seen in Figure 6-7. The range of useful frequencies is marked on this plot. The lower bound results from the integral for the velocity calculation being taken from the centre frequency of the transducer and the upper bound from the need to eliminate greatly increased errors at very high frequencies.

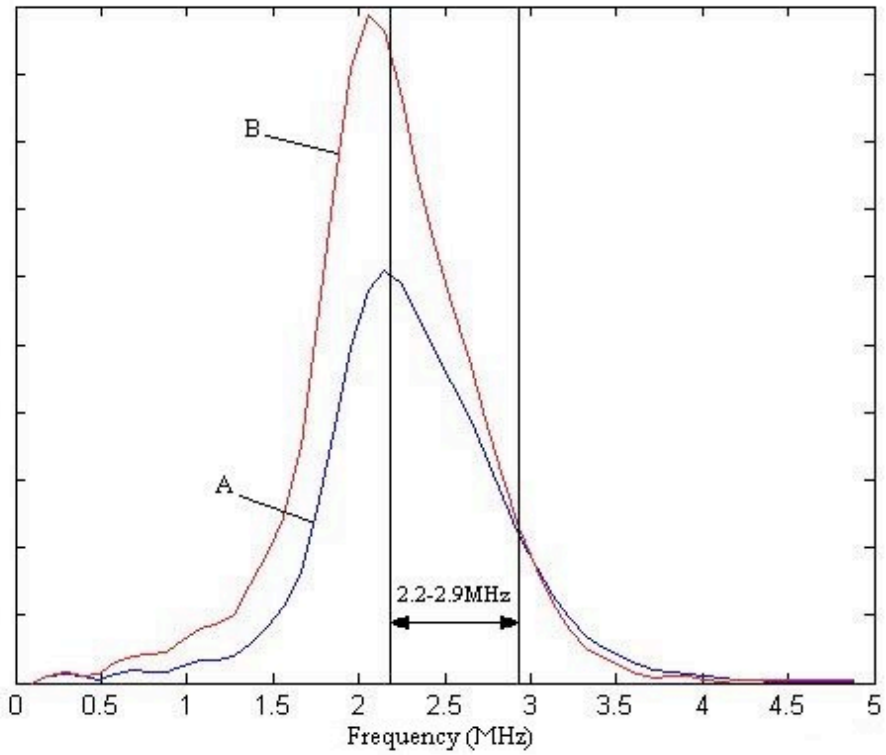

Figure 6-7 - Fourier spectra of both the first (A) and second (B) compressive wave echoes at the end of polymerisation.

By using the Fourier spectra of both the first echo (*A*) and the echo from air backed polyethylene (*A'*) the reflection coefficient at the polyethylene/PMMA interface was calculated. The reflection coefficient as a function of frequency is plotted in Figure 6-8. Although an increase in the reflection coefficient with frequency is observed, significant deviations from linearity are present. This may be as a result of electrical

noise within the system or acoustic noise from an external source since it is very difficult to completely acoustically isolate the equipment during the test.

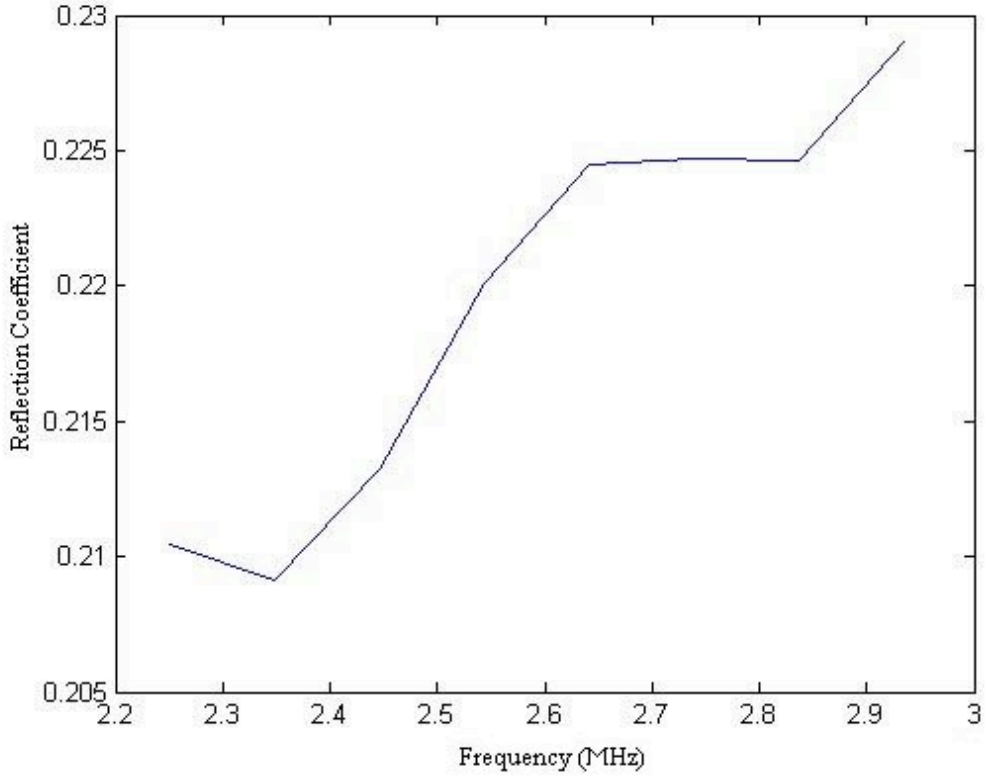

Figure 6-8 - Reflection coefficient at the polyethylene PMMA interface at the end of polymerisation.

The non-linearities shown in Figure 6-8 are also carried forward into the impedance calculation for PMMA (impedance plotted against frequency in Figure 6-9) and the calculation of the reflection coefficient at the PMMA/steel interface (Figure 6-10.). The reflection coefficient at the PMMA/steel interface was calculated from the relationship between the two materials impedances (equation 3-11).

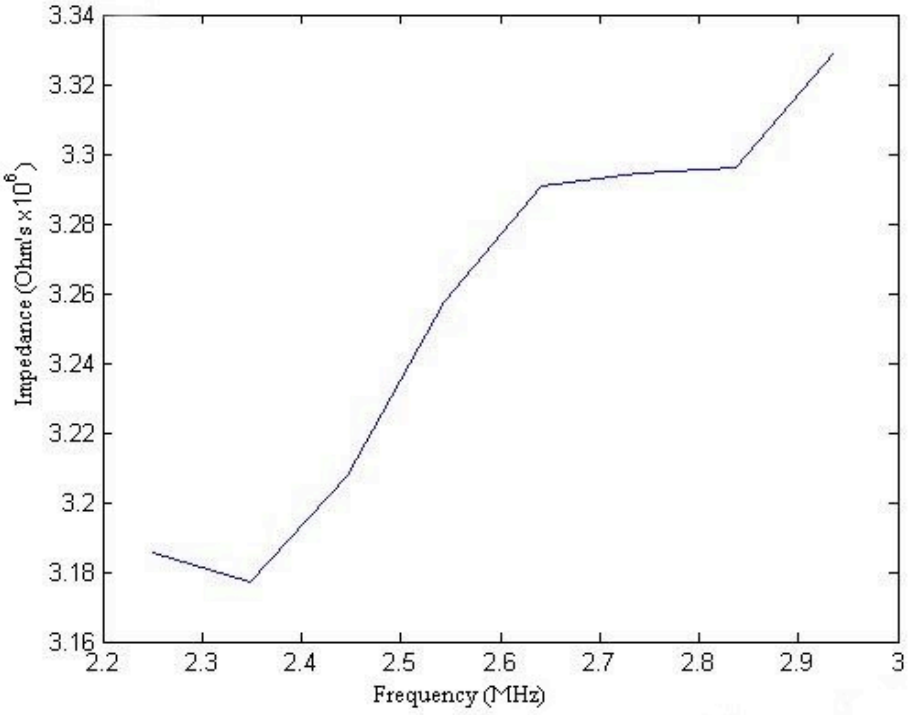

Figure 6-9 - Compressive wave impedance of PMMA at the end of polymerisation.

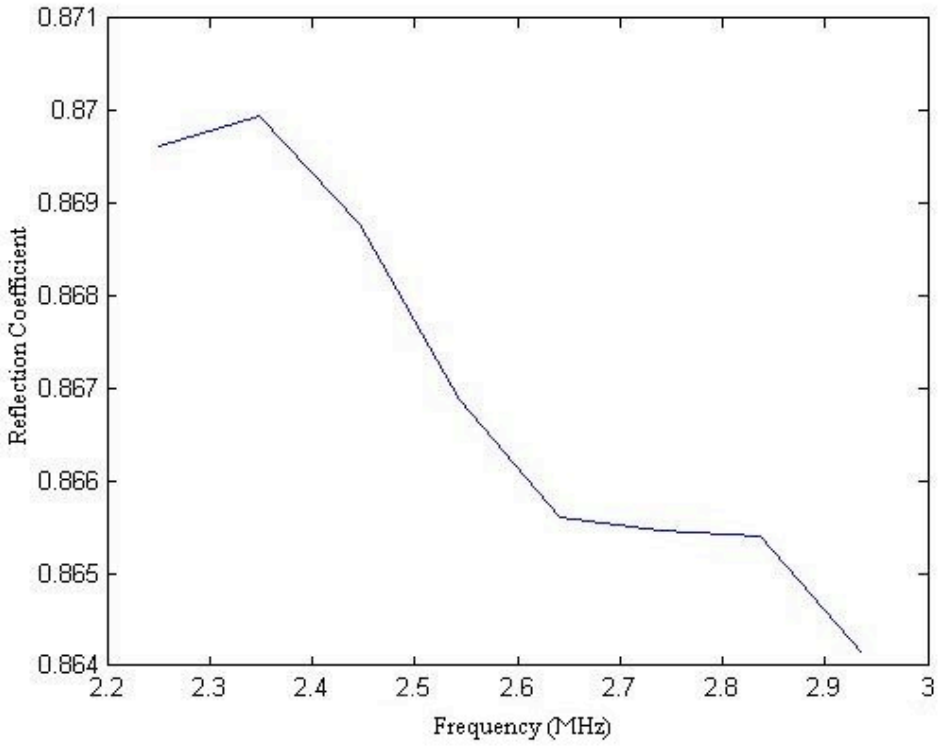

Figure 6-10 - Reflection coefficient at the PMMA/steel interface at the end of polymerisation.

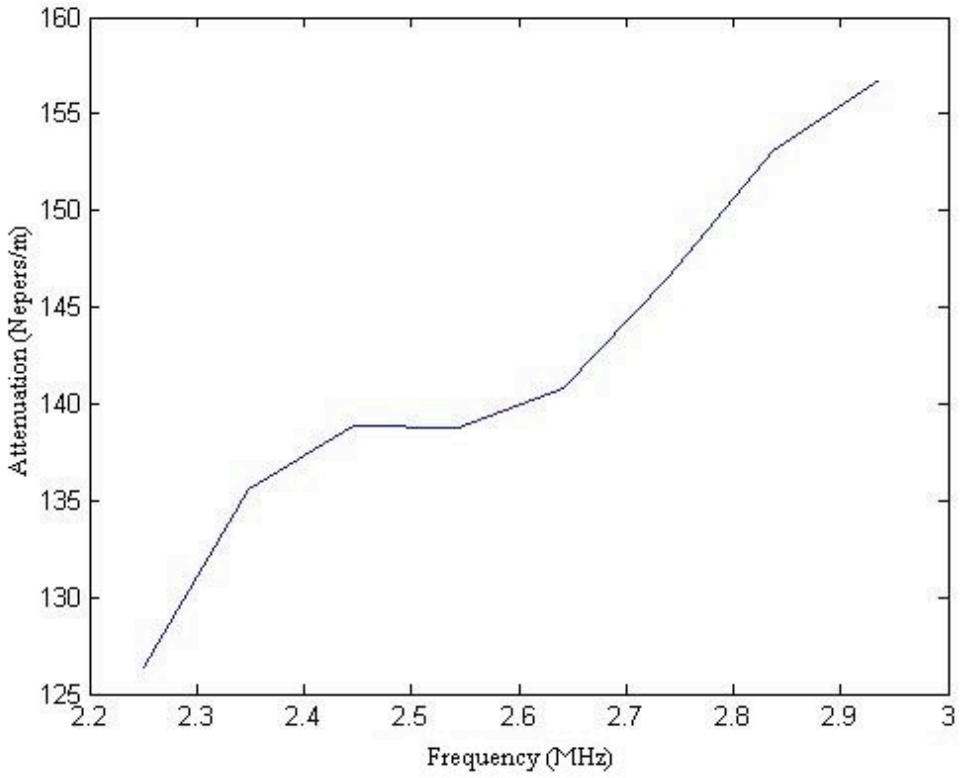

Figure 6-11 - Compressive wave attenuation as a function of frequency at the end of polymerisation.

Attenuation should increase with frequency as shown in the study by Wu [128]. Figure 6-11 shows that the calculated attenuation agrees with this theory.

Velocity was calculated using the Kramers-Kronig technique and is shown in Figure 6-12.

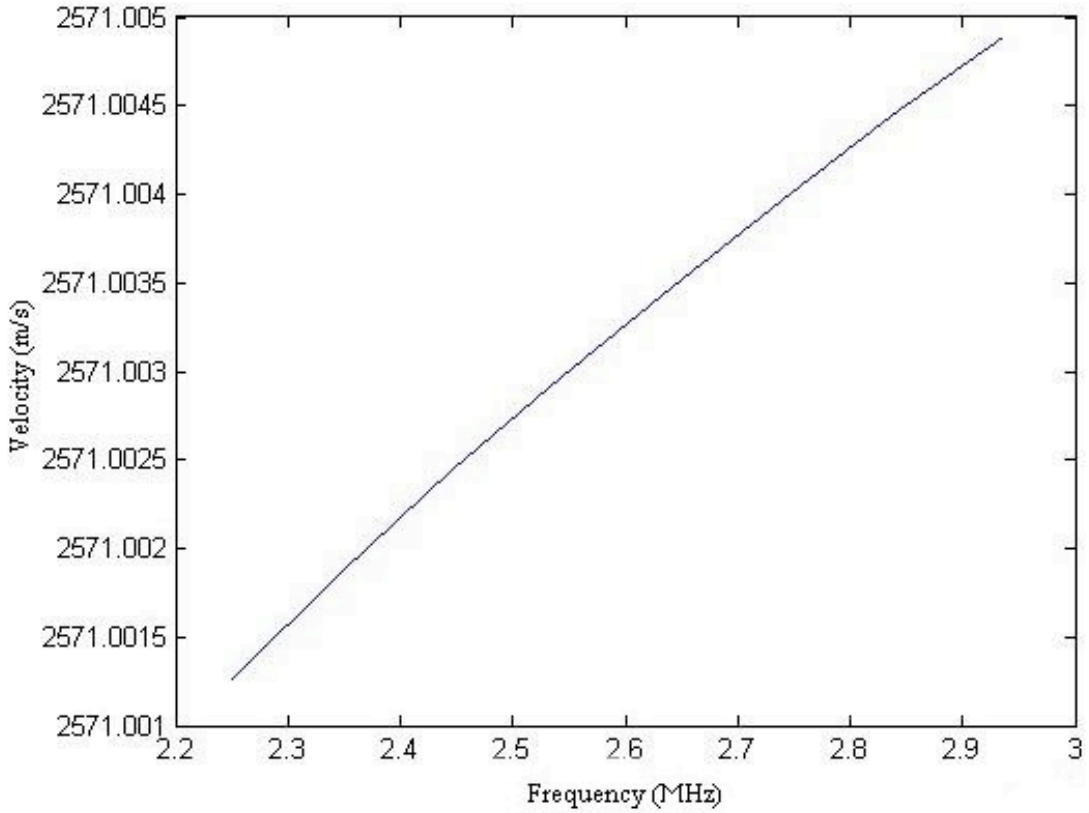

Figure 6-12 - Sonic velocity through bone cement at the end of polymerisation.

The density of the bone cement was then calculated from the velocity and the impedance as a function of frequency, Figure 6-13.

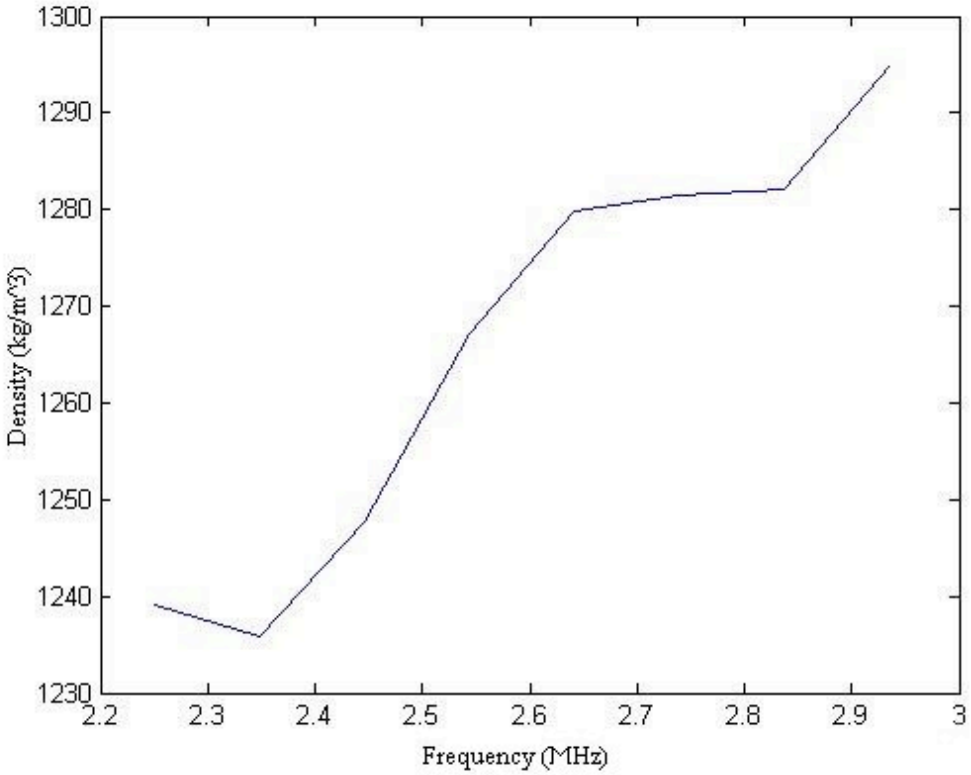

Figure 6-13 - Density of bone cement at the end of polymerisation.

The density of the bone cement should be a constant value with frequency and although this is not seen in Figure 6-13, the variation over this frequency range is less than 5%. The average over the frequency range considered was 1268kg/m^3. Values quoted in the literature for this type of bone cement range from 1180-1193kgm^3[7, 43]. The average value calculated in this time instant is 7% different from the average value determined from published results.

Similar analyses were performed on the results obtained at successive time intervals and a surface was plotted from the resulting series of curves. In Figure 6-14 the attenuation can be seen to reach a maximum at around 330s. At this moment the attenuation dispersion is also at a maximum and is greatly reduced later in polymerisation.

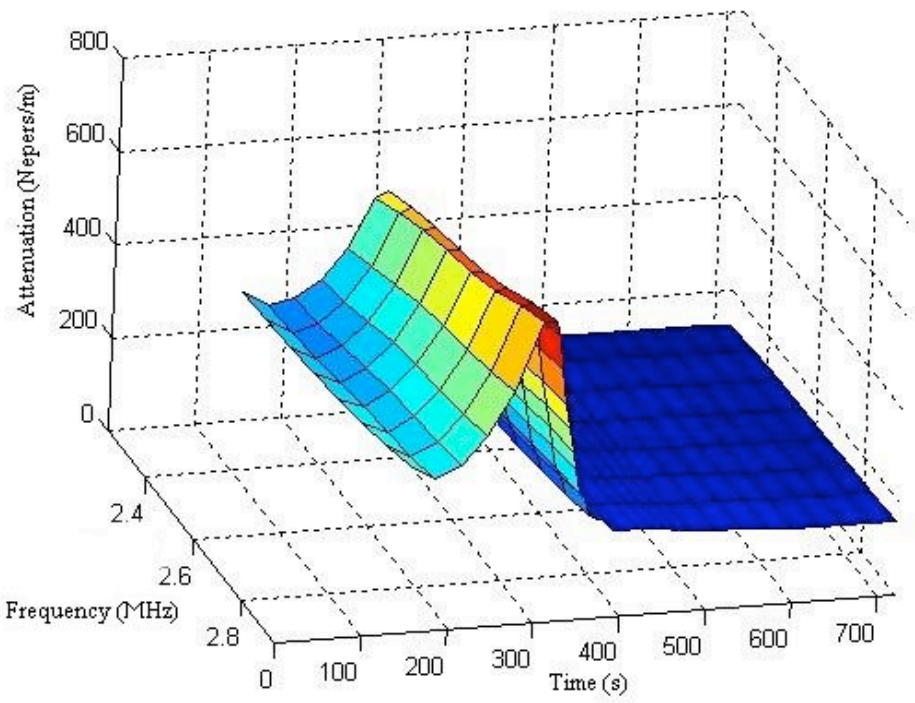

Figure 6-14 - Compressive wave attenuation through bone cement over time during polymerisation.

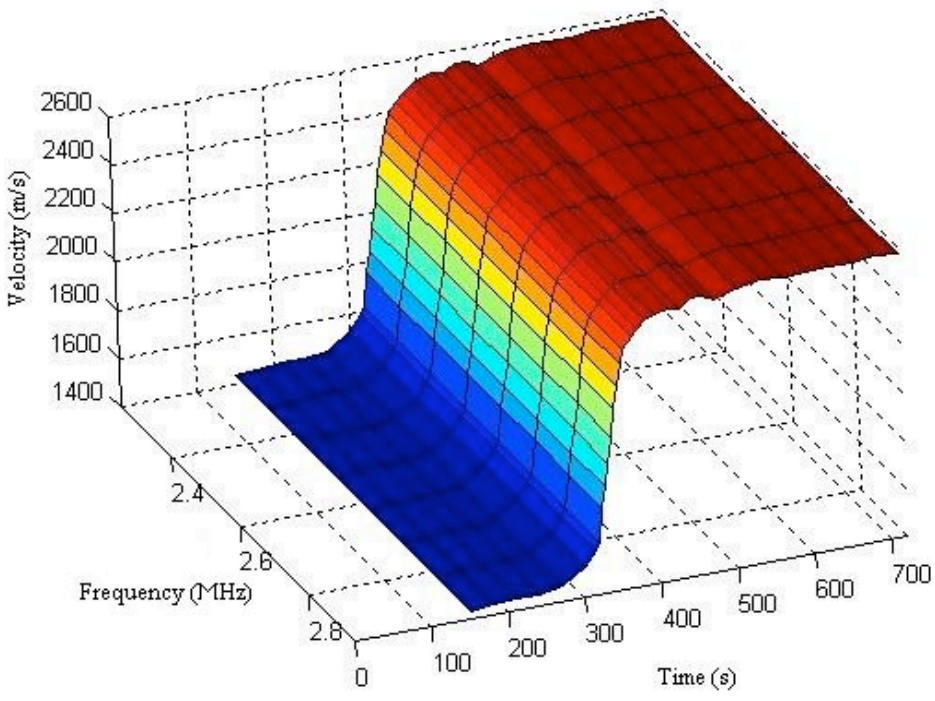

Figure 6-15 - Compressive wave velocity through bone cement during polymerisation.

From Figure 6-15 the velocity can be seen to undergo a rapid increase during polymerisation. This trend is expected as velocity is related to both stiffness and density and will increase with increases in either.

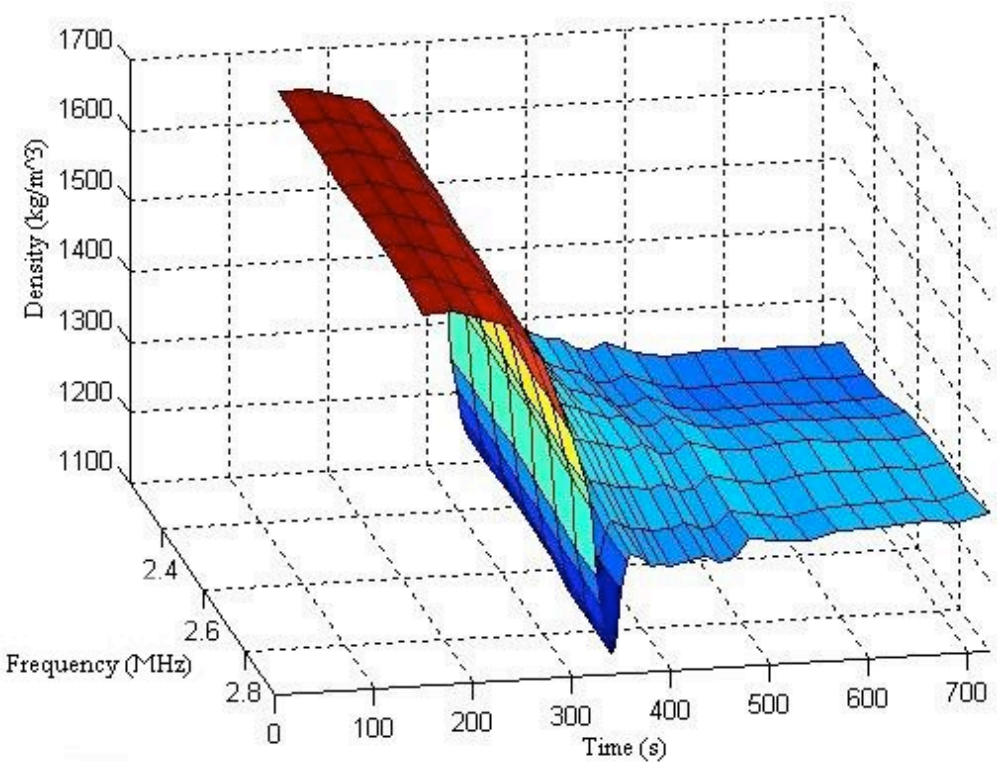

Figure 6-16 - Density of bone cement during polymerisation measured using compressive wave.

Figure 6-16 shows the calculated changes in density during polymerisation. The previous literature shows a tendency for an overall density increase and therefore a shrinkage at completion of polymerisation. Although the thickness measurements show a decrease during polymerisation (Figure 6-4), the calculated density shows a decrease from the start of polymerisation to the finish. There is also a minimum value shown to correspond in time with the rapid increase in velocity and the maximum attenuation during polymerisation.

6.3.2 Shear Wave Results

Similarly to the compressive wave results the results at the end of polymerisation were examined initially. The last trace was recorded at 900s in the shear wave experiment and is shown in Figure 6-17. The two echoes (*A* and *B*) can be easily identified and are in phase at this point. The two echoes are a slightly different shape however and this shows that there is dispersion and attenuation occurring within the bone cement. A similar series of calculations as for the compressive wave results was performed, the results are shown in Figure 6-18-Figure 6-22.

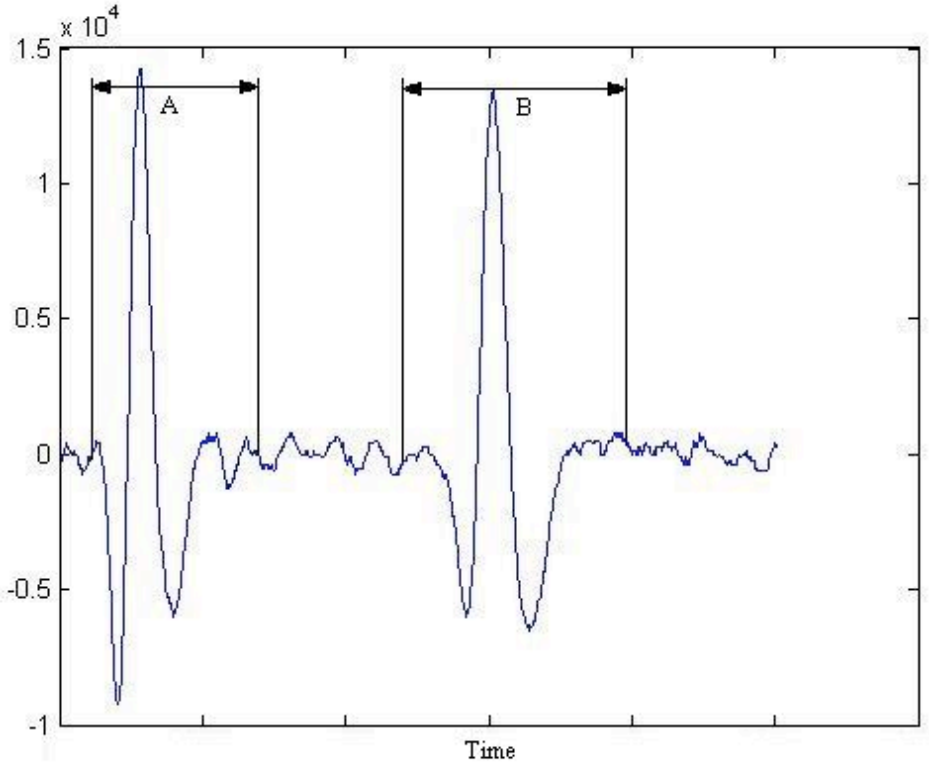

Figure 6-17 - Raw signal taken at 900s into shear wave experiment.

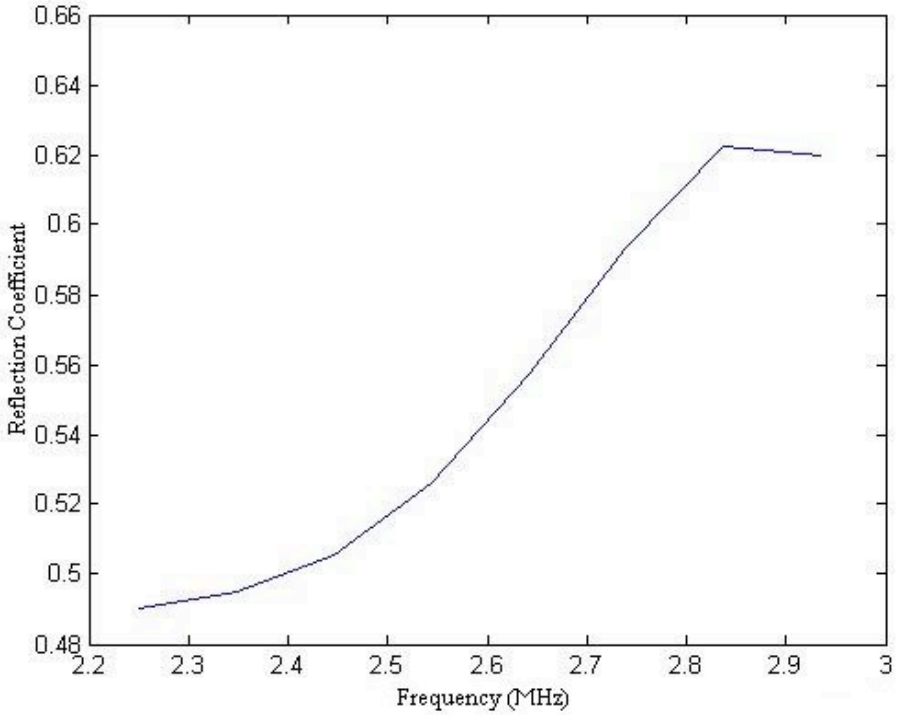

Figure 6-18 - Shear wave reflection coefficient from the polyethylene/bone cement interface at the end of polymerisation.

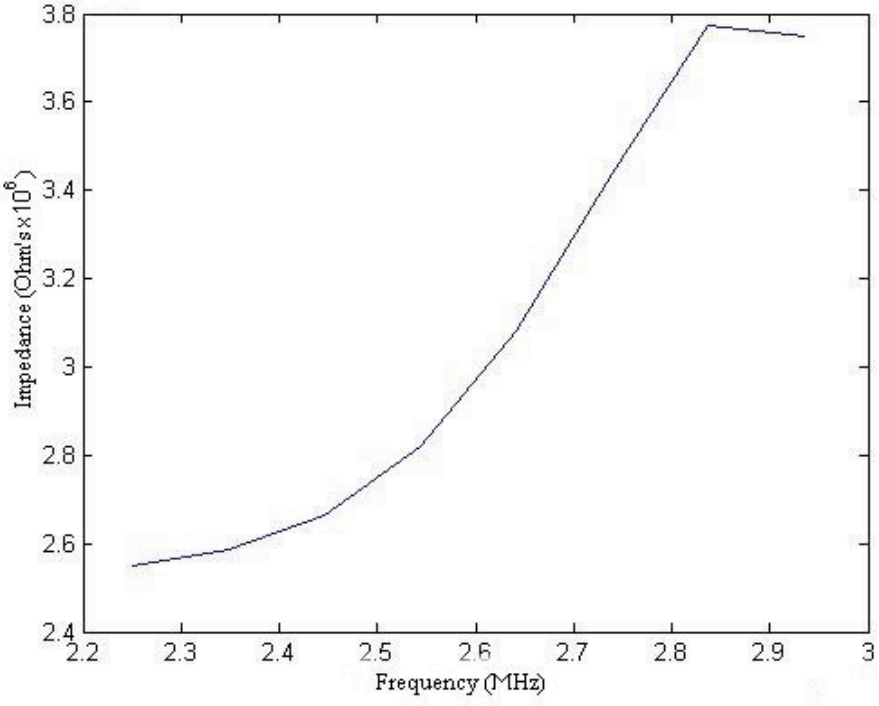

Figure 6-19 - Shear wave impedance of bone cement at the end of polymerisation.

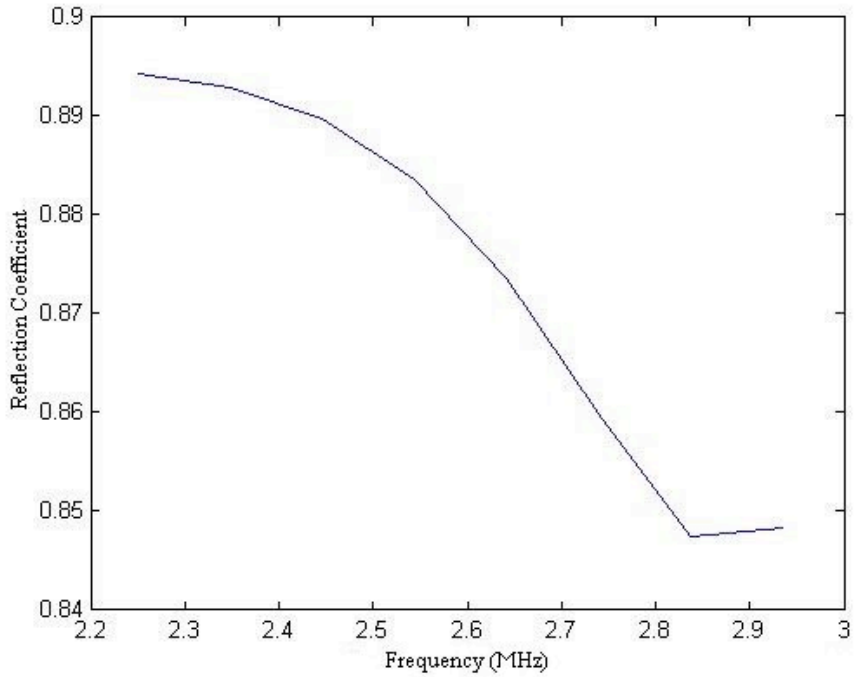

Figure 6-20 - Shear wave reflection coefficient from the bone cement/steel interface at the end of polymerisation.

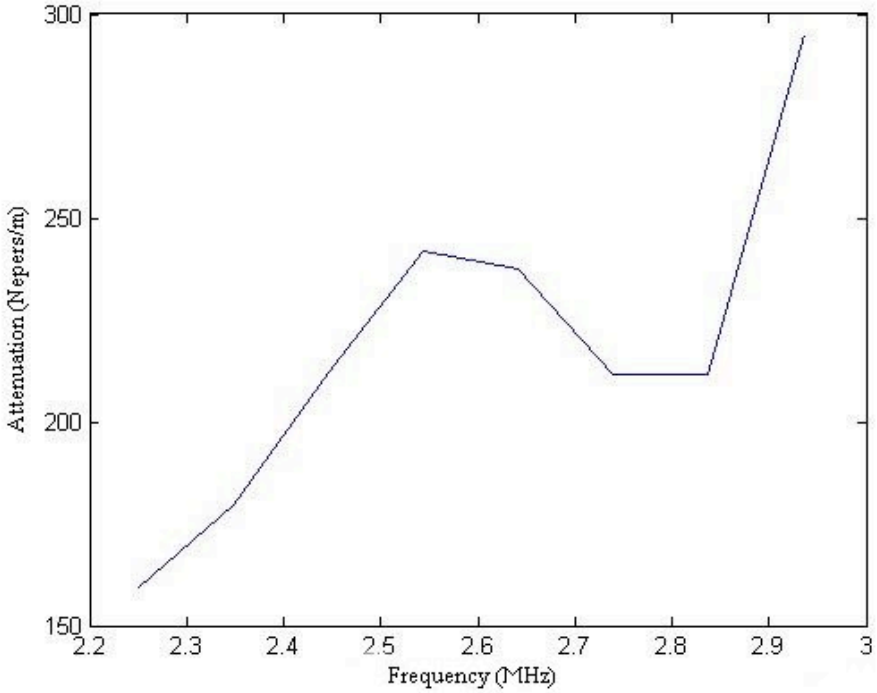

Figure 6-21 - Shear wave attenuation through bone cement at the end of polymerisation.

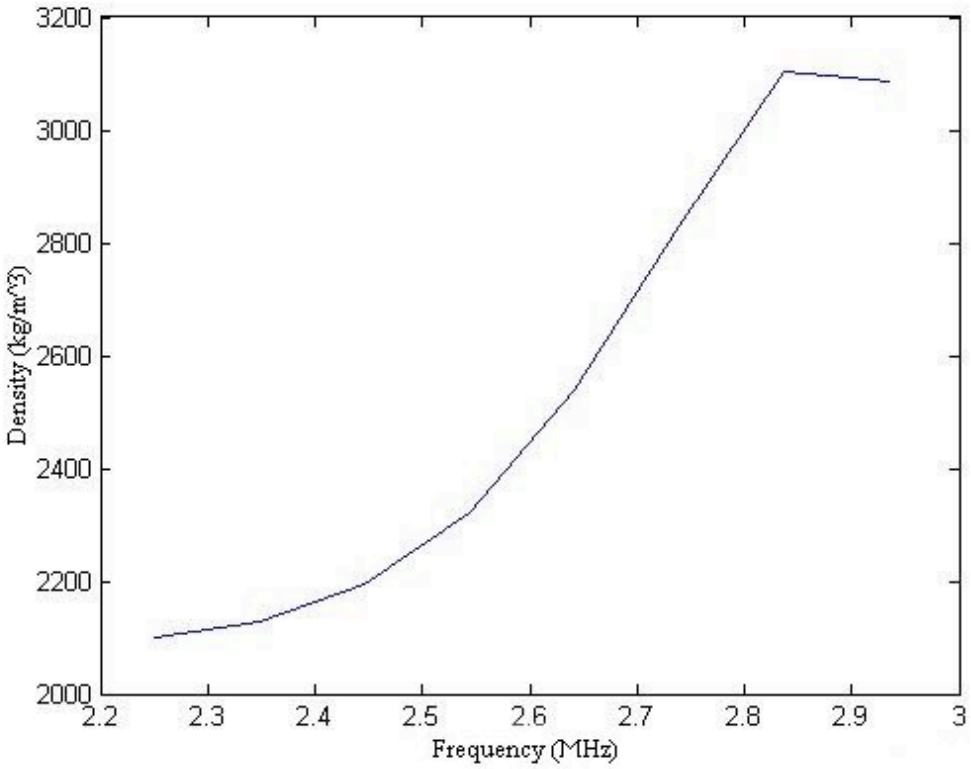

Figure 6-22 - Density measured using shear waves at the end of polymerisation.

As shown in Figure 6-18 to Figure 6-20, the curves for the impedance and reflection coefficients give smooth curves with similar trends to the compressive wave results. However, attenuation does not conform to the expected trend of increasing smoothly with frequency (Figure 6-21). Although similar curve shapes are shown with density as a function of frequency for both compressive and shear results, there is a large change with frequency during the period of rapid polymerisation. The densities derived from the shear wave experiment are also larger than expected and different to both those quoted in the literature and those calculated using the compressive wave experiment.

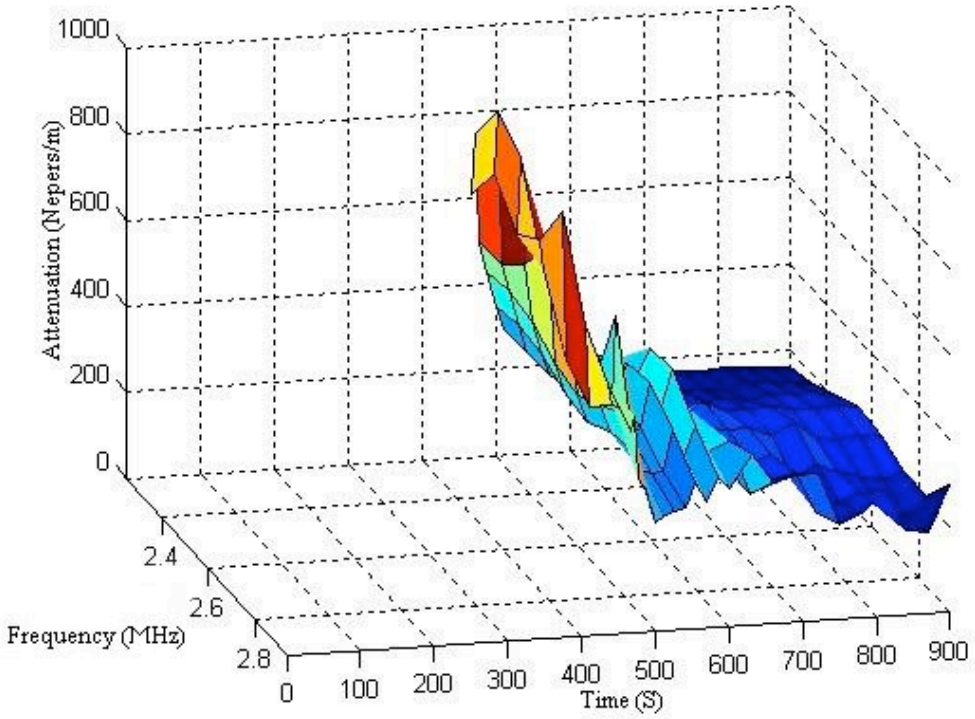

Figure 6-23 - Shear wave attenuation during polymerisation of bone cement.

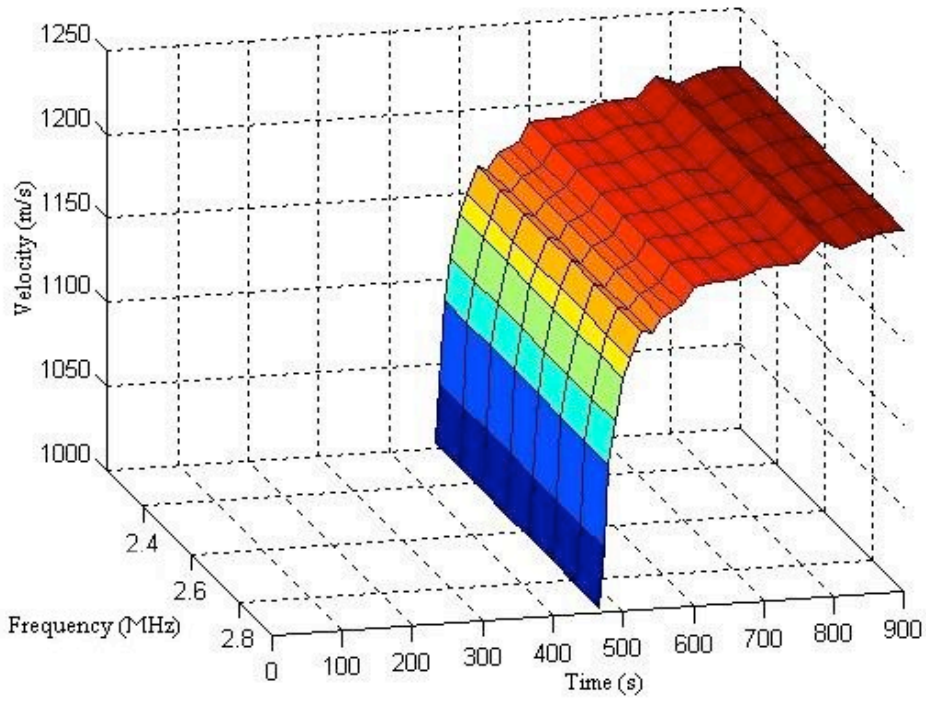

Figure 6-24 - Shear wave velocity through bone cement during polymerisation.

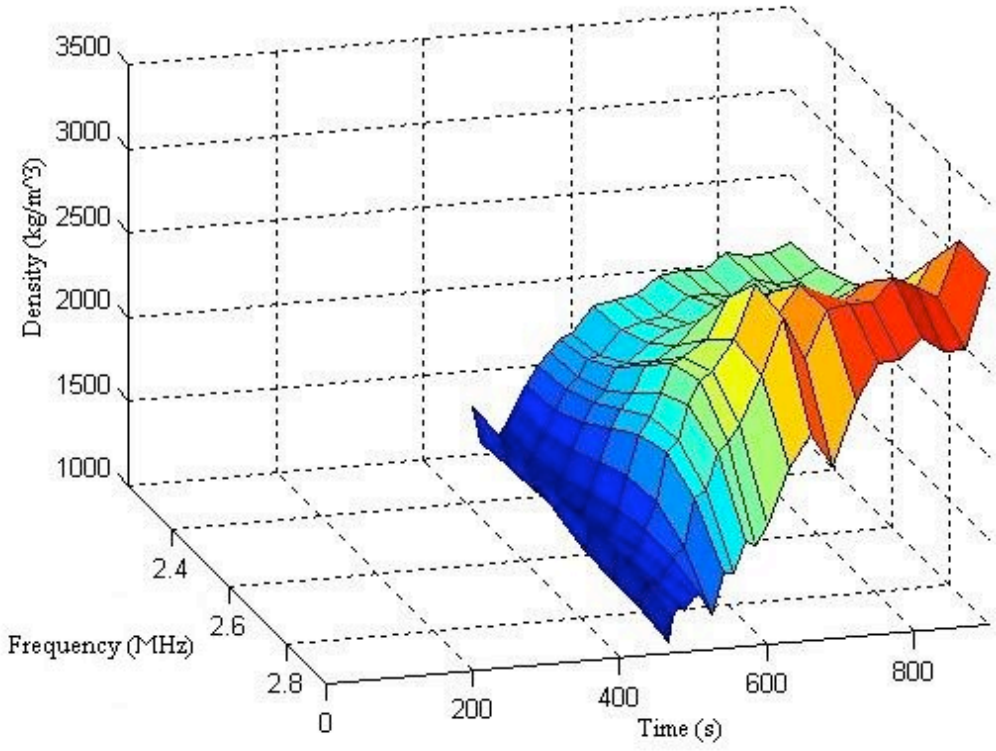

Figure 6-25 - Density calculated from shear wave experiment during polymerisation of bone cement.

Prior to a measurement taken at 466s into the shear wave experiment, attenuation was so high that the signal from the bone cement/steel interface was not discernable from the raw signal. This is to be expected since in a fluid a shear wave cannot be supported and so will not propagate through the polymerising bone cement. For this reason it is not possible to calculate attenuation, velocity or density at these early stages of the reaction.

Attenuation was seen to decrease from start to finish of polymerisation (Figure 6-23). This decrease in attenuation is expected as the material increases in stiffness and viscosity and so becomes able to support a shear wave. The velocity increases towards the completion of polymerisation (Figure 6-24). This is expected as the material increases in stiffness and density. The density calculated from the shear wave

experiment increased towards the completion of polymerisation (Figure 6-25). This trend is reported in the literature [83], however the magnitudes calculated are greatly increased compared to those reported.

6.3.3 Moduli

The experiments of both shear and compressive waves could not be directly combined since they were taken from different samples which may have polymerised at different rates. The samples were of differing thickness - the thicker sample (from the compressive wave experiment) would have been expected to produce more heat and hence polymerise faster. This is evident from the results already examined. The compressive sample was approximately 1mm thicker than the shear sample and it can be seen that the rapid changes taking place during polymerisation in all calculated parameters took place slightly earlier in the compressive experiment than in the shear experiment.

The results from the two samples were correlated using two separate thermal models of the experiments. The models (described in Chapter 4 - Thermal Modelling of Bone Cement Cure) generated curves for the degree of polymerisation as a function of time. By comparing the degree of polymerisation curves generated for the two different sample thicknesses it was possible to rescale the time axis of the shear experimental results with an ‘equivalent time’.

Where the ‘equivalent time’ did not coincide with one of the discrete experimental measurements, linear interpolation of adjacent results was performed. The results at this ‘equivalent time’ were then used in combination with the corresponding results from the compressive experiment.

To ensure that the model was valid for the experiments, a thermocouple was used to record the temperature during the experiment. This was compared to the temperature calculated during modelling of the experimental situation. The difference between the two peak temperatures was only 0.04ºC and the timing of the peak temperature was different by approximately 20s (Figure 6-26). This difference in timing was consistent

in both models when compared to their respective experiments. This meant that the relative timing of the two degrees of polymerisation modelled could be assumed as consistent with the real world situation.

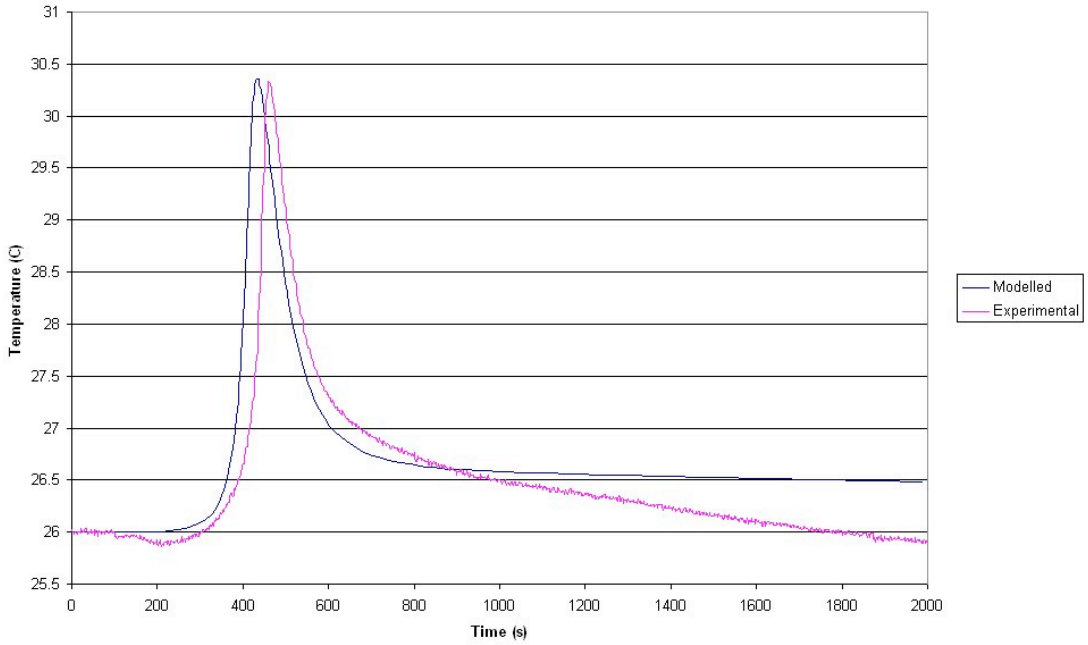

Figure 6-26 - Temperature modelled using finite element compared to temperature recorded during experimentation.

The compressive results were used to generate a complex modulus and this modulus (E_c*) is presented in Appendix III – Tables of results from Ultrasonic calculations, Table 1.

The real part of E* is shown in Figure 6-27. A steady increase in the compressive modulus was observed.

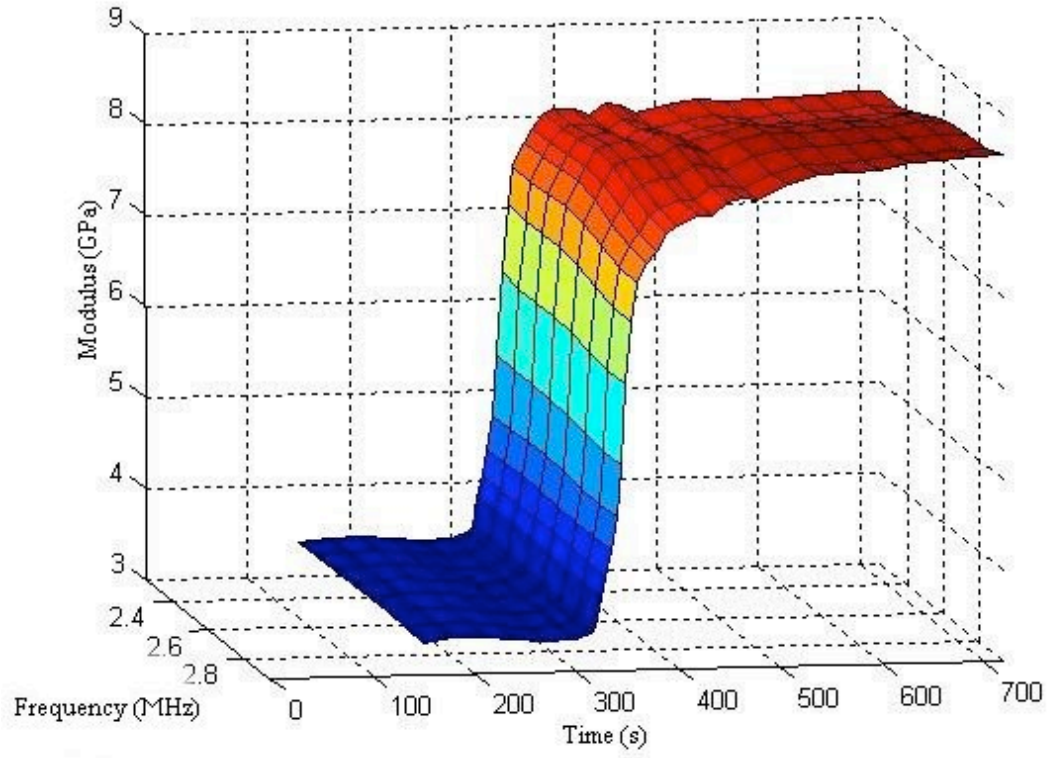

Figure 6-27 - Real part of compressive E* modulus (C_{11}).

The compressive modulus can be seen in Figure 6-27 to have increased throughout polymerisation to values of approximately $8.5x10^9$Pa at the end of polymerisation. The imaginary part (the loss part) is plotted in Figure 6-28 and again shows a consistent rise in the modulus throughout polymerisation. The path of the compressive loss modulus was somewhat noisier than that of the storage component. Also the timing of the rise was earlier in the loss modulus than in the storage modulus.

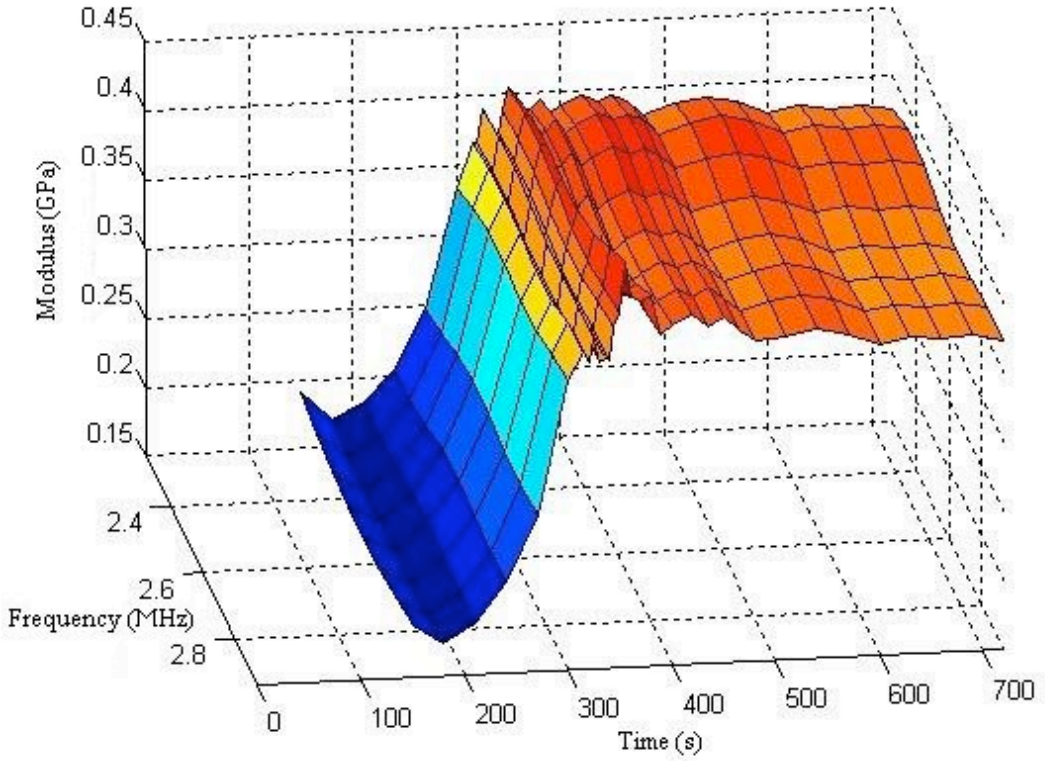

Figure 6-28 - Imaginary part of compressive E* modulus (C_{11}).

Similarly the complex shear modulus (G^* or C_{44}) was calculated and is tabulated in Appendix III – Tables of results from Ultrasonic calculations, Table 2. The plot of the real part of the shear modulus shows a rise occurring later than that of the compressive modulus (Figure 6-29). The plot of the imaginary part of the shear modulus shows a peak at about the same time as the rapid rise in the real component. This peak in the modulus would not be expected and may be simply an artefact of noise in the shear experiments.

The bulk modulus (K^*) was then plotted in a similar manner with the real and imaginary values separated (Figure 6-31 and Figure 6-32). The full values are presented in Appendix III – Tables of results from Ultrasonic calculations, Table 3. It may be noted that while at the beginning of the shear experiment no results could be obtained (since no shear wave could pass through the material), C_{44} is 0 and so, by equation 6-21, C_{11} is approximately equal to C_{12}. Therefore before shear readings can be taken K^* may be assumed to be equal to C_{11}^*.

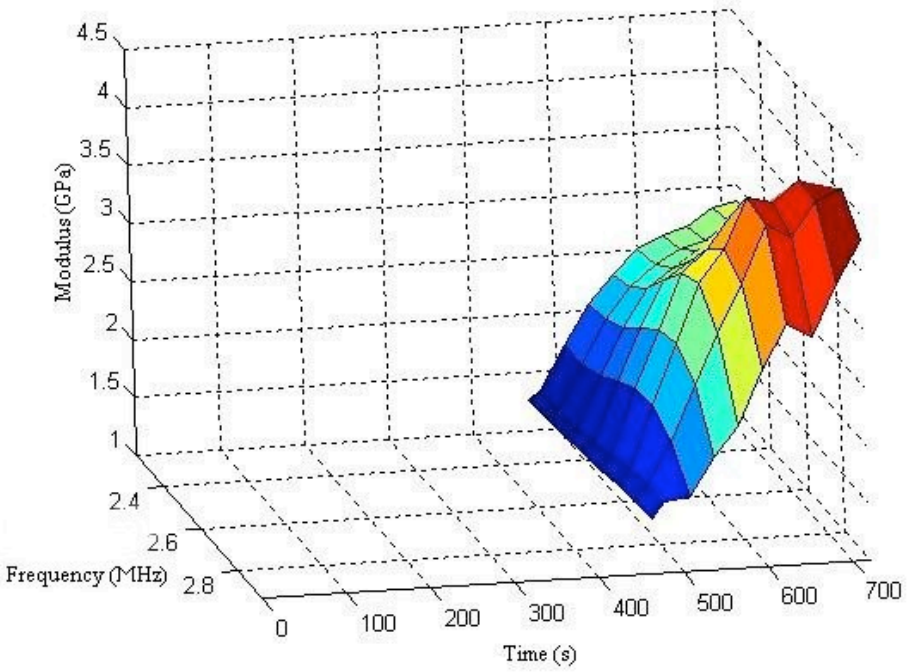

Figure 6-29 - Real component of shear modulus (C_{44}).

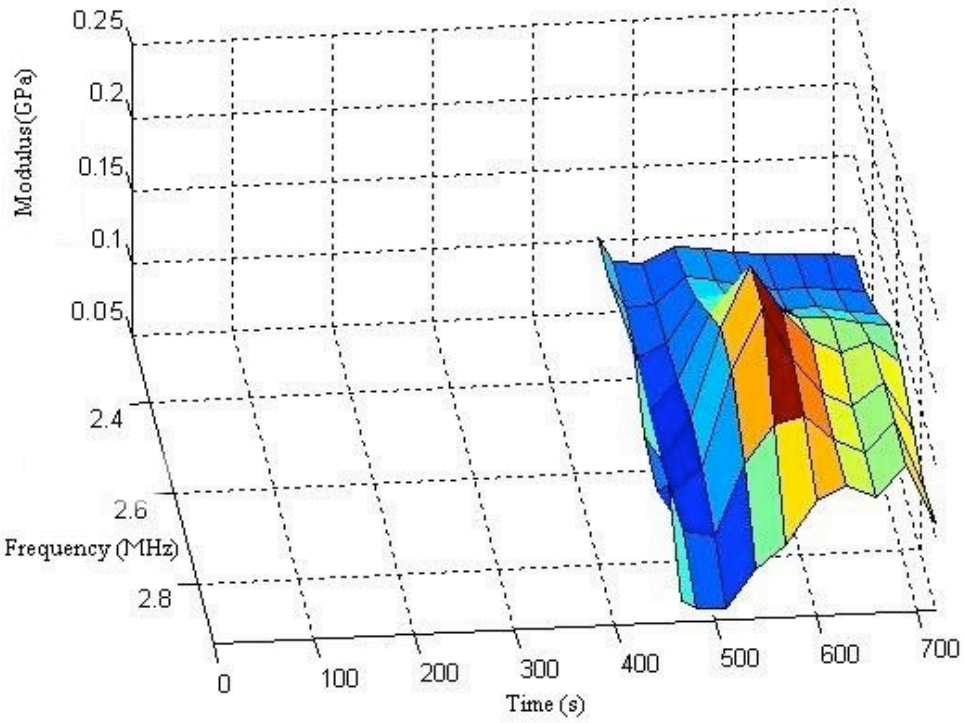

Figure 6-30 - Imaginary component of shear modulus (C_{44}).

The bulk modulus (K^*) shows the introduction of the shear modulus as a drop in the bulk modulus. Because the compressive modulus is already at a steady state, when the shear modulus is introduced, the bulk modulus must drop and subsequent increases in shear modulus will further reduce the bulk modulus.

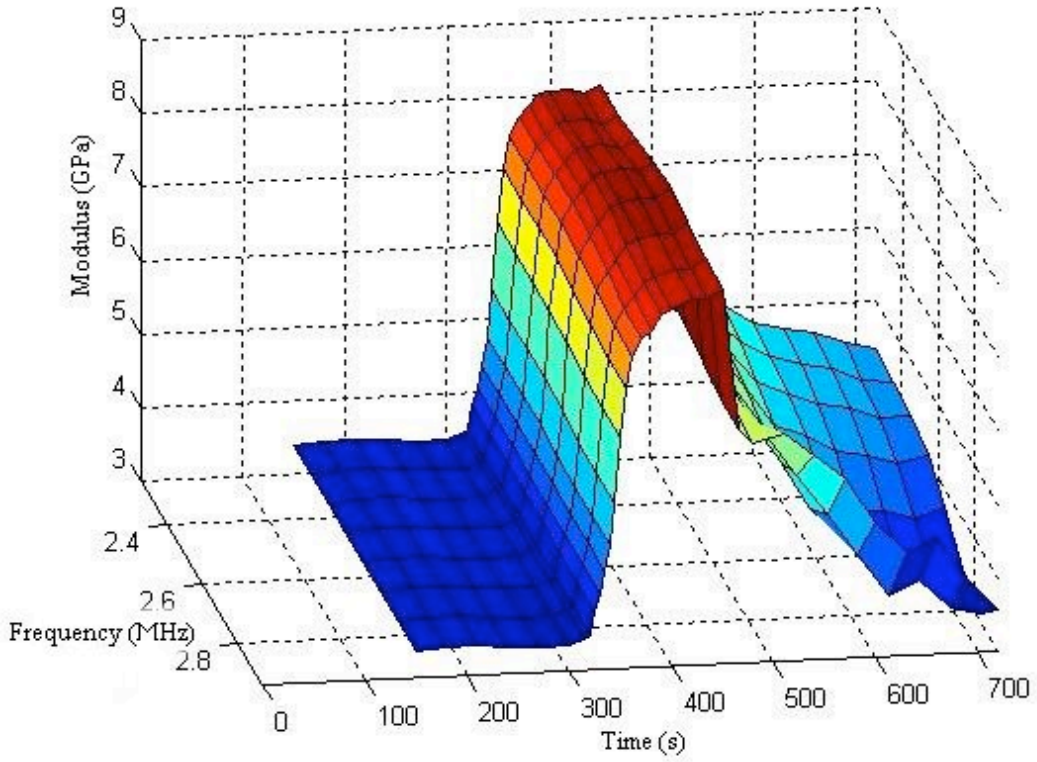

Figure 6-31 - Real component of the bulk modulus (K*) during polymerisation.

The same drop occurs in both the real and imaginary components of the bulk modulus as can be seen in Figure 6-31 and Figure 6-32.

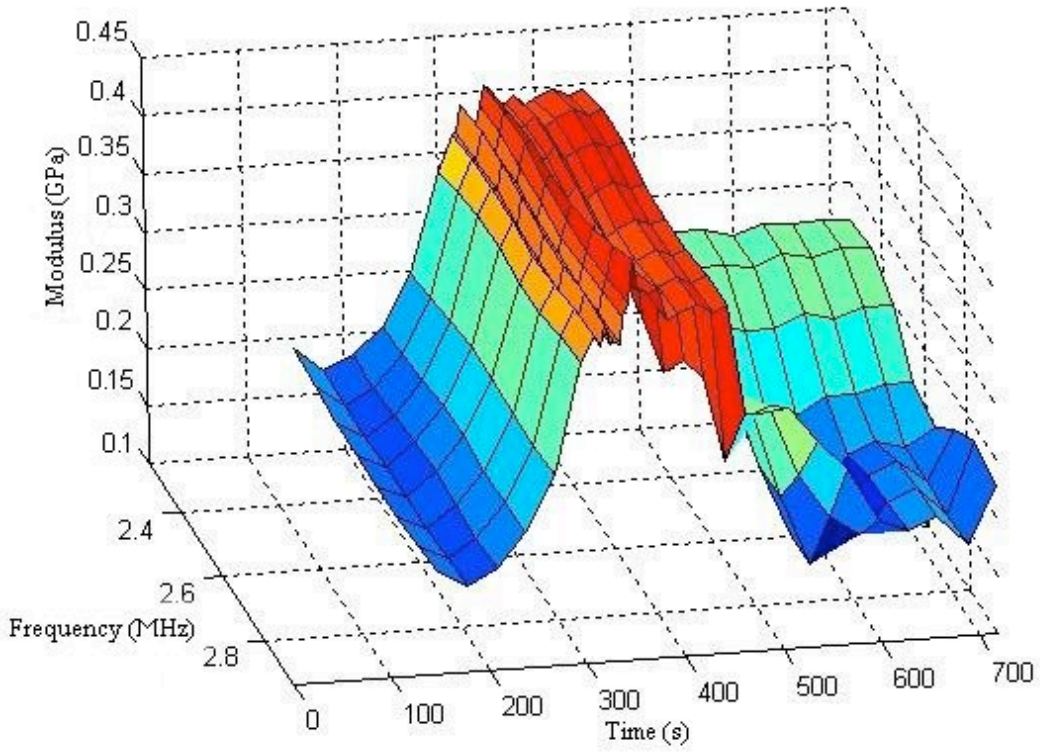

Figure 6-32 - Imaginary component of the bulk modulus during polymerisation.

Since there are no data for C_{44} at the beginning of the polymerisation process, C_{11} is equal to C_{12} and hence the Young's modulus is 0 during this period. When it was possible to retrieve data for the C_{44} value, the Young's modulus was calculated and showed a rise through the final stages of the experiment (Figure 6-33 and Figure 6-34).

The shape of the Young's modulus surface is similar to that of the shear modulus. This is to be expected since the compressive modulus is at a steady state and changes in the Young's modulus are solely due to changes in the shear modulus at this time.

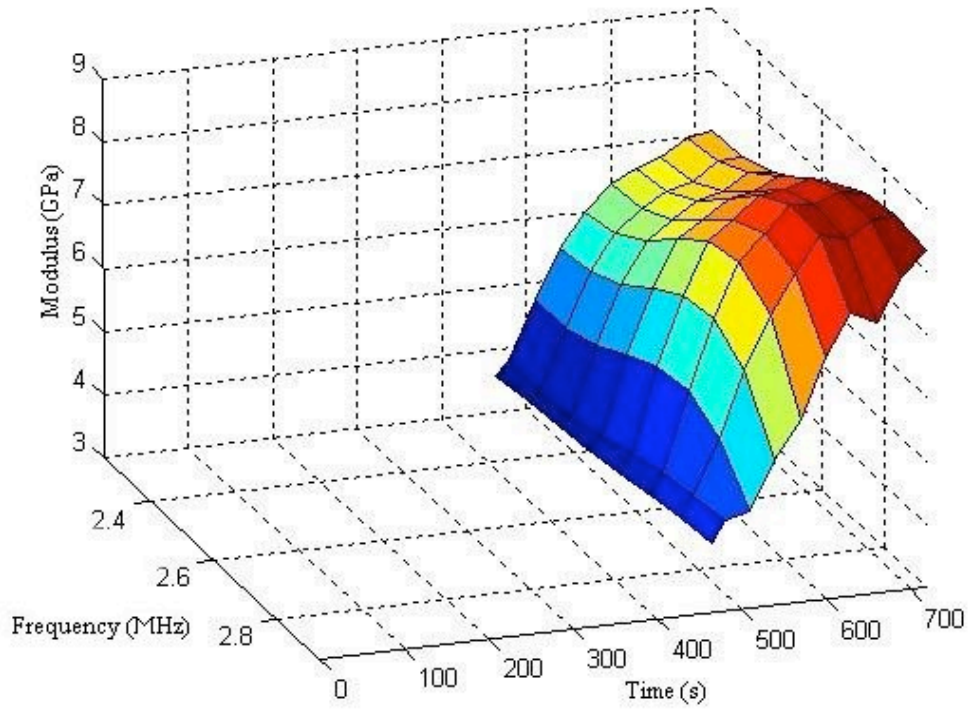

Figure 6-33 - Real component of the Young's modulus duringpolymerisation.

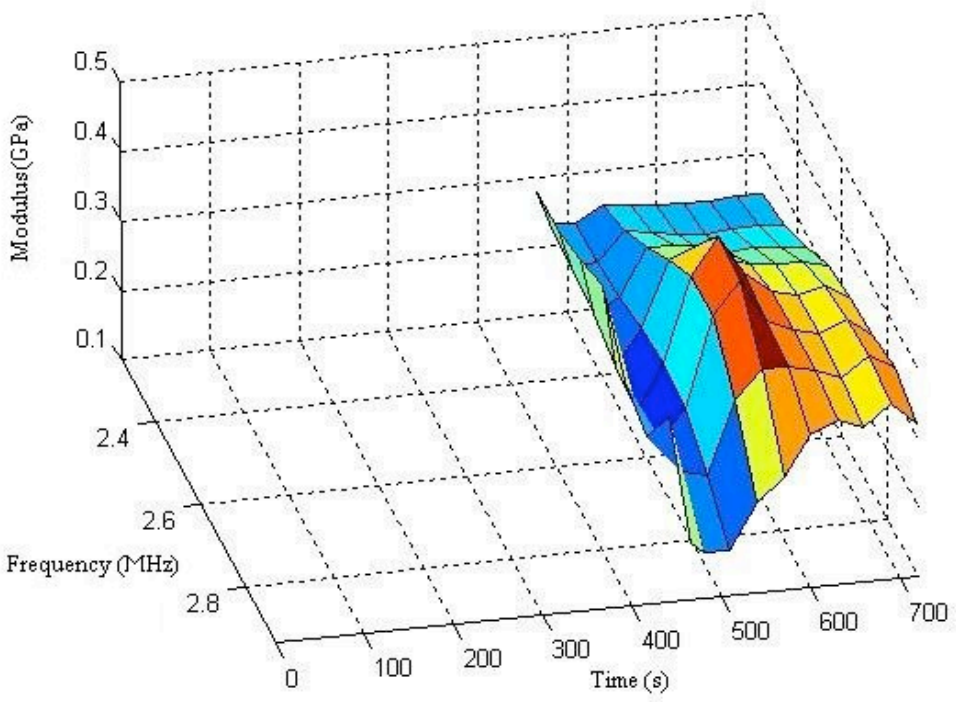

Figure 6-34 - Imaginary component of the Young's modulus during polymerisation.

At the end of polymerisation the static Young's modulus is reported in the literature at between 2 and 2.6GPa [61]. The Young's modulus was plotted against frequency and a straight line of best fit was calculated and used to extrapolate a static value for the real component of the Young's modulus. since Piché reported that density is proportional to the velocity and Wu showed that velocity is approximately proportional to frequency in our frequency range a straight line was a reasonable assumption for the young's modulus as a function of the frequency in polymers [94, 128]. The Y-intercept of our straight line was 1.74GPa.

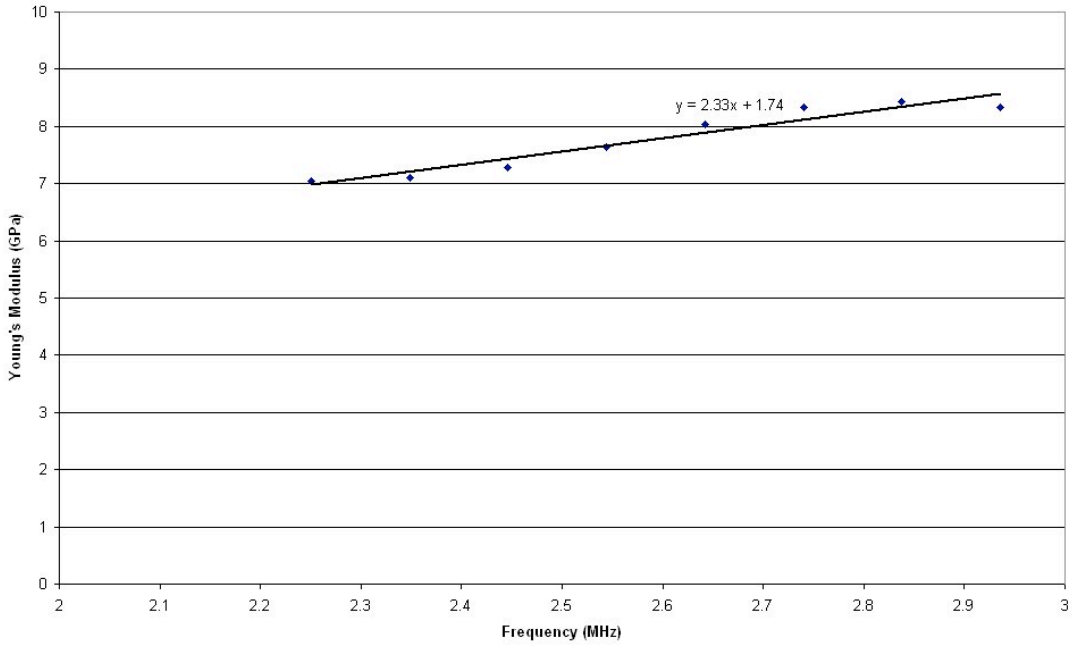

Figure 6-35 - Real component of Young's modulus at the end of polymerisation.

6.4 Discussion

The attenuation of the ultrasound beam by the cement in both the compressive and shear experiments showed an overall reduction throughout the polymerisation process. Attenuation is a measure of how much of the energy of the signal is lost as it passes through the material. Energy is most likely to be conserved in a stiff, dense material and so this increase in attenuation shows that it is possible to monitor some change in the material characteristics during polymerisation. The compressive experiment shows a prominent peak in the attenuation during the period of rapid polymerisation. This sudden increase in attenuation was not expected as it is known that the material is becoming denser and stiffer at this time. The timing of the increase in attenuation coincides with a rise in the temperature, so it may be possible that the rise in specimen temperature may be causing the increase in attenuation. Alternatively it may be explained by factors attributable to the polymerisation process itself. The polymerisation reaction requires some activation energy and while a very low energy ultrasonic wave was used it is possible that sufficient could have been absorbed in the polymerising cement to alter the reaction kinetics. The rise in the attenuation does not appear to have been caused by material property changes.

Further errors may have resulted from imperfect synchronisation between the results of the shear and compressive experiments. The two experiments were combined using data from models run separately. This method may not have sufficiently compensated for differences in the precise timing of polymerisation between the two experiments. This difference in timing between the two experiments may account for the drop in the bulk modulus after it has reached a peak. It would be expected that both the shear and compressive modulus would increase simultaneously and so the bulk modulus would exhibit a consistent increase during polymerisation.

The shear experiments provided no data until the second echo could be obtained and distinctly identified from the noise. This was expected since a fluid cannot support shear waves and the Young's modulus would be expected to tend towards 0Pa. The surface plot of the real part of the Young's modulus shows that towards the beginning

of the reaction the Young's modulus is certainly much lower than that at the end of the experiment.

The impedance of polyethylene (z_1) was obtained from the literature.

The noise seen in the shear experiments was, at times, comparable in size to the signal received. This made judging the start and end of the received echo very difficult, in the early stages of polymerisation. At the end of polymerisation it was very easy to distinguish the two signals and very clear that the two signals were in phase. During the polymerisation process a phase change took place in the signal from the polyethylene/bone cement interface and so at the beginning of the experiment the two signals in the compressive wave experiment were one half-wave out of phase. Therefore during the polymerisation process the signal undergoes a transition of phases. This combined with dispersion within the polyethylene caused the two echoes to look dissimilar (Figure 6-36) and so picking two peaks for measuring the time separation was very difficult and may have caused an error of up to one whole wavelength.

The errors discussed here seem to cause only a small error in the final Young's modulus value (approximately 0.5GPa). The trends displayed in most results were as expected and the timing of events during the experiments indicate the method is a promising tool for monitoring the polymerisation reaction. The results give an accurate prediction of the timing of the period of rapid polymerisation and good steady state values for the moduli of the material.

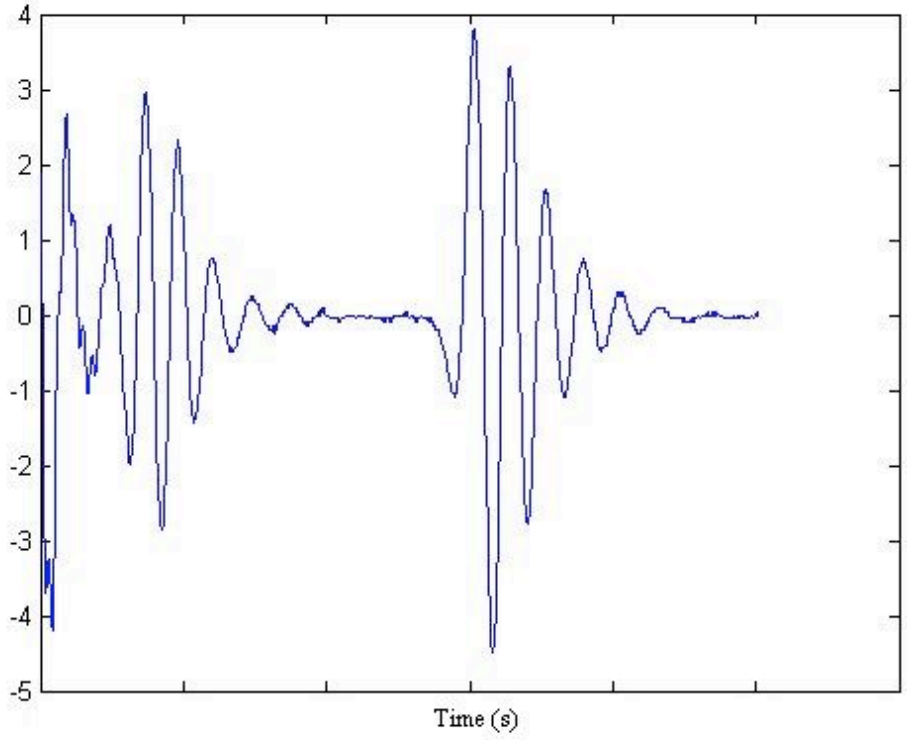

Figure 6-36 - Raw signal from compressive experiment in the middle of polymerisation.

The errors seen throughout the experiment were more apparent before and during the point at which the polymerisation reaction was proceeding fastest. This caused the values calculated for the density to be increasingly inaccurate toward the start of the compressive experiment. Since the density is equal to the quotient of impedance over velocity and the velocity at the start of the polymerisation process was lower (since velocity is higher in a stiffer material), it must then follow that impedance was lower at the start of the reaction. In the compressive experiment an initial impedance of approximately $2.35 \times 10^6 \Omega$ and a final impedance of approximately $3.26 \times 10^6 \Omega$ were calculated. The impedance at the end of the reaction was 1.4 times larger than the initial impedance which was not sufficiently low to offset the corresponding velocity change of a factor of 1.8 leading to an overall increase in density.

The final values obtained using this technique show correlations between the density found using the compressive wave test and the final calculated static Young's

modulus and published data. The errors discussed are not significant at this point during the polymerisation. Earlier during the experiment these errors appear to be magnified giving erroneous readings for the density and moduli. This magnification of errors may be due to a combination of the errors discussed. Since many of the errors introduced (such as those produced by noise in the signal) are difficult to quantify and there are no results for the moduli measured during the polymerisation in the literature, it is not possible to conclude which is the most important.

It would be very important in future experiments to develop a method to allow the simultaneous measurement for both shear and compressive waves. This would require two transducers, two pulser/receivers, two oscilloscopes and two computers to be used on one sample of curing cement and as such was not feasible for this study.

This study has established a technique for calculating all of the complex material properties in a polymer without making any prior assumptions about that sample. The results showed good agreement with published data for the Young's modulus of the final, steady state, polymerised material and the trends shown throughout the polymerisation show that the technique could be a valuable tool in the monitoring of materials whose properties are changing rapidly.

There are several sources of error involved in this technique, which must be investigated before relying on the results obtained, however the findings presented here show it is a feasible method. The method inputs very little energy into the system and so changes the reaction very little but is able to monitor several different variables simultaneously with little user intervention.

6.5 Ultrasonic Cure Monitoring Summary

- Ultrasound has been investigated in more detail than previous studies as a method for the determination of the mechanical properties of setting materials.
- During steady state conditions the measured properties are closer to expected values.
- Shear wave signals are more difficult to process due to the high shear attenuation when in the fluid state.
- During polymerisation the compressive signal goes through a pole change. During this period the first and second echo are more difficult to compare.
- The method developed can accurately monitor the polymerisation process and show the period of rapid polymerisation.
- With some further development the method will hopefully be able to accurately measure all complex moduli throughout the cure of many fast setting materials.

7 Tensile Cure Tests

During cure of vacuum mixed PMMA based bone cement there is typically a shrinkage of 2% linearly (8% volumetrically) [83]. When this shrinkage is constrained by the presence of an orthopaedic device residual stress in the cement mantle will result. The aim of the experiments described in this section was to determine the force generated by a curing cement mass of controlled dimensions. The problem of containing the cement mass in its initial fluid state was overcome by using a horizontally mounted tensile test rig. Load transfer between the cement and the rig was ensured by rigidly fixing acrylic plates (to which cement will chemically bond) to both the load cell and reaction face.

7.1 Materials and Methods

A schematic of the test set-up is shown in Figure 7-1. A 15mm x 15mm channel 50mm long was clamped to the test bed using legs used to raise its height. One end of the channel was blocked off using 3mm sheet acrylic bolted to the exterior. At the other end a piece of acrylic with a 15mm x 15mm square protrusion was bolted to the load cell and positioned so that the protruding face blocked off the channel. PVDC film (“clingfilm”) was used to line the channel to prevent mechanical bonding of the cement to the channel.

A data logger was connected to the horizontal load cell and recording was started at the start of mixing of the bone cement components. Immediately after mixing, the cement was injected into the channel, ensuring good contact with both acrylic ends. Load was recorded at a sampling frequency of 1Hz for approximately 2000s.

At the end of cement cure, an *in situ* tensile test was performed to test the bond strength at the interface between the acrylic plates and the bone cement.

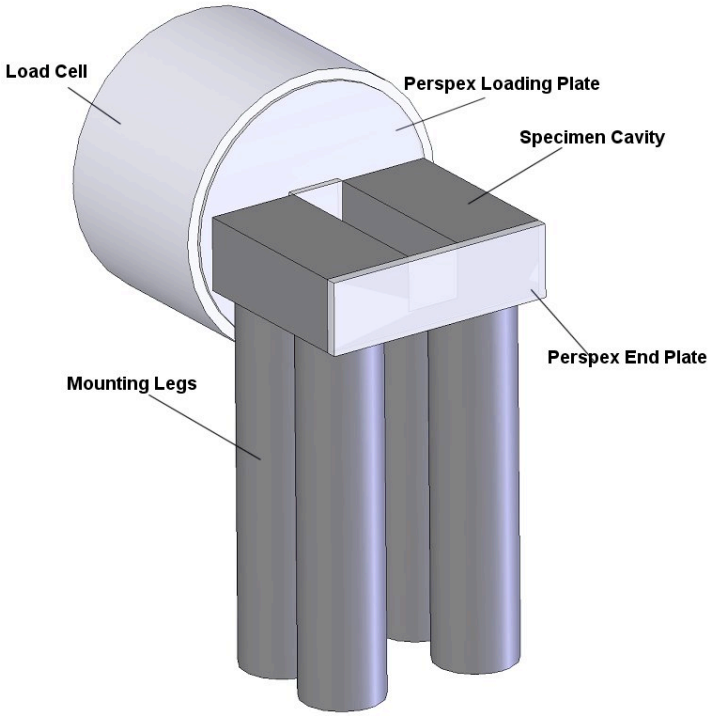

Figure 7-1 - Schematic of tensile cure test rig.

7.2 Results

Load time curves are shown in Figure 7-2.

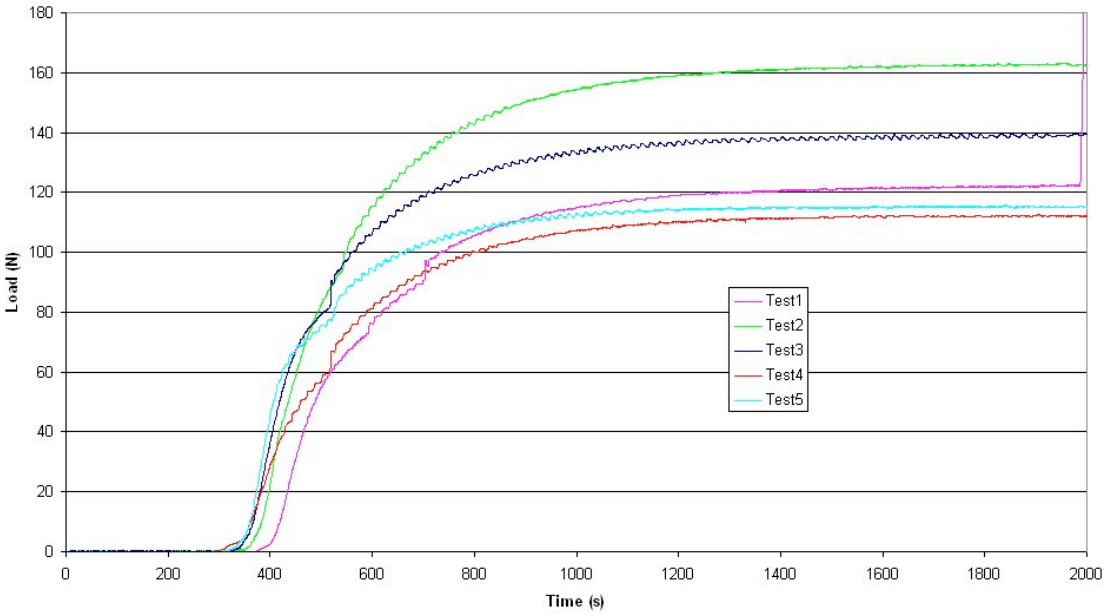

Figure 7-2 - Tensile Load produced during cure of PMMA bone cement.

Transmission of significant load by the curing cement mass began at 300-400 seconds (Figure 7-2). Subsequently the load increased until a plateau was reached at around 1200 seconds from mixing. The plateau load varied from 112N to 162N. This degree of variation may have been caused by variation in sample size since it was difficult to ensure a perfectly uniform fill of the open channel. Another source of variation could be imperfect bonding of the cement to the acrylic plates. If part of the cement block has not bonded to either plate then there will be an unconstrained portion of cement capable of shrinking, hence reducing the measured load. Conversely if the channel has been overfilled then it may bond with more than just the interior faces of the acrylic causing an increase in load.

An interesting, and unexpected, feature of each load curve was a sudden jump in the load at between 500 and 700 seconds. It can be hypothesised that this jump in the load may be due to stick-slip motion between the cement and the sides of the mould. It is impossible to ensure full coverage of the sides with the PVDC film and so the exposed cement may tend to stick to the channel walls. This cement would then be

likely to slip at higher loads. Alternatively the cling-film may not be providing the frictionless solution that is required and so the cement and film would slip against the walls. Any one or all of these scenarios may be taking place in these experiments.

The pull out tests performed after full cure showed that a good bond had been achieved between acrylic end surfaces and bone cement. It was not possible to measure the bond strength as the attachment of the acrylic plate to the load cell always failed first, however in each case the load reached 300-450N before this failure occurred.

7.3 Discussion

Results clearly show that there is a tensile force produced by the polymerising bone cement, the magnitude of the force exerted is lower than might be expected from this cement block geometry. By applying Hooke's Law, a 2% linear strain on fully polymerised cement of identical geometry (with an elastic modulus of approximately 2.5GPa) produces a force of 11.25kN. This sets an upper bound to the force that might be expected.

Some of the discrepancy between the upper-bound and recorded results may be a result of much of the shrinkage occurring while the cement was still in a fluid (plastic) state. Some may also be a result of friction between the rig and the specimen. While every effort was taken to minimise this friction it was impossible to completely eliminate it. Residual friction between the sides of the cavity and the cement specimen was sufficient to prevent specimens being removed by hand.

7.4 Tensile Cure Test Summary

- The cement polymerisation produced a tensile force in all cases with an average of 125N. This shows that the shrinkage was measurable in all cases.
- Values would be expected as significantly higher with this cement geometry.
- The bond with Perspex was shown to be stronger than the Perspex loading plate.
- Differences between measured and expected values of force may be explained by friction which could not be completely eliminated in the experiments.
- A jump in load was observed at approximately 75-95N which may suggest friction was causing a slipping scenario.
- Friction was sufficient to prevent removal of cast cement blocks from the cavity by hand.

8 Bone Cement Shrinkage Modelling

8.1 Introduction

Bone cement, which is used as a fixation material in total joint arthroplasty, is inserted into the cavity prepared in the bone to receive the implant, as a fluid of polymer powder mixed with liquid monomer. The implant is inserted into this fluid mass and as the bone cement polymerises, it hardens to form a viscoelastic solid. During the polymerisation process the physical properties of the cement change. Both the storage and loss modulus increase (as shown in Chapter 6 - Ultrasonic Cure Monitoring). The density increases and the volume decreases. Unconstrained cement shrinks, but if an implant is present the cement may be constrained and unable to shrink, this constrained shrinkage will generate residual stresses within the cement mantle. In-vitro experimentation has shown that this residual stress may be sufficient to cause pre-load cracking and may increase the rate of damage accumulation in the cement mantle during normal loading of the implant [58].

Attempts have been made to model residual stresses in cement mantles using finite element analysis. Previous models have used ad hoc methods such as a press fit or quasi-thermal techniques to generate residual stress fields, but to better understand the parameters that control residual stress development it is desirable to develop a model which takes into account the effects of heat generation, changes in cement mechanical properties and shrinkage effects throughout the polymerisation process.

A model of the thermal phase of polymerisation has been developed and validated and is reported in 4 - Thermal Modelling of Bone Cement Cure. This model predicts the thermal history of the cement and the local degree of polymerisation during the polymerisation process. By relating the shrinkage and material properties of the cement to the degree of polymerisation, residual stresses in the cement mantle may be predicted.

With a tool for predicting the residual stress field in a cement mantle it may be possible to suggest methods for reducing residual stresses, such as by controlling stem temperature, and to improve the accuracy of fatigue models of *in-vivo* total joint arthroplasty.

8.2 Method

The finite element mesh and element-by-element degree-of-polymerisation history from the model presented in Chapter 4.4 was used. The first step in developing the shrinkage model was to set the initial value of the degree of polymerisation for each element. The degree of polymerisation (α) has a value between 0 and 1 denoting the amount of polymerisation that has taken place so far. This value was used as a reference from which the density, the elastic modulus and the shrinkage strain were determined. Each of these dependent variables was given a start value (at α=0) and an end value (at α=1), and intermediate values calculated by linear interpolation. The range for each variable is shown in Table 8-1. The end value for each variable was determined from the literature and the start value as a small fraction of the end value.

Variable	Start value	End Value
Density	0.94×10^3	1.1×10^3
Young's modulus	2.5×10^6	2.5×10^9
Yield stress	1	56×10^6
Shrinkage	0	0.02

Table 8-1 - Variable ranges for shrinkage model variables.

Shrinkage was modelled using the Ansys User Programmable Function (UPF) USERSW developed to model radiation-induced swelling of materials in nuclear engineering applications. Swelling is defined in the UPF as the volumetric enlargement of a material in the presence of a neutron flux. Temperature dependence of the amount of swelling induced by a given neutron flux is also available in the default coding for the calculation of swelling strain, but was removed in the present implementation. Use of the USERSW UPF required a separate subroutine to be linked into a new 'user customised' version of the Ansys™ programme.

The degree of polymerisation of each element was communicated to the UPF using the neutron flux parameter, and the coding of the swelling law adapted to allow for a shrinkage proportional to the applied neutron flux. The constant of proportionality used was set within Ansys™ allowing very simple changes in the swelling law and was set as the maximum amount of shrinkage seen from the start to the end of polymerisation. This value was taken from the literature to be 2% linearly.

Two material models were compared for the elastic modulus of the cement. The first assumed simple proportionality between stress and strain with the modulus directly proportional to the degree of polymerisation. A second model was developed to include material plasticity. This model used a bilinear curve to determine cement stress from the applied shrinkage strain. The yield stress was calculated in the same manner as the shrinkage strain using a final value taken from four point bend tests carried out on CMW1 cement at the University of Southampton.

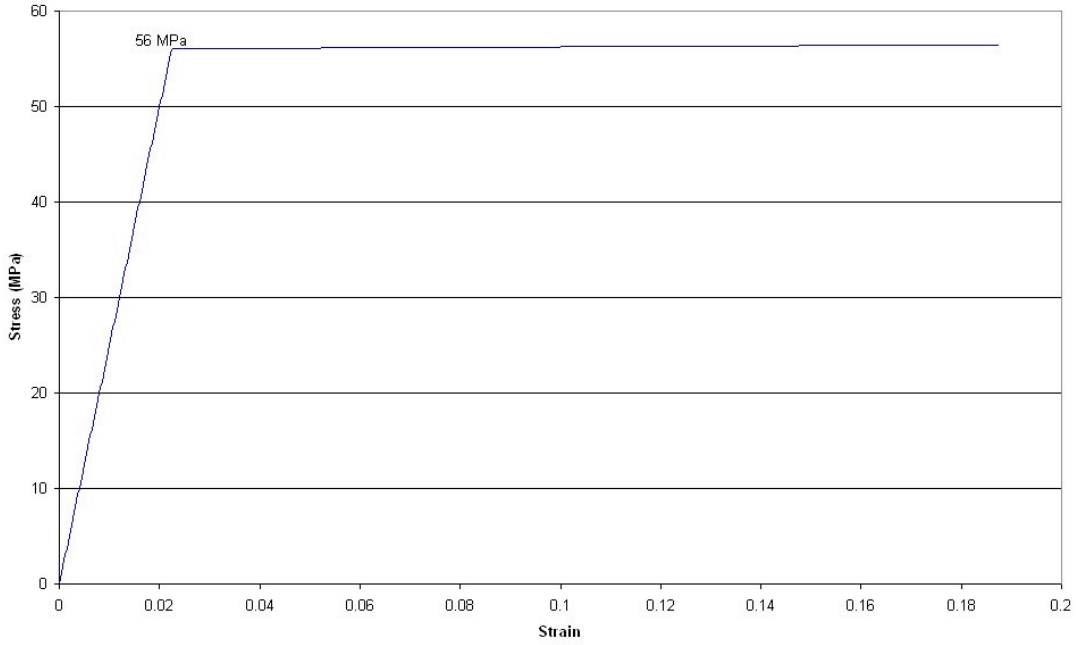

Figure 8-1 - Bilinear stress-strain curve used for the cement modulus at the end of polymerisation.

8.3 Results

Results were plotted as contours of the stress seen at the end of polymerisation and are shown in Figure 8-2. Models are labelled ‘a’ for the bilinear model and ‘b’ for the linear material model and ‘1’ or ’3’ in the figure labels refer to the 1st or 3rd principal stresses. In both models the 1st principal stress within the cement mantle was tensile and was oriented in the hoop direction and the 3rd principal stress within the cement mantle was predominantly compressive and was oriented in the radial direction. The peak value for the residual stress seen in the cement mantle after polymerisation using the bilinear material model was approximately 2.2MPa. The mode residual stress was approximately 1.5MPa. The peak stress predicted using a linearly elastic material model was 25MPa and the mode stress approximately 15MPa.

The distribution of stresses observed at the end of polymerisation also shows a large difference between the two different models. The hoop stresses (1st principal stresses) show a proximal peak in the bilinear material model. In the linear material model the peak hoop stress is located more distally. The radial stresses (3rd principal stresses) show a very similar distribution in both models with the peak stresses located uniformly along the bone-cement interface and with a very small proximal to distal stress gradient.

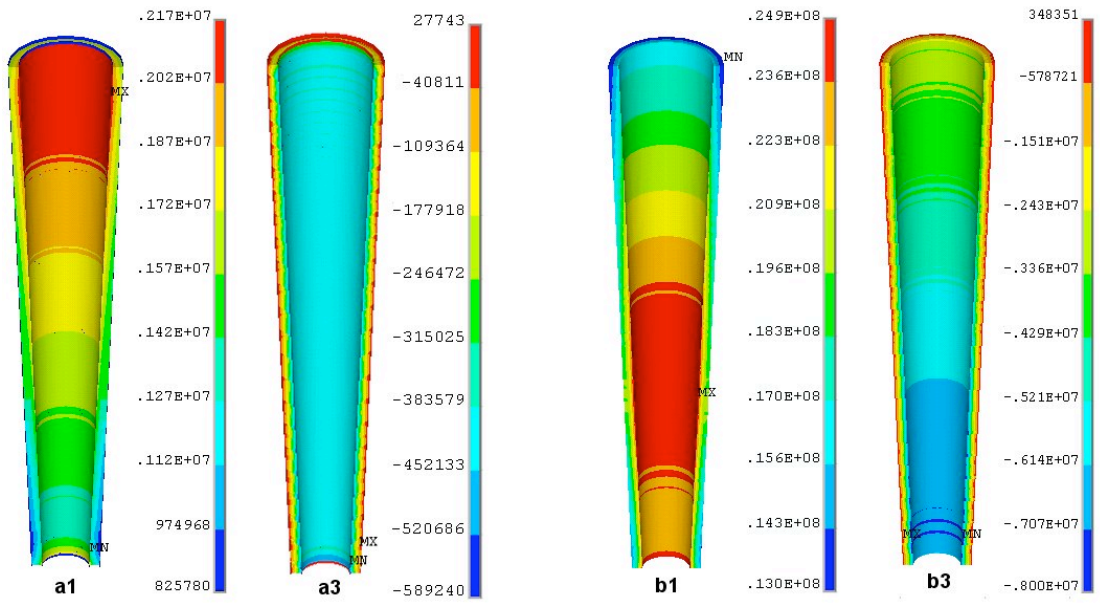

Figure 8-2 - Contour plots of the 1st (1) and 3rd (3) principal stresses in the idealised stem cement mantle at the end of polymerisation. Model a uses a bilinear material model while model b uses a linear elastic model.

Another difference between the two models was also noted. The bilinear material model exhibited higher stresses during the rapid polymerisation period than at the end of polymerisation. The peak stresses occurred at 309s into polymerisation and the peak 1st principal stresses (hoop stresses) were located in the external proximal corner of the cement mantle (shown in Figure 8-3). Figure 8-3 also shows that at this point in the polymerisation the 3rd principal stresses (radial stresses) were significantly higher than at the end and the peak values were located proximally on the internal side of the cement mantle.

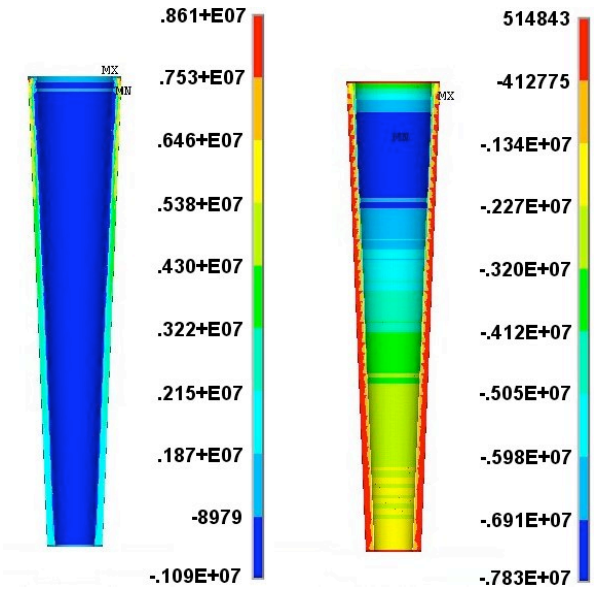

Figure 8-3 - 1st principal (left) and 3rd principal (right) stresses at 309s into the polymerisation period (when peak in stress occurred).

8.4 Discussion

The predicted residual stress was reduced by an order of magnitude with the bilinear material model compared to the linear elastic model. Also the stress distribution was altered dramatically by altering the material model. The peak stress for the bilinear model was located more proximally than for the elastic model. This could be related to regional differences in the rate of polymerisation of the cement. The thermal properties of the implanted femur mean that polymerisation is complete earliest in the distal cement mantle. The cement in the proximal femur, which is last to complete polymerisation, is therefore more constrained during the critical period when the rate of change of materials properties is the greatest, leading to higher residual stresses in this region. The stresses predicted by both models are within the range of those measured in experimental studies [1, 88, 99].

The reduction in stress in the latter stages of polymerisation may also be attributed to the stress gradient. Where a large polymerisation gradient is present stress may be built up in the fast curing area due to constrained shrinkage while when the slower portion shrinks the constraint may be removed and so stress may be relieved in the fast polymerising area.

The value of peak stresses compared very well with experimentally determined values from Roques *et al.* and numerical studies from Orr *et al.* and Lennon *et al.* [58, 91, 99].

8.5 Comparison Model

8.5.1 Introduction

A second shrinkage model was generated for comparison with an alternative model published by Lennon *et al.* In their model, Lennon *et al.* calculated residual stresses by assuming they were identical to those induced by thermal contraction upon cooling of the cement from the peak temperature predicted during polymerisation. The model is a quasi-two-dimensional representation of a femoral component of a hip replacement and was generated in parallel with a physical model used to investigate the location of pre-load cracks within the cement mantle.

8.5.2 Method

The geometry was generated in 2D to save computational time and the mesh was created using 8 node quadrilateral elements. Thermal contact (discussed in Chapter 4.4) was used to model the behaviour of the interfaces between cement and cancellous bone and between cement and stem. The mesh used is shown in Figure 8-4. The physical model of Lennon *et al.* consists of a steel stem with a 3-4mm cement mantle and a 2mm layer of foam to represent cancellous bone. Cortical bone was represented by an aluminium shell. The properties (both thermal and structural) were as those published by Lennon *et al.* and are shown in Table 8-2.

Material	Density (kg/m^3)	Thermal Conductivity (W/mK)	Specific Heat Capacity (J/KgK)	Youngs modulus (Pa)	Poissons Ratio
Cement	1190	0.18	1450	2.4e9	0.33
Stem	7800	14	460	210e9	0.33
Cancellous bone	1300	0.29	2292	2e9	0.3
Aluminium	2800	125.5	925	73e9	0.33

Table 8-2 - Material properties for comparative model.

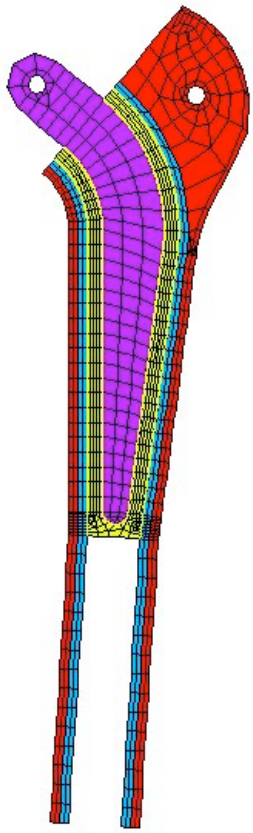

Figure 8-4 - Mesh for comparison model.

Additional properties (contact and cement yield stress) were kept consistent with the model discussed in Chapter 8 - Bone Cement Shrinkage Modelling.

8.5.3 Results

The 1st and 3rd principal stresses at the end of polymerisation are shown in Figure 8-5. The maximum stresses are seen in the longitudinal direction. The maximum stresses are tensile on the internal surface of each side of the cement mantle and are compressive on the external surface. This pattern shows that the majority of the shrinkage is in the longitudinal direction (as would be expected) and the proximal curve causes the cement to try and straighten as it shrinks.

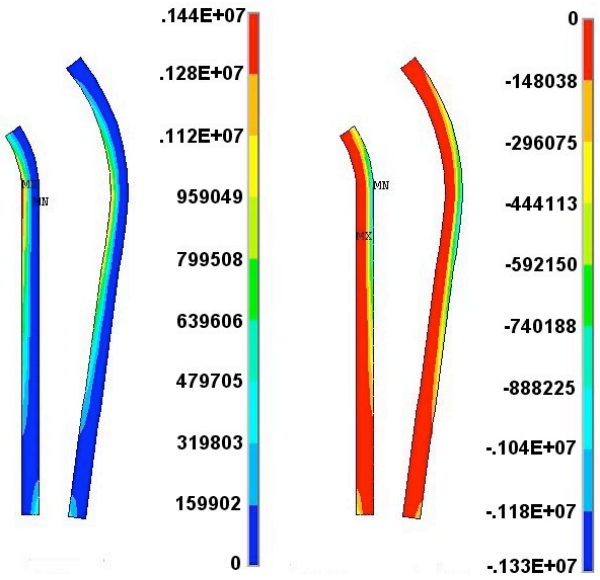

Figure 8-5 - 1st (left) and 3rd (right) principal stresses from comparative model at the end of polymerisation.

Similarly to the idealised stem model the maximum stresses seen in the cement occurred during the rapid polymerisation period. The peak stresses were seen at 455s into polymerisation. At this time the peak 1st principal stress is 3.4MPa tensile and the peak 3rd principal stress is 5.9MPa compressive. The tensile stresses are located in the middle of the cement in the medial-lateral direction of the distal sections of the cement.

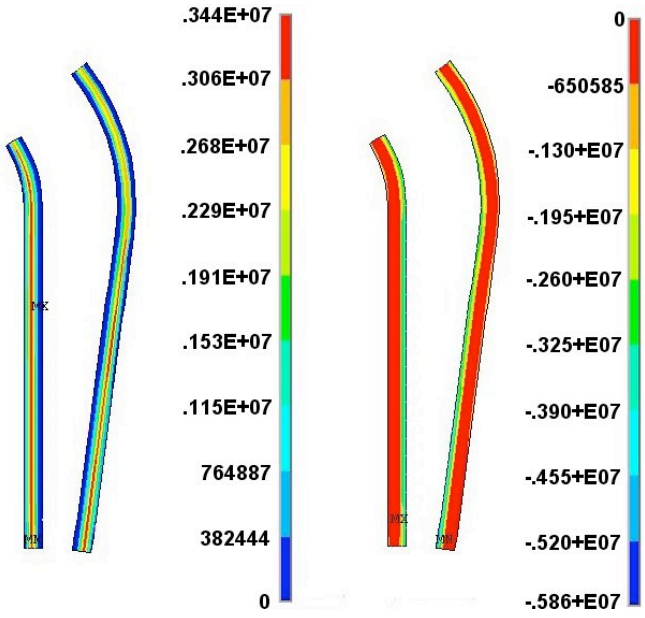

Figure 8-6 - 1st (left) and 3rd (right) principal stresses from comparative model at 455s into polymerisation (when peak in stress occurred).

8.5.4 Discussion

Lennon *et al.* reported stresses of between 1 and 7MPa after thermal shrinkage modelling. The principal direction of maximum stresses was in the longitudinal direction. Plots of the locations of pre-load cracks observed in the physical model are shown in Figure 8-7.

The residual stress model used in this study agreed well with the stress predictions published by Lennon *et al.* The final magnitudes of the residual stress predicted by both studies, would not be high enough to produce the pre-load cracks observed however. During polymerisation the failure stress is likely to be lower than at the end and so it is conceivable that the cracks observed would be caused by the higher stresses experienced during rapid polymerisation. The location of the high stresses at this time agrees well with the observed pre-load crack locations in the published study. The majority of the cracks found are located in the distal section of the cement and towards the middle through the thickness. The tensile stresses predicted in the longitudinal direction would be likely to cause a similar pattern of cracks.

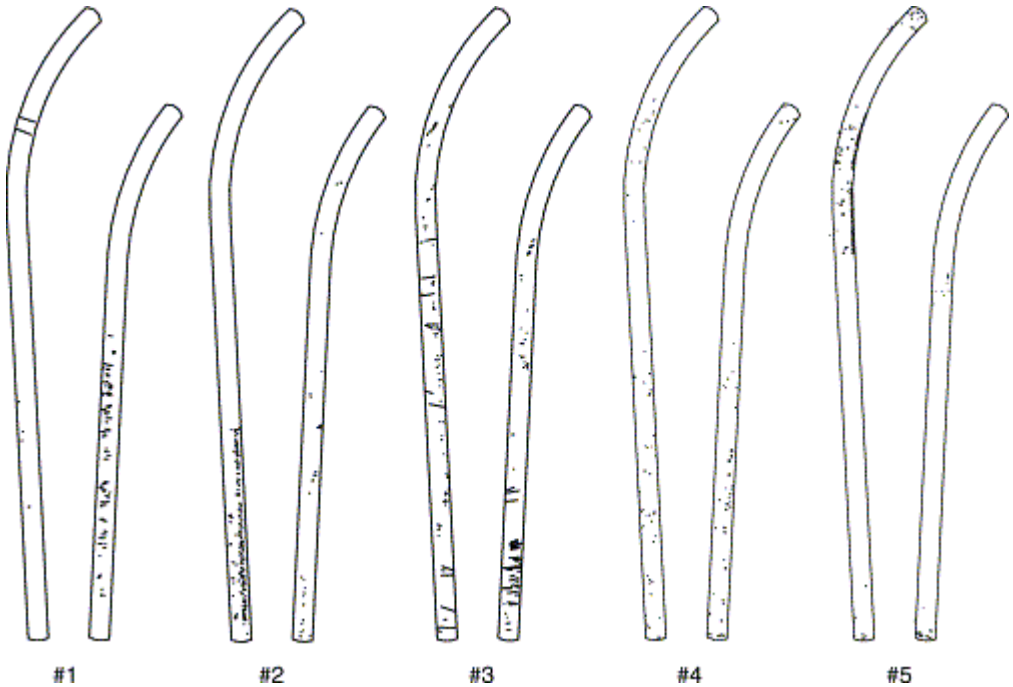

Figure 8-7 - Pre-load cracks observed in physical model by Lennon *et al.* [58].

8.6 Shrinkage Modelling Summary

- Shrinkage strain was applied proportionally to the degree of polymerisation with a final value of 2% linearly.
- Material properties were adjusted proportionally to the degree of polymerisation using final values measured experimentally.
- A bilinear material model was used to approximate the plasticity of the cement and produced residual stresses closer to published, experimentally and numerically, determined values.
- The bilinear material model changed the resulting stress field and produced a peak stress during polymerisation.
- The shrinkage model was compared with results published by Lennon *et al.* [58].
- The stresses modelled gave a peak stress field similar in pattern to the most common pre-load crack location plots from Lennon's experimental analysis.

9 Summary

The National Joint Register for England and Wales revealed that in 2004, aseptic loosening was the cause of 58.5% of knee revision procedures and 78.8% of hip revision procedures [113]. Aseptic loosening has often been attributed to fatigue fracture of the bone cement mantle in cemented arthroplasty [6, 45, 84]. Furthermore, fatigue fracture has been shown to be accelerated by, among other material defects, residual stresses generated during the polymerisation process. In work by Lennon *et al.* residual stresses have been shown to be high enough to cause pre-load cracking in cement mantles [58].

Revision surgery carries with it not only a great deal of discomfort and associated stress for the patient concerned but also a high financial cost. Considering the statistics above, the 3367 hip revision operations which comprise the 78.8% cost the NHS approximately £22million (based on data from O'Shea *et al.*) [90]. It is clear that investment in producing better pre-clinical testing techniques for the design of improved prostheses is a sensible proposal.

Pre-clinical testing techniques for cement mantle fatigue have been in use for some time and can be an important part of the design process. Techniques currently employed for bone cement include mechanical testing and now finite element modelling of fatigue crack growth and cement mantle damage [32, 52]. These tools can be used to rank new arthroplasty solutions in terms of their effects on cement fatigue failure. This may help in identifying poor implant designs and/or poor cement formulations based on the geometry and material properties. While the current finite element techniques are capable of ranking implant designs, life prediction models for the cement mantle require improvement before the quantitative results can be relied upon. It is important to note that when using computational techniques to model any experiment no factors are included unless the researching engineer specifically considers them and inserts coding to include them. When reproducing the fatigue of a total joint replacement a mechanical *in-vitro* test will automatically include the redistribution of stresses over time, the effects of residual stress, creep of materials

and any material defects which would be expected in the *in-vivo* environment. All of these considerations must be separately modelled when using any numerical technique.

The literature review in this thesis showed several studies which have attempted to model the residual stress generation but which have either over-simplified the problem or have not considered all its aspects. Lennon *et al.* have produced models of both the temperature history and the residual stress generation during polymerisation of bone cement. The study included a reaction based method for the generation of a temperature and polymerisation history using equations published by Baliga *et al.* [7]. Residual stress was then calculated by assigning a thermal expansion coefficient to the cement elements and cooling from the peak temperature. This study has included more variables than most other work published to date. However, the method for simulating the residual stress generation uses an assumption of stress locking occurring at the point at which peak cement temperature is reached. Mechanical properties evolve throughout the polymerisation process and so cannot be assumed to be present from a specified point during the polymerisation process.

Similar problems were observed in other areas considered in this thesis. Studies have been undertaken into the monitoring of material properties of bone cement during polymerisation. Viano *et al.* used an ultrasonic method to monitor attenuation and sonic velocity in order to derive the degree of polymerisation over time [122]. Carlson *et al.* used an approximation of the elastic modulus found using similar ultrasonic techniques to predict the degree of polymerisation [16]. These techniques both assume that the shear component is negligible which may not reflect the true behaviour of bone cement.

The motivation for this project was provided by a desire to improve the current techniques used to predict residual stresses. Current fatigue models require residual stresses to be specified as initial conditions and it is hoped that by producing a reliable and easily adaptable model to do this pre-clinical testing of new arthroplasty designs can be improved.

In the present project several new computational and experimental methods have been investigated and developed. These include models of the thermal and shrinkage behaviour and experimental methods for determining the mechanical properties of curing bone cement. Ultrasonic testing of the cement during polymerisation had previously only been performed to provide data on the timing of the rapid polymerisation period. This project has shown the potential for measuring a broad spectrum of complex mechanical properties as well as density using an ultrasonic technique employing both compressional and shear wave transducers. This technique has advantages over more traditional rheometry techniques such as an oscillatory rheometer as by using a low amplitude wave much less kinetic energy is introduced to the reacting mass. While further developments are required, this is a major step forward for monitoring fast setting materials of all kinds.

The thermal model was adapted from work carried out by Borzacchiello *et al.* and was tested against an experimental model of polymerisation of bone cement in a bone-cement-implant construct [12]. The models showed good agreement with experiment only when interface nodes were duplicated and a proper contact model was used which included thermal contact conductance values. The thermal model was used to show the effect of stems at different initial temperatures on the temperature and cure histories within the cement mantle [14]. By using an implant at 50ºC the proximal-to-distal cure gradient observed with room temperature stems was seen to reverse. The model was also used in pre-clinical testing of femoral hip resurfacing implants and tibial tray knee implants to investigate the effect of different cement configurations and thicknesses on temperatures in the cement and surrounding bone. The model was shown to be particularly sensitive to the activation energy used in the cement polymerisation model. Other variables affected temperature and degree of polymerisation during cure by varying degrees and in the case of the rate variable n and the total heat liberation value Q_{tot} only temperature and degree of polymerisation curves respectively were affected.

Parameters used to drive the thermal finite element model were taken from the literature [12]. This model using as many physical variables as possible (i.e. the activation energy and reaction rate constants), the intent being to limit the empirical nature of the model in order that these variables may be tuned to the curing kinetics of

different cement brands with minimal effort. DSC measurements were carried out in accordance with the method published by Starink and analysis was carried out to establish the activation energy using an innovative technique [109]. This technique uses DSC tests carried out at constant rates of temperature which is more physically relevant to in-vivo polymerisation conditions than the isothermal tests carried out in previous studies. Although the characteristics of the cement polymerisation reaction make it difficult to handle using these methods, as explained by Starink in a later paper [108], fitting techniques enabled a reasonable match between model and experimental data to be obtained. Although a general fit that enabled the accurate modelling of cement cure under all conditions was not possible, it was possible to 'tune' the model to the individual case being examined such that good results were obtained. Different parameters are likely to be needed to model large masses of cement and thin cement mantles, for example.

In order to determine mechanical property evolution during the polymerisation process, ultrasonic testing techniques were developed in collaboration with the Mechanical Engineering Department of University College London. While ultrasound has been used in previous studies to monitor the progress of the polymerisation reaction, the new techniques allow the determination of a much wider variety of mechanical properties than has previously been described. The technique was shown to be sound in principle, however problems with combining separate tests prevented the use of final results in any modelling of the mechanical property evolution. Further work should be aimed at unifying the compressional and shear wave tests in order to develop a method useful for the monitoring of many fast setting grouts, adhesives and composite matrices.

The thermal model served two purposes; firstly the temperature at the cement-bone interface and within the bone could be determined and the likelihood of thermal necrosis predicted, secondly a curve for the degree of polymerisation for the entire reaction could be generated. The polymerisation curve could then be used as a baseline to relate all mechanical parameters during a mechanical model of the cement shrinkage. Shrinkage of the cement was modelled using an algorithm designed for modelling the swelling behaviour of materials. Both shrinkage and the mechanical properties of the cement were assumed to be proportional to the degree of

polymerisation. For example, the elastic modulus was assumed to start at a very low level to simulate the initial fluid state and rise to the experimentally determined value of 2.5GPa when the cement was fully polymerised. The elastic modulus was found to be an important variable. Linear elastic models were found to generate high levels of residual stress and so the material model was modified to include a yield point and "almost perfectly plastic" post-yield behaviour. The resulting bilinear material model produced a residual stress contour with a peak stress after polymerisation of 2.2MPa in the hoop direction for the idealised stem model. This value of peak stress compared very well with experimentally determined values from Roques *et al.* and numerical studies from Orr *et al.* and Lennon *et al.* [58, 91, 99]. The model was then used in a geometrically similar model to Lennon *et al.* and resulting residual stress plots were compared with the pre-loading crack distributions observed by Lennon. Results agreed well with these data. Also the pattern of predicted stresses during rapid polymerisation agreed well with pre-load crack patterning reported from physical experiments in the same study. Stresses were predicted to be of greater magnitude during rapid polymerisation than at the end of polymerisation. This phenomenon may be as a result of gradients of fast and slow polymerising areas of cement within the cement mantle.

Because this method of generating residual stresses uses the reaction of the cement to drive the shrinkage rather than a quasi-thermal or press-fit technique the technique can be used on any given situation and would require little adaptation. Also the technique does not assume stress locking occurs at a particular time

A tensile test of polymerising bone cement was used as a comparison for the results of the residual stress model. The results from each were dramatically different although the model was producing results which would be expected from a 2% linear shrinkage. It was concluded that the test was an unfair comparison as the friction between the surfaces of the mould and the cement sample were not measurable and therefore were neglected from the finite element model. The frictional forces appeared to be larger than anticipated and so it was concluded that they would need to be included in any similar finite element model for any fair comparison.

10 Further Work

The modelling techniques described in this thesis for predicting residual stresses in acrylic bone cement agree well with other published data. The model does have some limitations however:

The material testing techniques discussed in Chapter 6 - Ultrasonic Cure Monitoring show promise, but require further development before the results could be used in modelling. A major improvements is anticipated by using both shear and compressive transducers simultaneously on a single specimen of cement to enable accurate synthesis of the shear and compressive data.

The polymerisation model used in the preceding work has been employed because it uses relatively few empirical values compared to others available in the literature and it was anticipated that comparisons between different cement brands would thereby be made simpler. The work discussed in Chapter 5 - Measurement of PMMA Curing Parameters Using Differential Scanning Calorimetry (DSC) has identified a possible need for the model to be 'tuned' for each individual scenario due to differences in the heat output curve during polymerisation for different rates of temperature increase. Alternatively the model used may be revised to allow for these differences between different geometries and/or boundary conditions.

The residual stress model is deterministic and takes no account of the effects of material defects and stress raisers such as porosity and agglomerates of barium sulphate. These effects should be investigated and this could be achieved using a Monte-Carlo technique to model random distributions and sizes of defect, such as the method used by Jeffers [50].

The models for predicting both the stresses and temperatures during polymerisation may be used for any application of bone cement. Realistic geometry can be generated using CT data such as those shown in Chapters 4.6 and 4.7. This geometry can then

be used to investigate the effects of different implant geometry as well as several other variables.

The method used for material property determination may be used in similar applications for alternative materials. This work has identified a new method for monitoring the material property evolution of fast curing materials. This may have application in adhesive and cast material monitoring.

11 Bibliography

1. Ahmed, A.M., W. Pak, D.L. Burke, and J. Miller, *Transient and Residual Stresses and Displacements in Self-Curing Bone Cement - Part I: Characterization of Relevant Volumetric Behavior of Bone Cement.* Journal of Biomechanical Engineering, 1982. **104**: p. 21-27.
2. Amstutz, H., P. Beaule, F. Dorey, M. Duff, P. Campbell, and T. Gruen, *Metal-on-Metal Hybrid Surface Arthroplasty: Two to Six-Year Follow-up Study.* Journal of Bone and Joint Surgery, 2004. **86**: p. 28-39.
3. Athanasou, N.A., J. Quinn, and C.J.K. Bulstrode, *Resorption of Bone by Inflammatory Cells Derived from the Joint Capsule of Hip Arthroplasties.* Journal of Bone and Joint Surgery-British Volume, 1992. **74**(1): p. 57-62.
4. Automation Creations, I., *Matweb Material Property Data*. 2003.
5. Azom.com, *Cobalt - Based Carbide - Hardened Alloys – Nature and Properties*. 2005.
6. Baleani, M., L. Cristofolini, C. Minari, and A. Toni, *Fatigue Strength of PMMA bone cement mixed with gentamicin and barium sulphate vs pure PMMA.* Proceedings of the Institution of Mechanical Engineers Part H-Journal of Engineering in Medicine, 2003. **217**: p. 9-12.
7. Baliga, B.R., P.L. Rose, and A.M. Ahmed, *Thermal modeling of polymerizing polymethylmethacrylate, considering temperature-dependent heat generation.* Journal of Biomechanical Engineering, 1992. **114**(2): p. 251-9.
8. Barrack, R.L., *Early failure of modern cemented stems.* Journal of Arthroplasty, 2000. **15**(8): p. 1036-1050.
9. Bayne, S.C., E.P. Lautenschlager, C.L. Compere, and R. Wildes, *Degree of polymerization of acrylic bone cement.* Journal of Biomedical Materials Research, 1975. **9**(1): p. 27-34.
10. Bettencourt, A., A. Calado, J. Amaral, F. Vale, J. Rico, J. Monteiro, and M. Castro, *The Influence of Vacuum Mixing on Methylmethacrylate Liberation from Acrylic Cement Powder.* International Journal of Pharmaceutics, 2001. **219**: p. 89-93.
11. Bhambri, S.K. and L.N. Gilbertson, *Micromechanisms of Fatigue-Crack Initiation and Propagation in Bone Cements.* Journal of Biomedical Materials Research, 1995. **29**(2): p. 233-237.
12. Borzacchiello, A., L. Ambrosio, L. Nicolais, E.J. Harper, K.E. Tanner, and W. Bonfield, *Comparison between the polymerization behavior of a new bone cement and a commercial one: modeling and in vitro analysis.* Journal of Materials Science-Materials in Medicine, 1998. **9**(12): p. 835-838.
13. Bowman, H., M. Balasubramanian, and A. Judge. *Thermal conductivity of of selected human tissue*. in *5th Annual meeting of the Society of Biomaterials*. 1979.
14. Briscoe, A., A. New, and M. Taylor. *Effect Of Pre-Cooling and Pre-Heating a Hip Stem on the Bone-Cement Interface Temperature History*. in *International Conference of Computational Bioengineering*. 2003. Zaragoza, Spain.
15. Buckley, P., J.F. Orr, I. Revie, S. Brensch, and N.J. Dunne, *Fracture Characteristics of Acrylic Bone Cement-Bone Composites.* Proceeding of the Institution of Mechanical Engineers:Part H, 2003. **217**: p. 419-427.

16. Carlson, J., M. Nilsson, E. Fernandez, and J.A. Planell, *An Ultrasonic pulse-echo technique for monitoring the setting of CaSO4-based bone cement.* Biomaterials, 2002. **24**: p. 71-77.
17. Chato, J.C. *A survey of thermal conductivity and diffusivity data on biological materials*. in *5th conference on thermal conductivity*. 1965. Denver, Colorado.
18. Chen, Y., Z.H. Xia, and F. Ellyin, *Evolution of residual stresses induced during curing processing using a viscoelastic micromechanical model.* Journal of Composite Materials, 2001. **35**(6): p. 522-542.
19. Clattenburg, R., J. Cohen, S. Conner, and N. Cook, *Thermal Properties Of Cancellous Bone.* Journal Of Biomedical Materials Research, 1975. **9**(2): p. 169-182.
20. Davis, C.T., R. Cabanela, M. Wenger, D., *Radiologic Assessment of the Failed Total Hip Arthroplasty.* University of Pennsylvania Orthopaedic Journal, 2001. **14**(Spring): p. 49-54.
21. Depuy, *Handling Guidelines for mixing of low, medium, and high viscosity bone cements*. 2005.
22. DePuy, L., *Patient Resources*. 2006.
23. DiPisa, J., G. Sih, and A. Berman, *The Temperature Problem at the Bone-Acrylic Cement Interface of the Total Hip Replacement.* Clinical Orthopaedics and Related Research, 1976. **121**: p. 95-98.
24. Dunne, N.J. and J.F. Orr, *Curing characteristics of acrylic bone cement.* Journal of Materials Science-Materials in Medicine, 2002. **13**(1): p. 17-22.
25. Dunne, N.J. and J.F. Orr, *Flow characteristics of curing polymethyl methacrylate bone cement.* Proceedings of the Institution of Mechanical Engineers Part H- Journal of Engineering in Medicine, 1998. **212**(H3): p. 199-207.
26. Dunne, N.J. and J.F. Orr, *Influence of Mixing Techniques on the Physical Properties of Acrylic Bone Cement.* Biomaterials, 2001. **22**: p. 1819-1826.
27. Farrar, D.F. and J. Rose, *Rheological properties of PMMA bone cements during curing.* Biomaterials, 2001. **22**(22): p. 3005-3013.
28. Feith, R., *Side Effects of Acrylic Cement Implanted into Bone.* Acta Orthopaedica Scandinavica, 1975. **46: Sup.**: p. 161.
29. Fisher, D., A. Tsang, N. Paydar, S. Millionis, and C. Turner, *Technical Note: Cement Mantle Thickness Affects Cement Strains in Total Hip Replacement.* Journal of Biomechanics, 1997. **30**(11/12): p. 1173-1177.
30. Gilbert, J.L., J.M. Hasenwinkel, R.L. Wixson, and E.P. Lautenschlager, *A theoretical and experimental analysis of polymerization shrinkage of bone cement: A potential major source of porosity.* Journal of Biomedical Materials Research, 2000. **52**(1): p. 210-218.
31. Ginbson, L. and M. Ashby, *Cellular Solids: Structure and Properties*. 1988: Pergamon Press plc.
32. Ginebra, M.P., L. Albuixech, E. Fernandez-Barragan, C. Aparicio, F.J. Gil, J. San Roman, B. Vazquez, and J.A. Planell, *Mechanical Performance of Acrylic Bone Cements Containing Different Radiopacifying Agents.* Biomaterials, 2002. **23**: p. 1873-1882.
33. Graf, K. and E. Stein, *Fortlaufende Registrierung der Knochenmarkdurchblutung des Menschen mit der Warmeleitsonde.* Zeitschrift f. die gesamte exp. Medizin, 1957. **129**: p. 1-14.
34. Graham, J., L. Pruitt, M. Ries, and N. Gundiah, *Fracture and fatigue properties of acrylic bone cement - The effects of mixing method, sterilization*

treatment, and molecular weight. Journal of Arthroplasty, 2000. **15**(8): p. 1028-1035.
35. Grigoris, P. and D. Hamblen, *The Control of New Prosthetic Implants.* Journal of Bone and Joint Surgery (Br), 1998. **80**(B): p. 941-943.
36. Gross, S. and E.W. Abel, *A finite element analysis of hollow stemmed hip prostheses as a means of reducing stress shielding of the femur.* Journal of Biomechanics, 2001. **34**(8): p. 995-1003.
37. Gruen, T.A., G.M. McNeice, and H.C. Amstutz, *"Modes of Failure" of Cemented Stem-type Femoral Components.* Clinical Orthopaedics and Related Research, 1979. **141**: p. 17-27.
38. CreatedBy,*Self Sensing Bone Cement Rheometer*,2003,http://www.mech-eng.leeds.ac.uk/menbmh/talula/index.htm
39. Harper, E.J. and W. Bonfield, *Tensile characteristics of ten commercial acrylic bone cements.* Journal of Biomedical Materials Research, 2000. **53**(5): p. 605-616.
40. Harrigan, T.P. and W.H. Harris, *A 3-Dimensional Nonlinear Finite-Element Study of the Effect of Cement-Prosthesis Debonding in Cemented Femoral Total Hip Components.* Journal of Biomechanics, 1991. **24**(11): p. 1047-1058.
41. Henschel, C.J., *Heat Impact of Revolving Instruments on Vital Dental Tubules.* Journal of Dental Research, 1943. **22**: p. 323-333.
42. Heuer, D.A. and K.A. Mann, *Fatigue fracture of the stem-cement interface with a clamped cantilever beam test.* Journal of Biomechanical Engineering-Transactions of the Asme, 2000. **122**(6): p. 647-651.
43. Huiskes, R., *Some Fundamental Aspects of Human Joint Replacement, Analyses of Stresses and Heat Conduction in Bone-Prosthesis Structures.* Acta Orthopaedica Scandinavica, 1980. **185 Supplement**: p. 1-208.
44. Huiskes, R. and S.J. Hollister, *From Structure to Process: Recent Developments of FE-Analysis in Orthopaedic Biomechanics.* Journal of Biomechanical Engineering-Transactions of the ASME, 1993. **115**: p. 520-527.
45. Hukkanen, M., S. Corbett, J. Batten, Y. Kontinnen, I. McCarthy, J. Maclouf, S. Santavirta, S. Hughes, and J. Polak, *Aseptic Loosening of Total Hip Replacement.* Journal of Bone and Joint Surgery, 1997. **79-B**: p. 467-474.
46. Ingham E and F. J, *Biological reactions to wear debris in total joint replacement.* Proceedings of the Institution of Mechanical Engineers Part H-Journal of Engineering in Medicine, 2000. **214**: p. 21-37.
47. Jafri, A.A., S.M. Green, P.F. Partington, A.W. McCaskie, and S.D. Muller, *Pre-heating of components in cemented total hip arthroplasty.* Journal of Bone and Joint Surgery-British Volume, 2004. **86-B**: p. 1214-1219.
48. James, S.P., M. Jasty, J. Davies, H. Piehler, and W.H. Harris, *A Fractographic Investigation of Pmma Bone-Cement Focusing on the Relationship between Porosity Reduction and Increased Fatigue Life.* Journal of Biomedical Materials Research, 1992. **26**(5): p. 651-662.
49. Jasty, M., W. Maloney, C. Bragdon, D. O'Connor, T. Haire, and W. Harris, *The Initiation of Failure in Cemented Femoral Components of Hip Arthroplasties.* Journal of Bone and Joint Surgery-British Volume, 1991. **73**(B): p. 551-558.
50. Jeffers, J., *In-Silico Simulation of Long Term Cement Failure in Total Hip Replacement*, in *Bioengineering Science Research group*. 2005, University of Southampton: Southampton.

51. Jeffers, J., *In Silico Simulation of Long Term Cement Mantle Failure in Total Hip Replacement*, in *School of Engineering Sciences*. 2005, University of Southampton: Southampton. p. 240.
52. Jeffers, J., M. Browne, and M. Taylor, *Damage Accumulation, Fatigue and Creep Behaviour of Vacuum Mixed Bone Cement.* Biomaterials, 2005. **26**: p. 5532-5541.
53. Jeffers, J.R.T. and M. Taylor. *Residual stress decreases the life of the cement mantle in total hip replacement*. in *International Conference on Computational Biomechanics*. 2003. Zaragoza, Spain.
54. Krause, W.R., J. Miller, and P. Ng, *The Viscosity of Acrylic Bone Cements.* Journal of Biomedical Materials Research, 1982. **16**: p. 219-243.
55. Kummer, B., *Biomechanics of Bone*. Biomechanics: Its foundation and objective, ed. Y. Fung. 1972: Prentice Hall.
56. Lee, A.J.C., R.S.M. Ling, S. Gheduzzi, J.P. Simon, and R.J. Renfro, *Factors affecting the mechanical and viscoelastic properties of acrylic bone cement.* Journal of Materials Science-Materials in Medicine, 2002. **13**(8): p. 723-733.
57. Lee, S., Y. Lai, and T. Hsu, *Influence of polymerization conditions on monomer elution and microhardness of autopolymerized polymethyl methacrylate resin.* European Journal of Oral Sciences, 2002. **110**: p. 179-183.
58. Lennon, A.B. and P.J. Prendergast, *Residual stress due to curing can initiate damage in porous bone cement: experimental and theoretical evidence.* Journal of Biomechanics, 2002. **35**(3): p. 311-321.
59. Lennon, A.B., P.J. Prendergast, M.P. Whelan, R.P. Kenny, and C. Cavalli. *Modelling of temperature history and residual stress generation due to curing in polymethylmethacrylate*. in *12th Conference of the European Society of Biomechanics*. 2000. Dublin.
60. Lewis, G., *Effect of mixing method and storage temperature of cement constituents on the fatigue and porosity of acrylic bone cement.* Journal of Biomedical Materials Research, 1999. **48**(2): p. 143-149.
61. Lewis, G., *Properties of acrylic bone cement: State of the art review.* Journal of Biomedical Materials Research, 1997. **38**(2): p. 155-182.
62. Li, C., J. Mason, and D. Yakimicki, *Thermal Characterization of PMMA-Based Bone Cement Curing.* Journal of Materials Science-Materials in Medicine, 2004. **15**: p. 85-89.
63. Li, C., Y. Wang, and J. Mason, *The effects of curing history on residual stresses in bone cement during hip arthroplasty.* Journal of Biomedical Materials Research, 2004. **70B**: p. 30-36.
64. Linder, L., *Reaction of Bone to the Acute Chemical Trauma of Bone Cement.* Journal of Bone and Joint Surgery-American Volume, 1977. **59-A**: p. 82-87.
65. Ling, R.S.M., *Observations on the Fixation of Implants to the Bony Skeleton.* Clinical Orthopaedics and Related Research, 1986. **210**: p. 80-95.
66. Lombardi, A.V., T.H. Mallory, B.K. Vaughn, and P. Drouillard, *Aseptic Loosening in Total Hip-Arthroplasty Secondary to Osteolysis Induced by Wear Debris from Titanium-Alloy Modular Femoral Heads.* Journal of Bone and Joint Surgery-American Volume, 1989. **71A**(9): p. 1337-1342.
67. CreatedBy,*TE 89 HIP AND KNEE JOINT FRICTION SIMULATOR*,2002,http://www.plint-tribology.fsnet.co.uk/cat/at2/leaflet/te89.htm

68. Lu, Z. and H.A. McKellop, *Effects of Cement Creep on Stem Subsidence and Stresses in the Cement Mantle of a Total Hip Replacement.* Journal of Biomaterials Research, 1997. **34**: p. 221-226.
69. Lundskog, J., *Heat and Bone TIssue.* Scandinavian Journal of Plastics and Reconstructive Surgery, 1972. **suppl. 9**.
70. Macaulay, W., C.W. DiGiovanni, A. Restrepo, K.J. Saleh, H. Walsh, L.S. Crossett, M.G.E. Peterson, S. Li, and E.A. Salvati, *Differences in bone-cement porosity by vacuum mixing, centrifugation, and hand mixing.* Journal of Arthroplasty, 2002. **17**(5): p. 569-575.
71. Malchau H, P. Herberts, Eisler T, G. Garellick, and S. Soderman, *The Swedish Total Hip Replacement Register.* Journal of Bone and Joint Surgery (Am), 2002. **84**: p. 2-20.
72. Malchau, H., Herberts P., Garellick G., Soderman P., Eisler T., *Prognosis of Total Hip Replacement*. 2002.
73. Manley, M.T., J.A. D'Antonio, W.N. Capello, and A.A. Edidin, *Osteolysis: A disease of access to fixation interfaces.* Clinical Orthopaedics and Related Research, 2002(405): p. 129-137.
74. Mann, K.A., F.W. Werner, and D.C. Ayers, *Modeling the tensile behavior of the cement-bone interface using nonlinear fracture mechanics.* Journal of Biomechanical Engineering-Transactions of the ASME, 1997. **119**(2): p. 175-178.
75. Markovsky, A., T.F. Soules, V. Chen, and M.R. Vukcevich, *Mathematical and Computational Aspects of a General Viscoelastic Theory.* Journal of Rheology, 1987. **31**(8): p. 785-813.
76. Martini, F.H., Bartholomew E.F., *Essentials of Anatomy and Biology*. Second ed. 2000: Prentice-Hall.
77. McCullough, S., F.J. Buchanan, J.F. Orr, and G.M. Walker, *Effect of temperature and mixing conditions on quality and consistency of poly(methyl methacrylate) bone cement.* Plastics Rubber and Composites, 2000. **29**(7): p. 378-384.
78. McKellop, H.A. and I.C. Clarke. *Degradation and Wear of Ultra-High-Molecular-Weight Polyethylene*. in *Corrosion and Degradation of Implant Materials: Second Symposium*. 1985. Philadelphia: American Society for Testing and Materials.
79. McSkimin, H.J., *Ultrasonic methods for measuring the mechanical properties of liquids and solids.* Physical Acoustics, 1964. **1**(A): p. 271-334.
80. Meyer, J., E. Lautenschlager, and E. Moore, *On the Setting Parameters of Acrylic Bone Cement.* Journal of Bone and Joint Surgery-American Volume, 1973. **55A**(149-156).
81. Mjoberg, B., G. Selvik, L.I. Hansson, R. Rosenqvist, and R. Onnerfalt, *Mechanical Loosening of Total Hip Prostheses - a Radiographic and Roentgen Stereophotogrammetric Study.* Journal of Bone and Joint Surgery-British Volume, 1986. **68**(5): p. 770-774.
82. Moritz, A.R. and F.C. Henriques, *The Relative Importance of Time and Surface Temperature in the Causation of Cutaneous Burns.* American Journal of Pathology, 1947. **23**: p. 695-720.
83. Muller, S.D., S.M. Green, and A.W. McCaskie, *The dynamic volume changes of polymerising polymethyl methacrylate bone cement.* Acta Orthopaedica Scandinavica, 2002. **73**(6): p. 684-687.

84. Murphy, B.P. and P.J. Prendergast, *The relationship between stress, porosity, and nonlinear damage accumulation in acrylic bone cement.* Journal of Biomedical Materials Research, 2002. **59**(4): p. 646-654.
85. Nilsson, M., J. Carlson, E. Fernandez, and J.A. Planell, *Monitoring the Setting of Calcium-Based Bone Cements Using Pulse-Echo Ultrasound.* Journal of Materials Science: Materials in Medicine, 2002. **13**: p. 1135-1141.
86. Noble, P., C., M. Collier, B., J. Maltry, A., E. Kamaric, and H. Tullos, S., *Pressurization and Centralization Enhance the Quality and Reproducibility of Cement Mantles.* Clinical Orthopaedics and Related Research, 1998. **355**: p. 77-89.
87. Nuno, N. and M. Amabili, *Modelling debonded stem-cement interface for hip implants: effects of residual stresses.* Clinical Biomechanics, 2002. **17**(1): p. 41-48.
88. Nuno, N. and G. Avanzolini, *Residual stresses at the stem-cement interface of an idealized cemented hip stem.* Journal of Biomechanics, 2002. **35**(6): p. 849-852.
89. Nzihou, A., P. Sharrock, and A. Ricard, *Reaction kinetics and heat transfer studies in thermoset resins.* Chemical Engineering Journal, 1999. **72**(1): p. 53-61.
90. O'Shea, K., E. Bale, and P. Murray, *Cost analysis of primary total hip replacement.* Irish Medical Journal, 2002. **95**(6): p. 177-180.
91. Orr, J.F., N.J. Dunne, and J.C. Quinn, *Shrinkage stresses in bone cement.* Biomaterials, 2003. **24**(17): p. 2933-2940.
92. Özisik, M.N., *Heat Conduction*. 2 ed. 1993: Wiley.
93. Paterson, M., P. Fulford, and R. Denham, *Loosening of The Femoral Component After Total Hip Replacement.* Journal of Bone and Joint Surgery-British Volume, 1986. **68-B**(3): p. 392-397.
94. Piche, L., *Ultrasonic velocity measurement for the determination of density in polyethylene.* Polymer Engineering and Science, 1984. **24**(17): p. 1354-1358.
95. Plastics, B., *CARP Brand Tufnol Fabric Laminates Data Sheet*. 2004.
96. Prendergast, P.J., *Finite element models in tissue mechanics and orthopaedic implant design.* Clinical Biomechanics, 1997. **12**(6): p. 343-366.
97. Revie, I., M. Wallace, and J.F. Orr, *The Effect of PMMA Thickness on Thermal Bone Necrosis Around Acetabular Sockets.* Proceedings of the Institute of Mechanical Engineers Part H: Engineering in Medicine, 1994(204): p. 45-51.
98. Rohlmann, A., U. Mossner, G. Bergmann, and R. Kolbel, *Finite Element Analysis and Experimental investigation in a femur with hip endoprosthesis.* Journal of Biomechanics, 1983. **16**: p. 727-742.
99. Roques, A., M. Browne, A. Taylor, A. New, and D. Baker, *Quantitative Measurement of the Stresses Induced During Polymerisation of Bone Cement.* Biomaterials, 2004. **25**: p. 4415-4424.
100. Roques, A., A. New, D. Baker, A. Taylor, and M. Browne, *A Quantitative Experiment to Assess the Effects of Physical Changes Due to Bone Cement Polymerisation on the Short and Long Term Structural Integrity of the Bone, PMMA Bone Cement, Implant System.* Journal of Biomaterials, 2003. **25**: p. 4415-4424.
101. Roux, W., *Der Kampf der Teile in Organisms.* 1881.
102. Saulgozis, Y., L. Slutskii, I. Knets, and K. Yanson, *Investigation of the Relations Between the Various Mechanical Properties and the Biochemical*

Composition of Human Bone Tissue. Polymer Mechanics, 1974. **9**(1): p. 119-125.
103. Scherer, G.W. and S.M. Rekhson, *Visco-Elastic Composites: I, General Theory.* Journal of the American Ceramic Society, 1982. **65**(7): p. 352-360.
104. Schmalzreid, T.P., M. Jasty, and W.H. Harris, *Periprosthetic Bone Loss in Total Hip Arthroplasty.* Journal of Bone and Joint Surgery-British Volume, 1992. **74-A**(6): p. 849-863.
105. CreatedBy,*Smith and Nephew - Orthopaedics*,2006,http://ortho.smith-nephew.com
106. Smith, S., D. Dowson, and A. Goldsmith, *The effect of femoral head diameter upon lubrication and wear of metal-on-metal total hip replacements.* Proceedings of the Institution of Mechanical Engineers, Part H: Journal of Engineering in Medicine, 2000. **215**(2): p. 161-170.
107. Stanczyk, M. and B. van Rietbergen, *Thermal Analysis of Bone Cement Polymerisation at the Cement-Bone Interface.* Journal of Biomechanics, 2004. **37**: p. 1803-1810.
108. Starink, M., *Activation Energy Determination for Linear Heating Experiments: Deviations Due to Neglecting the Low Temperature End of the Temperature Integral.* In Press.
109. Starink, M.J., *The Determination of Activation Energy from Linear Heating Rate Experiments: A comparison of the accuracy of isoconversion methods.* In Press, 2003.
110. Starke, G.R., C. Birnie, and P.A. van den Blink. *Numerical modelling of cement polymerisation and thermal bone necrosis*. in *Computer methods in biomechanics and biomedical engineering*. 2001. London: Gordon & Breach.
111. Stauffer, R., *Ten-Year Follow-up Study of Total Hip Replacement.* Journal of Bone and Joint Surgery-American Volume, 1982. **64**(7): p. 983-990.
112. Sunden, G., *Some aspects of longitudinal bone growth.* Acta. Orthopaedica Scandinavica, 1967. **suppl. 103**.
113. The Royal College of Surgeons Clinical Effectiveness Unit, The NJR Centre, and T.N.E.B.f.t.s.A. Report., *National Joint Registry for England and Wales: 2nd Annual Report*. 2005.
114. Treacy, R., C. McBryde, and P. Pynsent, *Birmingham Hip Resurfacing Arthroplasty: A Minimum Follow-Up of Five Years.* Journal of Bone and Joint Surgery, 2005. **87**(B): p. 167-170.
115. CreatedBy,*History of Total Joint Replacement*,http://www.utahhipandknee.com/history.htm
116. Vachon, R., F. Walker, D. Walker, and G. Nix. *In vivo determination of thermal conductivityof bone using the thermal comparator technique*. in *7th International conference on medical and biological engineering*. 1967. Stockholm.
117. Vallo, C.I., *Residual monomer content in bone cements based on poly(methyl methacrylate).* Polymer International, 2000. **49**(8): p. 831-838.
118. Verdonschot, N. and R. Huiskes, *Cement debonding process of total hip arthroplasty stems.* Clinical Orthopaedics and Related Research, 1997. **336**: p. 297-307.
119. Verdonschot, N. and R. Huiskes, *The effects of cement-stem debonding in THA on the long-term failure probability of cement.* Journal of Biomechanics, 1997. **30**(8): p. 795-802.

120. Verdonschot, N. and R. Huiskes, *Surface roughness of debonded straight-tapered stems in cemented THA reduces subsidence but not cement damage.* Biomaterials, 1998. **19**(19): p. 1773-9.
121. Verdonschot, N., E. Tanck, and R. Huiskes, *Effects of prosthesis surface roughness on the failure process of cemented hip implants after stem-cement debonding.* Journal of Biomedical Materials Research, 1998. **42**(4): p. 554-559.
122. Viano, A.M., J.A. Auwarter, J.Y. Rho, and B.K. Hoffmeister, *Ultrasonic characterization of the curing process of hydroxyapatite-modified bone cement.* Journal of Biomedical Materials Research, 2001. **56**(4): p. 593-599.
123. Wang, J.S., H. Franzen, S. Toksviglarsen, and L. Lidgren, *Does Vacuum Mixing of Bone-Cement Affect Heat-Generation - Analysis of 4 Cement Brands.* Journal of Applied Biomaterials, 1995. **6**(2): p. 105-108.
124. Waters KP, H.M., Mobley J and Miller JG, *Differential forms of the Kramers-Kronig Dispersion Relationships.* Trans. on Ultrasonics, Ferroelectrics and Frequency Control, 2003. **50**(1): p. 68-76.
125. Willert, H.-G. and P. Puls, *Die Reaction des Knochens auf Knochenzement bei der Allo-Arthroplastik der Hufte.* Archives of Orthopaedic and Trauma Surgery, 1972. **72**: p. 33-71.
126. Winter, M., *Chemistry: WebElements Periodic Table: Professional Edition: Titanium: thermal properties and temperatures*. 2005, The University of Sheffield.
127. Wolff, J., *Das Gesetz der Transformation der Knocken Hirschwald.* 1892.
128. Wu, J., *Determination of velocity and attenuation of shear waves using ultrasonic spectroscopy.* Journal of the Acoustic Society of America, 1996. **99**(5): p. 2871-2875.
129. Zimmer, *Patient Resources*. 2004.

Appendix I – Model Drawings and Dimensions

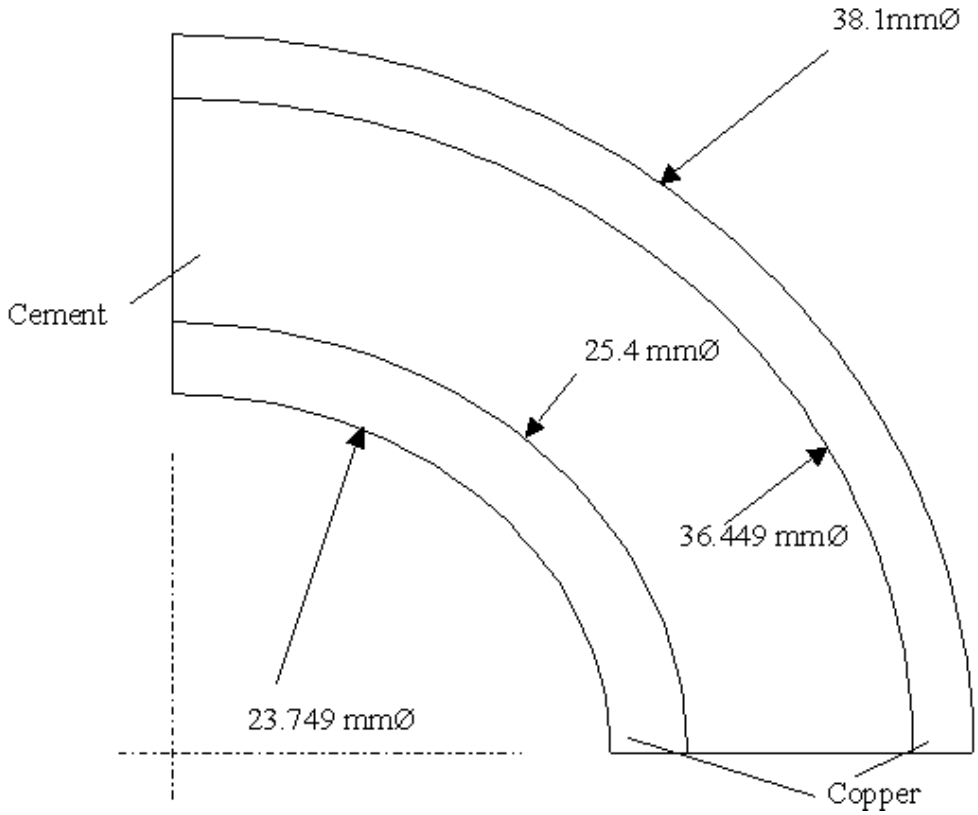

Figure 1 - Concentric cylinders thermal model geometry.

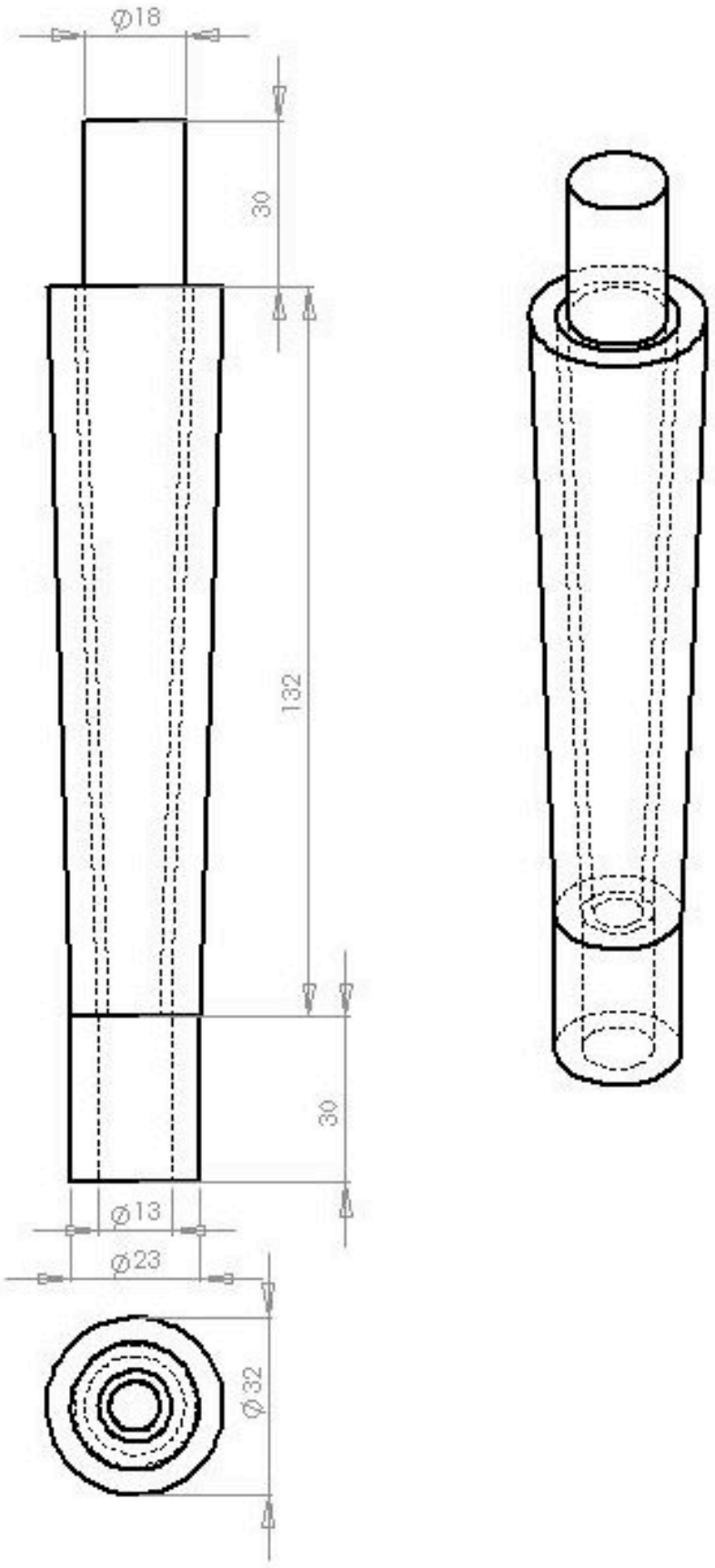

Figure 2 - Idealised stem thermal model geometry.

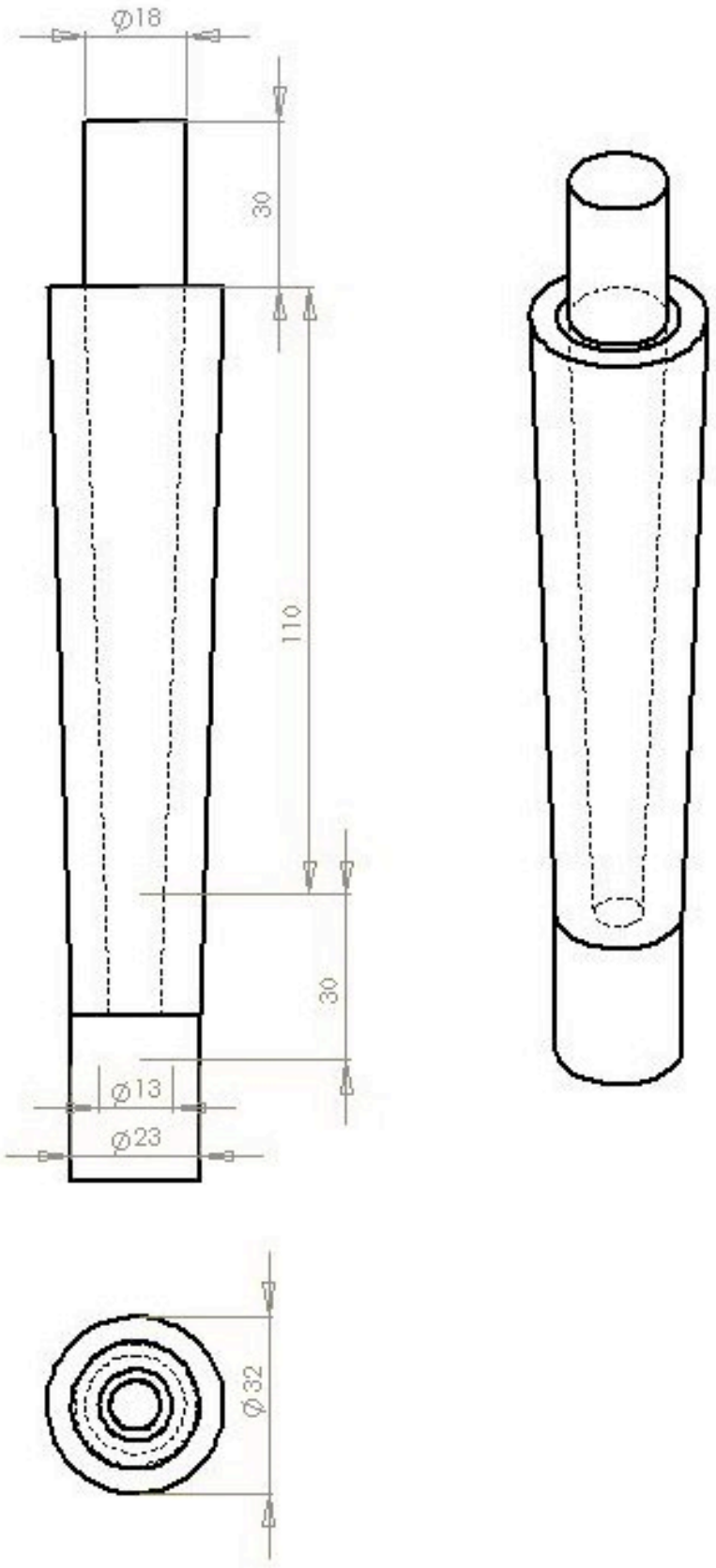

Figure 3 - Experimental idealised stem thermal model geometry.

Appendix II – Finite Element Modelling and Results Processing Codes

Thermal model of idealised stem with 2mm cement mantle

```
!*****************************************Begin Thermal Phase*****************************************

DAlph=0.025       !max amount of change in degree of cure allowed in one increment
Alphinit=6e-6     !initial degree of polymerisation
Qtot=1.55e8       !total amount of heat liberated per unit volume of cement (w/m2)
ConvCoef=10.0     !convection coefficient   (W/m2-K)
K0=9.1574         !ln(K0) taken from Harper model  (CMW1)
Ea_R=3763         !Ea/R taken from Harper model  (CMW1)
n=1.064           !n taken from Harper model  (CMW1)
m=0.98            !taken from Harper model  (CMW1)
TCCCS=5500        !Thermal contact conductance between cement and stem taken from Fried (W/m2-K)
TCCCB=375         !Thermal contact conductance between cement and bone taken from Fried (W/m2-K)

Densinit=0.94e3   !density of uncured cement   (kg/m3)
Dens=1.183e3      !density of cured cement   (kg/m3)
Cond=0.2          !thermal conductivity of cement (assumed constant)   (W/m-K)
CemPois=0.3       !poissons ratio of cement
CemEinit=25e6     !initial value of cement young's modulus (Pa)

StmCond=14.6      !thermal conductivity of stem (W/m-K)
StmSPC=450        !specific heat capacity of Stem (J/kg-K)
StmDens=8870      !density of stem (kg/m3)
StmPois=0.3       !poisson's ratio of stem
StmE=200e9        !stiffness of stem (Pa)

BoneCond=0.38     !conductivity of cortical bone taken from Chato (1965) (W/m-K)
BoneSPC=1260      !specific heat capacity of cortical bone taken from Henschel (1943) (J/kg-K)
BoneDens=2100     !density of cortical bone taken from Henschel (1943) (kg/m3)
BonePois=0.3      !poisson's ratio of cortical bone
BoneE=17e9        !stiffness of cortical bone (Pa)

Stoptime=2000     !time at which polymerisation is assumed to have finished   (s)
Ctime=0.001       !time at which calculations start   (s)
Tinit=296         !initial temperature of bulk (room temperature)   (K)
BodyTemp=310      !body temperature   (K)
StemTemp=296      !stem temperature   (K)
Tref=273          !zero celsius   (K)
DTinit=0.003      !initial timestep size   (s)
DTmax=25          !maximum timestep size   (s)

/PREP7
MPTEMP,,,,,,,,
MPTEMP,1,0
MPDATA,KXX,1,,0.2                !taken from Baliga
MPTEMP,,,,,,,,
MPTEMP,1,0
MPDATA,DENS,1,,Densinit              !taken from Baliga (needs to be found later based on alpha)
MPTEMP,,,,,,,,
MPTEMP,1,0
MPDATA,NUXY,1,,CemPois           !
MPTEMP,,,,,,,,
MPTEMP,1,0
MPDATA,EX,1,,CemEinit            !
MPTEMP,,,,,,,,
MPTEMP,1,273
MPTEMP,2,573
MPDATA,C,1,1,1250                !
MPDATA,C,1,2,3200                !taken from Baliga
MPTEMP,,,,,,,,
MPTEMP,1,0
MPDATA,KXX,2,,StmCond            !taken from Allegheny ludlum 316L stainless (on matweb)
```

```
MPTEMP,,,,,,,,
MPTEMP,1,0
MPDATA,DENS,2,,StmDens              !taken from Allegheny ludlum 316L stainless (on matweb)
MPTEMP,,,,,,,,
MPTEMP,1,0
MPDATA,NUXY,2,,StmPois              !
MPTEMP,,,,,,,,
MPTEMP,1,0
MPDATA,EX,2,,StmE                   !
MPTEMP,,,,,,,,
MPTEMP,1,0
MPDATA,C,2,,StmSPC                  !taken from Allegheny ludlum 316L stainless (on matweb)
MPTEMP,,,,,,,,
MPTEMP,1,0
MPDATA,KXX,3,,BoneCond
MPTEMP,,,,,,,,
MPTEMP,1,0
MPDATA,DENS,3,,BoneDens
MPTEMP,,,,,,,,
MPTEMP,1,0
MPDATA,NUXY,3,,BonePois             !
MPTEMP,,,,,,,,
MPTEMP,1,0
MPDATA,EX,3,,BoneE                  !
MPTEMP,,,,,,,,
MPTEMP,1,0
MPDATA,C,3,,BoneSPC
*SET,neck_l,30e-3                   !length of stem neck protruding from top of model
*SET,neck_w,9e-3                    !width of stem neck
*SET,cem_th,2e-3                    !thickness of cement mantle
*SET,bone_th,5e-3                   !thickness of bone
*SET,stem_l,110e-3                  !length from bottom of stem neck to stem tip
*SET,bone_l,30e-3                   !length of bonepotruding from bottom of model
*SET,stem_w,4.5e-3                  !radius of stem at stem tip
N,1,stem_w+cem_th,0,0
N,2,stem_w+cem_th+bone_th,0,0
N,3,0,bone_l,0
N,4,stem_w,bone_l,0
N,5,stem_w+cem_th,bone_l,0
N,6,stem_w+cem_th+bone_th,bone_l,0
N,7,0,bone_l+stem_l,0
N,8,neck_w,bone_l+stem_l,0
N,9,neck_w+cem_th,bone_l+stem_l,0
N,10,neck_w+cem_th+bone_th,bone_l+stem_l,0
N,11,0,bone_l+stem_l+neck_l,0
N,12,neck_w,bone_l+stem_l+neck_l,0
FLST,3,12,1,ORDE,2
FITEM,3,1
FITEM,3,-12
KNODE,0,P51XA,1,2,6,5
A,1,2,6,5
A,3,4,8,7
A,4,5,9,8
A,5,6,10,9
A,7,8,12,11
ASEL,S,,,1
AATT,3
ASEL,S,,,2
AATT,2
ASEL,S,,,3
AATT,1
ASEL,S,,,4
AATT,3
ASEL,S,,,5
AATT,2
ALLSEL

!*
ET,1,MESH200
KEYOPT,1,1,6
!*
ET,2,SOLID90
!*
TYPE,   1
REAL,
```

```
ESYS,      0
SECNUM,
!*
/UI,MESH,OFF
FLST,5,2,4,ORDE,2
FITEM,5,9
FITEM,5,11
CM,_Y,LINE
LSEL, , , ,P51X
CM,_Y1,LINE
CMSEL,,_Y
!*
LESIZE,_Y1, , ,10, , , , ,1
!*
FLST,5,4,4,ORDE,4
FITEM,5,6
FITEM,5,8
FITEM,5,10
FITEM,5,12
CM,_Y,LINE
LSEL, , , ,P51X
CM,_Y1,LINE
CMSEL,,_Y
!*
LESIZE,_Y1, , ,45, , , , ,1
!*
FLST,5,4,4,ORDE,4
FITEM,5,2
FITEM,5,4
FITEM,5,14
FITEM,5,16
CM,_Y,LINE
LSEL, , , ,P51X
CM,_Y1,LINE
CMSEL,,_Y
!*
LESIZE,_Y1, , ,3, , , , ,1
!*
MSHAPE,0,2D
MSHKEY,1
!*
CM,_Y,AREA
ASEL, , , ,      3
CM,_Y1,AREA
CHKMSH,'AREA'
CMSEL,S,_Y
!*
AMESH,_Y1
!*
CMDELE,_Y
CMDELE,_Y1
CMDELE,_Y2
!*
TYPE,   1
REAL,
ESYS,      0
SECNUM,
!*
FLST,5,2,5,ORDE,2
FITEM,5,2
FITEM,5,5
CM,_Y,AREA
ASEL, , , ,P51X
CM,_Y1,AREA
CHKMSH,'AREA'
CMSEL,S,_Y
!*
AMESH,_Y1
!*
CMDELE,_Y
CMDELE,_Y1
CMDELE,_Y2
!*
TYPE,   1
REAL,
```

```
ESYS,      0
SECNUM,
!*
FLST,5,2,5,ORDE,2
FITEM,5,1
FITEM,5,4
CM,_Y,AREA
ASEL, , , ,P51X
CM,_Y1,AREA
CHKMSH,'AREA'
CMSEL,S,_Y
!*
AMESH,_Y1
!*
CMDELE,_Y
CMDELE,_Y1
CMDELE,_Y2
!*
/UI,MESH,OFF
TYPE,   2
EXTOPT,ESIZE,10,0,
EXTOPT,ACLEAR,1
!*
EXTOPT,ATTR,0,0,0
REAL,_Z4
ESYS,0
!*
FLST,2,5,5,ORDE,2
FITEM,2,1
FITEM,2,-5
FLST,8,2,3
FITEM,8,3
FITEM,8,11
VROTAT,P51X, , , , , ,P51X, ,180,1,


NUMMRG,ALL                  !Merge coincident nodes
NUMCMP,ALL                  !Relabel nodes continuously


FLST,3,1,6,ORDE,1           !
FITEM,3,3                   !
VGEN,2,P51X, , , , , ,0     !Generate new copy of cement for contact analysis
VCLEAR,      3              !
VDELE,      3, , ,1         !

NUMCMP,ALL


! /COM, CONTACT PAIR CREATION - START
CM,_NODECM,NODE
CM,_ELEMCM,ELEM
CM,_LINECM,LINE
CM,_AREACM,AREA
! /GSAV,cwz,gsav,,temp
MP,MU,1,
MAT,1
MP,EMIS,1,
R,3
REAL,3
ET,3,170
ET,4,174
R,3,,,1.0,0.1,0,
RMORE,,,1.0E20,0.0,1.0,
RMORE,0.0,TCCCS,1.0,,1.0,0.5
RMORE,0,1.0,1.0,0.0,
KEYOPT,4,4,0
KEYOPT,4,5,3
KEYOPT,4,7,0
KEYOPT,4,8,0
KEYOPT,4,9,0
KEYOPT,4,10,1
KEYOPT,4,11,0
KEYOPT,4,12,0
KEYOPT,4,2,0
```

```
KEYOPT,3,5,0
KEYOPT,4,1,2
! Generate the target surface
ASEL,S,,,11
CM,_TARGET,AREA
TYPE,3
NSLA,S,1
ESLN,S,0
ESURF,ALL
CMSEL,S,_ELEMCM
! Generate the contact surface
ASEL,S,,,24
CM,_CONTACT,AREA
TYPE,4
NSLA,S,1
ESLN,S,0
ESURF,ALL
ALLSEL
ESEL,ALL
ESEL,S,TYPE,,3
ESEL,A,TYPE,,4
ESEL,R,REAL,,3
! /PSYMB,ESYS,1
! /PNUM,TYPE,1
! /NUM,1
! EPLOT
ESEL,ALL
ESEL,S,TYPE,,3
ESEL,A,TYPE,,4
ESEL,R,REAL,,3
CMSEL,A,_NODECM
CMDEL,_NODECM
CMSEL,A,_ELEMCM
CMDEL,_ELEMCM
CMSEL,S,_LINECM
CMDEL,_LINECM
CMSEL,S,_AREACM
CMDEL,_AREACM
! /GRES,cwz,gsav
CMDEL,_TARGET
CMDEL,_CONTACT
! /COM, CONTACT PAIR CREATION - END

!Repeat contact pair generation for all contact surfaces required

NUMCMP,ALL                      !Relabel nodes continuously

VSEL,S,VOLU,,5              !picks cement volumes
NSLV,S,1                  !selects associated nodes
CM,CEMNODES,NODE              !assigns the cement nodes to component CEMNODES
*GET,NCNode,NODE,0,COUNT      !finds number of cement nodes and assigns to NCNode

VSEL,S,VOLU,,1,3,2          !picks bone volumes
NSLV,S,1                  !selects associated nodes
CM,BNNODES,NODE               !assigns the Bone nodes to component BNNODES

VSEL,S,VOLU,,2,4,2          !picks Stem volumes
NSLV,S,1                  !selects associated nodes
CM,STNODES,NODE               !assigns the Stem nodes to component STNODES
CMSEL,U,CEMNODES              !deselect cement nodes
CMSEL,U,BNNODES               !deselect stem nodes
CM,STMNODES,NODE              !assigns the stem nodes to component STMNODES
*GET,NSNode,NODE,0,COUNT      !finds number of Stem nodes and assigns to NSNode
ALLSEL
CMSEL,U,CEMNODES              !deselect cement nodes
CMSEL,U,STNODES               !deselect stem nodes
CM,BONNODES,NODE              !assigns the stem nodes to component BONNODES
*GET,NBNode,NODE,0,COUNT      !finds number of Bone nodes and assigns to NBNode

ALLSEL                    !selects everything

VSEL,S,VOLU,,1,3,2          !picks bone volumes
ESLV,S,1                  !selects associated elements
ESEL,U,TYPE,,3
ESEL,U,TYPE,,4
```

```
CM,BONELEM,ELEM              !assigns the bone elements to component BONELEM
EMODIF,ALL,MAT,3             !set the bone properties to material type 3

VSEL,S,VOLU,,2,4,2           !picks stem volumes
ESLV,S,1                     !selects associated elements
ESEL,U,TYPE,,3
ESEL,U,TYPE,,4
CM,STMELEM,ELEM              !assigns the stem elements to component STMELEM
EMODIF,ALL,MAT,2             !set the stem properties to material type 2

ALLSEL


*GET,NNode,NODE,0,COUNT      !finds total number of nodes and assigns to NNode
ESEL,U,TYPE,,3
ESEL,U,TYPE,,4
*GET,NElem,ELEM,0,COUNT      !finds total number of Elements and assigns to NElem
*DIM,AE,ARRAY,NElem          !dimensions an array AE of length NElem

*DIM,ELEMNUM,ARRAY,NElem     !dimensions an array ELEMNUM of length NElem
*DIM,ELEMTEMP,ARRAY,NElem    !dimensions an array ELEMTEMP of length NElem
*DIM,ELEMMTRX,ARRAY,NElem,4  !dimensions an array ELEMMTRX of length NElem x 4

PNGR,TMOD,10
 VPLOT
 /ANG, 1 ,30.000000,XS,1
 /REP,FAST
 /GSAVE,'Planar',' ',        !saves view settings

FINISH


/SOLU

   *DIM,Temp1,ARRAY,NNode    !vector for temporary storage
   *DIM,Temp2,ARRAY,NNode    !vector for temporary storage
   *DIM,Temp3,ARRAY,NNode    !vector for temporary storage
   *DIM,Temp4,ARRAY,NNode    !vector for temporary storage

*DIM,Pars,ARRAY,NNode,4      !dimensions an array (NNode , 4) for parameters of all nodes

*DIM,CPars,ARRAY,NCNode,4    !dimensions an array (NCNode , 4) for parameters of cement nodes

*DIM,CemMask,ARRAY,Nnode     !mask vector for cement nodes
*DIM,BonMask,ARRAY,Nnode     !mask vector for bone nodes
*DIM,StemMask,ARRAY,Nnode    !mask vector for stem nodes
*DIM,BeleMask,ARRAY,NElem    !Mask vector for Bone elements
*DIM,SeleMask,ARRAY,NElem    !Mask vector for Stem elements

CMSEL,S,CEMNODES
*VGET,CemMask(1),NODE,,NSEL  !fill cement mask vector with cement nodes
ALLSEL
CMSEL,S,BONNODES
*VGET,BonMask(1),NODE,,NSEL  !fill bone mask vector with bone nodes
ALLSEL
CMSEL,S,STMNODES
*VGET,StemMask(1),NODE,,NSEL !fill stem mask vector with bone nodes
ALLSEL
CMSEL,S,BONELEM
*VGET,BeleMask(1),ELEM,,ESEL !fill bone element mask vector with bone elements
ALLSEL
CMSEL,S,STMELEM
*VGET,SeleMask(1),ELEM,,ESEL !fill stem element mask vector with stem elements
ALLSEL


*VFILL,Pars(1,1),RAMP,1,1    !set numbers (1-NNode) for all nodes in Pars array
*VFILL,ELEMNUM(1),RAMP,1,1   !Set numbers (1-NElem) for all elements in NUMELEM
*VFILL,ELEMTEMP(1),RAMP,Tinit,0!set initial element temperatures in ELEMTEMP

*VFILL,Pars(1,2),RAMP,Tinit,0  !set initial temperature in Pars array

*VFILL,Pars(1,3),RAMP,0,0    !set initial degree of polymerisation in Pars array
*VMASK,CemMask(1)            !performs the operation only for the cement nodes
*VFILL,Pars(1,3),RAMP,Alphinit,0 !set initial degree of polymerisation in Pars array
```

```
!initial volumetric heat generation rate (S) must now be found

 A0=1-Alphinit                    !1-alpha
 A1=A0**n                         !(1-alpha)**n
 A2=Alphinit**m                     !alpha**m
 A=A1*A2                          !alpha**m x (1-alpha)**n
 B0=Ea_R/Tinit                     !Ea/RT
 B1=K0-B0                         !ln(K0)-Ea/RT
 K=exp(B1)                        !e**(ln(K0)-Ea/RT)=K
 S=K*A*Qtot                        !K x (alpha**m x (1-alpha)**n) = S (Heat Generation Rate)
 *VMASK,CemMask(1)                    !performs the operation only for the cement nodes
 *VFILL,Pars(1,4),RAMP,S,0            !enter heat generation rates into Pars array


!stem Temperature must be applied to nodes

*VMASK,StemMask(1)                  !
*VFUN,Temp1(1),COMP,Pars(1,1)            !fills Temp1 with Stem node numbers
*DO,COUNT,1,NSNode                   !
Pars(Temp1(COUNT),2)=StemTemp            !puts stem temp into pars array for stem nodes initial conditions
*ENDDO                              !

!body Temperature must be applied to nodes

*VMASK,BonMask(1)                   !
*VFUN,Temp1(1),COMP,Pars(1,1)            !fills Temp1 with bone node numbers
*DO,COUNT,1,NBNode                   !
Pars(Temp1(COUNT),2)=BodyTemp            !puts body temp into pars array for bone nodes initial conditions
*ENDDO                              !

!heat generation rate must be applied to nodes

*VMASK,CemMask(1)                   !
*VFUN,Temp1(1),COMP,Pars(1,1)            !fills Temp1 with cement node numbers
*VMASK,CemMask(1)                   !
*VFUN,Temp2(1),COMP,Pars(1,4)            !fills Temp2 with cement node Heat Generation Rates

*DO,COUNT,1,NCNode                   !
BF,Temp1(COUNT),HGEN,Temp2(COUNT)        !applies Heat Generation rates to respective nodes
*ENDDO                              !


DT=DTInit

!solution loop must begin


*DO,DUMMY,1,100000,1

*IF,Ctime,LT,Stoptime,THEN           !apply nodal temperatures
 *DO,Count,1,Nnode
 IC,Pars(Count,1),TEMP,Pars(Count,2)
 *ENDDO

!heat flow equations for temperature must be solved

  OUTRES,,ALL
  ANTYPE,4
  TRNOPT,FULL
  TIME,DT                          !time at end of load step
  NSUBST,5                          !5 substeps to be taken in this load step
  FLST,2,4,5,ORDE,4                    !
  FITEM,2,7                        !
  FITEM,2,16                        !
  FITEM,2,11                        !
  FITEM,2,20                        !applies body temperature to external surfaces of bone
  /GO                            !
  !*                            !
  ASEL,S,AREA,,6,,1                    !
  NSLA,S,1                         !selects nodes associated with selected areas
  D,ALL,TEMP,BodyTemp                  !applies the constant temperature condition to the bone surface
```

```
  ASEL,S,AREA,,15,,,1                    !
  NSLA,S,1                          !selects nodes associated with selected areas
  D,ALL,TEMP,BodyTemp                    !applies the constant temperature condition to the bone surface
  ASEL,S,AREA,,18,,,1                    !
  SFA,ALL,,CONV,ConvCoef,Tinit           !applies convection conditions
  ASEL,S,AREA,,19,,,1                    !
  SFA,ALL,,CONV,ConvCoef,Tinit           !applies convection conditions

  !all other surfaces adiabatic by default
  ALLSEL
  KBC,1                             !step boundary condition as opposed to ramped loading
  CNVTOL,TEMP,50,0.0001                  !sets convergence values for temperature
  CNVTOL,HEAT,100,0.0001                 !and heat flow
  AUTOTS,ON                         !specifies that automatic time stepping is to be used
  OUTPR,BASIC,LAST                       !sets a printout of basic values at end of each load step

SOLVE

/POST1
SET,LAST                            !defines the data set to be read from the results file

 *VGET,Pars(1,2),NODE,Pars(1,1),TEMP     !read in nodal temperatures to Pars array
 *VMASK,CemMask(1)                  !performs the operation only for the cement nodes
 *VOPER,Temp1(1),Pars(1,4),MULT,DT/Qtot  !calculate new value of alpha
 *VOPER,Pars(1,3),Pars(1,3),ADD,Temp1(1) !store alpha values in Pars array
*DO,Count,1,Nnode
 *IF,Pars(Count,3),GT,1,THEN
  Pars(Count,3)=1
 *ENDIF
*ENDDO


 *VMASK,BonMask(1)
 *VFILL,Pars(1,3),RAMP,0,0
 *VMASK,StemMask(1)
 *VFILL,Pars(1,3),RAMP,0,0


  !calculate heat generation rate S for each node based on current T and Alph

  *VOPER,Temp1(1),1,SUB,Pars(1,3)        !1-alpha
  *VFUN,Temp1(1),PWR,Temp1(1),n          !(1-alpha)**n
  *VFUN,Temp2(1),PWR,Pars(1,3),m         !alpha**m
  *VOPER,Temp3(1),Temp1(1),MULT,Temp2(1)  !alpha**m x (1-alpha)**n
  *VOPER,Temp1(1),Ea_R,DIV,Pars(1,2)     !Ea/RT
  *VOPER,Temp1(1),K0,SUB,Temp1(1)        !ln(K0)-Ea/RT
  *VFUN,Temp1(1),EXP,Temp1(1)            !e**(ln(K0)-Ea/RT)=K
  *VOPER,Pars(1,4),Temp3(1),MULT,Temp1(1)  !K x (alpha**m x (1-alpha)**n) = dalph/dt (polymerisation Rate)
  *VOPER,Pars(1,4),Pars(1,4),MULT,Qtot    !dalph/dt x Qtot = S (heat generation rate)

 !plot the temperature contour and save a copy of this plot (for animation purposes)
 /SHOW,PNG
 PNGR,COMP,1,-1
 PNGR,ORIENT,HORIZ
 /GFILE,800,
 /GRESUME,'Planar',' ',' '
 /CONTOUR,,,295,,343
 !leave in next line for temperature plot
  !PLNSOL,TEMP, ,0,
 !plot the cure contour and save a copy of this plot (for animation purposes)
 /CONTOUR,,,0,,1

!Create array full of degree of polymerisation values for mechanical analysis
  *GET,CELEM,ELEM,0,NUM,MIN
  *DO,COUNT,1,NElem
   *GET,N1,ELEM,CELEM,NODE,1
   *GET,N2,ELEM,CELEM,NODE,2
   *GET,N3,ELEM,CELEM,NODE,3
   *GET,N4,ELEM,CELEM,NODE,4
   *GET,N5,ELEM,CELEM,NODE,5
   *GET,N6,ELEM,CELEM,NODE,6
   *GET,N7,ELEM,CELEM,NODE,7
   *GET,N8,ELEM,CELEM,NODE,8
   div=8
   *IF,N1,EQ,0,THEN
```

```
  N1=1
  div=div-1
  *ENDIF
  *IF,N2,EQ,0,THEN
  N2=1
  div=div-1
  *ENDIF
  *IF,N3,EQ,0,THEN
  N3=1
  div=div-1
  *ENDIF
  *IF,N4,EQ,0,THEN
  N4=1
  div=div-1
  *ENDIF
  *IF,N5,EQ,0,THEN
  N5=1
  div=div-1
  *ENDIF
  *IF,N6,EQ,0,THEN
  N6=1
  div=div-1
  *ENDIF
  *IF,N7,EQ,0,THEN
  N7=1
  div=div-1
  *ENDIF
  *IF,N8,EQ,0,THEN
  N8=1
  div=div-1
  *ENDIF
  AE(CELEM)=(PARS(N1,3)+PARS(N2,3)+PARS(N3,3)+PARS(N4,3)+PARS(N5,3)+PARS(N6,3)+PARS(N7,3)+PARS(N8,3))/div
!fills AE with degree of polymerisation values
  *GET,CELEM,ELEM,CELEM,NXTH
 *ENDDO
*VMASK,BeleMask(1)
 *VFILL,AE(1),RAMP,0,0
*VMASK,SeleMask(1)
 *VFILL,AE(1),RAMP,0,0
 ETABLE,arg1,
 *VPUT,AE(1),ELEM,1,ETAB,arg1

ESEL,U,TYPE,,3,4

!Leave in for cure plot
 PLETAB,arg1
 /REPLOT
 /SHOW,CLOSE
 /DEVICE,VECTOR,0

allsel

!Create array with element temperatures for mechanical analysis
 *GET,CELEM,ELEM,0,NUM,MIN
 *DO,COUNT,1,NElem
  *GET,N1,ELEM,CELEM,NODE,1
  *GET,N2,ELEM,CELEM,NODE,2
  *GET,N3,ELEM,CELEM,NODE,3
  *GET,N4,ELEM,CELEM,NODE,4
  *GET,N5,ELEM,CELEM,NODE,5
  *GET,N6,ELEM,CELEM,NODE,6
  *GET,N7,ELEM,CELEM,NODE,7
  *GET,N8,ELEM,CELEM,NODE,8
  div=8
  *IF,N1,EQ,0,THEN
  N1=1
  div=div-1
  *ENDIF
  *IF,N2,EQ,0,THEN
  N2=1
  div=div-1
  *ENDIF
  *IF,N3,EQ,0,THEN
  N3=1
  div=div-1
```

```
  *ENDIF
  *IF,N4,EQ,0,THEN
  N4=1
  div=div-1
  *ENDIF
  *IF,N5,EQ,0,THEN
  N5=1
  div=div-1
  *ENDIF
  *IF,N6,EQ,0,THEN
  N6=1
  div=div-1
  *ENDIF
  *IF,N7,EQ,0,THEN
  N7=1
  div=div-1
  *ENDIF
  *IF,N8,EQ,0,THEN
  N8=1
  div=div-1
  *ENDIF

ELEMTEMP(CELEM)=(PARS(N1,2)+PARS(N2,2)+PARS(N3,2)+PARS(N4,2)+PARS(N5,2)+PARS(N6,2)+PARS(N7,2)+PARS(N8,2))/
div !fills ELEMTEMP with Temperature values
  *GET,CELEM,ELEM,CELEM,NXTH
 *ENDDO


*MFUN,ELEMMTRX(1,1),COPY,ELEMNUM(1)
*MFUN,ELEMMTRX(1,2),COPY,ELEMTEMP(1)
*MFUN,ELEMMTRX(1,3),COPY,AE(1)
ELEMMTRX(1,4)=Ctime
*MWRITE,ELEMMTRX(1,1),File%DUMMY%,swell
(F20.10)

 FINISH
 /SOLU

!apply heat generation rate, S, to nodes

 Smax=0
 *VMASK,CemMask(1)                    !
 *VFUN,Temp1(1),COMP,Pars(1,1)            !sets Temp1 as mask vector of cement node numbers
 *VMASK,CemMask(1)                    !
 *VFUN,Temp2(1),COMP,Pars(1,4)            !sets Temp2 as mask vector of cement node heat generation rates
 *DO,Count,1,NCnode                  !
  BF,Temp1(Count),HGEN,Temp2(Count)       !applies heat generation rate to nodes
  *IF,Temp2(Count),GT,Smax,THEN          !
  Smax=Temp2(Count)                  !finds the largest heat generation rate of all nodes
  *ENDIF
  *ENDDO



!calculate appropriate time step

 *IF,Smax,NE,0,THEN                   !
  DT=(DAlph*Qtot)/Smax                !finds appropriate time step size
 *IF,DT,GT,DTMax,THEN                 !
  DT=DTMax                         !
 *ENDIF                            !
 *ELSE                             !
  DT=DTMax                         !
 *ENDIF                            !
  Ctime=Ctime+DT                     !finds current time

 *ELSE
  *EXIT

 *ENDIF

FINISH
/PREP7

!apply new material properties
```

```
*VMASK,AE(1)                          !use AE array as a cement element mask vector
*VFUN,Temp1(1),COMP,Pars(1,1)                 !fill temp1 with cement element numbers
*DO,Count,1,NElem
 *IF,AE(Count),GT,0,THEN
! MP,EX,Count+3,AE(Count)*(2.5e9-CemEinit)+CemEinit
! MP,NUXY,Count+3,0.3
 MP,DENS,Count+3,AE(Count)*(Dens-Densinit)+Densinit
 MP,KXX,Count+3,Cond
 MPTEMP,,,,,,,,
 MPTEMP,1,273
 MPTEMP,2,573
 MPDATA,C,Count+3,1,1250
 MPDATA,C,Count+3,2,3200
 EMODIF,Count,MAT,Count+3
 *ENDIF
*ENDDO

FINISH
/SOLU

*ENDDO                                !loops for next time increment


!close results file
 *CFCLOS

!*****************************************End of Thermal phase*************************************
/eof
```

Mechanical Analysis of Idealised stem with 2mm cement mantle

```
!*****************************************Begin Structural phase*************************************

DAlph=0.025       !max amount of change in degree of cure allowed in one increment
Alphinit=6e-6     !initial degree of polymerisation
Qtot=1.55e8       !total amount of heat liberated per unit volume of cement (w/m2)
ConvCoef=10.0     !convection coefficient  (W/m2-K)
K0=9.1574         !ln(K0) taken from Harper model  (CMW1)
Ea_R=3763         !Ea/R taken from Harper model  (CMW1)
n=1.064           !n taken from Harper model  (CMW1)
m=0.98            !taken from Harper model  (CMW1)

Densinit=0.94e3   !density of uncured cement mix   (kg/m3)
Dens=1.183e3      !density of cured cement   (kg/m3)
Cond=0.2          !thermal conductivity of cement (assumed constant)  (W/m-K)
CemPois=0.3       !poissons ratio of cement
CemEinit=2.5e7    !initial value of cement young's modulus (Pa)
CemE=2.5e9        !final value of cement youngs modulus  (Pa)

StmCond=14.6      !thermal conductivity of stem (W/m-K)
StmSPC=450        !specific heat capacity of Stem (J/kg-K)
StmDens=8870      !density of stem (kg/m3)
StmPois=0.3       !poisson's ratio of stem
StmE=200e9        !stiffness of stem (Pa)

BoneCond=0.38     !conductivity of cortical bone taken from Chato (1965) (W/m-K)
BoneSPC=1260      !specific heat capacity of cortical bone taken from Henschel (1943) (J/kg-K)
BoneDens=2100     !density of cortical bone taken from Henschel (1943) (kg/m3)
BonePois=0.3      !poisson's ratio of cortical bone
BoneE=17e9        !stiffness of cortical bone (Pa)

Stoptime=2000     !time at which polymerisation is assumed to have finished  (s)
Ctime=0.001       !time at which calculations start  (s)
Tinit=296         !initial temperature of bulk (room temperature)  (K)
BodyTemp=310      !body temperature  (K)
StemTemp=310      !stem temperature  (K)
Tref=273          !zero celsius  (K)
DTinit=0.003      !initial timestep size  (s)
DTmax=25          !maximum timestep size  (s)

/PREP7
MPTEMP,,,,,,,,
MPTEMP,1,0
MPDATA,KXX,1,,0.2                !taken from Baliga
MPTEMP,,,,,,,,
MPTEMP,1,0
MPDATA,DENS,1,,Densinit          !taken from Baliga (needs to be found later based on alpha)
MPTEMP,,,,,,,,
MPTEMP,1,0
MPDATA,NUXY,1,,CemPois           !
MPTEMP,,,,,,,,
MPTEMP,1,0
MPDATA,EX,1,,CemEinit            !
MPTEMP,,,,,,,,
MPTEMP,1,273
MPTEMP,2,573
MPDATA,C,1,1,1250                !
MPDATA,C,1,2,3200                !taken from Baliga
MPTEMP,,,,,,,,
MPTEMP,1,0
MPDATA,KXX,2,,StmCond            !taken from Allegheny ludlum 316L stainless (on matweb)
MPTEMP,,,,,,,,
MPTEMP,1,0
MPDATA,DENS,2,,StmDens           !taken from Allegheny ludlum 316L stainless (on matweb)
MPTEMP,,,,,,,,
MPTEMP,1,0
MPDATA,NUXY,2,,StmPois           !
MPTEMP,,,,,,,,
MPTEMP,1,0
MPDATA,EX,2,,StmE                !
MPTEMP,,,,,,,,
```

```
MPTEMP,1,0
MPDATA,C,2,,StmSPC                !taken from Allegheny ludlum 316L stainless (on matweb)
MPTEMP,,,,,,,,
MPTEMP,1,0
MPDATA,KXX,3,,BoneCond
MPTEMP,,,,,,,,
MPTEMP,1,0
MPDATA,DENS,3,,BoneDens
MPTEMP,,,,,,,,
MPTEMP,1,0
MPDATA,NUXY,3,,BonePois           !
MPTEMP,,,,,,,,
MPTEMP,1,0
MPDATA,EX,3,,BoneE                !
MPTEMP,,,,,,,,
MPTEMP,1,0
MPDATA,C,3,,BoneSPC
*SET,neck_l,30e-3                 !length of stem neck protruding from top of model
*SET,neck_w,9e-3                  !width of stem neck
*SET,cem_th,2e-3                  !thickness of cement mantle
*SET,bone_th,5e-3                 !thickness of bone
*SET,stem_l,110e-3                !length from bottom of stem neck to stem tip
*SET,bone_l,30e-3                 !length of bonepotruding from bottom of model
*SET,stem_w,4.5e-3                !radius of stem at stem tip
N,1,stem_w+cem_th,0,0
N,2,stem_w+cem_th+bone_th,0,0
N,3,0,bone_l,0
N,4,stem_w,bone_l,0
N,5,stem_w+cem_th,bone_l,0
N,6,stem_w+cem_th+bone_th,bone_l,0
N,7,0,bone_l+stem_l,0
N,8,neck_w,bone_l+stem_l,0
N,9,neck_w+cem_th,bone_l+stem_l,0
N,10,neck_w+cem_th+bone_th,bone_l+stem_l,0
N,11,0,bone_l+stem_l+neck_l,0
N,12,neck_w,bone_l+stem_l+neck_l,0
FLST,3,12,1,ORDE,2
FITEM,3,1
FITEM,3,-12
KNODE,0,P51XA,1,2,6,5
A,1,2,6,5
A,3,4,8,7
A,4,5,9,8
A,5,6,10,9
A,7,8,12,11
ASEL,S,,,1
AATT,3
ASEL,S,,,2
AATT,2
ASEL,S,,,3
AATT,1
ASEL,S,,,4
AATT,3
ASEL,S,,,5
AATT,2
ALLSEL

!*
ET,1,MESH200
KEYOPT,1,1,6
!*
ET,2,SOLID95
!*
TYPE,   1
REAL,
ESYS,      0
SECNUM,
!*
/UI,MESH,OFF
FLST,5,2,4,ORDE,2
FITEM,5,9
FITEM,5,11
CM,_Y,LINE
LSEL, , , ,P51X
CM,_Y1,LINE
```

```
CMSEL,,_Y
!*
LESIZE,_Y1, , ,10, , , , ,1
!*
FLST,5,4,4,ORDE,4
FITEM,5,6
FITEM,5,8
FITEM,5,10
FITEM,5,12
CM,_Y,LINE
LSEL, , , ,P51X
CM,_Y1,LINE
CMSEL,,_Y
!*
LESIZE,_Y1, , ,45, , , , ,1
!*
FLST,5,4,4,ORDE,4
FITEM,5,2
FITEM,5,4
FITEM,5,14
FITEM,5,16
CM,_Y,LINE
LSEL, , , ,P51X
CM,_Y1,LINE
CMSEL,,_Y
!*
LESIZE,_Y1, , ,3, , , , ,1
!*
MSHAPE,0,2D
MSHKEY,1
!*
CM,_Y,AREA
ASEL, , , ,       3
CM,_Y1,AREA
CHKMSH,'AREA'
CMSEL,S,_Y
!*
AMESH,_Y1
!*
CMDELE,_Y
CMDELE,_Y1
CMDELE,_Y2
!*
TYPE,   1
REAL,
ESYS,      0
SECNUM,
!*
FLST,5,2,5,ORDE,2
FITEM,5,2
FITEM,5,5
CM,_Y,AREA
ASEL, , , ,P51X
CM,_Y1,AREA
CHKMSH,'AREA'
CMSEL,S,_Y
!*
AMESH,_Y1
!*
CMDELE,_Y
CMDELE,_Y1
CMDELE,_Y2
!*
TYPE,   1
REAL,
ESYS,      0
SECNUM,
!*
FLST,5,2,5,ORDE,2
FITEM,5,1
FITEM,5,4
CM,_Y,AREA
ASEL, , , ,P51X
CM,_Y1,AREA
CHKMSH,'AREA'
```

```
CMSEL,S,_Y
!*
AMESH,_Y1
!*
CMDELE,_Y
CMDELE,_Y1
CMDELE,_Y2
!*
/UI,MESH,OFF
TYPE,   2
EXTOPT,ESIZE,10,0,
EXTOPT,ACLEAR,1
!*
EXTOPT,ATTR,0,0,0
REAL,_Z4
ESYS,0
!*
FLST,2,5,5,ORDE,2
FITEM,2,1
FITEM,2,-5
FLST,8,2,3
FITEM,8,3
FITEM,8,11
VROTAT,P51X, , , , , ,P51X, ,180,1,

NUMMRG,ALL                !Merge coincident nodes
NUMCMP,ALL                !Relabel nodes continuously


FLST,3,1,6,ORDE,1         !
FITEM,3,3                 !
VGEN,2,P51X, , , , , ,0   !Generate new copy of cement for contact analysis
VCLEAR,      3            !
VDELE,      3, , ,1       !

NUMCMP,ALL

! /COM, CONTACT PAIR CREATION - START
CM,_NODECM,NODE
CM,_ELEMCM,ELEM
CM,_LINECM,LINE
CM,_AREACM,AREA
! /GSAV,cwz,gsav,,temp
MP,MU,1,0.2
MAT,1
R,3
REAL,3
ET,3,170
ET,4,174
KEYOPT,4,9,0
R,3,
RMORE,
RMORE,,0
RMORE,0
! Generate the target surface
ASEL,S,,,11
CM,_TARGET,AREA
TYPE,3
NSLA,S,1
ESLN,S,0
ESURF,ALL
CMSEL,S,_ELEMCM
! Generate the contact surface
ASEL,S,,,24
CM,_CONTACT,AREA
TYPE,4
NSLA,S,1
ESLN,S,0
ESURF,ALL
ALLSEL
ESEL,ALL
ESEL,S,TYPE,,3
ESEL,A,TYPE,,4
ESEL,R,REAL,,3
! /PSYMB,ESYS,1
```

```
! /PNUM,TYPE,1
! /NUM,1
! EPLOT
ESEL,ALL
ESEL,S,TYPE,,3
ESEL,A,TYPE,,4
ESEL,R,REAL,,3
CMSEL,A,_NODECM
CMDEL,_NODECM
CMSEL,A,_ELEMCM
CMDEL,_ELEMCM
CMSEL,S,_LINECM
CMDEL,_LINECM
CMSEL,S,_AREACM
CMDEL,_AREACM
! /GRES,cwz,gsav
CMDEL,_TARGET
CMDEL,_CONTACT
! /COM, CONTACT PAIR CREATION - END

! /COM, CONTACT PAIR CREATION - START
CM,_NODECM,NODE
CM,_ELEMCM,ELEM
CM,_LINECM,LINE
CM,_AREACM,AREA
! /GSAV,cwz,gsav,,temp
MP,MU,1,0.2
MAT,1
R,4
REAL,4
ET,5,170
ET,6,174
KEYOPT,6,9,0
R,4,
RMORE,
RMORE,,0
RMORE,0
! Generate the target surface
ASEL,S,,,14
CM,_TARGET,AREA
TYPE,5
NSLA,S,1
ESLN,S,0
ESURF,ALL
CMSEL,S,_ELEMCM
! Generate the contact surface
ASEL,S,,,22
CM,_CONTACT,AREA
TYPE,6
NSLA,S,1
ESLN,S,0
ESURF,ALL
ALLSEL
ESEL,ALL
ESEL,S,TYPE,,5
ESEL,A,TYPE,,6
ESEL,R,REAL,,4
! /PSYMB,ESYS,1
! /PNUM,TYPE,1
! /NUM,1
! EPLOT
ESEL,ALL
ESEL,S,TYPE,,5
ESEL,A,TYPE,,6
ESEL,R,REAL,,4
CMSEL,A,_NODECM
CMDEL,_NODECM
CMSEL,A,_ELEMCM
CMDEL,_ELEMCM
CMSEL,S,_LINECM
CMDEL,_LINECM
CMSEL,S,_AREACM
CMDEL,_AREACM
! /GRES,cwz,gsav
CMDEL,_TARGET
```

```
CMDEL,_CONTACT
! /COM, CONTACT PAIR CREATION - END

!Repeat contact pair generation for all relevant surfaces

NUMCMP,ALL


VSEL,S,VOLU,,5              !picks cement volumes
NSLV,S,1                    !selects associated nodes
CM,CEMNODES,NODE            !assigns the cement nodes to component CEMNODES
*GET,NCNode,NODE,0,COUNT    !finds number of cement nodes and assigns to NCNode

VSEL,S,VOLU,,1,3,2          !picks bone volumes
NSLV,S,1                    !selects associated nodes
CM,BNNODES,NODE             !assigns the Bone nodes to component BNNODES

VSEL,S,VOLU,,2,4,2          !picks Stem volumes
NSLV,S,1                    !selects associated nodes
CM,STNODES,NODE             !assigns the Stem nodes to component STNODES
ALLSEL
CMSEL,U,CEMNODES            !deselect cement nodes
CMSEL,U,BNNODES             !deselect stem nodes
CM,STMNODES,NODE            !assigns the stem nodes to component STMNODES
*GET,NSNode,NODE,0,COUNT    !finds number of Stem nodes and assigns to NSNode
ALLSEL
CMSEL,U,CEMNODES            !deselect cement nodes
CMSEL,U,STNODES             !deselect stem nodes
CM,BONNODES,NODE            !assigns the stem nodes to component BONNODES
*GET,NBNode,NODE,0,COUNT    !finds number of Bone nodes and assigns to NBNode

ALLSEL                      !selects everything

VSEL,S,VOLU,,1,3,2          !picks bone volumes
ESLV,S,1                    !selects associated elements
ESEL,U,TYPE,,3
ESEL,U,TYPE,,4
ESEL,U,TYPE,,5
ESEL,U,TYPE,,6
ESEL,U,TYPE,,7
ESEL,U,TYPE,,8
ESEL,U,TYPE,,9
ESEL,U,TYPE,,10
CM,BONELEM,ELEM             !assigns the bone elements to component BONELEM
EMODIF,ALL,MAT,3            !set the bone properties to material type 3

VSEL,S,VOLU,,2,4,2          !picks stem volumes
ESLV,S,1                    !selects associated elements
ESEL,U,TYPE,,3
ESEL,U,TYPE,,4
ESEL,U,TYPE,,5
ESEL,U,TYPE,,6
ESEL,U,TYPE,,7
ESEL,U,TYPE,,8
ESEL,U,TYPE,,9
ESEL,U,TYPE,,10
CM,STMELEM,ELEM             !assigns the stem elements to component STMELEM
EMODIF,ALL,MAT,2            !set the stem properties to material type 2

ALLSEL


*GET,NNode,NODE,0,COUNT     !finds total number of nodes and assigns to NNode
ESEL,U,TYPE,,3              !Deselects contact elements
ESEL,U,TYPE,,4
ESEL,U,TYPE,,5
ESEL,U,TYPE,,6
ESEL,U,TYPE,,7
ESEL,U,TYPE,,8
ESEL,U,TYPE,,9
ESEL,U,TYPE,,10
*GET,NElem,ELEM,0,COUNT     !finds total number of Elements and assigns to NElem
*DIM,AE,ARRAY,NElem         !dimensions an array AE of length NElem

*DIM,ELEMNUM,ARRAY,NElem    !dimensions an array ELEMNUM of length NElem
```

```
*DIM,ELEMTEMP,ARRAY,NElem      !dimensions an array ELEMTEMP of length NElem
*DIM,ELEMMTRX,ARRAY,NElem,4    !dimensions an array ELEMMTRX of length NElem x 4
*DIM,ELEMMTRX_1,ARRAY,NElem,4    !dimensions an array ELEMMTRX_1 of length NElem x 4
*DIM,ELEMMTRX_2,ARRAY,NElem

*DO,DUMMY,1,100000,1                    !Begin Solution Loop

ALLSEL

/solu

*VREAD,ELEMMTRX_1,File%DUMMY%,swell,,JIK,4,NElem   !Read in Element Matrix
(F20.10)

*VOPER,ELEMMTRX(1,3),ELEMMTRX_1(1,3),SUB,ELEMMTRX_2(1) !Calculates the amount of cure that has taken place in last
timestep
*VFUN,ELEMMTRX(1,1),COPY,ELEMMTRX_1(1,1)                !
*VFUN,ELEMMTRX(1,2),COPY,ELEMMTRX_1(1,2)                !Moves all relevant data into ELEMMTRX for this time step.
*VFUN,ELEMMTRX(1,4),COPY,ELEMMTRX_1(1,4)                !
*VFUN,ELEMMTRX_2(1),COPY,ELEMMTRX_1(1,3)

Ctime=ELEMMTRX(1,4)

finish
/prep7

 *DO,Count,1,NElem

  BFE,ELEMMTRX(Count,1),TEMP,,ELEMMTRX(Count,2)  !Apply element temperatures
  BFE,ELEMMTRX(Count,1),FLUE,,ELEMMTRX(Count,3)  !Apply element degree of polymerisation as fluence (to be used in swelling
calculation)

 *IF,ELEMMTRX(Count,3),GT,0,THEN              !
   MP,EX,Count+3,ELEMMTRX_1(Count,3)*(CemE-CemEinit)+CemEinit
   MP,NUXY,Count+3,0.3
   MP,DENS,Count+3,ELEMMTRX_1(Count,3)*(Dens-Densinit)+Densinit
   TB,SWELL,Count+3                    !Activate Swelling option
   TBDATA,67,0.02,1,,,,10              !Set constants for use in swelling calculation (Last value, C72, must be kept as 10)
   EMODIF,Count,MAT,Count+3
 *ENDIF                              !Recalculate and re-apply material properties for cement

 *ENDDO

DA,5,UX
DA,5,UY
DA,1,UZ
DA,2,UZ
DA,3,UZ
DA,4,UZ
DA,9,UZ
DA,13,UZ
DA,17,UZ
DA,20,UZ
DA,25,UZ
DA,26,UZ
DA,19,UY


nsub,2

finish
/solu

ESEL,U,TYPE,,3
ESEL,U,TYPE,,4
ESEL,U,TYPE,,5
ESEL,U,TYPE,,6
ESEL,U,TYPE,,7
ESEL,U,TYPE,,8
ESEL,U,TYPE,,9
ESEL,U,TYPE,,10

!ISWRITE,ON

ALLSEL
```

```
SOLVE

finish


/post1

CMSEL,U,STMELEM
CMSEL,U,BONELEM
ESEL,U,TYPE,,3
ESEL,U,TYPE,,4
ESEL,U,TYPE,,5
ESEL,U,TYPE,,6
ESEL,U,TYPE,,7
ESEL,U,TYPE,,8
ESEL,U,TYPE,,9
ESEL,U,TYPE,,10
! CMSEL,u,bonelem
! cmsel,u,stmelem
 /SHOW,PNG
 PNGR,COMP,1,-1
 PNGR,ORIENT,HORIZ
 /GFILE,800,
 /GRESUME,'Planar',' ',' '
! /CONTOUR,,,0,,8969
 /DSCALE,1,1.0
 /GLINE,1,-1
 PLNSOL,S,EQV,0,              !plot von-mises stress distribution
 PLMAT,'EX','AVG'             !plot young's modulus distribution
 PLMAT,'DENS','AVG'             !plot density distribution
CMSEL,all
allsel
 PLNSOL,CONT,DIST               !plot contact sliding distance

*IF,Ctime+25,GT,Stoptime,THEN
  *EXIT
*ENDIF

finish
/sol
ALLSEL

ANTYPE,,rest

finish

*ENDDO
!*********************************************End of Structural Phase*********************************

/EOF
```

USERSW altered coding (for shrinkage of polymerising cement)

```
*deck,usersw          parallel          user                    pck dc
      subroutine usersw (option,elem,intpt,mat,proptb,ncomp,epswel,
     x epel,e,nuxy,fluen,dfluen,tem,dtem,toffst,timvll,timvnc,usvr)
c
c *** primary function:   allow users to write their own swelling laws.
c                         this logic is accessed with c72 = 10
c *** secondary function:    demonstrate the use of user-written swelling laws
c
c
c       *** ansys(r) copyright(c) 2000
c       *** ansys, inc.
c *** Notice - This file contains ANSYS Confidential information ***
c
c  input arguments:
c     option   (int,sc,in)      swelling option
c     elem     (int,sc,in)      element number (label)
c     intpt    (int,sc,in)      element integration point number
c     mat      (int,sc,in)      material reference number
c     proptb   (dp,ar(*),in)    nonlinear material table (tb commands)
c     ncomp    (int,sc,in)      number of strain components (=1, 4, or 6)
c                               1 - truss or beam elements
c                               4 - 2-d solids and pipe elements
c                               6 - 3-d solids and most shells
c     epswel   (dp,sc,inout)    total accumulated swelling strain
c                                 before this substep
c     epel     (dp,ar(ncomp),inout) elastic strain
c     e        (dp,sc,in)       elastic modulus
c     nuxy     (dp,sc,in)       poisson'S RATIO
c     fluen    (dp,sc,in)       total fluence (bf or bfe commands)
c     dfluen   (dp,sc,in)       increment in fluence for this substep
c     tem      (dp,sc,in)       temperature (bf or bfe commands)
c     dtem     (dp,sc,in)       increment in temperature for this substep
c     toffst   (dp,sc,in)       offset of temperature scale from absolute zero
c                                    (toffst command)
c     timvll   (dp,sc,in)       time at the end of this substep
c     timvnc   (dp,sc,in)       the increment of time this substep
c     usvr     (dp,ar(*),inout)  user-defined state variables(optional)
c
c   output arguments:
c     epswel   (dp,sc,inout)    total accumulated swelling strain
c                                 after this substep
c     epel     (dp,ar(ncomp),inout) elastic strain adjusted
c                                      for swelling increment
c     usvr     (dp,ar(*),inout)  updated user-defined state variables
c
#include "impcom.inc"


      external erhandler

#include "stepcm.inc"
      integer option,elem,intpt,mat,ncomp
      double precision  proptb(*),epswel,epel(ncomp),e,nuxy,
     x  fluen,dfluen,tem,dtem,toffst,timvll,timvnc,usvr(*),
     x  delswl,eptot(3)
c
c
c       the following conditions are checked before this routine is called
c          proptb(67) and proptb(68) are not both zero
c          fluen and dfluen are both positive
c          (temp + toffst) is .gt. zero
c          proptb(72) = 10 to activate user swelling option
c
c    *** the normal usage of the routine is for isotropic materials
c
      if (kfstps .eq. 1) then
c
        if (intpt .eq. 1)
     Xcall erhandler('usersw',5000,2,
     x 'A.Briscoe defined version of coding for USERSW has been used.'
```

```
     x ,0.0d0,' ')
c
      endif
c
c    *** customer should remove the below dummy logic when making any changes ***
c     **** dummy logic to use unused variables ****
c      delswl = option+elem+mat+ncomp
c      delswl = epel(1)+e+nuxy+(tem+dtem+toffst)+(timvll-timvnc)+dfluen
c      usvr(1) = usvr(1)
c
c      eptot(1) = epel(1) + epswel
c      if (ncomp .gt. 1) then
c        eptot(2) = epel(2) + epswel
c        eptot(3) = epel(3) + epswel
c      endif
c
c         ******* begin sample law ***************************
c     *** swelling strain is a proportional function of fluence
c     *** epswl = proptb(67)*fluen
c     *** let delswl = d(epswel)/d(fluen)
      delswl = -proptb(67)*fluen
c               write(80,*) proptb(67),fluen,delswl
c         ******* end sample law
c
c     *** the next executable statement is true for all laws
c     *** epswel(i) = epswel(i-1) + (d(epswel)/d(fluen))*dfluen
c     *** where i is the iteration counter
      epswel = epswel + delswl*dfluen
c
      epel(1) =  -epswel
      if (ncomp .gt. 1) then
        epel(2) = -epswel
        epel(3) = -epswel
      endif
      return
      end
```

Matlab coding for processing of ultrasonic results

```
%read in the two files
load -ascii CAprime2.mat    %compressional A' signal
load -ascii CAB2.mat        %compressional A and B signals

% choose the time slot
cab25=CAB2(25,:);

%enter thickness of specimen at chosen time slot
T2=3.e-3;
%specify the sampling interval in the freq domain, df (depends on N and
dt)
df=97656.25; %this current number is based on dt=10nsec and N=1024 in the
FFT (df=1/Ndt)

% do the proper scaling
cab25=cab25.*(1/260);
cab25=cab25.*(0.316); %depends on the particular attenuation setting at
the chosen time slot compared with the reference

% select the correct portion of trace - choosing the first echo from
polyethylene/PMMA interface
cp=CAprime2(70:365);
cabA25=cab25(85:380);

%select the second echo (from the PMMA/steel interface)
cabB25=cab25(480:775);

% apply zero-averaging
mcp=mean(cp);
mcabF25=mean(cabFst25);
mcabS25=mean(cabsec25);
for i=1:296,
cabFst25(i)=cabFst25(i)-mcabF25;
cabsec25(i)=cabsec25(i)-mcabS25;
cp(i)=cp(i)-mcp;
end

%perform FFT
fcp=fft(cp,1024);
fcabFst25=fft(cabFst25,1024);
fcabsec25=fft(cabsec25,1024);

%obtain the magnitude spectrum
acabFst25=abs(fcabFst25);
acabsec25=abs(fcabsec25);
acp=abs(fcp);

%calculate the reflection coefficient R12
R1225=acabFst25./acp;

z1=2.046e+06; %<---- this is where z1 must be entered for polyethylene
                  %(from Wu's paper or experimental measurements)

%calculate the impedance for PMMA
```

```
for i=1:1024,
z2(i)=(z1(1+R1225(i)))/(1-R1225(i));
end

%enter impedance of steel
z3=7890.*5790.;

%calculate the reflection coeff for PMMA/steel interface
R23=(z3-z2)./(z3+z2);

%calculate ratio of second over first echo
SovF=cabsec25./cab25;

%calculate the attenuation (in nepers per meter per Hz)
RR=((1-R1225^2)./R1225).*R23;
alph2=(log(RR)-log(SovF))/2.*T2;

%set up calculation of velocity and convert to angular frequency.
for i=1;1024
    w(i)=i*6.2831*df;
    F(i)=alph2(i)./(w(i)^2);
end

%specify the reference velocity <-- this value is measured by looking at
the separation between
%the first and second echoes (i.e. polyethylene/PMMA interface echo and
PMA/Steel interface echo)
%(notice that the lower limit of the integration below is the frequency at
which velocity = Vwo)
Vwo=2550;

% calculate velocity from attenuation using the Kramers-Kronig
relationship
for j=2:1025
    V(j)=((F(j)+F(j-1))/2)*(w(j)-w(j-1));
    Vel2(j)=Vwo+(((2*Vwo)/pi)*sum(V(1:j));
end
```

Appendix III – Tables of results from Ultrasonic calculations

		Rotational Frequency											
		14140848.13	14755667.62	15370487.1	15985306.59	16600126.07	17214945.55	17829765.04	18444584.52	19059404.01	19674223.49	20289042.97	20903862.46
Time	150	3.3904e+009 +1.9124e+008i	3.3838e+009 +1.8546e+008i	3.3783e+009 +1.8142e+008i	3.378e+009 +1.7956e+008i	3.3807e+009 +1.7947e+008i	3.3788e+009 +1.8043e+008i	3.3679e+009 +1.8262e+008i	3.3503e+009 + 1.868e+008i	3.341e+009 +1.9277e+008i	3.3575e+009 + 1.98e+008i	3.3865e+009 +2.0325e+008i	3.3901e+009 +2.1262e+008i
	180	3.4238e+009 +1.6999e+008i	3.4242e+009 +1.6657e+008i	3.4224e+009 +1.6632e+008i	3.4183e+009 +1.6832e+008i	3.4135e+009 +1.6988e+008i	3.4084e+009 +1.6958e+008i	3.4028e+009 +1.6957e+008i	3.3953e+009 + 1.734e+008i	3.3882e+009 +1.8368e+008i	3.3899e+009 +1.9804e+008i	3.4039e+009 +2.0857e+008i	3.4157e+009 +2.2701e+008i
	210	3.4369e+009 +1.8152e+008i	3.4376e+009 +1.8012e+008i	3.4371e+009 +1.8263e+008i	3.4336e+009 +1.8719e+008i	3.4266e+009 +1.8961e+008i	3.4173e+009 + 1.882e+008i	3.4079e+009 +1.8603e+008i	3.3998e+009 +1.8665e+008i	3.3966e+009 +1.9159e+008i	3.4033e+009 +1.9664e+008i	3.4195e+009 +1.9438e+008i	3.4349e+009 +1.9268e+008i
	240	3.4056e+009 +2.0454e+008i	3.4052e+009 +2.0631e+008i	3.4033e+009 +2.1126e+008i	3.3974e+009 +2.1667e+008i	3.3878e+009 +2.1796e+008i	3.3769e+009 +2.1543e+008i	3.3678e+009 +2.1356e+008i	3.3617e+009 +2.1511e+008i	3.3601e+009 +2.1941e+008i	3.3642e+009 +2.1937e+008i	3.3711e+009 +2.1234e+008i	3.3722e+009 +2.1132e+008i
	270	3.3765e+009 + 2.48e+008i	3.3722e+009 +2.5379e+008i	3.3674e+009 +2.6155e+008i	3.3602e+009 +2.6678e+008i	3.351e+009 + 2.657e+008i	3.3409e+009 +2.6229e+008i	3.3321e+009 +2.6129e+008i	3.3256e+009 +2.6331e+008i	3.3236e+009 +2.6376e+008i	3.3284e+009 +2.5436e+008i	3.3373e+009 +2.4101e+008i	3.343e+009 +2.3618e+008i
	300	3.3823e+009 + 3.338e+008i	3.3764e+009 +3.4254e+008i	3.372e+009 +3.4909e+008i	3.3673e+009 +3.4902e+008i	3.3602e+009 +3.4623e+008i	3.3511e+009 +3.4755e+008i	3.3435e+009 +3.5396e+008i	3.3406e+009 +3.5858e+008i	3.3445e+009 + 3.511e+008i	3.3524e+009 +3.3747e+008i	3.3607e+009 +3.3071e+008i	3.3721e+009 +3.3824e+008i
	315	3.4535e+009 +3.6525e+008i	3.4488e+009 +3.7116e+008i	3.4469e+009 +3.7329e+008i	3.4442e+009 +3.7012e+008i	3.437e+009 +3.6721e+008i	3.4257e+009 +3.6962e+008i	3.416e+009 +3.7634e+008i	3.4131e+009 +3.7916e+008i	3.4186e+009 +3.7423e+008i	3.425e+009 +3.7444e+008i	3.4256e+009 +3.8939e+008i	3.4226e+009 +4.2481e+008i
	320	3.504e+009 +3.6502e+008i	3.5005e+009 +3.6941e+008i	3.5002e+009 +3.7019e+008i	3.499e+009 +3.6655e+008i	3.4925e+009 +3.6353e+008i	3.4809e+009 +3.6517e+008i	3.4698e+009 +3.7008e+008i	3.4655e+009 +3.7166e+008i	3.4704e+009 +3.6882e+008i	3.4782e+009 +3.7435e+008i	3.4802e+009 +4.0271e+008i	3.4765e+009 +4.4896e+008i
	325	3.8301e+009 + 3.898e+008i	3.8261e+009 +3.9385e+008i	3.8286e+009 + 3.947e+008i	3.8301e+009 +3.9125e+008i	3.8215e+009 +3.8748e+008i	3.8043e+009 +3.8704e+008i	3.7898e+009 +3.8916e+008i	3.7862e+009 +3.8898e+008i	3.7893e+009 +3.8547e+008i	3.7861e+009 + 3.879e+008i	3.7754e+009 + 4.047e+008i	3.7786e+009 +4.2735e+008i
	330	4.0626e+009 +3.7506e+008i	4.0603e+009 +3.7755e+008i	4.0573e+009 +3.7733e+008i	4.0539e+009 + 3.743e+008i	4.0482e+009 +3.7186e+008i	4.039e+009 +3.7222e+008i	4.0285e+009 +3.7349e+008i	4.0196e+009 + 3.715e+008i	4.0137e+009 +3.6736e+008i	4.0087e+009 +3.7051e+008i	4.0035e+009 +3.8775e+008i	4.0043e+009 +4.0682e+008i
	335	4.3507e+009 +3.6725e+008i	4.3598e+009 +3.7072e+008i	4.3656e+009 +3.7123e+008i	4.354e+009 +3.6777e+008i	4.3289e+009 + 3.647e+008i	4.3104e+009 + 3.665e+008i	4.3086e+009 +3.7192e+008i	4.3108e+009 +3.7376e+008i	4.3003e+009 +3.6858e+008i	4.2805e+009 +3.6678e+008i	4.2792e+009 +3.8077e+008i	4.3084e+009 +4.0482e+008i
	340	4.7317e+009 +3.7205e+008i	4.7296e+009 +3.7505e+008i	4.7403e+009 +3.7478e+008i	4.7434e+009 + 3.712e+008i	4.7218e+009 +3.6812e+008i	4.6869e+009 +3.6849e+008i	4.668e+009 + 3.712e+008i	4.6772e+009 +3.7236e+008i	4.6933e+009 +3.7237e+008i	4.686e+009 +3.8016e+008i	4.6682e+009 +4.0515e+008i	4.7021e+009 +4.3564e+008i
	344	5.3929e+009 +3.8765e+008i	5.3691e+009 +3.9125e+008i	5.3635e+009 +3.9015e+008i	5.3572e+009 +3.8544e+008i	5.3279e+009 +3.8272e+008i	5.2813e+009 +3.8524e+008i	5.2476e+009 +3.9103e+008i	5.2502e+009 +3.9574e+008i	5.2838e+009 +4.0142e+008i	5.3177e+009 +4.2081e+008i	5.343e+009 +4.8952e+008i	5.4025e+009 +5.4279e+008i
	349	6.2985e+009 +4.0492e+008i	6.2651e+009 +4.0964e+008i	6.2669e+009 +4.0911e+008i	6.2687e+009 +4.0327e+008i	6.2329e+009 +3.9763e+008i	6.1717e+009 +3.9703e+008i	6.1326e+009 +4.0128e+008i	6.1363e+009 +4.0625e+008i	6.1432e+009 +4.1116e+008i	6.0986e+009 +4.2741e+008i	6.0494e+009 +4.7694e+008i	6.1203e+009 +5.5036e+008i
	355	7.0332e+009 +4.0043e+008i	7.007e+009 +4.0844e+008i	7.0156e+009 +4.1126e+008i	7.0172e+009 +4.0978e+008i	6.971e+009 +4.1002e+008i	6.8908e+009 +4.1671e+008i	6.827e+009 +4.2951e+008i	6.8054e+009 +4.4384e+008i	6.7961e+009 +4.5523e+008i	6.7433e+009 +4.6933e+008i	6.6738e+009 + 5.062e+008i	6.7019e+009 + 5.989e+008i
	360	7.4634e+009 + 3.855e+008i	7.4402e+009 +3.9186e+008i	7.4613e+009 +3.9027e+008i	7.4776e+009 +3.8387e+008i	7.4357e+009 +3.8097e+008i	7.3472e+009 +3.8662e+008i	7.2723e+009 +4.0001e+008i	7.2459e+009 + 4.166e+008i	7.2342e+009 +4.3234e+008i	7.1662e+009 +4.5108e+008i	7.0734e+009 +4.8409e+008i	7.1114e+009 +5.3368e+008i
	371	7.7212e+009 +3.8862e+008i	7.7031e+009 +3.9667e+008i	7.7331e+009 +3.9559e+008i	7.7514e+009 +3.8771e+008i	7.6968e+009 +3.8166e+008i	7.5859e+009 + 3.839e+008i	7.4913e+009 +3.9543e+008i	7.458e+009 +4.1362e+008i	7.451e+009 +4.3406e+008i	7.3805e+009 +4.5848e+008i	7.2545e+009 +5.0368e+008i	7.2334e+009 +5.9837e+008i
	380	7.8705e+009 + 3.954e+008i	7.8506e+009 +4.0455e+008i	7.8827e+009 +4.0414e+008i	7.9094e+009 +3.9696e+008i	7.8622e+009 +3.9148e+008i	7.7476e+009 +3.9329e+008i	7.6349e+009 +4.0269e+008i	7.574e+009 +4.1741e+008i	7.5395e+009 +4.3554e+008i	7.4504e+009 +4.6207e+008i	7.3189e+009 +5.1504e+008i	7.3014e+009 +6.2398e+008i
	390	8.0301e+009 +3.8523e+008i	8.0191e+009 +3.9407e+008i	8.0629e+009 +3.9285e+008i	8.0962e+009 +3.8506e+008i	8.0456e+009 +3.7897e+008i	7.9241e+009 +3.7882e+008i	7.8156e+009 + 3.833e+008i	7.7805e+009 +3.8924e+008i	7.7862e+009 + 3.956e+008i	7.7265e+009 +4.0714e+008i	7.6083e+009 +4.3044e+008i	7.626e+009 +4.6041e+008i
	400	8.0636e+009 +3.8996e+008i	8.0429e+009 +4.0002e+008i	8.0881e+009 +3.9989e+008i	8.1405e+009 +3.9266e+008i	8.1162e+009 +3.8645e+008i	8.009e+009 +3.8571e+008i	7.8964e+009 +3.8955e+008i	7.8513e+009 +3.9527e+008i	7.8611e+009 +4.0116e+008i	7.8122e+009 +4.0934e+008i	7.6652e+009 +4.2386e+008i	7.5898e+009 +4.4075e+008i
	420	8.0682e+009 +3.9655e+008i	8.0513e+009 +4.0718e+008i	8.1095e+009 +4.0618e+008i	8.1783e+009 +3.9852e+008i	8.1672e+009 +3.9338e+008i	8.0737e+009 +3.9397e+008i	7.9844e+009 +3.9771e+008i	7.9703e+009 +4.0165e+008i	7.9953e+009 +4.0626e+008i	7.9284e+009 + 4.154e+008i	7.7673e+009 +4.2946e+008i	7.7475e+009 +4.3871e+008i
	435	8.0038e+009 +3.9113e+008i	7.9794e+009 +4.0204e+008i	8.0407e+009 +4.0077e+008i	8.1319e+009 +3.9289e+008i	8.1509e+009 +3.8789e+008i	8.0725e+009 +3.8858e+008i	7.9768e+009 +3.9155e+008i	7.9574e+009 +3.9337e+008i	8.0153e+009 +3.9504e+008i	8.0156e+009 +4.0185e+008i	7.8855e+009 +4.1622e+008i	7.805e+009 +4.3139e+008i
	450	8.1142e+009 +3.9504e+008i	8.0949e+009 +4.0545e+008i	8.1577e+009 +4.0348e+008i	8.25e+009 +3.9541e+008i	8.2753e+009 +3.9124e+008i	8.2084e+009 +3.9337e+008i	8.1228e+009 +3.9752e+008i	8.1047e+009 +3.9969e+008i	8.1591e+009 +4.0144e+008i	8.1698e+009 +4.0909e+008i	8.0674e+009 +4.2376e+008i	7.9773e+009 +4.3288e+008i
	465	8.0931e+009 +3.9136e+008i	8.0716e+009 +4.0157e+008i	8.1357e+009 +3.9912e+008i	8.2293e+009 +3.9043e+008i	8.2542e+009 +3.8537e+008i	8.1909e+009 +3.8614e+008i	8.1229e+009 +3.8869e+008i	8.1403e+009 +3.8998e+008i	8.2324e+009 + 3.925e+008i	8.2575e+009 +4.0206e+008i	8.1572e+009 +4.1829e+008i	8.1139e+009 +4.2905e+008i
	480	7.9989e+009 + 3.799e+008i	7.981e+009 +3.9012e+008i	8.05e+009 +3.8838e+008i	8.1529e+009 + 3.805e+008i	8.1941e+009 +3.7591e+008i	8.1523e+009 +3.7703e+008i	8.1026e+009 +3.8006e+008i	8.1207e+009 +3.8151e+008i	8.1854e+009 +3.8276e+008i	8.1694e+009 +3.8902e+008i	8.0503e+009 +4.0157e+008i	8.033e+009 +4.1294e+008i
	510	8.0914e+009 +3.8783e+008i	8.0651e+009 +3.9759e+008i	8.1345e+009 +3.9498e+008i	8.2505e+009 +3.8677e+008i	8.312e+009 +3.8268e+008i	8.2884e+009 +3.8391e+008i	8.2544e+009 +3.8524e+008i	8.2951e+009 +3.8325e+008i	8.3984e+009 +3.8207e+008i	8.4289e+009 +3.8991e+008i	8.3421e+009 +4.0715e+008i	8.3372e+009 +4.1896e+008i
	540	8.1438e+009 + 3.917e+008i	8.1201e+009 +4.0136e+008i	8.1978e+009 +3.9823e+008i	8.326e+009 +3.8975e+008i	8.3963e+009 +3.8589e+008i	8.3741e+009 +3.8775e+008i	8.3399e+009 +3.8966e+008i	8.3948e+009 +3.8797e+008i	8.5424e+009 +3.8696e+008i	8.6321e+009 +3.9531e+008i	8.5653e+009 +4.1382e+008i	8.4921e+009 +4.2873e+008i
	570	8.1091e+009 +3.8771e+008i	8.0818e+009 +3.9664e+008i	8.1608e+009 +3.9289e+008i	8.2972e+009 +3.8446e+008i	8.3796e+009 +3.8107e+008i	8.3692e+009 +3.8314e+008i	8.3462e+009 +3.8476e+008i	8.4113e+009 +3.8271e+008i	8.5594e+009 +3.8159e+008i	8.631e+009 +3.8875e+008i	8.5457e+009 +4.0241e+008i	8.509e+009 +4.0993e+008i
	600	8.1286e+009 +3.7785e+008i	8.1065e+009 +3.8716e+008i	8.1813e+009 +3.8429e+008i	8.3126e+009 +3.7608e+008i	8.3982e+009 + 3.721e+008i	8.3944e+009 + 3.736e+008i	8.3677e+009 +3.7559e+008i	8.4161e+009 +3.7537e+008i	8.559e+009 +3.7749e+008i	8.6667e+009 +3.8925e+008i	8.6353e+009 +4.0903e+008i	8.5925e+009 + 4.219e+008i
	630	8.1532e+009 +3.8216e+008i	8.134e+009 +3.9126e+008i	8.2101e+009 +3.8807e+008i	8.3376e+009 +3.7932e+008i	8.4181e+009 +3.7469e+008i	8.4204e+009 +3.7583e+008i	8.4194e+009 +3.7817e+008i	8.502e+009 +3.7882e+008i	8.6524e+009 +3.8076e+008i	8.7221e+009 +3.8917e+008i	8.6577e+009 +4.0113e+008i	8.6575e+009 +4.0502e+008i
	660	8.1644e+009 +3.7841e+008i	8.1454e+009 +3.8795e+008i	8.2179e+009 +3.8527e+008i	8.3443e+009 +3.7661e+008i	8.4308e+009 +3.7191e+008i	8.4403e+009 +3.7332e+008i	8.4365e+009 +3.7626e+008i	8.5055e+009 +3.7716e+008i	8.6501e+009 +3.7885e+008i	8.743e+009 +3.8829e+008i	8.7152e+009 + 4.068e+008i	8.7266e+009 +4.2511e+008i
	690	8.1995e+009 +3.8038e+008i	8.1852e+009 +3.8985e+008i	8.2624e+009 +3.8697e+008i	8.3887e+009 +3.7835e+008i	8.4683e+009 +3.7401e+008i	8.4692e+009 +3.7576e+008i	8.4642e+009 +3.7854e+008i	8.5446e+009 +3.7873e+008i	8.7049e+009 +3.7994e+008i	8.7948e+009 +3.9006e+008i	8.7321e+009 +4.0915e+008i	8.6986e+009 +4.2329e+008i
	720	8.1777e+009 +3.7595e+008i	8.1644e+009 +3.8599e+008i	8.2421e+009 +3.8299e+008i	8.3702e+009 +3.7363e+008i	8.455e+009 +3.6881e+008i	8.4643e+009 +3.7075e+008i	8.4681e+009 +3.7394e+008i	8.5539e+009 +3.7403e+008i	8.717e+009 +3.7512e+008i	8.8184e+009 +3.8702e+008i	8.7934e+009 +4.1035e+008i	8.8238e+009 +4.2381e+008i

Table 1 - Values for E_c* or C_{11}

		Rotational Frequency											
		14140848.13	14755667.62	15370487.1	15985306.59	16600126.07	17214945.55	17829765.04	18444584.52	19059404.01	19674223.49	20289042.97	20903862.46
Time	150												
	180												
	210												
	240												
	270												
	300												
	315												
	320												
	325												
	330												
	335												
	340												
	344												
	349												
	355												
	360												
	371												
	380												
	390												
	400												
	420												
	435												
	450												
	465	1.2664e+009 +1.0235e+008i	1.2905e+009 +1.0353e+008i	1.316e+009 +1.0966e+008i	1.342e+009 +1.1867e+008i	1.3767e+009 +8.7091e+007i	1.414e+009 +7.9035e+007i	1.4473e+009 +1.1449e+008i	1.4705e+009 +6.4498e+007i	1.4331e+009 +4.0854e+007i	1.2995e+009 +4.2927e+007i	1.1457e+009 +3.7305e+007i	1.1464e+009 +1.8777e+007i
	480	1.3523e+009 +8.4865e+007i	1.3332e+009 +8.2857e+007i	1.3596e+009 +7.8962e+007i	1.4171e+009 + 7.221e+007i	1.4851e+009 + 7.003e+007i	1.5461e+009 +7.7323e+007i	1.5889e+009 +8.2481e+007i	1.6097e+009 +5.8526e+007i	1.6037e+009 +4.4616e+007i	1.5665e+009 +4.6753e+007i	1.5039e+009 +6.2931e+007i	1.4696e+009 +4.0665e+007i
	510	1.7218e+009 + 8.308e+007i	1.7251e+009 +8.4539e+007i	1.8053e+009 + 8.829e+007i	1.9319e+009 + 9.371e+007i	2.0472e+009 +9.8126e+007i	2.0746e+009 +9.4202e+007i	1.9446e+009 +7.7777e+007i	1.6494e+009 +5.7353e+007i	1.3387e+009 + 4.285e+007i	1.6179e+009 +5.2521e+007i	2.3608e+009 +9.6632e+007i	2.5832e+009 +1.2677e+008i
	540	2.061e+009 +9.3383e+007i	2.0948e+009 +1.0252e+008i	2.2099e+009 +1.1798e+008i	2.3814e+009 +1.3843e+008i	2.5447e+009 +1.5794e+008i	2.5938e+009 +1.5993e+008i	2.414e+009 + 1.266e+008i	1.9701e+009 + 8.418e+007i	1.3909e+009 +5.2154e+007i	1.402e+009 +5.1865e+007i	2.4348e+009 +1.0107e+008i	3.3678e+009 +7.4456e+007i
	570	2.2999e+009 +9.0643e+007i	2.3653e+009 +9.9017e+007i	2.5337e+009 +1.1812e+008i	2.78e+009 + 1.527e+008i	3.0215e+009 +2.0109e+008i	3.1065e+009 +2.0153e+008i	2.8549e+009 +1.5161e+008i	2.2334e+009 + 9.903e+007i	1.4785e+009 +5.5729e+007i	1.554e+009 +4.9766e+007i	3.2547e+009 +9.0582e+007i	5.6453e+009 + 2.891e+008i
	600	2.5073e+009 +8.7745e+007i	2.5487e+009 +9.4556e+007i	2.6879e+009 +1.1232e+008i	2.9231e+009 +1.4237e+008i	3.2023e+009 +1.6918e+008i	3.391e+009 +1.6555e+008i	3.2725e+009 +1.5737e+008i	2.7055e+009 +1.2843e+008i	1.8475e+009 +6.8932e+007i	1.2943e+009 +4.4326e+007i	2.3276e+009 +8.5159e+007i	4.0709e+009 +6.7941e+007i
	630	2.6076e+009 + 8.505e+007i	2.6603e+009 +9.0617e+007i	2.8228e+009 +1.0678e+008i	3.1109e+009 +1.3265e+008i	3.49e+009 + 1.478e+008i	3.8109e+009 +1.4123e+008i	3.7596e+009 +1.4004e+008i	3.0694e+009 +1.3805e+008i	1.9688e+009 +1.0741e+008i	1.2266e+009 +4.6847e+007i	2.9177e+009 +9.7645e+007i	9.5909e+009 +9.7942e+007i
	660	2.6736e+009 +8.3619e+007i	2.727e+009 +9.1671e+007i	2.8872e+009 +1.0931e+008i	3.1618e+009 + 1.312e+008i	3.5028e+009 +1.3811e+008i	3.7527e+009 +1.3143e+008i	3.6322e+009 +1.2983e+008i	2.9527e+009 +1.2951e+008i	1.952e+009 +1.0013e+008i	1.3353e+009 +6.4191e+007i	2.5469e+009 +1.2664e+008i	5.4909e+009 +1.0409e+008i
	690	2.8168e+009 + 8.304e+007i	2.8794e+009 +8.8842e+007i	3.0337e+009 +1.0404e+008i	3.2954e+009 +1.2692e+008i	3.6364e+009 +1.4426e+008i	3.9363e+009 +1.4716e+008i	3.9416e+009 + 1.504e+008i	3.3975e+009 +1.5059e+008i	2.4093e+009 +1.0797e+008i	1.5379e+009 +6.8304e+007i	1.8754e+009 +9.5368e+007i	3.0206e+009 +7.4206e+007i
	720	2.8637e+009 +8.1166e+007i	2.898e+009 +8.6668e+007i	3.0038e+009 +1.0196e+008i	3.2073e+009 +1.2395e+008i	3.5083e+009 +1.2914e+008i	3.8411e+009 +1.1236e+008i	4.0195e+009 +1.0148e+008i	3.7511e+009 +1.0903e+008i	2.9169e+009 +1.3356e+008i	1.9153e+009 +1.0781e+008i	1.5017e+009 +5.7604e+007i	1.9645e+009 +5.0848e+007i

Table 2 - Values for E_s* or G* or C_{44}

		Rotational Frequency											
		14140848.13	14755667.62	15370487.1	15985306.59	16600126.07	17214945.55	17829765.04	18444584.52	19059404.01	19674223.49	20289042.97	20903862.46
Time	150	3.3904e+009 +1.9124e+008i	3.3838e+009 +1.8546e+008i	3.3783e+009 +1.8142e+008i	3.378e+009 +1.7956e+008i	3.3807e+009 +1.7947e+008i	3.3788e+009 +1.8043e+008i	3.3679e+009 +1.8262e+008i	3.3503e+009 + 1.868e+008i	3.341e+009 +1.9277e+008i	3.3575e+009 + 1.98e+008i	3.3865e+009 +2.0325e+008i	3.3901e+009 +2.1262e+008i
	180	3.4238e+009 +1.6999e+008i	3.4242e+009 +1.6657e+008i	3.4224e+009 +1.6632e+008i	3.4183e+009 +1.6832e+008i	3.4135e+009 +1.6988e+008i	3.4084e+009 +1.6958e+008i	3.4028e+009 +1.6957e+008i	3.3953e+009 + 1.734e+008i	3.3882e+009 +1.8368e+008i	3.3899e+009 +1.9804e+008i	3.4039e+009 +2.0857e+008i	3.4157e+009 +2.2701e+008i
	210	3.4369e+009 +1.8152e+008i	3.4376e+009 +1.8012e+008i	3.4371e+009 +1.8263e+008i	3.4336e+009 +1.8719e+008i	3.4266e+009 +1.8961e+008i	3.4173e+009 + 1.882e+008i	3.4079e+009 +1.8603e+008i	3.3998e+009 +1.8665e+008i	3.3966e+009 +1.9159e+008i	3.4033e+009 +1.9664e+008i	3.4195e+009 +1.9438e+008i	3.4349e+009 +1.9268e+008i
	240	3.4056e+009 +2.0454e+008i	3.4052e+009 +2.0631e+008i	3.4033e+009 +2.1126e+008i	3.3974e+009 +2.1667e+008i	3.3878e+009 +2.1796e+008i	3.3769e+009 +2.1543e+008i	3.3678e+009 +2.1356e+008i	3.3617e+009 +2.1511e+008i	3.3601e+009 +2.1941e+008i	3.3642e+009 +2.1937e+008i	3.3711e+009 +2.1234e+008i	3.3722e+009 +2.1132e+008i
	270	3.3765e+009 + 2.48e+008i	3.3722e+009 +2.5379e+008i	3.3674e+009 +2.6155e+008i	3.3602e+009 +2.6678e+008i	3.351e+009 + 2.657e+008i	3.3409e+009 +2.6229e+008i	3.3321e+009 +2.6129e+008i	3.3256e+009 +2.6331e+008i	3.3236e+009 +2.6376e+008i	3.3284e+009 +2.5436e+008i	3.3373e+009 +2.4101e+008i	3.343e+009 +2.3618e+008i
	300	3.3823e+009 + 3.338e+008i	3.3764e+009 +3.4254e+008i	3.372e+009 +3.4909e+008i	3.3673e+009 +3.4902e+008i	3.3602e+009 +3.4623e+008i	3.3511e+009 +3.4755e+008i	3.3435e+009 +3.5396e+008i	3.3406e+009 +3.5858e+008i	3.3445e+009 + 3.511e+008i	3.3524e+009 +3.3747e+008i	3.3607e+009 +3.3071e+008i	3.3721e+009 +3.3824e+008i
	315	3.4535e+009 +3.6525e+008i	3.4488e+009 +3.7116e+008i	3.4469e+009 +3.7329e+008i	3.4442e+009 +3.7012e+008i	3.437e+009 +3.6721e+008i	3.4257e+009 +3.6962e+008i	3.416e+009 +3.7634e+008i	3.4131e+009 +3.7916e+008i	3.4186e+009 +3.7423e+008i	3.425e+009 +3.7444e+008i	3.4256e+009 +3.8938e+008i	3.4226e+009 +4.2481e+008i
	320	3.504e+009 +3.6502e+008i	3.5005e+009 +3.6941e+008i	3.5002e+009 +3.7019e+008i	3.499e+009 +3.6655e+008i	3.4925e+009 +3.6353e+008i	3.4809e+009 +3.6517e+008i	3.4698e+009 +3.7008e+008i	3.4655e+009 +3.7166e+008i	3.4704e+009 +3.6882e+008i	3.4782e+009 +3.7435e+008i	3.4802e+009 +4.0271e+008i	3.4765e+009 +4.4896e+008i
	325	3.8301e+009 + 3.898e+008i	3.8261e+009 +3.9385e+008i	3.8286e+009 + 3.947e+008i	3.8301e+009 +3.9125e+008i	3.8215e+009 +3.8748e+008i	3.8043e+009 +3.8704e+008i	3.7898e+009 +3.8916e+008i	3.7862e+009 +3.8547e+008i	3.7893e+009 +3.8879e+008i	3.7861e+009 + 3.879e+008i	3.7754e+009 + 4.047e+008i	3.7786e+009 +4.2735e+008i
	330	4.0626e+009 +3.7506e+008i	4.0603e+009 +3.7755e+008i	4.0573e+009 +3.7733e+008i	4.0539e+009 + 3.743e+008i	4.0482e+009 +3.7186e+008i	4.039e+009 +3.7222e+008i	4.0285e+009 +3.7349e+008i	4.0196e+009 + 3.715e+008i	4.0137e+009 +3.6736e+008i	4.0087e+009 +3.7051e+008i	4.0035e+009 +3.8775e+008i	4.0043e+009 +4.0682e+008i
	335	4.3507e+009 +3.6725e+008i	4.3598e+009 +3.7072e+008i	4.3656e+009 +3.7123e+008i	4.354e+009 +3.6777e+008i	4.3289e+009 + 3.647e+008i	4.3104e+009 + 3.665e+008i	4.3086e+009 +3.7192e+008i	4.3108e+009 +3.7376e+008i	4.3003e+009 +3.6858e+008i	4.2805e+009 +3.6678e+008i	4.2792e+009 +3.8077e+008i	4.3084e+009 +4.0482e+008i
	340	4.7317e+009 +3.7205e+008i	4.7296e+009 +3.7505e+008i	4.7403e+009 +3.7478e+008i	4.7434e+009 + 3.712e+008i	4.7218e+009 +3.6812e+008i	4.6869e+009 +3.6849e+008i	4.668e+009 + 3.712e+008i	4.6772e+009 +3.7236e+008i	4.6933e+009 +3.7237e+008i	4.686e+009 +3.8016e+008i	4.6682e+009 +4.0515e+008i	4.7021e+009 +4.3564e+008i
	344	5.3929e+009 +3.8765e+008i	5.3691e+009 +3.9125e+008i	5.3635e+009 +3.9015e+008i	5.3572e+009 +3.8544e+008i	5.3279e+009 +3.8272e+008i	5.2813e+009 +3.8524e+008i	5.2476e+009 +3.9103e+008i	5.2502e+009 +3.9574e+008i	5.2838e+009 +4.0142e+008i	5.3177e+009 +4.2081e+008i	5.343e+009 +4.6952e+008i	5.4025e+009 +5.4279e+008i
	349	6.2985e+009 +4.0492e+008i	6.2651e+009 +4.0964e+008i	6.2669e+009 +4.0911e+008i	6.2687e+009 +4.0327e+008i	6.2329e+009 +3.9763e+008i	6.1717e+009 +3.9703e+008i	6.1326e+009 +4.0128e+008i	6.1363e+009 +4.0625e+008i	6.1432e+009 +4.1116e+008i	6.0986e+009 +4.2741e+008i	6.0494e+009 +4.7694e+008i	6.1203e+009 +5.5036e+008i
	355	7.0332e+009 +4.0043e+008i	7.007e+009 +4.0844e+008i	7.0156e+009 +4.1126e+008i	7.0172e+009 +4.0978e+008i	6.971e+009 +4.1002e+008i	6.8908e+009 +4.1671e+008i	6.827e+009 +4.2951e+008i	6.8054e+009 +4.4384e+008i	6.7961e+009 +4.5523e+008i	6.7433e+009 +4.6933e+008i	6.6738e+009 + 5.062e+008i	6.7019e+009 + 5.989e+008i
	360	7.4634e+009 + 3.855e+008i	7.4402e+009 +3.9186e+008i	7.4613e+009 +3.9027e+008i	7.4776e+009 +3.8387e+008i	7.4357e+009 +3.8097e+008i	7.3472e+009 +3.8662e+008i	7.2723e+009 +4.0001e+008i	7.2459e+009 + 4.166e+008i	7.2342e+009 +4.3234e+008i	7.1662e+009 +4.5108e+008i	7.0734e+009 +4.8409e+008i	7.1114e+009 +5.3368e+008i
	371	7.7212e+009 +3.8862e+008i	7.7031e+009 +3.9667e+008i	7.7331e+009 +3.9559e+008i	7.7514e+009 +3.8771e+008i	7.6968e+009 +3.8166e+008i	7.5859e+009 + 3.839e+008i	7.4913e+009 +3.9543e+008i	7.458e+009 +4.1362e+008i	7.451e+009 +4.3406e+008i	7.3805e+009 +4.5848e+008i	7.2545e+009 +5.0368e+008i	7.2334e+009 +5.9837e+008i
	380	7.8705e+009 + 3.954e+008i	7.8506e+009 +4.0455e+008i	7.8827e+009 +4.0414e+008i	7.9094e+009 +3.9696e+008i	7.8622e+009 +3.9148e+008i	7.7476e+009 +3.9329e+008i	7.6349e+009 +4.0269e+008i	7.574e+009 +4.1741e+008i	7.5395e+009 +4.3554e+008i	7.4504e+009 +4.6207e+008i	7.3189e+009 +5.1504e+008i	7.3014e+009 +6.2398e+008i
	390	8.0301e+009 +3.8523e+008i	8.0191e+009 +3.9407e+008i	8.0629e+009 +3.9285e+008i	8.0962e+009 +3.8506e+008i	8.0456e+009 +3.7897e+008i	7.9241e+009 +3.7882e+008i	7.8156e+009 + 3.833e+008i	7.7805e+009 +3.8924e+008i	7.7862e+009 + 3.956e+008i	7.7265e+009 +4.0714e+008i	7.6083e+009 +4.3044e+008i	7.626e+009 +4.6041e+008i
	400	8.0636e+009 +3.8996e+008i	8.0429e+009 +4.0002e+008i	8.0881e+009 +3.9989e+008i	8.1405e+009 +3.9266e+008i	8.1162e+009 +3.8645e+008i	8.009e+009 +3.8571e+008i	7.8964e+009 +3.8955e+008i	7.8513e+009 +3.9527e+008i	7.8611e+009 +4.0116e+008i	7.8122e+009 +4.0934e+008i	7.6652e+009 +4.2386e+008i	7.5898e+009 +4.4075e+008i
	420	8.0682e+009 +3.9655e+008i	8.0513e+009 +4.0718e+008i	8.1095e+009 +4.0618e+008i	8.1783e+009 +3.9852e+008i	8.1672e+009 +3.9338e+008i	8.0737e+009 +3.9397e+008i	7.9844e+009 +3.9771e+008i	7.9703e+009 +4.0165e+008i	7.9953e+009 +4.0626e+008i	7.9284e+009 + 4.154e+008i	7.7673e+009 +4.2946e+008i	7.7475e+009 +4.3871e+008i
	435	8.0038e+009 +3.9113e+008i	7.9794e+009 +4.0204e+008i	8.0407e+009 +4.0077e+008i	8.1319e+009 +3.9289e+008i	8.1509e+009 +3.8789e+008i	8.0725e+009 +3.8858e+008i	7.9768e+009 +3.9155e+008i	7.9574e+009 +3.9337e+008i	8.0153e+009 +3.9504e+008i	8.0156e+009 +4.0185e+008i	7.8855e+009 +4.1622e+008i	7.805e+009 +4.3139e+008i
	450	8.1142e+009 +3.9504e+008i	8.0949e+009 +4.0545e+008i	8.1577e+009 +4.0348e+008i	8.25e+009 +3.9541e+008i	8.2753e+009 +3.9124e+008i	8.2084e+009 +3.9337e+008i	8.1228e+009 +3.9752e+008i	8.1047e+009 +4.0144e+008i	8.1591e+009 +4.0969e+008i	8.1698e+009 +4.0909e+008i	8.0674e+009 +4.2376e+008i	7.9773e+009 +4.3288e+008i
	465	6.4045e+009 +2.5489e+008i	6.351e+009 +2.6353e+008i	6.381e+009 + 2.529e+008i	6.44e+009 + 2.322e+008i	6.4187e+009 +2.6925e+008i	6.3057e+009 +2.8076e+008i	6.1932e+009 +2.3604e+008i	6.1796e+009 +3.0398e+008i	6.3216e+009 +3.3803e+008i	6.5248e+009 +3.4482e+008i	6.6296e+009 +3.6855e+008i	6.5853e+009 +4.0401e+008i
	480	6.1959e+009 +2.6675e+008i	6.2034e+009 +2.7965e+008i	6.2373e+009 + 2.831e+008i	6.2634e+009 +2.8421e+008i	6.2139e+009 +2.8254e+008i	6.0909e+009 +2.7394e+008i	5.9841e+009 +2.7008e+008i	5.9744e+009 +3.0348e+008i	6.0471e+009 +3.2327e+008i	6.0808e+009 +3.2669e+008i	6.0452e+009 +3.1766e+008i	6.0735e+009 +3.5872e+008i
	510	5.7957e+009 +2.7685e+008i	5.7649e+009 +2.8487e+008i	5.7275e+009 +2.7726e+008i	5.6746e+009 +2.6182e+008i	5.5824e+009 +2.5184e+008i	5.5223e+009 +2.5831e+008i	5.6616e+009 +2.8153e+008i	6.0959e+009 +3.0678e+008i	6.6134e+009 +3.2494e+008i	6.2717e+009 +3.1988e+008i	5.1944e+009 + 2.783e+008i	4.8929e+009 +2.4994e+008i
	540	5.3957e+009 +2.6719e+008i	5.327e+009 +2.6466e+008i	5.2512e+009 +2.4093e+008i	5.1507e+009 +2.0517e+008i	5.0033e+009 + 1.753e+008i	4.9157e+009 +1.7451e+008i	5.1211e+009 +2.2087e+008i	5.768e+009 +2.7573e+008i	6.6878e+009 +3.1743e+008i	6.7627e+009 +3.2615e+008i	5.3188e+009 +2.7907e+008i	4.0017e+009 +3.2946e+008i
	570	5.0426e+009 +2.6685e+008i	4.9282e+009 +2.6461e+008i	4.7825e+009 + 2.354e+008i	4.5905e+009 +1.8086e+008i	4.3509e+009 +1.1295e+008i	4.2273e+009 +1.1443e+008i	4.5398e+009 +1.8261e+008i	5.4334e+009 +2.5067e+008i	6.5881e+009 +3.0729e+008i	6.5589e+009 +3.2239e+008i	4.2061e+009 +2.8163e+008i	9.8193e+008 +2.4468e+007i
	600	4.7855e+009 +2.6085e+008i	4.7083e+009 +2.6109e+008i	4.5974e+009 +2.3454e+008i	4.4151e+009 +1.8625e+008i	4.1284e+009 +1.4652e+008i	3.8731e+009 +1.5286e+008i	4.0044e+009 +1.6577e+008i	4.8087e+009 +2.0413e+008i	6.0956e+009 +2.8558e+008i	6.941e+009 +3.3015e+008i	5.5319e+009 +2.9549e+008i	3.1646e+009 +3.3131e+008i
	630	4.6765e+009 +2.6876e+008i	4.5869e+009 +2.7044e+008i	4.4463e+009 + 2.457e+008i	4.1897e+009 +2.0245e+008i	3.7648e+009 +1.7763e+008i	3.3392e+009 +1.8752e+008i	3.4066e+009 +1.9145e+008i	4.4095e+009 +1.9474e+008i	6.0273e+009 +2.3754e+008i	7.0866e+009 +3.2671e+008i	4.7674e+009 +2.7094e+008i	-4.1303e+009 +2.7443e+008i
	660	4.5996e+009 +2.6692e+008i	4.5094e+009 +2.6572e+008i	4.3683e+009 +2.3952e+008i	4.1285e+009 +2.0167e+008i	3.7604e+009 +1.8777e+008i	3.4366e+009 +1.9808e+008i	3.5936e+009 +2.0316e+008i	4.5685e+009 +2.0448e+008i	6.0474e+009 +2.4534e+008i	6.9626e+009 + 3.027e+008i	5.3193e+009 +2.3795e+008i	1.4055e+009 +2.8632e+008i
	690	4.4438e+009 +2.6966e+008i	4.346e+009 +2.7139e+008i	4.2174e+009 +2.4824e+008i	3.9949e+009 +2.0913e+008i	3.6197e+009 +1.8166e+008i	3.2207e+009 +1.7955e+008i	3.2087e+009 +1.7801e+008i	4.0146e+009 +1.7794e+008i	5.4925e+009 +2.3598e+008i	6.7443e+009 +2.9899e+008i	6.2316e+009 +2.8199e+008i	4.67 1e+009 +3.2435e+008i
	720	4.3594e+009 +2.6773e+008i	4.3004e+009 +2.7043e+008i	4.237e+009 +2.4705e+008i	4.0938e+009 +2.0837e+008i	3.7772e+009 +1.9662e+008i	3.3428e+009 +2.2094e+008i	3.1088e+009 +2.3863e+008i	3.5525e+009 +2.2866e+008i	4.8278e+009 +1.9703e+008i	6.2646e+009 +2.4328e+008i	6.7912e+009 +3.3355e+008i	6.2045e+009 +3.5601e+008i

Table 3 - Values for K*

		Rotational Frequency											
		14140848.13	14755667.62	15370487.1	15985306.59	16600126.07	17214945.55	17829765.04	18444584.52	19059404.01	19674223.49	20289042.97	20903862.46
Time	150	3.3904e+009 +1.9124e+008i	3.3838e+009 +1.8546e+008i	3.3783e+009 +1.8142e+008i	3.378e+009 +1.7956e+008i	3.3807e+009 +1.7947e+008i	3.3788e+009 +1.8043e+008i	3.3679e+009 +1.8262e+008i	3.3503e+009 + 1.868e+008i	3.341e+009 +1.9277e+008i	3.3575e+009 + 1.98e+008i	3.3865e+009 +2.0325e+008i	3.3901e+009 +2.1262e+008i
	180	3.4238e+009 +1.6999e+008i	3.4242e+009 +1.6657e+008i	3.4224e+009 +1.6632e+008i	3.4183e+009 +1.6832e+008i	3.4135e+009 +1.6988e+008i	3.4084e+009 +1.6958e+008i	3.4028e+009 +1.6957e+008i	3.3953e+009 + 1.734e+008i	3.3882e+009 +1.8368e+008i	3.3899e+009 +1.9804e+008i	3.4039e+009 +2.0857e+008i	3.4157e+009 +2.2701e+008i
	210	3.4369e+009 +1.8152e+008i	3.4376e+009 +1.8012e+008i	3.4371e+009 +1.8263e+008i	3.4336e+009 +1.8719e+008i	3.4266e+009 +1.8961e+008i	3.4173e+009 + 1.882e+008i	3.4079e+009 +1.8603e+008i	3.3998e+009 +1.8665e+008i	3.3966e+009 +1.9159e+008i	3.4033e+009 +1.9664e+008i	3.4195e+009 +1.9438e+008i	3.4349e+009 +1.9268e+008i
	240	3.4056e+009 +2.0454e+008i	3.4052e+009 +2.0631e+008i	3.4033e+009 +2.1126e+008i	3.3974e+009 +2.1667e+008i	3.3878e+009 +2.1795e+008i	3.3769e+009 +2.1543e+008i	3.3678e+009 +2.1356e+008i	3.3617e+009 +2.1511e+008i	3.3601e+009 +2.1941e+008i	3.3642e+009 +2.1937e+008i	3.3711e+009 +2.1234e+008i	3.3722e+009 +2.1132e+008i
	270	3.3765e+009 + 2.48e+008i	3.3722e+009 +2.5379e+008i	3.3674e+009 +2.6155e+008i	3.3602e+009 +2.6678e+008i	3.351e+009 + 2.657e+008i	3.3409e+009 +2.6229e+008i	3.3321e+009 +2.6129e+008i	3.3256e+009 +2.6331e+008i	3.3236e+009 +2.6376e+008i	3.3284e+009 +2.5436e+008i	3.3373e+009 +2.4101e+008i	3.343e+009 +2.3618e+008i
	300	3.3823e+009 + 3.338e+008i	3.3764e+009 +3.4254e+008i	3.372e+009 +3.4909e+008i	3.3673e+009 +3.4902e+008i	3.3602e+009 +3.4623e+008i	3.3511e+009 +3.4755e+008i	3.3435e+009 +3.5396e+008i	3.3406e+009 +3.5858e+008i	3.3445e+009 + 3.511e+008i	3.3524e+009 +3.3747e+008i	3.3607e+009 +3.3071e+008i	3.3721e+009 +3.3824e+008i
	315	3.4535e+009 +3.6525e+008i	3.4488e+009 +3.7116e+008i	3.4469e+009 +3.7329e+008i	3.4442e+009 +3.7012e+008i	3.437e+009 +3.6721e+008i	3.4257e+009 +3.6962e+008i	3.416e+009 +3.7634e+008i	3.4131e+009 +3.7916e+008i	3.4186e+009 +3.7423e+008i	3.425e+009 +3.7444e+008i	3.4256e+009 +3.8938e+008i	3.4226e+009 +4.2481e+008i
	320	3.504e+009 +3.6502e+008i	3.5005e+009 +3.6941e+008i	3.5002e+009 +3.7019e+008i	3.499e+009 +3.6655e+008i	3.4925e+009 +3.6353e+008i	3.4809e+009 +3.6517e+008i	3.4698e+009 +3.7008e+008i	3.4655e+009 +3.7166e+008i	3.4704e+009 +3.6882e+008i	3.4782e+009 +3.7435e+008i	3.4802e+009 +4.0271e+008i	3.4765e+009 +4.4896e+008i
	325	3.8301e+009 + 3.898e+008i	3.8261e+009 +3.9385e+008i	3.8286e+009 + 3.947e+008i	3.8301e+009 +3.9125e+008i	3.8215e+009 +3.8748e+008i	3.8043e+009 +3.8704e+008i	3.7898e+009 +3.8916e+008i	3.7862e+009 +3.8898e+008i	3.7893e+009 +3.8547e+008i	3.7861e+009 + 3.879e+008i	3.7754e+009 + 4.047e+008i	3.7786e+009 +4.2735e+008i
	330	4.0626e+009 +3.7506e+008i	4.0603e+009 +3.7755e+008i	4.0573e+009 +3.7733e+008i	4.0539e+009 + 3.743e+008i	4.0482e+009 +3.7186e+008i	4.039e+009 +3.7222e+008i	4.0285e+009 +3.7349e+008i	4.0196e+009 + 3.715e+008i	4.0137e+009 +3.6736e+008i	4.0087e+009 +3.7051e+008i	4.0035e+009 +3.8775e+008i	4.0043e+009 +4.0682e+008i
	335	4.3507e+009 +3.6725e+008i	4.3598e+009 +3.7072e+008i	4.3656e+009 +3.7123e+008i	4.354e+009 +3.6777e+008i	4.3289e+009 + 3.647e+008i	4.3104e+009 + 3.665e+008i	4.3086e+009 +3.7192e+008i	4.3108e+009 +3.7376e+008i	4.3003e+009 +3.6858e+008i	4.2805e+009 +3.6678e+008i	4.2792e+009 +3.8077e+008i	4.3084e+009 +4.0482e+008i
	340	4.7317e+009 +3.7205e+008i	4.7296e+009 +3.7505e+008i	4.7403e+009 +3.7478e+008i	4.7434e+009 + 3.712e+008i	4.7218e+009 +3.6812e+008i	4.6869e+009 +3.6849e+008i	4.668e+009 + 3.712e+008i	4.6772e+009 +3.7236e+008i	4.6933e+009 +3.7237e+008i	4.686e+009 +3.8016e+008i	4.6682e+009 +4.0515e+008i	4.7021e+009 +4.3564e+008i
	344	5.3929e+009 +3.8765e+008i	5.3691e+009 +3.9125e+008i	5.3635e+009 +3.9015e+008i	5.3572e+009 +3.8544e+008i	5.3279e+009 +3.8272e+008i	5.2813e+009 +3.8524e+008i	5.2476e+009 +3.9103e+008i	5.2502e+009 +3.9574e+008i	5.2838e+009 +4.0142e+008i	5.3177e+009 +4.2081e+008i	5.343e+009 +4.6952e+008i	5.4025e+009 +5.4279e+008i
	349	6.2985e+009 +4.0492e+008i	6.2651e+009 +4.0964e+008i	6.2669e+009 +4.0911e+008i	6.2687e+009 +4.0327e+008i	6.2329e+009 +3.9763e+008i	6.1717e+009 +3.9703e+008i	6.1326e+009 +4.0128e+008i	6.1363e+009 +4.0625e+008i	6.1432e+009 +4.1116e+008i	6.0986e+009 +4.2741e+008i	6.0494e+009 +4.7694e+008i	6.1203e+009 +5.5036e+008i
	355	7.0332e+009 +4.0043e+008i	7.007e+009 +4.0844e+008i	7.0156e+009 +4.1126e+008i	7.0172e+009 +4.0978e+008i	6.971e+009 +4.1002e+008i	6.8908e+009 +4.1671e+008i	6.827e+009 +4.2951e+008i	6.8054e+009 +4.4384e+008i	6.7961e+009 +4.5523e+008i	6.7433e+009 +4.6933e+008i	6.6738e+009 + 5.062e+008i	6.7019e+009 + 5.989e+008i
	360	7.4634e+009 + 3.855e+008i	7.4402e+009 +3.9186e+008i	7.4613e+009 +3.9027e+008i	7.4776e+009 +3.8387e+008i	7.4357e+009 +3.8097e+008i	7.3472e+009 +3.8662e+008i	7.2723e+009 +4.0001e+008i	7.2459e+009 + 4.166e+008i	7.2342e+009 +4.3234e+008i	7.1662e+009 +4.5108e+008i	7.0734e+009 +4.8409e+008i	7.1114e+009 +5.3368e+008i
	371	7.7212e+009 +3.8862e+008i	7.7031e+009 +3.9667e+008i	7.7331e+009 +3.9559e+008i	7.7514e+009 +3.8771e+008i	7.6968e+009 +3.8166e+008i	7.5859e+009 + 3.839e+008i	7.4913e+009 +3.9543e+008i	7.458e+009 +4.1362e+008i	7.451e+009 +4.3406e+008i	7.3805e+009 +4.5848e+008i	7.2545e+009 +5.0368e+008i	7.2334e+009 +5.9837e+008i
	380	7.8705e+009 + 3.954e+008i	7.8506e+009 +4.0455e+008i	7.8827e+009 +4.0414e+008i	7.9094e+009 +3.9696e+008i	7.8622e+009 +3.9148e+008i	7.7476e+009 +3.9329e+008i	7.6349e+009 +4.0269e+008i	7.574e+009 +4.1741e+008i	7.5395e+009 +4.3554e+008i	7.4504e+009 +4.6207e+008i	7.3189e+009 +5.1504e+008i	7.3014e+009 +6.2398e+008i
	390	8.0301e+009 +3.8523e+008i	8.0191e+009 +3.9407e+008i	8.0629e+009 +3.9285e+008i	8.0962e+009 +3.8506e+008i	8.0456e+009 +3.7897e+008i	7.9241e+009 +3.7882e+008i	7.8156e+009 + 3.833e+008i	7.7805e+009 +3.8924e+008i	7.7862e+009 + 3.956e+008i	7.7265e+009 +4.0714e+008i	7.6083e+009 +4.3044e+008i	7.626e+009 +4.6041e+008i
	400	8.0636e+009 +3.8996e+008i	8.0429e+009 +4.0002e+008i	8.0881e+009 +3.9989e+008i	8.1405e+009 +3.9266e+008i	8.1162e+009 +3.8645e+008i	8.009e+009 +3.8571e+008i	7.8964e+009 +3.8955e+008i	7.8513e+009 +3.9527e+008i	7.8611e+009 +4.0116e+008i	7.8122e+009 +4.0934e+008i	7.6652e+009 +4.2386e+008i	7.5898e+009 +4.4075e+008i
	420	8.0682e+009 +3.9655e+008i	8.0513e+009 +4.0718e+008i	8.1095e+009 +4.0618e+008i	8.1783e+009 +3.9852e+008i	8.1672e+009 +3.9338e+008i	8.0737e+009 +3.9397e+008i	7.9844e+009 +3.9771e+008i	7.9703e+009 +4.0165e+008i	7.9953e+009 +4.0626e+008i	7.9284e+009 + 4.154e+008i	7.7673e+009 +4.2946e+008i	7.7475e+009 +4.3871e+008i
	435	8.0038e+009 +3.9113e+008i	7.9794e+009 +4.0204e+008i	8.0407e+009 +4.0077e+008i	8.1319e+009 +3.9289e+008i	8.1509e+009 +3.8789e+008i	8.0725e+009 +3.8858e+008i	7.9768e+009 +3.9155e+008i	7.9574e+009 +3.9337e+008i	8.0153e+009 +3.9504e+008i	8.0156e+009 +4.0185e+008i	7.8855e+009 +4.1622e+008i	7.805e+009 +4.3139e+008i
	450	8.1142e+009 +3.9504e+008i	8.0949e+009 +4.0545e+008i	8.1577e+009 +4.0348e+008i	8.25e+009 +3.9541e+008i	8.2753e+009 +3.9124e+008i	8.2084e+009 +3.9337e+008i	8.1228e+009 +3.9752e+008i	8.1047e+009 +3.9969e+008i	8.1591e+009 +4.0144e+008i	8.1698e+009 +4.0909e+008i	8.0674e+009 +4.2376e+008i	7.9773e+009 +4.3288e+008i
	465	5.5603e+009 +1.8666e+008i	5.4907e+009 +1.9451e+008i	5.5037e+009 +1.7979e+008i	5.5453e+009 +1.5309e+008i	5.5009e+009 +2.1119e+008i	5.363e+009 +2.2807e+008i	5.2283e+009 +1.5972e+008i	5.1992e+009 +2.6099e+008i	5.3662e+009 + 3.108e+008i	5.6585e+009 + 3.182e+008i	5.8658e+009 +3.4368e+008i	5.821e+009 + 3.915e+008i
	480	5.2944e+009 +2.1017e+008i	5.3145e+009 +2.2441e+008i	5.3309e+009 +2.3045e+008i	5.3187e+009 +2.3607e+008i	5.2238e+009 +2.3586e+008i	5.0601e+009 +2.2239e+008i	4.9248e+009 +2.1509e+008i	4.9013e+009 +2.6446e+008i	4.9779e+009 +2.9353e+008i	5.0364e+009 +2.9552e+008i	5.0426e+009 +2.7571e+008i	5.0938e+009 +3.3161e+008i
	510	4.6478e+009 +2.2147e+008i	4.6148e+009 +2.2851e+008i	4.5239e+009 + 2.184e+008i	4.3866e+009 +1.9935e+008i	4.2176e+009 +1.8642e+008i	4.1393e+009 +1.9551e+008i	4.3652e+009 +2.2968e+008i	4.9963e+009 +2.6855e+008i	5.7209e+009 +2.9637e+008i	5.1931e+009 +2.8487e+008i	3.6206e+009 +2.1388e+008i	3.1708e+009 +1.6543e+008i
	540	4.0217e+009 +2.0493e+008i	3.9305e+009 +1.9632e+008i	3.7779e+009 +1.6228e+008i	3.5631e+009 +1.1289e+008i	3.3069e+009 +7.0007e+007i	3.1865e+009 +6.7891e+007i	3.5118e+009 +1.3647e+008i	4.4546e+009 +2.1961e+008i	5.7605e+009 +2.8266e+008i	5.828e+009 +2.9158e+008i	3.6956e+009 +2.1169e+008i	1.7565e+009 +2.7982e+008i
	570	3.5094e+009 +2.0642e+008i	3.3513e+009 + 1.986e+008i	3.0934e+009 +1.5665e+008i	2.7371e+009 + 7.906e+007i	2.3365e+009 - 2.1104e+007i	2.1563e+009 - 1.9927e+007i	2.6365e+009 +8.1538e+007i	3.9445e+009 +1.8465e+008i	5.6024e+009 +2.7014e+008i	5.5229e+009 +2.8922e+008i	2.0363e+009 +2.2125e+008i	-2.7816e+009 - 1.6826e+008i
	600	3.1139e+009 +2.0236e+008i	3.0091e+009 +1.9805e+008i	2.8054e+009 +1.5966e+008i	2.4663e+009 +9.1333e+007i	1.9936e+009 +3.3737e+007i	1.6124e+009 +4.2493e+007i	1.8228e+009 +6.0858e+007i	3.005e+009 +1.1852e+008i	4.8639e+009 +2.3962e+008i	6.0781e+009 + 3.006e+008i	3.9802e+009 +2.3872e+008i	4.5068e+008 +2.8602e+008i
	630	2.9381e+009 +2.1206e+008i	2.8134e+009 +2.1003e+008i	2.5645e+009 +1.7451e+008i	2.1158e+009 +1.1402e+008i	1.4382e+009 +7.9101e+007i	7.9858e+008 +9.3372e+007i	9.0013e+008 +9.8091e+007i	2.3632e+009 +1.0271e+008i	4.7148e+009 +1.6593e+008i	6.2689e+009 +2.9547e+008i	2.8222e+009 +2.0584e+008i	-1.0524e+010 +2.0913e+008i
	660	2.8172e+009 +2.1117e+008i	2.6914e+009 +2.0461e+008i	2.4435e+009 +1.6665e+008i	2.0207e+009 + 1.142e+008i	1.4253e+009 +9.5695e+007i	9.3478e+008 +1.1046e+008i	1.1721e+009 + 1.166e+008i	2.6001e+009 +1.1814e+008i	4.7461e+009 +1.7859e+008i	6.0724e+009 +2.5991e+008i	3.6214e+009 +1.5353e+008i	-2.2551e+009 +2.1692e+008i
	690	2.566e+009 + 2.143e+008i	2.4264e+009 +2.1217e+008i	2.1949e+009 +1.7888e+008i	1.798e+009 +1.2452e+008i	1.1954e+009 +8.5485e+007i	5.9651e+008 +8.1444e+007i	5.81e+008 +7.7744e+007i	1.7496e+009 +7.7543e+007i	3.8862e+009 + 1.64e+008i	5.719e+009 +2.5345e+008i	4.9813e+009 +2.1842e+008i	2.6573e+009 +2.7488e+008i
	720	2.4502e+009 +2.1362e+008i	2.3684e+009 +2.1265e+008i	2.2344e+009 +1.7908e+008i	1.9555e+009 +1.2574e+008i	1.4384e+009 +1.1053e+008i	7.8202e+008 +1.4603e+008i	4.2913e+008 +1.7097e+008i	1.0518e+009 +1.5597e+008i	2.8832e+009 +1.0799e+008i	4.9878e+009 +1.7141e+008i	5.79e+009 +2.9514e+008i	4.8949e+009 +3.2211e+008i

Table 4 - Values for C_{12}

		Rotational Frequency											
		14140848.13	14755667.62	15370487.1	15985306.59	16600126.07	17214945.55	17829765.04	18444584.52	19059404.01	19674223.49	20289042.97	20903862.46
Time	150												
	180												
	210												
	240												
	270												
	300												
	315												
	320												
	325												
	330												
	335												
	340												
	344												
	349												
	355												
	360												
	371												
	380												
	390												
	400												
	420												
	435												
	450												
	465	3.5647e+009 +2.7901e+008i	3.6261e+009 +2.8197e+008i	3.6945e+009 +2.9743e+008i	3.7652e+009 +3.2006e+008i	3.8546e+009 +2.3835e+008i	3.9469e+009 +2.1749e+008i	4.0286e+009 +3.0669e+008i	4.0874e+009 +1.8087e+008i	3.9974e+009 +1.2095e+008i	3.6558e+009 +1.2527e+008i	3.25e+009 +1.0989e+008i	3.251e+009 +6.1239e+007i
	480	3.7817e+009 +2.3227e+008i	3.7324e+009 +2.2769e+008i	3.8024e+009 +2.1757e+008i	3.9532e+009 +1.9989e+008i	4.1267e+009 +1.9407e+008i	4.2765e+009 +2.1219e+008i	4.3792e+009 +2.2491e+008i	4.4313e+009 +1.6638e+008i	4.4206e+009 +1.3217e+008i	4.3281e+009 +1.3733e+008i	4.1662e+009 +1.7775e+008i	4.0801e+009 +1.2243e+008i
	510	4.6999e+009 +2.2658e+008i	4.706e+009 +2.3079e+008i	4.9009e+009 +2.3946e+008i	5.2051e+009 +2.5122e+008i	5.4726e+009 +2.6063e+008i	5.5311e+009 + 2.52e+008i	5.2346e+009 +2.1459e+008i	4.5389e+009 +1.6366e+008i	3.7624e+009 +1.2449e+008i	4.4695e+009 +1.5164e+008i	6.1506e+009 +2.6198e+008i	6.5899e+009 +3.2537e+008i
	540	5.4848e+009 +2.5112e+008i	5.556e+009 +2.7239e+008i	5.8142e+009 +3.0502e+008i	6.1905e+009 + 3.447e+008i	6.5281e+009 +3.7954e+008i	6.6181e+009 +3.8211e+008i	6.2587e+009 + 3.203e+008i	5.3062e+009 +2.2948e+008i	3.9023e+009 +1.4884e+008i	3.9343e+009 +1.4839e+008i	6.3375e+009 +2.7225e+008i	7.8948e+009 +2.7819e+008i
	570	5.9892e+009 +2.4671e+008i	6.1172e+009 +2.6606e+008i	6.4603e+009 + 3.037e+008i	6.9395e+009 +3.6304e+008i	7.3625e+009 +4.3364e+008i	7.4874e+009 + 4.299e+008i	7.0809e+009 + 3.602e+008i	5.8929e+009 +2.6256e+008i	4.1268e+009 +1.5812e+008i	4.321e+009 +1.4378e+008i	7.7639e+009 +2.7819e+008i	5.8081e+009 +1.9702e+008i
	600	6.4039e+009 +2.4266e+008i	6.4776e+009 +2.5846e+008i	6.7487e+009 +2.9215e+008i	7.184e+009 +3.4143e+008i	7.6336e+009 +3.7607e+008i	7.8749e+009 +3.6781e+008i	7.7157e+009 +3.5998e+008i	6.8348e+009 +3.1902e+008i	5.0341e+009 +1.9223e+008i	3.6557e+009 +1.2804e+008i	6.124e+009 +2.3672e+008i	8.5614e+009 +3.6732e+008i
	630	6.5972e+009 +2.4083e+008i	6.6885e+009 +2.5475e+008i	6.9897e+009 +2.8564e+008i	7.4812e+009 +3.2742e+008i	7.9985e+009 +3.4785e+008i	8.2827e+009 +3.5048e+008i	8.2461e+009 +3.4913e+008i	7.4739e+009 +3.3502e+008i	5.3266e+009 +2.8268e+008i	3.4791e+009 +1.3437e+008i	7.2706e+009 +2.7205e+008i	1.1709e+011 +3.1363e+010i
	660	6.7196e+009 +2.3928e+008i	6.8092e+009 +2.5775e+008i	7.0982e+009 +2.9046e+008i	7.5565e+009 +3.2486e+008i	8.0188e+009 +3.3611e+008i	8.2547e+009 +3.3885e+008i	8.1512e+009 + 3.34e+008i	7.288e+009 +3.2082e+008i	5.2873e+009 + 2.657e+008i	3.7652e+009 +1.7996e+008i	6.5891e+009 + 3.231e+008i	7.2144e+009 +8.7751e+008i
	690	6.9773e+009 +2.4358e+008i	7.0766e+009 +2.5869e+008i	7.3417e+009 +2.8661e+008i	7.7542e+009 +3.2177e+008i	8.1727e+009 +3.4577e+008i	8.3912e+009 +3.5825e+008i	8.3901e+009 + 3.623e+008i	7.9499e+009 +3.5237e+008i	6.306e+009 + 2.811e+008i	4.2878e+009 +1.9041e+008i	5.1132e+009 +2.5741e+008i	7.4571e+009 +2.4233e+008i
	720	7.049e+009 +2.4156e+008i	7.1004e+009 +2.5519e+008i	7.2897e+009 +2.8132e+008i	7.6297e+009 +3.1419e+008i	8.0371e+009 +3.2478e+008i	8.3342e+009 +3.2862e+008i	8.4314e+009 + 3.432e+008i	8.3256e+009 +3.1832e+008i	7.2838e+009 +3.2744e+008i	5.2147e+009 +2.8508e+008i	4.1959e+009 +1.6404e+008i	5.3313e+009 +1.5399e+008i

Table 5 - Values for Young's modulus

Appendix IV - Conference abstracts and journal publications

1. Briscoe, A., New, A.M., Taylor, M. Effect of pre-cooling and pre-heating a hip stem on the bone-cement interface temperature history, in International Conference on Computational Bioengineering, 2003, Zaragoza, Spain.

2. Briscoe, A., Saffari, N., Browne, M., New, A., Ultrasonic Measurement Of Mechanical Properties Of PMMA Bone Cement During Cure For Modelling Of Residual Stresses, in ASME Summer Bioengineering Conference, Vail, CO.

3. Chandler, M., Kowalski, R. S. Z., Watkins, N. D., Briscoe, A., New, A. M. R., Cementing techniques in hip resurfacing, Proc. IMechE vol. 220 Part H: J. Engineering in Medicine, 321-331.

INTERNATIONAL CONGRESS ON COMPUTATIONAL BIOENGINEERING
M. Doblaré , M. Cerrolaza and H. Rodrigues (Eds.)

EFFECT OF PRE-COOLING AND PRE-HEATING A HIP STEM ON THE BONE-CEMENT INTERFACE TEMPERATURE HISTORY

Adam Briscoe[1], Andrew New[1], Mark Taylor[1]

[1]*Bioengineering Sciences Research Group*
University of Southampton, England

SUMMARY

The polymerisation of PMMA bone cement is exothermic and can cause thermal bone necrosis. Dunne *et al.* found temperatures and times that are acceptable for bone to experience during this cure process [1]. A thermal model of the polymerisation process of cement in an idealized femoral component of a total hip arthroplasty was created. This model was then used to investigate the effects of implanting a hip stem of known initial temperature.

The cure gradient was also investigated in order to observe local stress concentrations that may initiate early damage in the cement mantle, which may then cause an acceleration of damage accumulation in the cement mantle leading to loosening and require joint revision.

It was found that by altering the initial stem temperature both the cure gradient and the peak temperature could be controlled. A stem temperature of body temperature was desirable for creating minimal cure gradient. Cooler stems cause a reduction in peak temperature.

1. INTRODUCTION

Aseptic loosening was the reason for 75.7% of hip joint revision operations reported in the Swedish Hip Register for the period between 1979 and 1998 [2].

Thermal bone necrosis is suspected to be a cause of short term loosening in Total Hip Arthroplasty (THA). Bone material has been shown to die if held at temperatures above approximately 45˚C for more than 1 minute. Differing values for these temperatures and times are reported by various authors but this is an approximate average [3,4].

During polymerisation of PMMA bone cement (used for fixation of both components in a THA) the cement itself can reach similar temperatures to those required for bone necrosis to take place, due to the exothermic nature of the reaction.

A further effect of the cement polymerisation is to generate residual stress in the cement. During the cooling phase of the polymerisation reaction the cement shrinks. At this stage the cement has hardened sufficiently to allow load transfer, thus creating a residual tensile stress in the hoop direction. During cure the cement also undergoes a volumetric shrinkage associated with the density increase in converting MMA monomer to PMMA [5].

It has been a matter of contention over recent years whether residual stresses are a significant parameter in mechanical modelling of total hip replacement. Some authors have argued that the magnitude of these stresses is low when compared to the upper tensile stress of PMMA cement (approximately 10MPa compared with 40-50MPa [6]) and can thus be ignored. However, this magnitude has been seen to almost double the cement stress upon application of external load. This significant increase in the stress will have serious consequences when looking at the fatigue and damage accumulation rates in the cement mantle.

Although relaxation processes in the cement may cause peak stresses to relax, complete relaxation does not occur and the remaining stress still combines with the stresses due to the applied load [7]. Residual stresses can be locally increased by gradients in the polymerisation process. These stress concentrations can lead to early damage initiation and so increase the rate of subsequent damage accumulation in the cement mantle in service.

Modelling of the polymerisation of acrylic bone cement requires some complex mathematical modelling as the polymerisation rate is temperature dependent and the heat generation rate from the reaction is dependent on the degree of polymerisation [8].

Several polymerisation models may be found in the literature. Baliga *et al.* generated an expression for the instantaneous heat generation rate as a function of temperature from differential scanning calorimetry (DSC) results [9]. Bone cement was cured in a DSC at several different isotherms similar to the range of temperatures expected during clinical polymerisation. From these results a 6^{th} order polynomial was fitted to

the data, generating an empirical equation with several coefficients that have no physical interpretation:-

$$f(T) = 4.4\times10^6\left(a_0 + a_1\frac{T}{100} + a_2\left(\frac{T}{100}\right)^2 + a_3\left(\frac{T}{100}\right)^3 + a_4\left(\frac{T}{100}\right)^4 + a_5\left(\frac{T}{100}\right)^5\right)$$

where *f(T)* gives a heat function used to determine the heat generation rate, T is the local temperature and a_n are the DSC determined polynomial coefficients.

The large number of empirical coefficients that must be determined make the model difficult to modify to suit different manufacturers cements

A different model proposed by Borzacchiello *et al.* 1998 uses more identifiable parameters, each with a physical interpretation [10]:-

$$f(T) = K_0 e^{\frac{-Ea}{RT}},$$

where *f(T)* gives the equivalent heat function used to determine the heat generation rate, K_0 is a rate coefficient, Ea is the activation energy, R is the universal gas constant and T is the temperature.

Since each parameter in Borzacchiello's model has a physical interpretation, it is significantly easier to justify it as an approximation of the polymerisation. Each parameter can be found using very little DSC experimental time using methods set out by Starink 2003 [11].

An idealised finite element model of the polymerisation of PMMA based bone cement used for fixation of the femoral component in a THA has been developed. Using this model the effect of the initial temperature of the hip stem on the temperature history of the bone-cement interface was investigated. The finite element model was also used to investigate the cure gradients in the mantle in an attempt to identify conditions that would reduce localised increases in residual tensile stress. The effects of initial stem temperature were investigated.

2. METHOD

A finite element mesh of a simplified femoral hip replacement was generated. The mesh consists of three components; the stem, the cortical bone and the cement mantle. The stem has a neck diameter of 18mm, a stem length of 132mm and a taper beginning distal to the neck to a tip of diameter 4.5mm. A 2mm thick layer of cement surrounds the stem, which is in turn surrounded by a 5mm layer of cortical bone, protruding 30mm distally. The model can be seen in Figure 1.

Each separate material was given appropriate thermal properties (Table 1). The initial conditions were set with body temperature for the bone, room temperature for the cement and the initial stem temperature was varied.

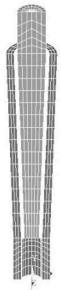

Figure 1 - Finite element mesh of idealized hip stem

A convection term was applied to the stem neck, which is slightly higher than would ordinarily be expected to allow for conduction through the surgeons hand and any forced convection. A constant body temperature boundary condition was applied to the outer surface of the cortical bone.

Table 1 - Thermal properties for model materials

Material Property	Value
Bone Density	2100 kg/m^3
Bone Specific Heat Capacity	1260 J/kgK
Bone Conductivity	0.38 W/mK
Stem Density	8870 kg/m^3
Stem Specific Heat Capacity	450 J/kgK
Stem Conductivity	14.6 W/mK
Cement Density	1100 kg/m^3
Cement Specific Heat Capacity	1250+6.5(T) J/kgK
Cement Conductivity	0.2 W/mK

The properties for the cement, stem and bone were taken from Baliga *et al.* [5], Matweb [12] and Henschel [13] and Chato [14] respectively.

At each time step results were output and a new degree of polymerisation calculated from the amount of heat liberated during the last time step (Flowchart 1). The degree of polymerisation α, was calculated from the ratio of the amount of heat liberated to the total heat of polymerisaton.

$$\alpha = \frac{Q}{Q_{tot}},$$

where Q is the amount of heat liberated so far and Q_{tot} is the total amount of heat that the cement will liberate during polymerisation.

From the degree of polymerisation and the local temperature, the nodal heat generation rate can be calculated for the next time step.

$$S = f(T)\times(1-\alpha)^n\alpha^m,$$

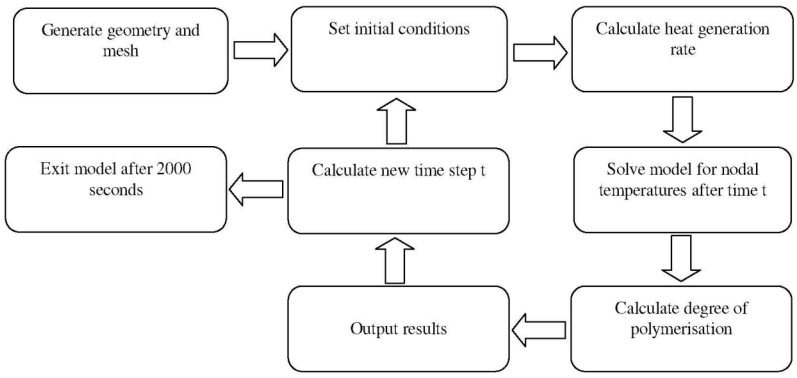

Flowchart 1 – Model procedure

where S is the volumetric heat generation rate of the PMMA bone cement and n and m are non-temperature dependent constants (also determinable from DSC experiments [7]).

To optimise the computation the time step used in the model was varied to control the degree of polymerisation increment. In order for the polymerisation to start the degree of polymerisation (α) must be set as a number greater than 0, typically $1x10^{-6}$. After 2000 seconds the model exits (Flowchart 1).

The initial stem temperature was altered from 5˚C to 50˚C to give realistic limits for clinical usage (if the stem were any colder then condensation would form on the stem prior to implantation, any hotter and the surgeon could not hold and manipulate it easily).

3. RESULTS

Data was recorded from nodes in the cement and cortical bone. The data included the time, temperature, degree of polymerisation and nodal heat generation rate. The bone temperatures were also analysed to find the depth to which necrosis may occur. Contour plots of the degree of polymerisation were obtained at the end of each time step.

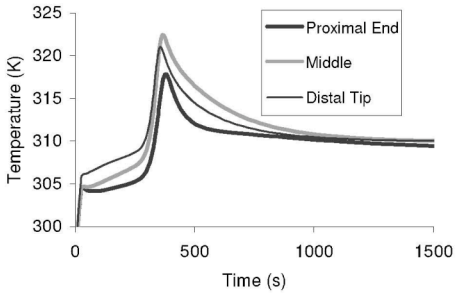

Figure 2 - Temperature at bone-cement interface with a room temperature stem

Figure 2 shows the temperature at the bone-cement interface for the room temperature stem. The temperature reached a peak of 49˚C halfway down the cement bone interface. The bone experienced temperatures greater than 45˚C to a depth of 1mm (Figure 3). Further from the cement interface the bone was heated for a short enough time for no bone necrosis to take place.

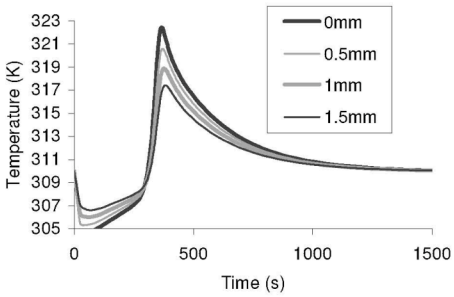

Figure 3 - Temperature across bone from cement interface in room temperature stem model

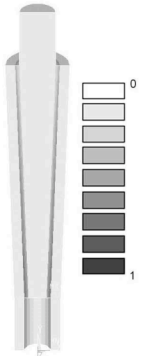

Figure 4 - Cure contour of cement in room temperature stem model

The cure in the room temperature stem model progressed from distal to proximal (Figure 4).

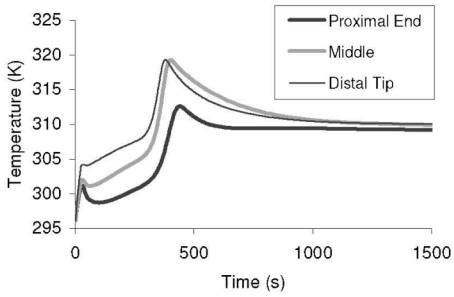

Figure 5 - Temperature at bone-cement interface with a 5°C stem

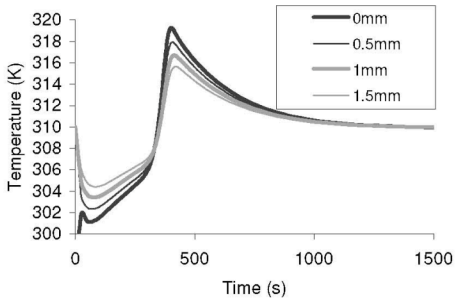

Figure 6 - Temperature across bone from cement interface in 5°C stem model

The refrigerated stem reduced the peak bone-cement interface temperature by 3°C (Figure 5). The effect on cure gradient was to increase it in the distal-proximal direction (Figure 7).

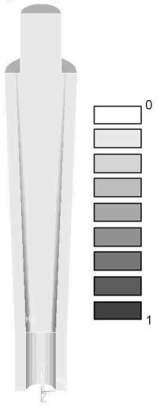

Figure 7 - Cure contour of cement with 5°C stem model

By increasing the initial stem temperature the danger of bone necrosis was increased, with peak bone temperatures of 55°C being obtained (Figure 8). This danger also carries further into the bone (Figure 9). The effect on the cure gradient was to completely reverse it with more rapid curing occurring in the proximal region (Figure 10).

A fourth model with a body temperature stem was also run. By implanting a body temperature stem the rise in peak temperature when compared to a room temperature stem is negligible (Figure 11 shows a 3°C difference).

The bone experiences temperatures above 45°C to approximately the same depth as the room temperature stem model (Figure 12). The cure gradient however is greatly reduced. There is negligible cure gradient in the distal-proximal direction throughout the polymerisation process (Figure 13).

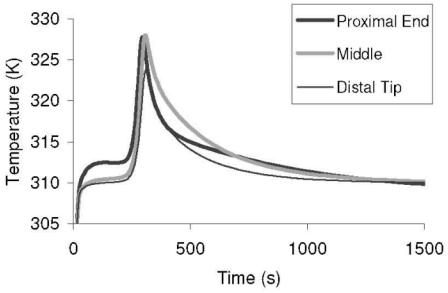

Figure 8 - Temperature at bone-cement interface with a 50°C stem

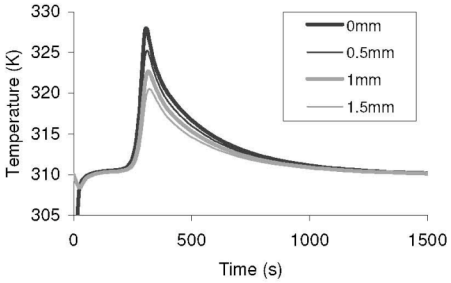

Figure 9 - Temperature across bone from cement interface in 50°C stem model

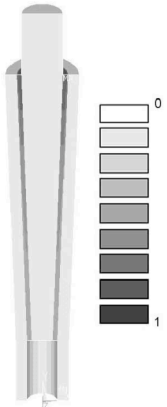

Figure 10 - Cure contour of cement with 50°C stem model

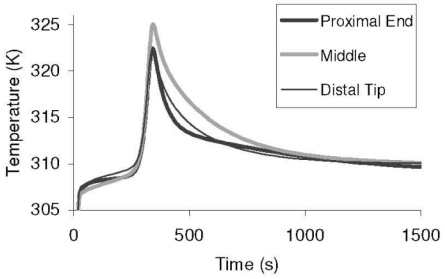

Figure 11 - Temperature at bone-cement interface with a body temperature stem

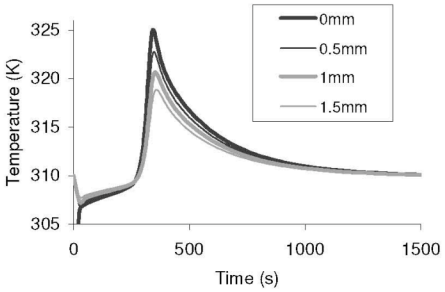

Figure 12 - Temperature across bone from cement interface in body temperature stem model

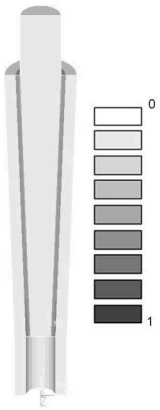

Figure 13 - Cure contour of cement with body temperature model

4. DISCUSSION

Results obtained from this study show that by changing the initial stem temperature within suitable limits, the change in peak temperature at the cement bone interface (and therefore in the amount of bone necrosis) is not as significant as the potential gains to be made by reducing the cure gradient.

Some surgeons have been cooling stems in order to reduce bone necrosis during implantation. The results of the current work show that this may not be achieving the effect to a degree that would be desirable. The cooled stem may actually be causing a greater cure gradient and so causing residual stress concentrations and initiating pre-load cracks in the cement.

From the results of the body temperature stem model it can be seen that it may be possible to achieve a uniform cure gradient with negligible increase in bone necrosis. This uniform cure may be expected when using a body temperature stem as the cement experiences an identical temperature on both sides.

By reducing the occurrence of residual tensile stress concentration sites within the cement it may be possible to extend the service life of the cement mantle and the THA. In this way it may be possible to treat younger and more active patients.

In future the model will be adapted to include mechanical property evolution during cure as well as volumetric changes. The aim is to generate a complete and accurate residual stress field for use in damage accumulation and service life modelling.

10. BIBLIOGRAPHY

[1] Dunne, N. J. and J. F. Orr (2002). "Curing characteristics of acrylic bone cement." Journal of Materials Science-Materials in Medicine **13**(1): 17-22.

[2] Malchau, H., Herberts P., Garellick G., Soderman P., Eisler T. (2002). Prognosis of Total Hip Replacement.

[3] Starke, G. R., C. Birnie, *et al.*. (2001). Numerical modelling of cement polymerisation and thermal bone necrosis. Computer methods in biomechanics and biomedical engineering, London, Gordon & Breach.

[4] Rodop, O., A. Kiral, *et al.*. (2002). "Effects of stem design and pre-cooling prostheses on the heat generated by bone cement in an in vitro model." Journal of International Medical Research **30**(3): 265-270.

[5] Orr, J. F., N. J. Dunne, *et al.*. (2003). "Shrinkage stresses in bone cement." Biomaterials **24**(17): 2933-2940.

[6] Harper, E. J. and W. Bonfield (2000). "Tensile characteristics of ten commercial acrylic bone cements." Journal of Biomedical Materials Research **53**(5): 605-616.

[7] Jeffers, J. R. T. and M. Taylor (2003). Residual stress decreases the life of the cement mantle in total hip replacement. International Conference on Computational Biomechanics, Zaragoza, Spain.

[8] Hansen, E. (2003). "Modelling heat transfer in a bone-cement-prosthesis system." J Biomech **36**(6): 787-95.

[9] Baliga, B. R., P. L. Rose, *et al.*. (1992). "Thermal modeling of polymerizing polymethylmethacrylate, considering temperature-dependent heat generation." J Biomech Eng **114**(2): 251-9.

[10] Borzacchiello, A., L. Ambrosio, *et al.*. (1998). "Comparison between the polymerization behavior of a new bone cement and a commercial one: modeling and in vitro analysis." Journal of Materials Science-Materials in Medicine **9**(12): 835-838.

[11] Starink, M. J. (2003). "The Determination of Activation Energy from Linear Heating Rate Experiments: A comparison of the accuracy of isoconversion methods." In Press. Thermochimica Acta.

[12] Automation Creations, I. (2003). Matweb Material Property Data. **2003**.

[13] Henschel, C. J. (1943). "Heat Impact of Revolving Instruments on Vital Dental Tubules." Journal of Dental Research **22**: 323.

[14] Chato, J. C. (1965). A survey of thermal conductivity and diffusivity data on biological materials. 5th conference on thermal conductivity, Denver, Colorado.

ULTRASONIC MEASUREMENT OF MECHANICAL PROPERTIES OF PMMA BONE CEMENT DURING CURE FOR MODELLING OF RESIDUAL STRESSES

Adam Briscoe (1), Nader Saffari (2), Andrew New (1), Martin Browne (1)

(1) Bioengineering Sciences Research Group
University of Southampton
Southampton, Hampshire
United Kingdom

(2) Department of Mechanical Engineering
University College London
London
United Kingdom

INTRODUCTION

Residual stress is an important factor to consider when predicting the fatigue performance of poly (methylmethacrylate) (PMMA) bone cement *in vivo* [1]. Residual stress is generated within the cement mantle surrounding all cemented joint replacement components as a result of mechanical property changes, chemical shrinkage and thermal expansion and subsequent contraction during cure. Each of these factors must be modeled to gain an accurate picture of the residual stress fields created during cure.

Some attempts have been made to measure the shrinkage and mechanical properties using independent experiments [3, 4]. These studies do not account for interactions of independent variables and separate parameters cannot be extracted. The volumetric change results produced by Muller et al. [3] could, in principle be used in combination with the mechanical property functions produced by Viano et al. [4] to completely characterize polymerization. However, in practice this is not possible since results were obtained under different conditions.

Until now, the only mechanical property derived has been restricted to the linear elastic compressional modulus. This has been used to quantify the rate of polymerization. The Young's and shear moduli for bone cement are complex however, containing a real (elastic or storage) part and an imaginary (plastic or loss) part.

The current work aims to address these two problems by developing a method of measurement that can yield results for volume change and mechanical property evolution simultaneously and by measuring all mechanical properties including real and complex modulus.

THE ULTRASONIC MEASUREMENT METHOD

A pulser/receiver is used to excite a compressional or a shear wave transducer, operating at a centre frequency of 2.5 MHz. A short pulse (of either compressional or shear waves) is transmitted through a thickness of bone cement with initial amplitude, A_o (Figure 1). The pulse is reflected from a flat stainless steel reflector plate at the other side of the mould, with a reflection coefficient R_{PS}.

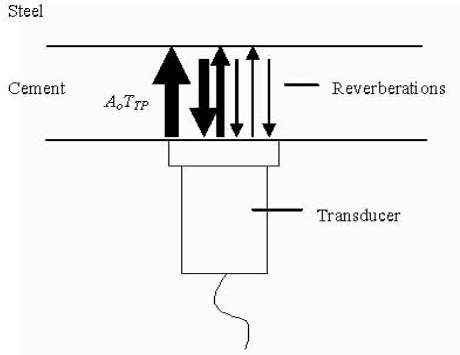

The pulse reverberates between the transducer and the reflecting plate a number of times while being attenuated by an amount $e^{-2n\alpha x}$, where x is the cement thickness, α the attenuation coefficient for cement and n, the number of reverberations. If the direction dependent transmission coefficients at the transducer-cement interface are T_{TP} and T_{PT}, the amplitude of the first reflected pulse received at the transducer can be written as:

$$A_{1st} = A_o \times R_{PS} \times T_{TP} \times T_{PT} \times e^{-2\alpha x},$$

while that for the second reflected pulse is:

$$A_{2nd} = A_o \times R_{PS}^2 \times R_{PT} \times T_{TP} \times T_{PT} \times e^{-4\alpha x},$$

where R_{PT} is the reflection coefficient at the cement-transducer interface.

From the ratio of the above two consecutive echoes together with independent measurement of the wave velocities through the cement layer the attenuation coefficients for the cement (for either

compressional or shear waves) and the cement density can be calculated. These values enable us to calculate the two independent complex elastic constants for the cement, C_{11} and C_{12}.

It is thus possible to obtain all the complex moduli involved in the complete description of the mechanical behavior of PMMA bone cement. Shear (G), bulk (K) and Young's (E) moduli can be calculated in their complex forms.

The shear modulus and bulk modulus can be defined in terms of C_{11} and C_{12}, which are two independent constants that can be used to describe material behaviour:

$$G = \frac{C_{11} - C_{12}}{2},$$

$$K = \frac{C_{11} + 2C_{12}}{3}.$$

Young's modulus can be described using the terms already found:

$$E = \frac{G(C_{11} + 2C_{12})}{C_{12} + G}.$$

Density can also be used to calculate volume by assuming conservation of mass within the test chamber.

MATERIALS AND EQUIPMENT

The ultrasonic rig consisted of a transducer (Panametrics™ V604 or V514), a Panametrics™ 5052 pulser/receiver with the output captured on a LeCroy™ 9310 oscilloscope. The transducer was mounted in the lower surface of a mould cavity (Figure 2). The reflective surface (opposite the active transducer surface) was free to translate under gravity towards and away from the transducer to enable the cement to expand and contract. The thickness of the cement mantle was measured using a micrometer, mounted on the back face of the mould. The transducer face was protected from the cement using cellophane. A thermocouple measured cement temperature.

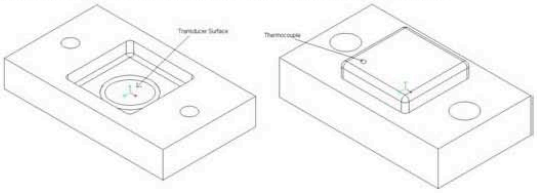

Figure 2. Mould Cavity and Reflective Face.

Immediately after mixing, cement was injected into the mould cavity using a cementing gun, ensuring total coverage of the active face of the transducer. The reflective surface of the mould was then lowered onto the cement and firmly pressed down to ensure good coupling at both interfaces. The cement mantle thickness was then measured and the first readings from the transducer and thermocouple were recorded at 2min30sec after initial mixing time. Data was then collected every 30sec (or less) for 15min30sec at which time no further change was observed and the cement was considered to be fully set. The experiment was repeated 4 times using a compressional wave transducer.

RESULTS

Figure 3 shows the waves received at the transducer as a function of experiment time for 4 compressional wave tests. The first two coloured band along the x-axis are the first two reflected pulses that are used for the analysis described above. Further echoes can be identified in each trace, but these later reverberations are not used in the analysis, although their origins are known.

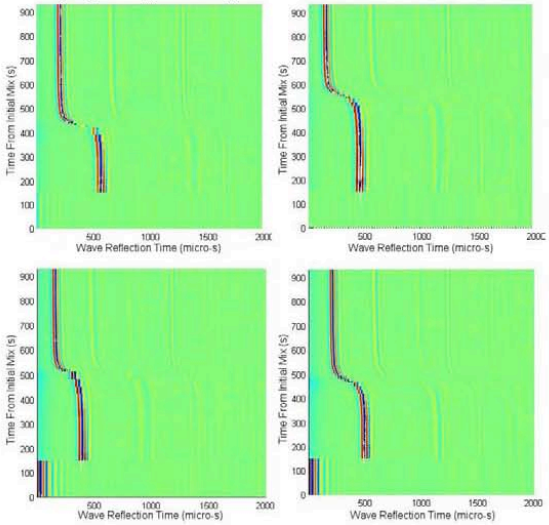

Figure 3. Wave profiles as a function of time

The wave profiles clearly show that there is a short period of time (around 400-500s from mixing) during which a large change in the velocity of sound through the specimen is observed. During this period it can be seen that the speed of sound is increased through the sample and the second echo can be seen much more clearly than earlier in the test. This increase in the velocity of the wave and the reduced attenuation can be attributed to combined effects of increasing material stiffness and density. The timing of this period is not constant through all 4 experiments and this difference may be explained by differences in specimen thickness. The thicker specimens would be expected to produce earlier polymerisation due to higher exotherms [2]. This theory is further born out by thickness readings taken after the experiment was finished; the fastest experiment (d) has the thickest cement layer etc.

CONCLUSIONS

The current work has shown that it is possible to measure the evolution in mechanical properties that is experienced during the cure of PMMA bone cement. A method has been developed to extract values for all complex moduli as well as density and volume. This data can be used to model residual stresses generated within the cured cement mantle and so assist in the life prediction of cemented joint replacement components *in-vivo*.

REFERENCES

1. Jeffers JRT, Taylor M. In *International Conference on Computational Biomechanics*. 2003. Zaragoza, Spain.
2. Li C, et al. J. Mater. Sci.-Mater. Med. 15: 85-89, 2004.
3. Muller SD, et al.Acta Orthop. Scand. 73: 684-687, 2002.
4. Viano AM, et al. J. Biomed. Mater. Res. 56: 593-599, 2001.

SPECIAL ISSUE PAPER 321

Cementing techniques in hip resurfacing

M Chandler[1], **R S Z Kowalski**[1], **N D Watkins**[1]*, **A Briscoe**[2], and **A M R New**[2]
[1] DePuy CMW, Blackpool, UK
[2] Bioengineering Science Research Group, School of Engineering Sciences, University of Southampton, Southampton, UK

The manuscript was received on 17 October 2005 and was accepted after revision for publication on 10 November 2005.

DOI: 10.1243/09544119JEIM113

Abstract: The subject of the cementing technique in hip resurfacing has been poorly studied to date. The hip resurfacing prosthesis is unique in the family of cemented prostheses because the cement mantle is blind (hidden underneath the implant) and is radiographically obscured. This presents an immediate challenge to the surgeon at the time of surgery, but also has a longer-term implication in terms of lack of post-operative clinical observation. This should be compared with total hip replacement or total knee replacement where the cement mantle can at least be partially observed both intra- and post-operatively. With this in mind, the objective of this review is, firstly, to understand the cement mantles typically achieved in current clinical practice and, secondly, to identify those factors affecting the cement mantle and to consolidate them into an improved and reproducible cementing technique. The outcome of this work shows that the low-viscosity technique can commonly lead to excessive cement penetration in the proximal femoral head and an incompletely seated component, whereas a more consistent controlled cement mantle can be achieved with a high-viscosity cementing technique. Consequently, it is recommended that a high-viscosity technique should be used to minimize the build-up of excessive cement, to reduce the temperature created by the exothermic polymerization, and to help to ensure correct seating of the prosthesis. A combination of these factors is potentially critical to the clinical success of some articular surface replacement (ASR) procedures.

It is important to note that we specifically studied the DePuy ASR system; therefore only the general principles (and not the specifics) of the cementing technique may apply to other resurfacing prostheses, because of differences in internal geometry, clearance, and surgical technique.

Keywords: bone cement, cementing technique, hip resurfacing

1 INTRODUCTION

Acrylic bone cements have been widely used for the fixation of artificial joint replacement implants for many years. The bone cement forms a mantle adjacent to the implant and acts as an elastic zone between the implant and the bone, cushioning the load forces and beneficially affecting bone remodelling whilst sealing the interfaces against ingress of wear particles. Extensive clinical data have confirmed that, when an appropriate cementing technique is applied, acrylic bone cement provides a safe and highly effective fixation method, with results at least as good as cementless procedures.

All acrylic bone cements currently marketed are based on the same chemical substance: methyl methacrylate (MMA). Extensive development of MMA and its derivatives began in the 1920s with Otto Rohm, who later founded the Rohm and Haas company. By the 1930s, MMA was used in dentures [1] and the discovery was made that a dough could be produced by mixing poly(methyl methacrylate) (PMMA) with its monomer, MMA, which in turn could be heat cured and hardened in the presence of benzoyl peroxide (BPO) [2]. The heat-cured polymer was used, in a preformed state, to repair cranial defects in humans from the early 1940s [3].

Within a short time, the discovery was made that the polymerization of MMA could be made to occur at room temperature in the presence of a peroxide initiator and an amine activator [4]. This discovery opened the door for 'self-setting' cement in cranial defect repair, in denture repair, and in the development of implant fixation. Kiaer [5] used PMMA as an anchoring material for fixing acrylic caps on

Corresponding author: DePuy CMW, Cornford Road, Blackpool, Lancashire FY4 4QQ, UK. email: nwatkins@dpygb.jnj.com

the femoral head after first removing the cartilage, Haboush [6] used PMMA as a seating compound for a femoral head replacement prosthesis, whilst Sir John Charnley [7] also succeeded in anchoring a femoral head prosthesis in the femur with self-setting acrylic bone cement.

The adoption of acrylic cement in total hip replacement began in the late 1950s. The first generation cementing technique, generally regarded as having been developed by Charnley, is based on the use of a high-viscosity cement, introduced by hand, digital pressurization, limited bone bed preparation, and open-air cement mixing. A preference to introduce the bone cement with a gun and syringe led to a modified cementing technique, sometimes referred to as second generation. Perhaps owing to the limitations of the early cement guns, a lower-viscosity cement tended to be used. Other refinements were made, including acetabular cement pressurization devices, proximal femoral pressurization devices, and distal cement plugs, these being used to increase cement penetration and to maintain cement pressure above bleeding pressure, preventing blood ingress into the cement. Blood ingress can lead to the creation of blood laminations in cement; a study carried out by Gruen [8] showed that blood laminations can significantly reduce the strength of the acrylic bone cement. Furthermore, it had been recognized, including by Charnley [9], that bone cement functions as a grout and not as a glue. To achieve good fixation to the bone and therefore long-term survival of the implant, the cement must first penetrate the trabecular bone and then harden, forming a physical micro-interlock. As part of the second-generation cementing technique and to increase cement penetration into the bone, improved bone bed preparation was introduced, requiring such factors as irrigation and drying.

As cementing techniques continued to develop, further improvements to bone bed preparation, such as the use of pulsatile lavage, were introduced. Better cement guns were introduced, allowing the use of higher-viscosity cements, and in addition vacuum mixing was used to eliminate cement fumes from the operating theatre and to increase the strength of the cement by porosity removal. It has been acknowledged that the risk of revision for cemented hip replacements is reduced when a modern cementing technique is used compared with early or old techniques [10]. However, it has also been suggested that the risk of revision varies greatly across different orthopaedic clinics even when evaluating optimal techniques [11, 12], a finding which suggests that good cementing technique is far from straightforward, and arguably far from understood.

The development of a good cementing technique relies on an understanding of the nature and effect of the handling characteristics of bone cement, these being crucial to achieving good cement penetration and resistance to blood ingress. Bone cement rheology is a complex property, reflecting the viscoelastic behaviour of cements during their curing phase. It can be best thought of as a combination of its stiffness (or elasticity) and its ability to flow. If the bone cement is too stiff and does not flow, then it may not penetrate into the cancellous bone. Conversely, if the cement has high flow without adequate stiffness, then it can be easily displaced by blood unless continuously and meticulously pressurized, and very little cement pressure will be generated during insertion of the prosthesis. Cement viscosity is not constant over time and is affected by environmental factors such as temperature and humidity during storage and use. Furthermore, different commercial brands of cement are available with specific degrees of viscosity and different working and setting times. It is important to understand that all cements eventually reach the same viscosity; however, this will be at different times after mixing. It is therefore critical to appreciate the optimum times for cement introduction, cement pressurization, and implant insertion.

2 ARTICULAR SURFACE REPLACEMENT CEMENTING

2.1 Background

Resurfacing of the hip is not a new procedure, and the origins of the resurfacing technique predate even total hip replacement (THR). Charnley was one of the pioneers of this technique and had experimented with hip resurfacing designs long before he established the principles of low-friction arthroplasty, which is one of the guiding principles of modern THR.

However, in contrast with the situation for cemented THR, a literature search of cementing technique in hip resurfacing reveals a paucity of data. At the time of writing, prospective clinical data have not been reported in the public domain. Furthermore, findings from cadaveric or animal studies, or even simple bench-top data, are extremely limited. Since knowledge of the cementing technique is most prolific in relation to THR, as a starting point it is necessary to examine whether the same guiding principles can apply to hip resurfacing.

2.2 Specific cementing technique for DePuy articular surface replacement

It is assumed that certain basic principles for hip resurfacing, and in particular for the DePuy articular surface replacement (ASR) system, can be inferred from cemented THR. Firstly, for optimized fixation and load transfer, there must be a complete cement layer covering the entire prepared bone surface. An incomplete cement mantle can lead to mechanical weakness and an opportunity for wear debris ingress, thereby constituting a potential failure site [13]. Secondly, since the central pin of the DePuy ASR femoral prosthesis is designed to be unloaded (a feature which is positively reinforced by the fact that the pin reamer creates a cavity larger than the pin), cement must be prevented from entering the central hole. A cemented pin may result in unloading of the proximal implant, resulting in stress shielding and poor bone remodelling. Thirdly, and arguably most importantly, an excess of cement at the pole must be avoided. Not only do larger cement masses become hotter as the cement cures, but also excess cement at the pole can lead to incomplete seating of the component. This presents a very real danger to the success of the prosthesis and has been positively associated with early failure [14].

An analysis of current hip resurfacing methodologies, of cementing techniques for other joint replacements, and of the types and behaviours of acrylic bone cements leads to the conclusion that cementing techniques used in current hip resurfacing can be categorized into two types.

1. *Low-viscosity cementing technique.* Cement is poured into the femoral component in as low a viscosity state as possible prior to placement of the prosthesis.
2. *High-viscosity cementing technique.* Cement is applied to the prepared bone surface in a high-viscosity state prior to placement of the prosthesis.

It has been noted previously that the description of the viscosity of bone cements is somewhat arbitrary since variables such as time from mixing and environmental conditions during storage and use will significantly affect the viscosity. All cements can be made to exhibit lower or higher viscosities depending on the interplay of these variables. Nevertheless, it is conventional to classify cements as high or medium viscosity based on how their behaviour compares on a like-for-like basis. Table 1 shows such a classification for several commercial brands of bone cements. It can be inferred that, in general, the high-viscosity cements are more suitable for the resurfacing cementing technique, and the medium-viscosity cements for the low-viscosity technique. However, the differing characteristics of individual cements require that the specific method used in resurfacing must be tailored to an individual cement. It must also be borne in mind that the design of different femoral resurfacing components may significantly affect the result obtained from alternative cements and cementing techniques.

Table 1 Viscosities of commercial bone cements

High viscosity	Medium viscosity
SmartSet GHV (DePuy)	Endurance (DePuy)
Palacos R (Schering Plough)	Palamed (Biomet)
CMW 1 (DePuy)	Simplex (Stryker Howmedica)

3 CLINICAL PRACTICE: DESCRIPTION OF THE HIGH-VISCOSITY TECHNIQUE

What follows is a description of the current clinical practice of Mr Tadgh O'Sullivan (Lourdes Orthopaedic Hospital, Kilkenny, Ireland).

Prior to the application of any cement, a visible mark is made on the bone at the base of the plastic trial piece, using either a pen or a diathermy. This can later be used to verify correct placement of the component, since it is critical to avoid excessive impaction that can lead to microfracture of the bone. (In 25 cases, this marking technique was employed and was found to be accurate on all occasions.)

SmartSet GHV is mixed as per manufacturers instructions and left until 2.0–2.5 min (until not sticky). A pattie is formed of sufficient size to cover the circumference of the femoral head, and approximately 3–4 mm in thickness. The cement is applied to the head at approximately 4 min using direct thumb pressure. A neck vacuum vent is placed at the lesser trochanter and a stop is inserted in the guide hole to prevent cement ingress down the guide tunnel. The component is applied at between 4.5 and 6 min, at which point the component can often be seen being sucked down into place to the predetermined length without any further impaction required. It is critical that all the prepared bone is covered by the implant and that all the cement is contained within the component, with no cement left exposed. The high-viscosity cement is easily cleaned away, leaving nothing behind to create debris. The internal taper of the femoral component encourages excess cement to escape, avoiding a large cementophyte at the dome and eliminating the

initial cement lock as the component is presented to the prepared bone. (Compare this with parallel-sided (cylindrical) components that lock into place as soon as the component touches the bone and have to be forced into place.) To date, this technique has worked successfully with no cases of incomplete seating.

Additionally, the use of high-viscosity cement prevents tissue contamination that can occur with low-viscosity cement, and this type of cement is generally easier to work with, allowing a more controlled procedure. The cement has a longer working time under all temperature conditions, resulting in less time pressure on the operating team to achieve rapid seating of the component, as required with the low-viscosity technique.

Cadaver tests performed by Professor Michael Morlock (Hamburg) demonstrated that under torsional loading there was no failure of the cement interfaces; instead fracture occurred across the femoral neck. It was ascertained that 1–2 mm of interdigitation and 1–2 mm of cement mantle were optimum for fixation and stability. Minimizing the excess cement in this way also reduces the exothermic cement reaction, thereby helping to mitigate bone avascularity and death.

4 EXPERIMENTAL STUDIES: CEMENTING TECHNIQUE IN DEPUY ASR

As has been described, there is little published information concerning the cementing technique for hip resurfacing. To address this, a series of experiments was performed with dual purpose. Firstly, since the cement mantle is 'blind', i.e. restricted from view inside the prosthesis and obstructed radiographically (and therefore arguably unique amongst all cemented prostheses), it was required to observe typical cement mantles achieved using accepted surgical techniques, with emphasis on the depth of cement penetration, the degree of coverage around the bone surface, and the ease of seating of the prosthesis. Secondly, and with these results in mind, it was proposed to define and demonstrate an optimized method to achieve consistent reproducible cement results.

5 MATERIALS AND METHODS

5.1 Experiment 1: influence of cement viscosity (cement type) on interdigitation

For these studies, the two currently adopted methods of cementing technique were used:

(a) low-viscosity cement poured into the prosthesis prior to implantation;
(b) high-viscosity cement applied manually to the bone (finger packed).

SmartSet GHV cement was used for the high-viscosity technique and Endurance cement for the low-viscosity technique.

Cadaver studies were performed using four sets of paired femurs (under the guidance of Professor Michael Morlock at the Technical University Hamburg, Germany [**15**, **16**]). All cements were mixed according to their instructions using the Cemvac vacuum mixing system. Cemvac is a high-vacuum (93 per cent) syringe mixing system designed to eliminate porosity and to provide a fume-free mixing environment. In these experiments it provided reproducible efficient mess-free mixing.

5.1.1 Low-viscosity technique

For the low-viscosity technique, Endurance cement was mixed in the Cemvac system using 10–13 strokes of the mixing paddle. This took approximately 30–45 s. (It is important to note that true low-viscosity cements are not commercially common; therefore this technique calls for a medium-viscosity cement that is used very early, whilst still in the wet runny phase.) The cement was immediately extruded (i.e. 45–60 s) from the nozzle into the upturned prosthesis, filling the prosthesis to approximately one-quarter of the volume. The prosthesis was swirled to allow cement to flow around the inside of the implant and coat the walls and then quickly implanted on to the prepared bone (at approximately 90 s). It was seated using a standard impactor and the cement was left to harden. The whole process was performed as quickly as possible to ensure that the cement was low viscosity, with all the required hardware and accessories immediately to hand.

Typical timings (low-viscosity technique) are as follows: mix cement, 30–45 s; *then immediately* extrude cement into prosthesis, 45–60 s; *then immediately* insert prosthesis, 90 s.

5.1.2 High-viscosity technique

For the high-viscosity technique, SmartSet GHV cement was mixed using 10–13 strokes of the mixing paddle and then left until the dough time was reached (i.e. the time at which the cement did not stick to a gloved finger). The dough time of SmartSet GHV was typically 2 min, but this is commonly dependent on storage and theatre temperatures. In our experience, theatre temperatures in different

hospitals can vary between 18 and 23 °C, and country-to-country variation can result in an even greater range. Cooler temperatures (i.e. towards the lower end of this range) are typically more common, both for the comfort of the theatre staff and also to reduce the spread of infection, but at these temperatures the cement possesses a longer dough time, a longer working time, and a longer setting time. Conversely, warmer temperatures speed up the cement reaction and it is important to know how fast the dough time and setting time can be in the local conditions.

Once the dough time was reached, approximately half of the cement quantity was extruded into the hand, manipulated into a ball, and applied to the bone. The cement was slowly and meticulously finger packed into all areas of the prepared bone surface. Particular care was taken to avoid cement down the central pinhole, since the pin is designed to be unloaded in the DePuy ASR system (to ensure that load transfer occurs directly beneath the bearing surface). Excess cement was removed (with particular attention paid to the proximal-most surface), prior to placement of the prosthesis. Upon seating, a doughy ring of excess cement was collected around the base of the prosthesis; this was removed in good time prior to cement hardening.

Typical timings (high viscosity technique): mix cement, 45–60 s; extrude cement into hand, 2–3 min; finger-pack cement into bone, 3–4 min; insert prosthesis, 4–5 min.

For each cement type, once the cement had set, the cadaver bones were cross-sectioned using a water-cooled bandsaw, and the sections were analysed for quality and quantity of cement mantle.

5.2 Experiment 2: effect of cement mantle thickness on exotherm temperature

The exotherm temperature generated during the cement setting process can be significant; large volumes of cement can commonly achieve up to 90 °C [**17**] and can even exceed 100 °C at their peak temperature. Two methods were developed to evaluate the relevance of the exotherm in a hip resurfacing application.

5.2.1 Finite element analysis [**18**]

A solid model of a femur was generated from computer tomography scans of a cadaveric femur, from a donor of mass 77 kg. For each slice, the outer contour of the femur was defined as a polynomial spline (Mimics, Materialise NV, Leuven). These curves were then lofted together (I-DEAS10 EDS, Texas) to form a geometrical three-dimensional model of the femur. The femur was then virtually implanted with a suitably sized generic design of femoral component (Fig. 1).

Two models were generated in which the prosthesis was considered as having a cemented inner surface, with a thickness of either 1.5 mm or 3.5 mm. In both cases the metaphasal stem was modelled as debonded and over-reamed over its length. The models were meshed using linear tetrahedral elements. A more refined mesh (1.5–1.6 mm) was used in the head and neck regions, with larger elements (4–6.5 mm) being used in the femoral shaft to reduce computational running costs. Material properties were applied to the bone using the freeware program BoneMat [**19**]. Young's modulus for a bone element was calculated from the average apparent density determined from CT scans and automatically assigned to the finite element (FE) model using Bonemat. The apparent density was related to Young's modulus by

$$E = 7821\rho^{1.53}$$

where E is Young's modulus (MPa) and ρ is the apparent density (g/cm^3). Poisson's ratio for bone was assumed to be 0.3. The prosthesis was modelled as having Young's Modulus equal to 200 GPa and Poisson's ratio equal to 0.3. The PMMA bone cement was modelled as having Young's Modulus equal to 2.8 GPa and Poisson's ratio equal to 0.3.

A thermal analysis was performed to look at the potential impact on thermal necrosis. Polymerization of the bone cement during component fixation generates heat, which causes temperature rises in the cement, prosthesis, and surrounding tissues. Materials properties for the regions of the model corresponding to bone were assigned using data from the literature. The prosthesis was assumed to be manufactured from Co–Cr alloy, and all materials were assumed to be homogeneous and isotropic. Material and other properties required for the specification of the model are shown in Table 2. The temperature of the nodes on the whole of the external surface of the cortical bone was fixed at body temperature [37° C (310 K)] throughout the simulation.

Table 2 Material properties (T is temperature)

Material	Density (kg/m^3)	Specific heat capacity (J/kg K)	Thermal conductivity (W/m^2 K)
Cortical bone	2.1×10^3	1.26×10^3	0.38
Prosthesis	8.87×10^3	0.45×10^3	14.6
Bone cement	1.1×10^3	$6.5T+1.25\times10^3$	0.2

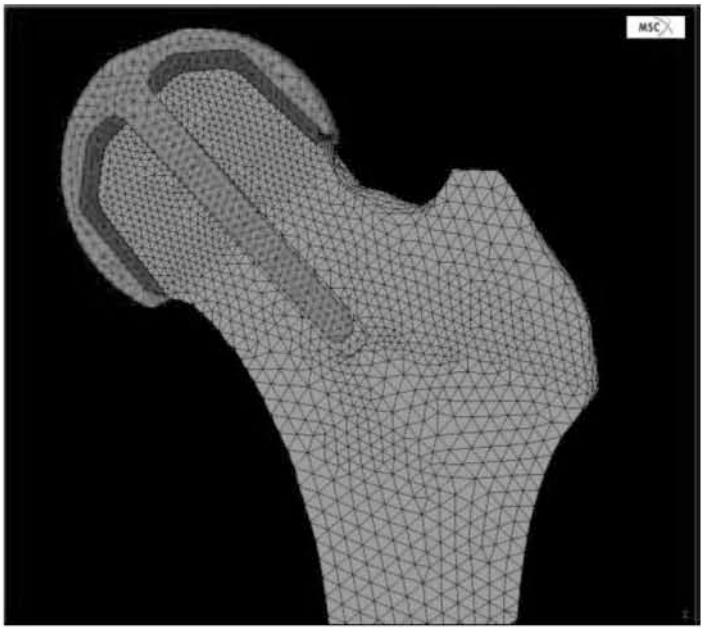

Fig. 1 FE model of a resurfaced femoral head

The initial temperature of the cement and prosthesis was room temperature [23 °C (296 K)] and the initial temperature of the bone component was body temperature. The cement was given an initial (very small) degree of polymerization (6×10^{-6}), this being necessary to initiate the polymerization in the numerical model (see below). The cement curing reaction was modelled using the kinetic equation

$$S = K_0 \, e^{-E_a/RT} (\alpha_{max} - \alpha)^n \alpha^m \quad (1)$$

relating the instantaneous local volumetric heat generation rate S in the cement, to the local degree α of polymerisation of the cement, and the local temperature T via an exponential function describing the effect of temperature on the reaction rate, where K_0, m, and n are constants, E_a is the activation energy, and R is the universal gas constant. The quantity α_{max} represents the maximum degree of polymerization, and for the present study was set to unity.

The constant K_0 and the activation energy E_a used in these equations were determined for CMW 1® cement using differential scanning calorimetry. These values and others required for specification of the model are shown in Table 3. The curing model was incorporated into the FE model using the procedure illustrated in Fig. 2. Each simulation was allowed to run for a total of 2000 s to ensure complete polymerization throughout the cement mantle and return of bone temperatures to below the threshold for cell necrosis (44 °C; see below).

Table 3 Constants used in heat generation rate calculations

Equation constant	Value
K_0	9484.37
E_a	31286 J
R	8.314 kg/mol K
M	0.98
N	1.064

Necrosis of the bone is a function of time and temperature. In this study, the necrosis index was calculated at each of three nodes on a line running from the cement–bone interface into the bone, as shown in Fig. 2.

For each node and each time step in the analysis, a necrosis index increment was calculated by dividing the time step size by the time to thermal damage at temperature T, where T is the average temperature in the element over the time step. The time to thermal damage at temperature T was calculated using an exponential function fitted to the data of Moritz and Henriques [**20**]. In order to avoid problems with extrapolating beyond the range of temperatures for which Moritz and Henriques provide data, temperatures above 65 °C were assumed to cause a necrosis

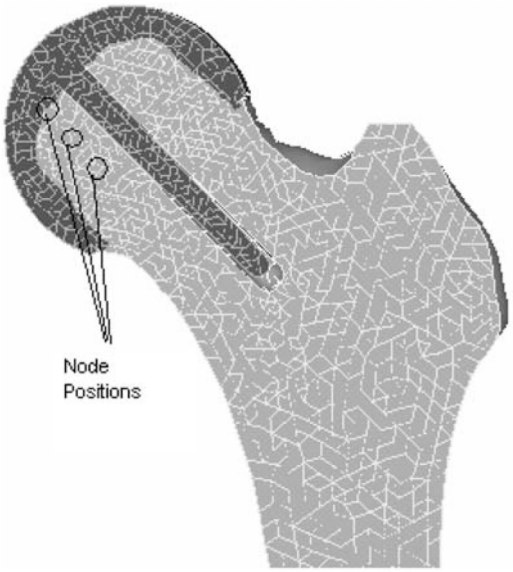

Fig. 2 FE analysis: position of nodes to record temperature

index increment of 1 for the time step, and temperatures below 44 °C a necrosis index increment of 0. Finally, the necrosis index increments were summed to calculate the necrosis index, with total values at the end of the analysis greater than 1 indicative of thermal necrosis of the bone (Fig. 3).

5.2.2 Cement exotherm measurements

Cement specimen discs (SmartSet GHV) were created in five different thicknesses (2.5, 4, 6, 9, and 13 mm), and a thermocouple wire was inserted into the exact centre of each cement specimen before the cement was set. This was based on the accepted International standard for acrylic bone cement (ISO 5833:2002 [**17**]), but with some modifications; a stainless steel plate with a hole of 80 mm diameter through the middle was used, and placed on to a wooden block to create a solid base. This was intended to mimic crudely a cemented prosthesis, i.e. a thermally conductive metal surface (the prosthesis) against a non-conductive substrate (the bone), in order to model the dissipation of heat away from the cement during the polymerization reaction. The thermocouple wires were attached to a digital reader (Yokogawa 3081 hybrid recorder), and the thermal profile and peak exotherm temperatures were recorded. A graph was plotted of cement thickness versus peak exotherm temperature.

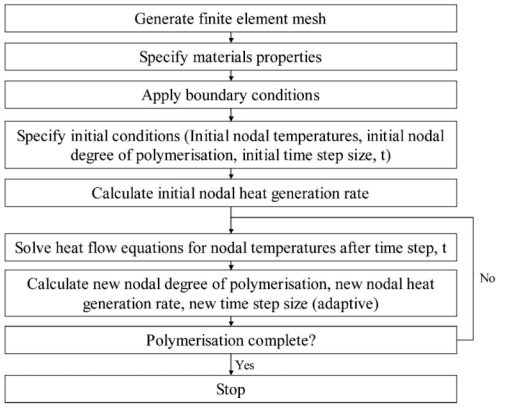

Fig. 3 Incorporation of the kinetic equation into the FE model

6 RESULTS

6.1 Experiment 1: influence of cement viscosity (cement type) on interdigitation

6.1.1 Low-viscosity technique

There is a significant depth of cement penetration with the low-viscosity technique, typically greater than 10 mm (Fig. 4). This very large degree of cement penetration is most prominent directly at the pole (or proximal-most part), which is consistent with the pressures exerted in this direction during placement of the prosthesis. Conversely, there is very little, if any, cement penetration around the circumference, consistent with the lack of pressure exerted in this direction during placement of the prosthesis.

Another interesting observation was the incomplete seating of the prosthesis (Fig. 5). This was seen

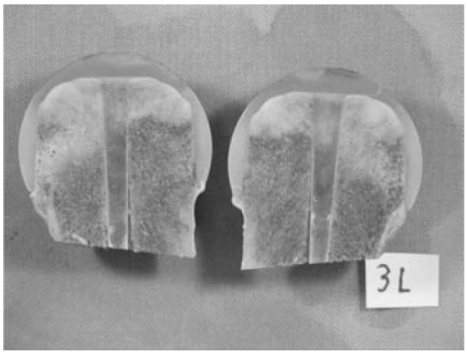

Fig. 4 Low-viscosity cement: excessive penetration

Fig. 5 Low-viscosity cement: incomplete seating

in almost every case and is defined by a clearance of greater than 1 mm between implant and bone (this is the maximum clearance given by reamers). Specimens were consistently created where the prosthesis had at least 5 mm of stand-off. In fact, in the very best case the prosthesis was still approximately 2 mm too high.

6.1.2 High-viscosity technique

A much more consistent cement mantle was seen with the high-viscosity technique. The depth of cement penetration was typically 2 mm. A layer of interdigitated cement was present around the entire bone surface (i.e. in all the places it had been applied) (Fig. 6) and, significantly, complete seating of the prostheses was achieved (Fig. 7).

6.2 Experiment 2: effect of cement mantle thickness on exotherm temperature

6.2.1 Finite element analysis

Increasing the cement thickness increases the extent of the zone of necrosis in the bone surrounding the cement. The thin cement mantle produces a maximum temperature of 47 °C (Fig. 8); the thick cement mantle produces a maximum temperature of 57 °C (Fig. 9). This 10 °C difference in temperature reduces the amount of time that it takes for bone necrosis to take place. It also causes the bone to experience these elevated temperatures for an extended period. These two factors produce a necrosis depth of greater than 2 mm when a thick cement mantle is used.

6.2.2 Cement exotherm measurements

Increasing the cement thickness increases the peak exotherm temperature (Fig. 10). At the maximum thickness (12.6 mm) the cement achieved a peak curing temperature of 80.8 C. At the minimum thickness (2.5 mm) the cement achieved a peak curing temperature of 37.4 °C.

7 DISCUSSION

During the course of these experiments a number of factors were evaluated that may be important to the

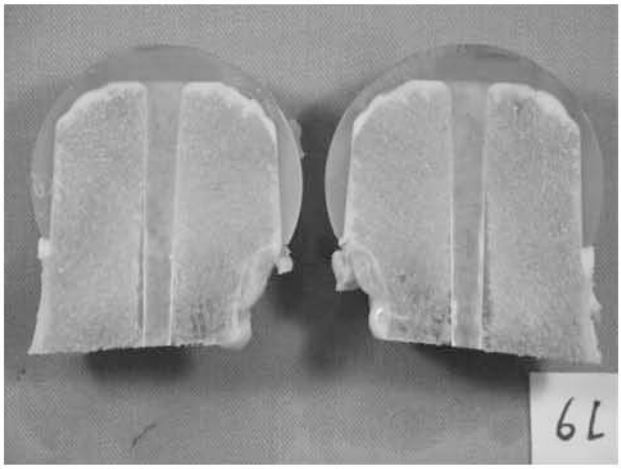

Fig. 6 High-viscosity cement: controlled even interdigitation

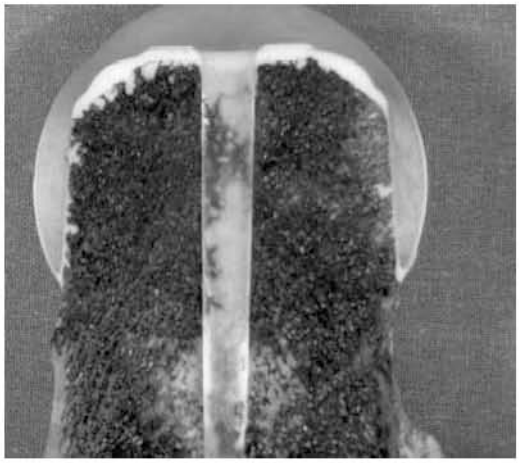

Fig. 7 High-viscosity cement: complete seating

correct implantation and subsequent clinical success of the ASR resurfacing prosthesis. These factors can be combined to create a set of guidelines for optimized clinical implantation with respect to cementing technique.

The outcome of this work shows that the low-viscosity technique can commonly lead to excessive cement penetration in the proximal femoral head, and that a more consistent controlled cement mantle can be achieved with the high-viscosity technique. Consequently an appropriate technique should be used to minimize the build-up of excessive cement, which in turn helps to reduce the exothermic cement temperature and also helps to ensure correct seating of the prosthesis.

The cement polymerization reaction involves the conversion of liquid momomer (MMA) to solid polymer (PMMA). This is a free-radical polymerization, induced and controlled by the availability of a peroxide initiator (BPO) in the powder and an amine activator (dimethyl *p*-toluidine) in the liquid. The conversion of monomer to polymer results in the creation of energy, and this energy is released as heat. Since the quantity of energy is directly related to the quantity of cement, larger masses became hotter than smaller masses.

At first, this would appear a significant issue, considering that protein denaturation occurs at 44 °C, with the associated risk of thermal necrosis to bone and soft tissue. However, in the case of a

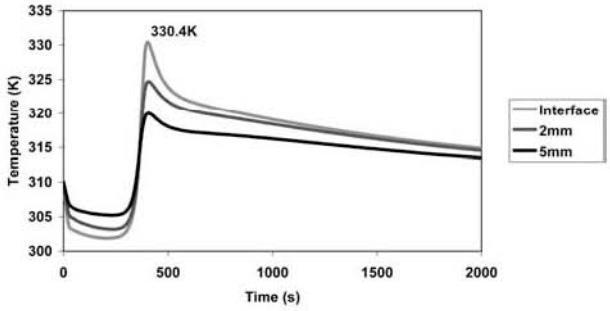

Fig. 8 FE exotherm temperature for a thin cement mantle

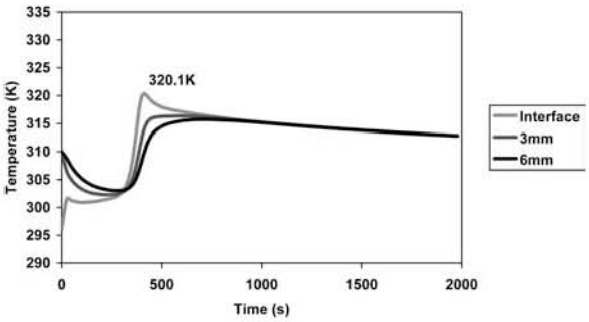

Fig. 9 FE exotherm temperature for a thick cement mantle

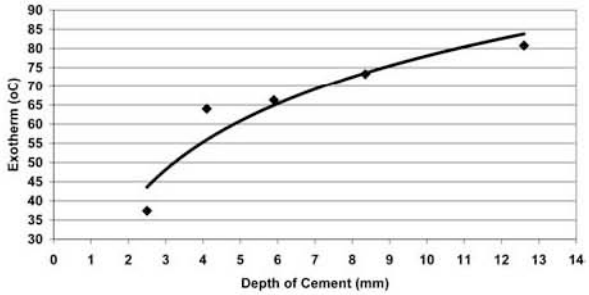

Fig. 10 Cement thickness versus peak exotherm temperature

conventional cemented femoral component (in THR), a number of factors may potentially combine to mitigate the thermal risk: the relatively large bulk of the metal hip prosthesis, the large surface area of the cement mantle, and the fluid flow around the femur, all acting as heat sinks, dissipating heat away from the cement. Kuhn [**21**] discussed the fact that, whilst the cement exotherm can achieve above 80 °C in the laboratory (using the procedure in ISO 5833:2002 [**17**], for example), this only translates to a maximum of 40–50 °C in the clinical setting (in a conventional cemented femoral stem, for example). However, there are differences between a cemented femoral stem and a hip resurfacing construct; the large implant, surface area, and fluid flow are not as significant in resurfacing; so a controlled technique is required and the creation of an optimum cement mantle is vital.

8 CONCLUSION

The outcome of this work shows that the low-viscosity technique can commonly lead to excessive cement penetration in the proximal femoral head, and that a more consistent controlled cement mantle can be achieved with the high-viscosity technique. Consequently, it is prudent to recommend that an appropriate technique should be used to minimize the build-up of excessive cement, which in turn helps to reduce the exothermic cement temperature and also helps to ensure correct seating of the prosthesis. A combination of these factors is potentially important to the clinical success of the ASR resurfacing procedure.

ACKNOWLEDGEMENTS

The present authors acknowledge Mr Tadgh O'Sullivan for his input regarding cementing technique in clinical practice. They acknowledge Professor Michael Morlock and Dr Nick Bishop (Technical University Hamburg, Germany) for their guidance and expertise in the cadaver studies and mechanical testing, and also Dr Mark Taylor, Dr Andrew New, and Adam Briscoe (all University of Southampton, UK) for their guidance and expertise in the FE Analyses.

REFERENCES

1 **Bauer, W.** Rohm & Haas, DRP Patent 652821, Verfahren zür Herstellung Prothesen für zarnarztliche 2 weche, 1935.
2 Kulzer & Co., GmbH, DRP Patent 737058, Verfahren zür Herstellung von Prothesen für zarnarztliche order andere zweck aus polymerisierten organischen Verbindungen, 1936.
3 **Kleinschmitt, O.** Plexiglas zur Deckund von Schadellucken. *Chirurg*, 1941, **13**, 273.
4 Kulzer & Co., GmbH, DRP Patent 973590, Verfahren zür Herstellung von Prothesen für zahnarztliche order andere zweck aus polymerisierten organischen Verbindungen, 1943.
5 **Klaer, S.** Preliminary report on arthroplasty by the use of acrylic head. Cliniquiem Congress International de Chirurgie Orthopedique, Stockholm, 1951.
6 **Haboush, E. J.** A new operation for arthroplasty of the hip based on biomechanics, photoelasticity, fast setting dental acrylic and other considerations. *Bull. Hosp. Jt Dts. N.Y.*, 1953, **14**, 242–277.
7 **Charnley, J.** Anchorage of the femoral head prosthesis of the shaft of the femur. *J. Bone Jt Surg.*, 1960, **42B**, 28–30.
8 **Gruen, T. A., Markoff, K. L.,** and **Amstutz, H. C.** Effects of laminations and blood entrapment on the strength of acrylic bone cement. *Clin. Orthop. Rel. Res.*, 1976, **119**, 250–255.
9 **Charnley, J.** *Acrylic Cement in Orthopaedic Surgery*, 1972, p. 19 (Churchill Livingstone, Edinburgh).
10 **Malchau, H.** and **Herberts, P.** Prognosis of total hip replacement, surgical and cementing technique in THR: a revision-risk study of 134,056 primary operations. Scientific Exhibition Presented at the

62nd Annual Meeting of the American Academy of Orthopaedic Surgeons, Atlanta, Georgia, USA, 22–26 February, pp. 1–12.

11 **Havelin, L.,** *et al. Prospective Studies of Hip Prosthesis and Cements: A Presentation of the Norwegian Arthroplasty Register 1987–1999*, p. 7.

12 **Malchau, H.** and **Herberts, P.** How outcome studies have changed total hip arthroplasty practices in Sweden. *Clin. Orthop.*, 1997, **344**, 44–60.

13 **Amstutz, H. C.** History of hip resurfacing, University of California, Los Angeles, Medical Center, http://www.jri-oh.com/hipsurgery/Surface.asp.

14 **Amstutz, H. C.** Fracture of the neck of femur after surface arthroplasty of the hip. *J. Bone Jt Surg.*, 2004, **86A**(9), 1874–1877.

15 **Bishop, N.** and **Morlock, M.** Effect of high and low viscosity cementing technique on cement penetration and torsional stability. Unpublished data, November 2003.

16 **Bishop, N.** ASR hip resurfacing femoral component: influence of cementing technique on cement penetration and distribution – a study with cadaveric femoral heads. Unpublished data, June 2004.

17 ISO 5833:2002, *Implants for surgery – acrylic resin cements*, 2002 (International Standardization Organization, Geneva).

18 **Briscoe, A., Taylor, M.,** and **New, A.** The potential for bone thermal necrosis during cementation of the femoral head resurfacing component. Unpublished data, School of Engineering Sciences, University of Southampton, April 2004.

19 **Zannoni, C., Mantovani, R.,** and **Viceconti, M.** Material properties assignment to finite element models of bone structures: a new method. *Med. Engng Physics*, 1998, **20**(10), 735–740.

20 **Moritz, A. R.** and **Henriques, F. C.** The relative importance of time and surface temperature in the causation of cutaneous burns. *Am. J. Pathol.*, 1947, **23**, 695–720.

21 **Kuhn, K. D.** *Bone Cements: Up-to-Date Comparison of Physical and Chemical Properties of Commercial Materials*, 2000, p. 27 (Springer-Verlag, New York).

Appendix V – List of Acronyms

MMA	Methylmethacrylate
PMMA	Polymethylmethacrylate
PTFE	Polytetrafluoroethylene
UHMWPE	Ultra High Molecular Weight Polyethylene
PVDC	Polyvinylidene Chloride
N, N-DMPT	Nitro, Nitro-dimethylparatoluidene
HA	Hydroxyapatite
Et-O	Ethylene Oxide
THR	Total Hip Replacement
THA	Total Hip Arthroplasty
TKR	Total Knee Replacement
TKA	Total Knee Arthroplasty
DSC	Differential Scanning Calorimetry
CT	Computed Tomography
KAS	Kissinger-Akahira-Sunose
FEM	Finite Element Method
FEA	Finite Element Analysis
UPF	User Programmable Function

Appendix VI - List of Biological Terms

Bone cement	Any material used as a grout to fix prostheses to bone. In this thesis, it refers almost exclusively to acrylic bone cement based on polymethylmethacrylate (PMMA).
Cancellous bone	Porous, sponge-like bone material, typically found close to joints.
Cortical bone	Dense bone material, typically found in the shafts of the long bones (e.g. femur, tibia) or at the bone surface.
Arthritis	Inflammation of a joint, usually accompanied by pain, swelling and stiffness.
Osteoarthritis	Arthritis relating to degeneration of the joint cartilage and surrounding bone.
Prosthesis	Device implanted into patient to replace dysfunctional or painful tissue.
Arthroplasty	Operation for construction of new movable joint *in vivo*.
Lysis/osteolysis	Active resorption of bone tissue as part of an ongoing disease process.
Subluxation	Incomplete or partial dislocation of a joint.
Acetabulum	Concave part of the pelvis meets with the femur in the hip joint.
Femur	Commonly referred to as the thigh bone this is the proximal leg bone.
Tibia	Commonly referred to as the shin bone this, along with the fibula, constitutes the distal leg bones.

Aseptic loosening	Loosening attributable to non-infection related causes.
Synovial	Group of musculoskeletal joints which allow a large range of motion.
Osteocyte/osteoblast/osteoclast	Bone cells involved in the maintenance of the bony matrix including increases and decreases of local bone density.
Primary	First replacement of dysfunctional or painful tissues at a joint.
Revision	Subsequent replacement of previously implanted joints after the joint replacement has failed.
Radiolucency	Evidence from a radiograph showing an area of low material density in the bone matrix.
Necrosis	The death of any living tissue often referring specifically to bone cell death.
Proximal	Of an anatomical structure, closer to a point of reference, usually the mid-line or notional mid-point of the body. E.g. the hip is proximal to the knee, meaning the hip is closer to the mid-point of the body than the knee.
Distal	Of an anatomical structure, further from a point of reference, usually the mid-line or notional mid-point of the body. E.g. the knee is distal to the hip, meaning the knee is further from the mid-point of the body than the hip.
Interdigitation	The mechanical interlock between two materials e.g. the cement interdigitates with the cancellous bone.
In vitro	Outside of the body.

In vivo	Inside of the body.
Resurfacing	Arthroplasty involving replacement of just the dysfunctional joint surfaces with minimal removal of additional healthy tissue.
Computed tomography (CT)	Medical imaging technique whereby a series of radiographs are taken around a common axis and digital processing is then used to generate a three-dimensional image.